Case in Points: Developing a Patient-specific Model of the Human Left Ventricle using the Material Point Method

NATHAN DANIEL GAVIN

Case in Points: Developing a Patient-specific Model of the Human Left Ventricle using the Material Point Method

Nathan Daniel Gavin

A thesis presented for the degree of

Doctor of Philosophy

Department of Engineering

Durham University

United Kingdom

May 2024

"*Near, far, wherever you are, I believe that the heart does go on...*"

— Celine Dion

Case in Points: Developing a Patient-specific Model of the Human Left Ventricle using the Material Point Method

Nathan Daniel Gavin

Abstract

The heart is an extremely important organ in the human body and has been studied using numerical models for many years, typically using Finite Element Analysis to model the myocardium. However, heart simulations will normally require large deformation mechanics which means that a finite element mesh may encounter large mesh distortion and volumetric locking. An intensive pre-processing stage is also required, using various software to segment the medical imaging data and generate the mesh.

The Material Point Method (MPM) discretises a physical domain using material points which deform through an unchanging background finite element mesh. This work develops the "tools" used to produce a patient-specific model of the Left Ventricle (LV) and analyse stress in the myocardium without the need for user input after the segmentation stage. B-spline boundary representations of the endocardial and epicardial surfaces are created using the segmented MRI data of a patient. These surfaces have two uses, to aid in the generation of the material point domain and to apply non-conforming boundary conditions throughout the analysis. Myocardium is often modelled as a rubber-like material, therefore, isotropic and anisotropic hyperelastic models are implemented here. As large deformation, non-linear analyses often encounter highly non-linear responses, the arc-length method is adapted for the MPM to overcome this issue and aid in validation of the material models. A study is performed using this new framework to investigate the effects of patient geometry and material properties on the stress and displacement fields of the LV model. Through this study, it was found that the orientation of the muscle fibres has the most substantial effect on the results of the analysis.

Supervisors: William M. Coombs, John C. Brigham and Charles E. Augarde

Declaration

The work in this thesis is based on research carried out in the Computational Mechanics Node, Department of Engineering, Durham University. No part of this thesis has been submitted elsewhere for any other degree or qualification, and it is the sole work of the author unless referenced to the contrary in the text.

Some of the work presented in this thesis has been published in conference proceedings and journals - the relevant publications are listed below.

Conferences

UKACM 2022 - Nottingham:
Oral presentation,"MRI to MPM: Developing a Patient-specific Material Point Method Model of the Human Heart".
ESMC 2022 - Galway:
Oral presentation, "MRI to MPM: Developing a Patient-specific Material Point Method Model of the Human Heart".
UKACM 2023 - Warwick:
Oral presentation, "On the development of a material point method compatible arc-length solver for large deformation solid mechanics".

Journal articles

N. D. Gavin *et al.*, 'On the implementation of a material point-based arc-length method,' *International Journal for Numerical Methods in Engineering*, vol. 125, no. 9, e7438, 2024

Acknowledgements

The following research would not have been possible without the generous funding from the UKRI Engineering and Physical Sciences Research Council (Grant number EP/T518001/1), for which I am very grateful. I would also like to thank the Newcastle Medical Resonance Centre (NMRC) for providing me with the medical imaging data, this work would not exist without it.

This PhD has been an amazingly fulfilling experience, if not unbelievably stressful at times. The past three years have helped me develop academically and as a person. I would not have been able to do this without the incredible supervision of Will Coombs, John Brigham and Charles Augarde. Thank you for your patience and guidance to help me through this journey and the many off topic conversations.

I want to thank the Computational Mechanics Research Node in the Department of Engineering, Durham University and the Computational Diagnostics & Inverse Mechanics group in the Swanson School of Engineering, University of Pittsburgh. Thank you for our many discussions and allowing me to bounce ideas around, hopefully you found them as helpful as I did.

I would also like to acknowledge the Grey college community of which I have been part of since I arrived in Durham as a scared 18 year old back in 2015, Grey will always feel like a second home. Thank you to all the people that I am lucky enough to call my friends, who have supported me through this. To Izaak, Hugo and Callum who have gone through the PhD journey alongside me, thank you for all your help, whether it was just that little “keep it up” or the chat over a pint, it really gave me the gusto to push to the end.

Finally, to Darren, Jenni and Chloe and the rest of my family, thank you for your love and support (and the many jokes about me hopefully finishing school soon), your encouragement through all of this has helped me keep going. I love you all!

Contents

List of Figures

List of Tables

List of Algorithms

Acronyms

AMPLE	A Material Point Learning Environment
CPDI	Convected Particle Domain Interpolation
CPDI2	Second-order Convected Particle Domain Interpolation
cpGIMPM	contiguous particle Generalised Interpolation Material Point Method
CT	Computed Tomography
CVD	Cardiovascular Disease
ED	End-Diastole
EDP	End-Diastolic Pressure
ES	End-Systole
FE	Finite Element
FEA	Finite Element Analysis
FEM	Finite Element Method
FLIP	FLuid Implicit Particle
GIMP	Generalised Interpolation Material Point
GIMPM	Generalised Interpolation Material Point Method
H-O	Holzapfel-Ogden
IBM	Implicit Boundary Method
LV	Left Ventricle

MMS	Method of Manufactured Solutions
MP	Material Point
MP-BALM	Material Point-Based Arc-Length Method
MPM	Material Point Method
MRI	Magnetic Resonance Imaging
N-R	Newton-Raphson
NMRC	Newcastle Magnetic Resonance Centre
NURBS	Non-Uniform Rational B-Splines
PIC	Particle-In-Cell
RV	Right Ventricle
uGIMPM	unchanged Generalised Interpolation Material Point Method

Nomenclature

Identifiers

$(\cdot)^{\pm}$	$(\cdot)$ associated with positive/negative elements of a face
$(\cdot)^{\mathrm{p}}$	plastic component of $(\cdot)$
$(\cdot)^{a}$	analytical value of $(\cdot)$
$(\cdot)^{base}$	$(\cdot)$ associated with baseline LV model
$(\cdot)^{endo}$	$(\cdot)$ associated with endocardial surface
$(\cdot)^{epi}$	$(\cdot)$ associated with epicardial surface
$(\cdot)^{E}$	$(\cdot)$ associated with mesh element
$(\cdot)^{e}$	elastic component of $(\cdot)$
$(\cdot)^{h}$	calculated value of $(\cdot)$
$(\cdot)^{model}$	$(\cdot)$ associated with modified LV model
$(\cdot)_{B}$	$(\cdot)$ associated with the boundary
$(\cdot)_{c}$	$(\cdot)$ associated with material point domain corner
$(\cdot)_{dev}$	deviatoric component of $(\cdot)$

$(\cdot)_f$	$(\cdot)$ associated with muscle fibre
$(\cdot)_G$	$(\cdot)$ associated with ghost stabilisation
$(\cdot)_{iso}$	isochoric component of $(\cdot)$
$(\cdot)_k$	$(\cdot)$ associated with iteration k
$(\cdot)_m$	$(\cdot)$ associated with the material point domain edge midpoint
$(\cdot)_n$	$(\cdot)$ associated with load step n
$(\cdot)_p$	$(\cdot)$ associated with material point
$(\cdot)_s$	$(\cdot)$ associated with muscle sheet
$(\cdot)_{vol}$	volumetric component of $(\cdot)$
$(\cdot)_v$	$(\cdot)$ associated with background mesh node
$\Delta(\cdot)$	increment in $(\cdot)$
$\delta(\cdot)$	iterative increment in $(\cdot)$

Scalars

$\alpha_1, \alpha_2, \alpha_3$	arc-length constraint quadratic equation coefficients
α_{al}	arc length iteration exponent
α_k, β_k	B-spline sample point tangent coefficient
α_{pr}	extrapolation coefficient
$\bar{\lambda}_i^*$	isochoric principal stretch
$\bar{\lambda}_i$	principal stretch
$\bar{\sigma}$	net vertical stress
$\bar{\varepsilon}^{\mathrm{p}}$	accumulated plastic strain

$\bar{p}$	Lagrange multiplier
$\Delta\lambda$	load factor increment
$\delta\lambda$	iterative load factor increment
Δl	arc length
Δl_0	initial arc length
ϵ	error measure
ϵ_σ	relative stress error
ϵ_c	B-spline curve local interpolation fitting error
ϵ_f	B-spline least squares fitting error
ϵ_r	relative inner radius error
ϵ_u	relative displacement error
ϵ_V	relative volume error
γ_{al}	minimum arc length multiplier
γ_G	ghost stabilisation penalty parameter
λ	load factor
μ	shear modulus
μ^*	normalised shear modulus
μ_r, α_r	isotropic Ogden model material parameters
ν	Poisson's ratio
ν_{ext}	external stiffness – Poisson's ratio
ϕ^0	level set

Ψ	strain-energy function
ψ	arc-length constraint scaling parameter
ρ	density
ρ_0	initial density
σ_{ij}	Cauchy stress
σ_{lim}	Prandtl limit load stress
σ_y	uniaxial yield stress
$\sigma_y(\bar{\varepsilon}^{\mathrm{p}})$	current von Mises yield stress
σ_y^0	initial von Mises yield stress
τ_i	principal Kirchhoff stress
θ	angle
θ_f	muscle fibre rotation angle
θ_s	muscle sheet rotation angle
$\tilde{\xi}, \tilde{\eta}$	integration space local coordinate
ς	B-spline control point position coefficient
ξ, η	local coordinates
ξ_{ck}, η_{ck}	B-spline curve/surface closest knot local coordinate
ξ_d, η_d	B-spline curve/surface foot point local coordinate
ξ_i	B-spline knot value
ζ	B-spline least squares fitting strength parameter
A	enclosed area

a, b, a_i, b_i	Holzapfel-Ogden model material parameters ($i = f, s, fs$)
$a_{k,j}$	B-spline basis function derivative coefficient
a_{mesh}	mesh refinement factor
B	plate ligament width
C_1, C_2	material constants
D	diameter
d_r	transmural depth ratio
E	Young's modulus
E_{ext}	external stiffness – Young's modulus
F	force
f_{err}	residual force error
F_R	reaction force
g	gravitational acceleration
g_0	initial gravitational acceleration
g_n	gravitational acceleration at end of analysis
H	height
h	mesh size
H^{p}	plastic hardening modulus
h_f	size of element face
h_s^{max}	maximum background mesh size
I_1, I_2, I_3	principal invariants

I_{4f}, I_{4s}	directional invariant
I_{8fs}	coupling invariant
J	volume ratio
J_2	second invariant of the deviatoric stress
K	bulk modulus
k_{des}	desired number of Newton-Raphson iterations
k_n	actual number of Newton-Raphson iterations
K_{ref}	baseline model bulk modulus
L	length
L_0	initial length
L_0^x, L_0^y, L_0^z	background mesh lengths
l_{p0}	initial material point domain half-length
l_p	material point domain half-length
m	number of B-spline knots
n	number of non-zero p-degree B-spline basis function
n_ξ, n_η	number of B-spline curve/surface control points
$n_{bp}, n_{bp}^\xi, n_{bp}^\eta$	number of B-spline boundary sampling points
n_{dp}	number of data points
n_D	number of dimensions
n_{el}	number of elements
$n_{el}^c, n_{el}^l, n_{el}^r$	number of elements in circumferential, longitudinal and radial direction

$n_{el}^x, n_{el}^y, n_{el}^z$	number of elements in x, y and z directions
n_{en}	number of element nodes
n_{gp}	number of Gauss points
$N_{i,p}$	B-spline basis function
$N_{i,p}^{(k)}$	k-th derivative of the B-spline basis function with respect to local coordinates
n_k, n_l	number of B-spline curve/surface sampling points
n_{ls}	number of B-spline curve sampling points for least squares fitting
n_{max}	prescribed maximum number of load steps
n_{mp}	number of material points
n_{mp}^e	number of material points per direction in an element
n_{mp}^{tar}	target number of material points
n_s	number of subdivision steps
n_v	number of background mesh nodes
P	pressure
p	B-spline order
P^*	normalised pressure
R	radius
r	radial distance from origin
R_i	initial inner radius
r_i	deformed inner radius
r_l, s_k	B-spline sampling point chord length

R_o	initial outer radius
S	far field stress
S_{vp}	basis function of particle p associated with node v
S_v	standard FE shape function
S_v^{app}	approximate CPDI1 basis function
T	thickness
U	prescribed displacement
$U(J)$	volumetric component of strain-energy function
V_0	initial volume of physical domain
V_p	current material point volume
V_p^0	initial material point volume
V_p^n	material point volume in previous configuration
W	width
w_i	integration weight associated with point i
w_p	weight associated with material point
x, y, z	current global coordinates
Y	original vertical position

Tensors

$[I_s]$	fourth order symmetric identity tensor
$[B^D]$	fourth-order tensor of left Cauchy-Green strain
$[L^D]$	derivative of tensor logarithm of left Cauchy-Green strain

$[S^D]$	fourth-order tensor of Cauchy stress
$\boldsymbol{\sigma}$	Cauchy Stress
$\mathbb{P}$	isochoric projection tensor

Vectors

$\bar{\mathbf{f}}_t$	prescribed traction forces
$\bar{\mathbf{u}}$	prescribed displacement
$\mathbf{f}_b$	body force
$\mathbf{f}_t$	boundary traction forces
$\mathbf{u}$	displacement
$\mathbf{v}$	velocity
$\mathbf{w}$	virtual displacement
$\{\bar{f}\}$	deformed material fibre direction
$\{\bar{s}\}$	deformed material sheet direction
$\{\delta\bar{u}\}$	iterative tangential displacement increment
$\{\Delta u\}$	nodal displacement increment
$\{\delta u\}$	iterative nodal displacement increment
$\{\delta u^*\}$	iterative Newton-Raphson displacement increment
$\{\Delta u_n\}$	change in nodal displacement in previous load step
$\{\Delta u_p^a\}$	material point displacement from previous load step
$\{\Delta u_s\}$	scaled nodal displacement increment
$\{\sigma\}$	Cauchy stress vector

$\{\tau\}$	Kirchhoff stress vector
$\{\tilde{X}\}$	global coordinates at start of load step
$\{\varepsilon\}$	strain vector
$\{\Xi\}, \{H\}$	B-spline knot vector
$\{B_{k,l}(\xi, \eta)\}$	Bézier surface patch
$\{C(\xi)\}$	B-spline curve global coordinate
$\{C^{(k)}(\xi)\}$	k-th derivative of B-spline curve with respect to local coordinates
$\{C^{\perp}(\xi)\}$	normal to B-spline curve
$\{C_i(\xi)\}$	Bézier curve segment
$\{D_k\}$	tangent to B-spline sampling point (three-point method)
$\{d_k\}$	chord length gradient
$\{f^{body}\}$	body force vector
$\{f^{ext}\}$	external force vector
$\{f_0^{ext}\}$	initial applied external force
$\{f^{int}\}$	internal force vector
$\{f^R\}$	residual force vector
$\{f_0\}$	material fibre direction
$\{f_p\}$	point force associated with a material point
$\{f_t\}$	traction force vector
$\{f_v\}$	difference between external and internal force vectors
$\{n\}$	unit normal vector

$\{n_0\}$	material normal direction
$\{P\}$	B-spline control point vector
$\{P^{(k,l)}\}$	control point for derivative of B-spline surface
$\{S(\xi,\eta)\}$	B-spline surface global coordinate
$\{S^{(k,l)}(\xi,\eta)\}$	derivative of B-spline surface with respect to local coordinates
$\{S_p^{endo}\}$	foot point on endocardial B-spline surface
$\{S_p^{epi}\}$	foot point on epicardial B-spline surface
$\{s_0\}$	material sheet direction
$\{t\}$	prescribed traction force
$\{u\}$	displacement vector
$\{u_n\}$	previously converged nodal displacement
$\{u_p\}$	material point displacement vector
$\{u_v\}$	nodal displacement vector
$\{V_k\}$	tangent vector to B-spline sampling point (five-point method)
$\{X\}$	original (reference) coordinates
$\{x\}$	current global coordinates
$\{x_m\}$	current global coordinate of material point domain edge midpoint
$\{x_p\}$	current global coordinates of material point
$\{x_v\}$	current global coordinates of element node
$\{\bar{t_i}\}$	eigenvector of left Cauchy-Green strain
$\{C(\xi_d)\}$	foot point on a B-spline curve

$\{D_{k,l}^{\xi\eta}\}$	B-spline surface inner control point positioning vector
$\{D_{k,l}^{\xi}\}, \{D_{k,l}^{\eta}\}$	B-spline surface inner control point tangent vector
$\{J_B\}$	boundary Jacobian vector
$\{P^{ls}\}$	B-spline least squares fitting control point vector
$\{q_k\}$	direction vector between B-spline sampling points
$\{Q_k\}, \{Q_{k,j}\}$	B-spline sampling point
$\{r^{ls}\}$	B-spline least squares fitting residual vector
$\{S^{\perp}(\xi,\eta)\}$	normal to B-spline surface
$\{T_{k,l}^{\xi}\}, \{T_{k,l}^{\eta}\}$	tangent vector to B-spline surface sampling point in ξ and η direction
$\{T_k\}$	unit tangent vector to B-spline sampling point (five-point method)
$\{u_c\}$	circumferential direction vector
$\{u_l\}$	longitudinal direction vector
$\{u_r\}$	radial direction vector
$\{X_d\}$	data point global coordinate

Matrices

$[\bar{B}], [\bar{C}]$	isochoric component of left and right Cauchy-Green strain
$[\bar{F}]$	F-bar modified deformation gradient
$[\bar{N}]$	diagonal nodal basis function matrix
$[\bar{t}]$	eigenvector matrix of left Cauchy-Green strain
$[\Delta F]$	deformation gradient increment
$[\nabla_x S_{vp}]$	spatial derivatives of basis functions

$[\sigma]$	Cauchy stress matrix
$[\tau]$	Kirchhoff stress matrix
$[\tilde{N}]$	arc-length nodal displacement scaling matrix
$[\varepsilon^{\mathrm{p}}]$	plastic strain matrix
$[A]$	consistent tangent matrix
$[A^s]$	spatial tangent matrix
$[B]$	left Cauchy-Green strain
$[b]$	eigenvalue matrix of left Cauchy-Green strain
$[C]$	right Cauchy-Green strain
$[D^e]$	elastic material stiffness matrix
$[F]$	deformation gradient
$[F^0]$	deformation gradient at centroid of element
$[F^n]$	previously converged deformation gradient
$[F_{dev}]$	deviatoric component of deformation gradient
$[F_{iso}]$	isochoric component of deformation gradient
$[F_{vol}]$	volumetric component of deformation gradient
$[F^0_{vol}]$	volumetric component of $[F^0]$
$[G]$	strain-displacement matrix
$[I]$	identity matrix
$[J]$	Jacobian matrix
$[K]$	global stiffness matrix

$[K^E]$	element stiffness matrix
$[K_p]$	material point stiffness matrix
$[L]$	differential operator matrix
$[Q]$	six component mapping matrix
$[R]$	material rotation matrix
$[S_{vp}]$	basis function matrix
$[S_v]$	standard FE shape function matrix
$[U]$	material stretch matrix
$[\tau_{iso}]$	isochoric component of Kirchhoff stress
$[G_G]$	ghost stabilisation FE shape function derivative matrix
$[J_B]$	boundary Jacobian matrix
$[J_G]$	global ghost stabilisation term
$[K_G]$	ghost stabilisation stiffness matrix
$[n]$	normal matrix
$[N^{ls}]$	B-spline least squares fitting basis function matrix
$[R_f]$	muscle fibre rotation matrix
$[R_s]$	muscle sheet rotation matrix
$[s]$	deviatoric stress matrix
$[W_f]$	muscle fibre rotation axis matrix
$[W_s]$	muscle sheet rotation axis matrix

Operators

$(\cdot) \otimes (\cdot)$	tensor product
$(\cdot)^T$	transpose of $(\cdot)$
$\boldsymbol{\nabla}$	nabla operator with respect to current coordinates
$\det([\cdot])$	determinant of $[\cdot]$
$\det([\cdot])$	determinant of $[\cdot]$
$\frac{\partial}{\partial(\cdot)}$	derivative with respect to $(\cdot)$
$[\cdot]^{-1}$	inverse of $[\cdot]$
$\nabla_{\tilde{X}}$	nabla operator with respect to coordinates at start of load step
A	standard assembly operator
$\mathrm{tr}([\cdot])$	trace of $[\cdot]$

Other

χ_p	material point characteristic function
δ_{ij}	Kronecker delta function
Γ	boundary element face
Ω	problem domain
Ω_p	material point domain
$\partial\Omega$	domain boundary
$\partial\Omega_t$	domain boundary (Neumann)
$\partial\Omega_u$	domain boundary (Dirichlet)
φ	motion of material domain

Chapter 1

Introduction

The heart is an incredibly important organ which acts as the pump to drive blood flow around the body. According to the British Heart Foundation [32], Cardiovascular Disease (CVD) affects approximately 7.6 million people in the UK, which is twice as many as those living with cancer and Alzheimer's disease combined. Around 27% of all deaths in the UK each year are due to CVD, this equates to 480 deaths per day, or one every three minutes. It is estimated that CVD costs the UK economy £25 billion each year through premature death and disability with healthcare costs roughly around £10 billion per year. Looking globally, CVD is by far the leading cause of death in the population, being responsible for 18 million deaths in 2019 (around one-third of all deaths that year) [68]. In 2021, almost 1 million people died in the US due to CVD, with 600 000 deaths occurring under the age of 85 [213].

There are two main categories of heart failure, diastolic and systolic [44], and many studies have been undertaken into the causes, diagnosis and treatment of heart failure [31, 120, 212, 264]. Diastolic heart failure is seen with concentric hypertrophy, a thickening of the ventricular wall, which results in inadequate filling of the chambers of the heart and a reduction in blood flow, whereas, systolic heart failure sees eccentric hypertrophy, ventricular dilation, which means that the pumping function of the heart is negatively affected [44, 108]. It has been

found that the stresses and strains in the heart tissue can be linked to multiple physiological factors, such as: the pumping function; coronary blood flow; and myocardium growth and remodelling rates [114, 149].

Computational modelling can be used to provide insights into the stresses and strains that will be present in the heart tissue without the need for invasive surgery which may put a patient at further risk. It also allows a cardiologist to investigate where heart failure may occur based on the stress state in the tissue, and plan strategies for future treatment. The first computational model of a Left Ventricle (LV) was presented in 1979 by Arts *et al.* [8] as a set of thick walled cylinders with varying fibre directions to mimic the fibrous structure of the LV tissue. Since then, there has been a plethora of cardiac models, which will be discussed later in this chapter. For a review of the history of the mathematical modelling of cardiac mechanics, the reader is referred to [231]. Until now, the majority of models of the heart have utilised Finite Element Analysis (FEA). While this is a well established technique and will often produce exceptional results, there are drawbacks to using FEA. The Finite Element Method (FEM) is susceptible to large mesh distortion for problems involving large deformation mechanics [75, 257], which is detrimental to the accuracy of the results and may cause numerical failure in the analysis. On top of this, due to the intricate geometry of the heart, a fine mesh will typically be required which is computationally expensive to produce, especially in order to ensure that the mesh is of high quality. Added complexity comes with patient-specific models where the geometry of the model comes from medical imaging data. This process often requires multiple processing stages, including segmentation, mesh generation, application of boundary conditions and the analysis of the model (as seen in [255]). This is not only computationally expensive, but often requires significant user interaction and a considerable amount of time.

The Material Point Method (MPM) is a semi-meshless method in which a problem domain is discretised with particles (or Material Points, MPs) that are immersed in a background finite element mesh. A brief introduction of the MPM is given

later in this chapter and a full discussion of the MPM is given in Chapter 2. To the author's knowledge, this thesis presents the first use of the MPM to model the human LV, with specific focus on the passive filling of the LV. By exploiting the principles of MPM, an automated approach for the LV model generation can be created which takes a segmented image stack as input and produces the LV model which can be analysed with little to no user interaction. This will greatly reduce the computational and time cost of the pre-processing stage of an analysis. The background mesh used with the MPM is commonly formed of a regular distribution of uniform elements as it is the MPs that represent the actual material being modelled, meaning that the need for an extremely fine mesh (like those seen in FEA models, such as [108]) is greatly reduced.

This chapter serves as a justification for the work of this thesis as to why it is advantageous to model a patient's LV using the MPM. Firstly, the anatomy and function of the heart is presented, followed by a review of previous efforts of modelling the heart with a particular focus on LV modelling. A brief overview of the MPM is then given to provide context to the reader of the method. And finally, the scope and outline of this thesis is given.

1.1 Anatomy

In order to create a model, some knowledge of the structure and working mechanisms of the heart is needed. Therefore, this section presents the basic anatomy of the human heart and its function.

The heart is a four chambered, hollow muscle which is roughly conical in shape, approximately 12 cm long and 9 cm wide. It is positioned obliquely across the midline of the chest wall between the lungs and the diaphragm [188]. It is responsible for receiving and pumping blood from and to the cardiovascular system through rhythmic contractions of the muscles. It weights around 250–350 g and will pump approximately 200 million litres of blood with 3 billion contractions over an

average lifetime. The two halves of the heart have distinct functions. The left side of the heart is responsible for providing the blood flow to the circulatory system (pumps oxygenated blood from the lungs around the body) and the right side is responsible for blood flow to the pulmonary system (pumps deoxygenated blood from the body to the lungs for re-oxygenation). The two sides of the heart are separated by a muscular wall called the septal wall. Each side of the heart is comprised of two chambers. The upper chamber is called the atrium and the lower chamber is the ventricle. The atrium takes in blood at a relatively low pressure and transmits it into the ventricle which contracts, pressurising the blood to produce the flow to the lungs (right) or the rest of the body (left). The four chambers of the heart are built from a fibrous fatty ring, named the annulus fibrosus, at the atrioventricular junction which has three roles: it acts as a mechanical base for the atria and ventricles; it contains the four apertures (containing the valves) which control the blood flow to and from each chamber; and it provides electrical insulation between the ventricles and the atria to ensure that the excitation of the chambers occur at the appropriate time in the cardiac cycle. This work will refer to this part of the heart as the basal plane. Figure 1.1 provides a diagram of the heart, showing the four chambers and the blood flow through each chamber via the black arrows. Due to the fact that the right side of the heart only pumps blood to the nearby lungs, there is no need for a high pressure to be created to drive this flow, meaning that the thickness of the free wall of the Right Ventricle (RV) is relatively thin, on average around 0.5 cm thick. In comparison, the LV is responsible for blood flow around the entire body, meaning that the blood must be pressurised considerably more. To account for such a high pressure, the LV free wall is three times thicker than that of the RV free wall [188]. The atrial walls are thin in comparison to the ventricular walls due to the low pressure of the blood and as it will quickly be transported into the ventricles. A full cardiac cycle consists of two phases, diastole and systole. The diastole phase is where the cardiac muscle relaxes and blood moves from the atria into the ventricles. The systole phase

involves the rapid contraction of the cardiac muscle to pump the blood out of the ventricle while the atria are refilled.

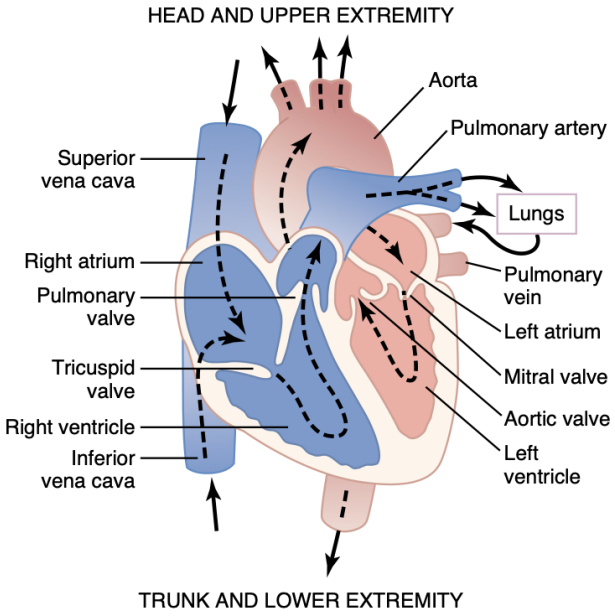

Figure 1.1: Structure of the heart and blood flow through the chambers of the heart. Taken from Guyton and Hall [128].

The heart wall is made of up three layers: the inner layer is called the endocardium, the outer layer is called the epicardium and the intermediate layer is the myocardium. The endocardium, myocardium and epicardium are shown in Figure 1.2. The entire heart is suspended in a lubricant fluid within a fibrous sac called the pericardium which acts as protection for the heart from damage and disease [87, 164] and as lubrication to reduce the friction between the heart and the surrounding structures [164]. The pericardial sac and cavity is also shown in Figure 1.2. The endocardium is made up of a thin layer of endothelial cells over connective tissue and smooth muscle cells. The function of the endocardium is to line the chambers of the heart and act as a barrier between the heart tissue and the blood [67]. The myocardium is the thickest layer of the heart wall which is primarily made up of cardiac muscle cells (also called myocytes) and is responsible for the muscle contractions which drive the blood flow [67]. The epicardial surface is made of mesothelium, fat and connective tissue and acts as protection for the heart which

also secretes the fluid that provides the lubrication within the pericardial cavity. An explanation of the structure of the three surfaces has been given here for completeness, however, it is common practice when modelling the heart to treat the heart wall as if it is made of only the myocardium. To the author's knowledge, when a description of the heart tissue has been given, it is presented as a single type of material from the endocardial surface to the epicardial surface (see [9, 109] for examples), no mention of any special treatment for the endocardium or the epicardium is given as the layered structure of the myocardium can be accounted for in the constitutive model [232].

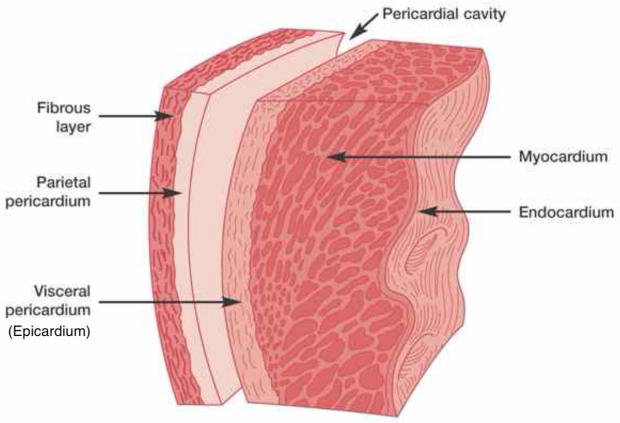

Figure 1.2: Layers of heart wall and surrounding pericardial sac. Taken from Venkatesan [307].

Only passive filling (pressure applied over the endocardial surface to mimic the blood pressure) of the LV to reach End-Diastole (ED) of the cardiac cycle is considered in this work. The electromechanical functions for the active contraction of the myocardium is not considered here and is therefore omitted from this review of cardiac function. For further information on the anatomy of the heart and the cardiovascular system, the reader is directed to the numerous resources which have been produced such as [1, 107, 128, 129, 188].

1.2 Past modelling efforts

The first computational mechanical model of the heart was created by Arts *et al.* [8] in 1979. Since then, the number of cardiac models has greatly increased, and they have been used to advance our understanding of the heart as well as to aid cardiologists in the diagnosis and treatment of heart diseases [108, 109, 137, 171, 174, 181, 193, 221, 327, 328]. The initial models focussed on the LV, which is subjected to the greatest pressures compared to the other three chambers of the heart and will see greater stresses due to this. Computational models of the LV have been used for many reasons, for example: to study the effect of myocardial architecture [92, 112, 302]; to investigate myocardial viscoelasticity [272]; to estimate the load free LV geometry [325]; as well as estimating the material properties of the myocardium [105, 232, 325]. Arts and co-workers modelled the LV as a thick walled cylinder, this approach was also used by Humphrey and Yin [155] and Guccione *et al.* [122] to model the equatorial region of the LV. As for any model, it is important to validate the results from a model either with an analytical solution or experimental data. For ethical reasons, experimental data of human myocardium is not widely available. However, is is more commonplace to obtain experimental data from animals as it is more beneficial to test ex-vivo tissue in as fresh a state as possible, giving availability of stress-strain data for non-human myocardium which can be used to validate computational models. The LVs of many animals have been modelled in the past such as dogs [10, 123, 304], rabbits [309], pigs [121, 232] and sheep [291]. When generating the LV geometry (both human and non-human), there are two methods that are typically used in the presented literature. The first is an approximation of the shape of the LV using prolate spheroid coordinates [62, 123, 146] or elliptical coordinates [21, 115, 135]. The second approach is to generate patient-specific LV geometry using Magnetic Resonance Imaging (MRI) data [9, 54, 86, 109, 220, 308, 322] or Computed Tomography (CT) scans [311, 332]. If the aim of the cardiac mechanical model is for diagnosis or treatment, this

second approach would clearly be the preferred option as it will generate results on a patient by patient basis.

Many extensions have been made to cardiac mechanical modelling of the LV over the years, such as: including the interaction between the LV and RV across the septum wall with a biventricular model [20, 21, 88, 116, 117, 157, 172, 176, 241, 242, 281]; modelling the atria [96, 108, 311]; as well as including electromechanics to model the active contraction of the muscle tissue [78, 117, 156, 245, 253, 305]. The majority of models of the heart discussed so far have used FEA, and other FEA-based methods have been used to model the heart such as isogeometric analysis [299, 331] and the immersed boundary method [311].

This review has by no means exhausted the list of examples of heart models, and multiple reviews of cardiac modelling have been produced in the past. The author recommends the reader references [11, 193, 238, 299] for further reading on the modelling of the heart.

1.3 The Material Point Method in brief

The MPM was developed by Sulsky and co-workers [287, 290] as an extension of a particle method for history-dependent materials in which the problem domain is discretised by MPs which are immersed into a (often unchanging) background finite element mesh. For a given load step, relevant data such as mass, volume, stiffness and force contributions are determined at the individual MPs, with these MPs acting as the integration points throughout the analysis as they move through the background mesh. This data is mapped onto the corresponding mesh nodes where the force vector and stiffness matrix are assembled as in standard finite element techniques, and the mesh displacements are computed and mapped back onto the MPs, whose positions are updated, finally, the mesh is reset at the end of the load step. For large deformation problems, the MPM has an advantage over FEA as re-meshing may not be needed due to the fact that the mesh is

reset at the end of every load step, reducing the effect of large mesh distortion. Another advantage of the MPM is that it may lead to fewer pre-processing steps, as a rigorous mesh generation step is not necessarily required. Once the problem geometry has been obtained, the volume of this geometry is populated with MPs that can be placed into a regular Cartesian mesh, negating the need for fine mesh elements to represent intricate geometry. Even though the meshing process can be inexpensive compared to FEA, because the MPs move through the mesh during the analysis, the MPs are often in non-optimal integration positions (as compared to a Gaussian integration scheme), therefore, a large number of MPs are required, increasing the computational cost. Investigations have been made into the convergence of the MPM. Charlton *et al.* [43] compared the rate of convergence of the MPM (specifically the Generalised Interpolation MPM) to linear and quadratic finite elements, with the convergence rate of the MPM lying between the two. Coombs *et al.* [59] showed that, in order to obtain continued convergence with mesh refinement, the minimum number of MPs required is proportional to the reciprocal of the square of the size of the background mesh.

While the MPM has been used widely in geotechnics [197, 215, 317], fracture [111, 127, 226], collision modelling [208, 317, 343, 348], manufacturing [186, 196, 324] and computer graphics [173, 283, 333], among other application areas, to the author's knowledge, the MPM has never been used to model cardiac mechanics. In fact, very little work in the biomechanics field of research has used the MPM [344]. Examples of the use of the MPM to model biological materials include: estimation of stress fields in the skull and brain of a woodpecker [199, 200]; modelling 3D vascular scaffolds under tension [124]; penetration testing of soft tissue [159–161]; and models of the human head and skull [206, 295, 303].

A more in-depth discussion on the MPM is given in Chapter 2 which gives further information on the background of the method, its applications and the formulation of the method for small deformation and large deformation elasticity.

1.4 Thesis scope and outline

The aim of this work is to develop the first mechanical model of a portion of the human heart using the MPM. For simplicity, only the LV of the heart will be considered as this is the chamber which is under the highest pressure and will see the highest stresses. This choice aligns with how initial heart models were developed, starting with the LV and expanding the model to include more physiological features and extra geometric features over time. No active contraction of the muscle fibres will be considered, and only the passive filling of the LV from approximate End-Systole (ES) to ED will be modelled in this work. Furthermore, this work focusses on the generation of the patient-specific LV geometry and the modelling of the myocardial tissue as an anisotropic hyperelastic material. It is acknowledged that the resulting model is not completely physiologically accurate, but serves as a proof of concept for the MPM modelling of cardiac mechanics and provides the first step for development in the future. The framework of the modelling procedure was developed such that the model is patient-specific, that is, a stack of segmented image slices are the input to the analysis so that the geometry of the model is based on a particular patient. To utilise the power of the MPM, the process of model setup is automated such that little user interaction is required in the pre-processing stage of the analysis.

This thesis is separated into four main sections: Section 1 (Chapter 1) introduces the thesis and provides the background of cardiac modelling; Section 2 (Chapters 2–5) focusses on the underlying theory required for this LV modelling; Section 3 (Chapters 6 and 7) puts these "tools" into practice to produce and analyse a patient-specific LV model using the MPM; and Section 4 (Chapter 8) summarises the work of this thesis and looks towards potential future advancements. For brevity's sake, reviews of the current literature are presented in each of the relevant sections.

- **Chapter 1** (this chapter) has presented an initial introduction to the thesis, discussing the need for heart modelling, the anatomy and function of the heart, past efforts of modelling the heart with particular interest in the LV and a brief justification of developing the first model of a LV using the MPM.

The second section presents the tools required to generate and analyse a model of the LV using the MPM.

- **Chapter 2** details the MPM, from the background of the method and its current uses in published literature to the formulation of the MPM to analyse a problem.
- **Chapter 3** covers the generation of B-spline curves and surfaces to be used as representations of non-conforming boundaries for 2D and 3D MPM analyses, as well as the imposition of Neumann boundary conditions over the B-spline boundaries.
- **Chapter 4** presents the first implementation of the arc-length method within the MPM formulation to handle large deformation problems with snap-through responses which could not previously be modelled using the load controlled MPM formulation.
- **Chapter 5** considers hyperelastic material behaviour, focusing on a simple isotropic model and an anisotropic model, with the latter being used to model the LV myocardium.

Using these tools, a patient-specific model of the LV can be analysed using the MPM. The third section is formed of two chapters:

- **Chapter 6** details the procedure to setup the LV model in the most automated fashion possible, by taking in the segmented image stack of a patient and returning B-spline representations of the endocardial and

epicardial surfaces, the discretised physical domain made up of MPs with assigned fibre orientations and the background computational mesh;

- **Chapter 7** presents the results of the first patient-specific LV model using the MPM, examining the stress distribution and displacement field throughout the LV, considering various factors including material properties and patient geometry.

Finally, **Chapter 8** presents the conclusions made across the developed work in this thesis and provides recommendations on possible directions for future work on this project.

1.5 Notation

Throughout this thesis, the majority of quantities are displayed in vector or matrix notation which will be denoted as $\{\cdot\}$ and $[\cdot]$ respectively. Any deviation from this standard convention will be highlighted in the text.

The numerical methods in this text were initially developed in MATLAB due to its many advantages in ease of code development and debugging. Due to the memory limitations of MATLAB, code development and analysis was moved to use the Julia language [23], an open-source language designed for high performance and ease of use. This work does not focus on code optimisation or parallelisation for large problems, therefore, no specialised algorithms will be presented. The code which has been developed for this work (both in MATLAB and Julia) has been built based on the AMPLE framework [56].

Chapter 2

The Material Point Method

The Material Point Method (MPM) was first developed by Sulsky *et al.* [287, 290] as an extension of the FLuid Implicit Particle (FLIP) method [28, 29], which itself was an extension of the Particle-In-Cell (PIC) method [93] used in fluid mechanics. In the MPM, a physical domain is discretised by material points which are immersed in a background mesh of finite elements.

A Material Point (MP) acts as an integration point and moves through the background mesh which often remains unchanged throughout the analysis, however, it can be easily replaced if required without disrupting the analysis. Each MP individually stores relevant information such as mass, volume, stress and global positions which is mapped onto the nodes of the background mesh where the governing equations for force and stiffness are assembled and solved for unknown nodal displacements etc, the updated values are then mapped back to the MP positions where the MP information is updated, the mesh is reset and the next analysis step begins. Having an unchanging background mesh avoids the issue of large mesh distortion often seen in the Finite Element Method (FEM).

In numerical simulations, two primary schemes are used: explicit and implicit. The explicit scheme calculates the state of the system at a future time based on the current state, allowing direct computation without iterative methods, making it simple to implement and computationally efficient for large models. However, it

can become unstable with large time steps, necessitating smaller increments for stability, which increases computational costs for long-duration simulations. Its simplicity also facilitates easy parallelisation for improved efficiency. Conversely, the implicit scheme calculates the state of the system using both the current and future states, often requiring an iterative approach involving the inversion of a system matrix. The advantage of the implicit approach is its unconditional stability, enabling larger time steps suitable for long-duration or slow-dynamics problems, though it is more computationally expensive due to the need to solve a system of equations at each time step. The original work by Sulsky and co-workers [287, 290] constructed the MPM with an explicit formulation which is a common formulation in subsequent work [13–16, 34, 46, 47, 113, 139, 151, 163, 194, 195, 209–211, 273, 274, 289, 330, 336, 338, 352]. This is possibly due to the relative simplicity of the explicit formulation compared to the implicit formulation. However, the implicit formulation, first published by Guilkey and Weiss [125], is becoming more popular with more work being performed using the implicit formulation [22, 24, 43, 56, 57, 59, 124, 203, 204, 225, 317, 320]. The reader is directed to [276] for a discussion on the implicit and explicit formulations of the MPM. Due to the improved stability of the scheme and the fact that dynamics are not considered, this work uses a quasi-static implicit MPM formulation.

The MPM is a versatile tool and has been used to model various problems including manufacturing [288, 324], geomechanics [51, 52, 197, 246, 339, 341, 351], fracture [111, 126, 127, 201, 226], contact [53, 149, 189, 317, 343], impact [150, 190, 191, 208, 348] and granular flow [353]. As well as modelling physical processes, the MPM is a key tool in the computer graphics community [48, 83, 132, 165, 173, 207, 270, 333], with a recognisable example of the use of the MPM in computer graphics coming from the Disney movie Frozen based on the work by Stomakhin and co-workers [283, 284]. The list above demonstrates the use of the MPM in varying types of situations, however, the MPM has rarely been used in the biomechanical modelling field. The majority of work has been performed on modelling the head, for example,

Tan *et al.* [295] used the MPM to model the interaction between the human skull, the cerebrospinal fluid and the brain due to blast exposure; Liu and co-workers [199, 200] modelled the skull and brain of a woodpecker during pecking to investigate the design of the woodpecker's skull for the prevention of brain damage; Lu *et al.* [206] modelled the human head during dynamic rotation and extension using the MPM; Upadhyaya and co-workers [303] modelled the deformation of a human brain during impact; and Fang *et al.* [95] modelled the complex trabecular bone in a porcine skull. Other efforts to use the MPM in biomechanics have come from Guilkey *et al.* [124] who used the MPM to model 3D multicellular constructs and Li and co-workers [192] who modelled the interaction between a needle and skin during the process of injecting biological tissue. Ionescu and co-workers used the MPM to model myocardial tissue simulating soft tissue failure [160] and penetrating trauma [159], both cases modelled the myocardium as a slab with rotated muscle fibres through the thickness of the slab. Ionescu *et al.* [161] modelled the ballistic injury to a porcine heart, generating the geometry of the left and right ventricles as a Finite Element (FE) mesh and populating the mesh with MPs. The tissue was modelled as a transversely isotropic hyperelastic material, however, no pressure was applied to the tissue to simulate blood pressure, the simulation was only to demonstrate the effect of the ballistic impact of a projectile. To the author's knowledge, there is nothing in the present literature which demonstrate the modelling of a heart (human or otherwise) under typical in-vivo conditions using the MPM.

This chapter covers the basic formulation of the MPM, while everything has not been covered here, there are a plethora of resources that have covered specific MPM formulations. The author recommends reading the orignal MPM papers [287, 290] as well as the comprehensive MPM reviews [77, 276] and textbooks [99, 229, 349]. This work bases the formulation on A Material Point Learning Environment (AMPLE) [56] which is a quasi-static implicit implementation of the MPM (this is the predominant MPM framework used by the Non-Linear Solid Mechanics group in Durham University).

2.1 Formulation

The governing differential equations for purely mechanical loading are derived from the strong form equations for the conservation of mass and linear momentum given as

$$\frac{\mathrm{d}\rho}{\mathrm{d}t} + \rho\boldsymbol{\nabla}\cdot\mathbf{v} = 0 \tag{2.1}$$

$$\rho\frac{\mathrm{d}\mathbf{v}}{\mathrm{d}t} = \boldsymbol{\nabla}\cdot\boldsymbol{\sigma} + \mathbf{f}_b \tag{2.2}$$

respectively, where ρ is the mass density, $\mathbf{v}$ is the velocity, $\boldsymbol{\sigma}$ is the Cauchy stress and $\mathbf{f}_b$ is the body force (due to gravity, for example). The mass of a MP throughout an analysis is independent of time, therefore, the mass in (2.1) is always conserved. For a quasi-static approach, there is no dependence on time, therefore the time derivative in (2.2) can be neglected such that the strong form becomes

$$\boldsymbol{\nabla}\cdot\boldsymbol{\sigma} + \mathbf{f}_b = 0. \tag{2.3}$$

Dirichlet and Neumann boundary conditions are applied over the boundary of the domain such that

$$\begin{aligned} \mathbf{u} &= \bar{\mathbf{u}} \ \text{ on } \ \partial\Omega_u \\ \mathbf{f}_t &= \bar{\mathbf{f}}_t \ \text{ on } \ \partial\Omega_t \end{aligned} \tag{2.4}$$

respectively, where $\bar{\mathbf{u}}$ are prescribed displacements and $\bar{\mathbf{f}}_t$ are prescribed tractions. It is worth noting that the domain boundary is divided into to disjoint pieces such that $\partial\Omega = \partial\Omega_u \cup \partial\Omega_t$, where $\partial\Omega$ is the entire boundary of the domain, $\partial\Omega_u$ is the section of the boundary subjected to Dirichlet boundary conditions and $\partial\Omega_t$ is the part of the boundary subjected to Neumann boundary conditions. It is also essential that the two types of boundaries do not coincide, $\partial\Omega_u \cap \partial\Omega_t = \emptyset$.

From the strong form in (2.3), test functions are introduced and by integrating over the domain, the weak form of the updated Lagrangian formulation can be obtained such that

$$\int_\Omega \boldsymbol{\sigma} : \boldsymbol{\nabla}\mathbf{w}\,\mathrm{d}v - \int_\Omega \mathbf{f}_b\cdot\mathbf{w}\,\mathrm{d}v - \int_{\partial\Omega_t} \mathbf{f}_t\cdot\mathbf{w}\,\mathrm{d}s = 0 \tag{2.5}$$

assuming a field of virtual displacements, $\mathbf{w}$, where Ω is the domain of the body with boundary $\partial\Omega$. Integration of the first two terms of (2.5) is performed over the volume of the domain while the integration of the third term is performed over the surface of the domain boundary. The weak form statement in (2.5) is valid for both small deformation (infinitesimal strain) and large deformation (finite strain) mechanics provided that (2.5) is expressed in terms of the deformed configuration for the large deformation case. Infinitesimal strain linear elasticity will be introduced where the reference and deformed configurations are assumed to be the same. Small deformation MPM is unusual in the way that the configuration is updated as the MPs move throughout the analysis but it is not a large deformation formulation, it is in fact a incrementally linear strain formulation.

For both small and large deformation MPM, a prescribed load or displacement may not be applied in a single step. Instead, the prescribed value is applied incrementally over a series of "time steps"* where the prescribed value is scaled based on the current progress through the analysis and the number of desired steps. This work only involves load controlled problems (where a load is prescribed), therefore, these time steps will be referred to as "load steps" from here.

The section begins with a review of the concept of basis functions which are used to interpolate data from the MPs to the background mesh nodes and vice versa. There are many different variations of basis functions that can be used, each with their advantages and disadvantages, which will be discussed. Infinitesimal strain linear elasticity will then be covered, giving the basic framework of a MPM analysis, followed by large deformation elasticity.

*As this work uses a quasi-static implicit MPM approach, the use of the term "time steps" does not really have any physical meaning and is just following a typical naming convention. The analysis can be thought of as stepping through pseudo-time.

2.1.1 Basis functions

Interpolation within elements of the background mesh is performed through the use of basis functions such that values at the MP positions are mapped to the nodes of the mesh at the start of a load step and solution values at the mesh nodes are mapped back onto the MP positions at the end of a load step.

A common choice for basis functions (and widely used in FEA) are the linear Lagrange shape functions where each element in the background mesh has a set of local coordinates, ξ. This work only considers quadrilateral elements in 2D and hexahedral elements in 3D. Therefore, the values of ξ vary between -1 and 1 for each dimension. The shape functions for a given point in the element can then be calculated for each node, for example, for 1D, 2-noded line element, the shape functions for nodes $i = 1, 2$ are

$$S_v = \frac{1 \pm \xi}{2}. \tag{2.6}$$

Figure 2.1 shows the 1D, 2-noded line element showing the local coordinate system where $\xi = -1$ at node 1 and $\xi = 1$ at node 2. It is also worth noting that the $\xi = 0$ is situated at the centre point of the element. Below the diagram of the line element in Figure 2.1 is a plot of the nodal shape functions along the element where the value of a nodal shape function at a node is equal to 1 and zero for every other node. The sum of the nodal shape functions throughout the element is unity at any point in the element.

For some MPMs, the 1D basis functions, $S_{vp}(\tilde{X}_p)$, can be expressed as

$$S_{vp}(\tilde{X}_p) = \frac{1}{V_p} \int_{\Omega_p} \chi_p S_v(\tilde{X}_p) \, \mathrm{d}x \tag{2.7}$$

where Ω_p is the domain of influence of the MP, χ_p is the characteristic function which describes the domain of the MP, V_p is the volume associated with the MP and S_v are the standard FE shape functions of the background mesh elements based on the position of the MP at the start of the load step, $\tilde{X}_p$. Subscripts $(\cdot)_v$

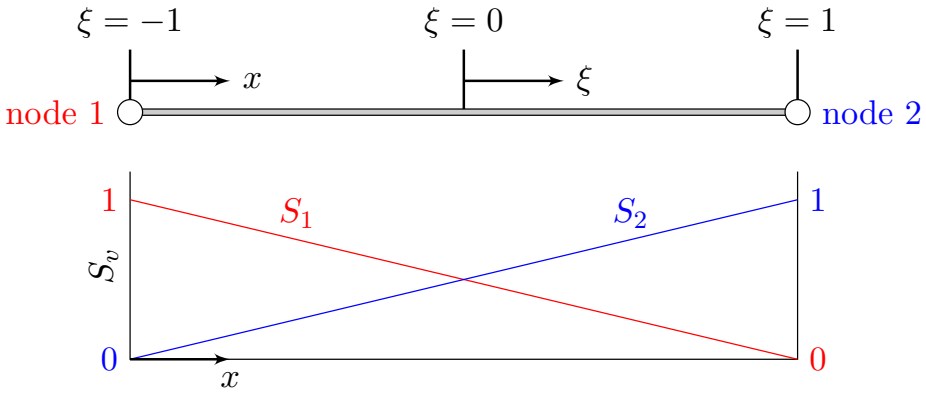

Figure 2.1: Shape functions for a 1D, 2-noded line element showing the global and local coordinates (above) and the nodal shape function values throughout the element (below).

and $(\cdot)_p$ refer to values at the nodes of the background mesh and a given point respectively. For multiple dimensions, the basis functions are calculated for each direction, S_{vp}^i, using (2.7) and the product of each value is taken such that

$$S_{vp}(\{\tilde{X}_p\}) = \prod_{i=1}^{n_D} S_{vp}(\tilde{X}_p^i). \tag{2.8}$$

The gradient of the basis functions can be found for each direction as

$$\nabla_{\tilde{X}} S_{vp}(\tilde{X}_p) = \frac{1}{V_p} \int_{\Omega_p} \chi_p \nabla_{\tilde{X}} S_v(\tilde{X}_p)\, \mathrm{d}x \tag{2.9}$$

with the global derivatives of the basis functions for one direction being the product of the gradient in that direction and the basis functions in the other directions. For a 2D problem, the derivative of the basis functions with respect to $\tilde{X}$ becomes

$$\frac{\partial S_{vp}(\tilde{X}_p, \tilde{Y}_p)}{\partial \tilde{X}} = \nabla_{\tilde{X}} S_{vp}(\tilde{X}_p)\, S_{vp}(\tilde{Y}_p). \tag{2.10}$$

It is important that the basis functions should be smooth and continuous across element boundaries as to mitigate errors. For example, standard MPM basis functions take the standard FE shape functions which are continuous but not smooth. The discontinuity in the derivatives of the shape functions cause significant issues when MPs cross over the boundaries between elements of the background mesh. This error is referred to as the "cell crossing instability". It is also important to satisfy the partition of unity ($\sum_{\forall v} S_{vp}(\tilde{X}_p) = 1$) as well as ensuring

non-negativity ($S_{vp}(\tilde{X}_p) \geq 0 \ \forall \tilde{X}_p$). The non-negativity is important to ensure positive nodal masses and avoid the instabilities that may arise for negative nodal masses.

This section comprises of a description of the most commonly used formulations in MPM including the standard linear interpolation, generalised interpolation, convected particle domain interpolation and the B-spline interpolation.

Standard linear interpolation

With the standard MPM, the basis functions are the standard shape functions of the background FE mesh. Here, linear shape functions will be considered, but higher order shape functions can also be used. It is possible to calculate the 1D basis functions for standard MPM using (2.7) and taking the MP characteristic function to be the Dirac delta function. If a uniform background mesh is used with element boundaries aligned with the global coordinate system (typical practice with MPM), the basis functions can be calculated directly from the global coordinates of the MP. The 1D basis functions can be calculated as

$$\begin{aligned} S_{vp} &= 1 + \frac{\tilde{X}_p - \tilde{X}_v}{h} \quad -h < \tilde{X}_p - \tilde{X}_v \leq 0 \\ S_{vp} &= 1 - \frac{\tilde{X}_p - \tilde{X}_v}{h} \quad 0 < \tilde{X}_p - \tilde{X}_v \leq h \end{aligned} \tag{2.11}$$

where h is the size of the background mesh element and $\tilde{X}_v$ is the position of the node (or vertex) associated with the basis function at the start of the load step. Figure 2.2 shows the standard 1D shape functions centred at zero, taking a value of one at the centre and reducing linearly until a distance of h away.

The gradients of the basis functions with respect to the MP position are calculated as

$$\begin{aligned} \nabla_{\tilde{X}} S_{vp} &= \frac{1}{h} \quad -h < \tilde{X}_p - \tilde{X}_v \leq 0 \\ \nabla_{\tilde{X}} S_{vp} &= -\frac{1}{h} \quad 0 < \tilde{X}_p - \tilde{X}_v \leq h \end{aligned} \tag{2.12}$$

Due to the fact that the basis functions are C^0 continuous, it is clear from (2.12) that the gradients of the basis functions are discontinuous across element

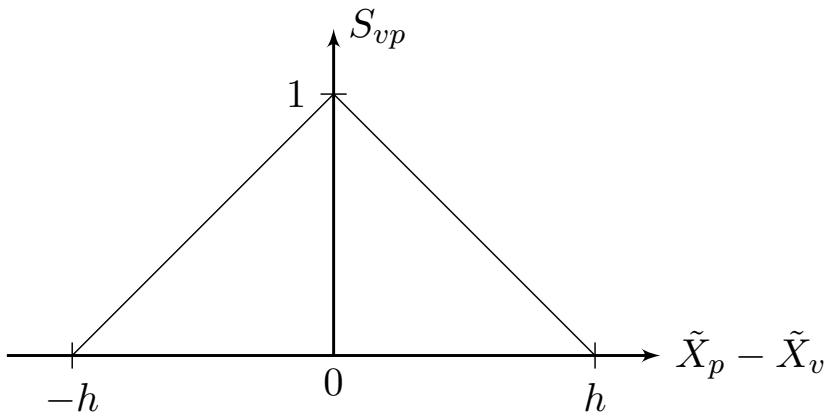

Figure 2.2: 1D standard MPM basis functions for a single node based on the position of the MP relative to the node.

boundaries which leads to the cell crossing instability. This has been well documented, for instance see [16, 43, 279], and significant work has been performed to mitigate this error, whether by modifying the properties of the MPs or changing the underlying basis functions.

Generalised interpolation

Bardenhagen and Kober [16] presented a major advance in the MPM with the Generalised Interpolation Material Point Method (GIMPM) which reduced the cell crossing errors mentioned above by introducing an area (or volume) to each MP which acts as a domain of influence in the background mesh. These MP domains are rectangular in 2D and cuboidal in 3D and maintain their shape throughout the analysis.

For the GIMPM formulation, a unity characteristic function of length $2l_p$, and centred at $\tilde{X}_p$, is taken with a value of one inside the MP domain and zero outside. The convolution of the characteristic function with the standard FE basis functions

gives

$$
\begin{aligned}
&\text{A: } S_{vp} = \frac{(h + l_p + \tilde{X}_p - \tilde{X}_v)^2}{4hl_p} && -h - l_p < \tilde{X}_p - \tilde{X}_v \leq -h + l_p \\
&\text{B: } S_{vp} = 1 + \frac{\tilde{X}_p - \tilde{X}_v}{h} && -h + l_p < \tilde{X}_p - \tilde{X}_v \leq -l_p \\
&\text{C: } S_{vp} = 1 - \frac{(\tilde{X}_p - \tilde{X}_v)^2 + l_p^2}{2hl_p} && -l_p < \tilde{X}_p - \tilde{X}_v \leq l_p \\
&\text{D: } S_{vp} = 1 - \frac{\tilde{X}_p - \tilde{X}_v}{h} && l_p < \tilde{X}_p - \tilde{X}_v \leq h - l_p \\
&\text{E: } S_{vp} = \frac{(h + l_p - \tilde{X}_p + \tilde{X}_v)^2}{4hl_p} && h - l_p < \tilde{X}_p - \tilde{X}_v \leq h + l_p.
\end{aligned}
\tag{2.13}
$$

Figure 2.3 shows the 1D GIMPM basis functions over a series of elements (top) and the convolution of the standard FE shape functions with the MP characteristic function is depicted (bottom). Focusing on node 2, the regions A through E depicted in Figure 2.3 correspond to the five conditions in (2.13). It is worth noting that the calculation of the GIMPM basis functions in regions B and D are the same as for standard MPM in (2.11), this is due to the fact that the characteristic hat function lies fully within a single element of the background mesh. For regions A, C and E, the standard MPM basis functions are augmented as there is an overlap of the MP characteristic function over multiple elements.

The 1D gradients of the GIMPM basis functions with respect to the MP position at the start of the load step are given as

$$
\begin{aligned}
&\nabla_{\tilde{X}} S_{vp} = \frac{(h + l_p + \tilde{X}_p - \tilde{X}_v)}{2hl_p} && -h - l_p < \tilde{X}_p - \tilde{X}_v \leq -h + l_p \\
&\nabla_{\tilde{X}} S_{vp} = \frac{1}{h} && -h + l_p < \tilde{X}_p - \tilde{X}_v \leq -l_p \\
&\nabla_{\tilde{X}} S_{vp} = -\frac{(\tilde{X}_p - \tilde{X}_v)}{hl_p} && -l_p < \tilde{X}_p - \tilde{X}_v \leq l_p \\
&\nabla_{\tilde{X}} S_{vp} = -\frac{1}{h} && l_p < \tilde{X}_p - \tilde{X}_v \leq h - l_p \\
&\nabla_{\tilde{X}} S_{vp} = -\frac{(h + l_p - \tilde{X}_p + \tilde{X}_v)}{2hl_p} && h - l_p < \tilde{X}_p - \tilde{X}_v \leq h + l_p.
\end{aligned}
\tag{2.14}
$$

As with the GIMPM basis functions, if the MP domain is contained within a single element of the background mesh, the gradient of the basis function is the same as the standard FE shape function derivative.

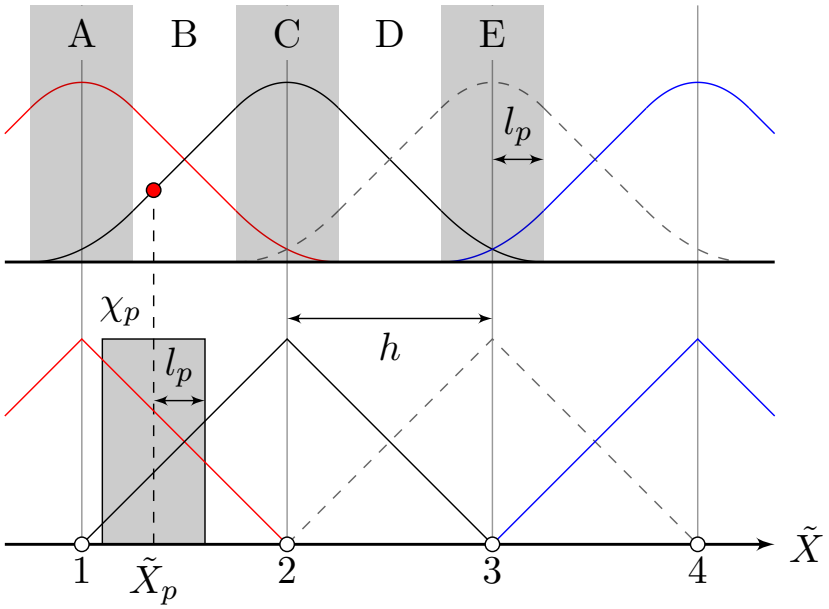

Figure 2.3: 1D GIMPM basis functions (top) and the convolution of the GIMPM characteristic function with the standard FE shape functions (bottom). Reproduced from Coombs *et al.* [57].

There are various GIMPM formulations depending on the treatment of the MP domain at the end of each load step. One approach is the unchanged Generalised Interpolation Material Point Method (uGIMPM) where the MP domain is kept fixed throughout the analysis ($l_p = l_{p0}$). While this is a simple approach and will keep the computational expense low, it is often the case that the MP domains will overlap or separate. An alternative approach which mitigates this issue is the contiguous particle Generalised Interpolation Material Point Method (cpGIMPM) which updates the size of the MP domain at the end of each load step. While the cpGIMPM fixes the issue of domain overlapping or separation, issues can still occur in the case of material rotation.

Convected particle domain interpolation

Sadeghirad *et al.* [265] developed a new MPM formulation called Convected Particle Domain Interpolation (CPDI) where MP domains are able to deform into parallelograms in 2D. This gives more freedom compared to the GIMPM where

the MP domains are strictly rectangles and cuboids and this formulation is also referred to as CPDI1. CPDI improves on the GIMPM formulation by mitigating issues that may occur. For example, the GIMPM domains are allowed to change size but always maintain the same alignment (often aligned with the Cartesian background grid). However, the CPDI domains can take a more general shape, and are thus more suitable to handle problems involving material rotation and shear deformation. On the other hand, with the CPDI1 formulation having the restriction of parallelogram shaped domains, it is still possible that gaps or overlaps between MP domains will occur, therefore, the CPDI method was extended further in Sadeghirad *et al.* [266] to allow elements to deform into arbitrary quadrilaterals (in 2D) by tracking each vertex of the domain separately and ensuring the MP domains remain contiguous throughout an analysis. This method is referred to as Second-order Convected Particle Domain Interpolation (CPDI2). Nguyen *et al.* [228] introduced the use of triangular and tetrahedral domains as well as arbitrary polygonal and polyhedral MP domains.

The CPDI method does not use the same method of calculating the basis functions as the GIMPM. Where the GIMPM integrates the standard FE shape functions over the MP domain, the CPDI method assumes a linear approximation between the standard FE shape function values at each corner and calculates the basis functions based on this.

Using the example of a 2D MP domain with four corners ($\alpha = 1, 2, 3, 4$), the CPDI1 formulation approximate basis functions are calculated at each of these corners and averaged such that

$$S_v^{app} = \sum_{\alpha=1}^{4} S_\alpha(\{\tilde{X}_p\}) S_v(\{\tilde{X}_c^\alpha\}) \tag{2.15}$$

where $S_\alpha(\{\tilde{X}_p\})$ is the standard linear quadrilateral FE shape functions related to the α-th corner of the MP domain and $S_v(\{\tilde{X}_c^\alpha\})$ are the standard grid basis functions at α-th corner of the MP domain. The basis functions are then calculated

using the approximate basis functions as

$$S_{vp} = \frac{1}{V_p} \sum_{\alpha=1}^{4} S_v(\{\tilde{X}_c^\alpha\}) \int_{\Omega_p} S_\alpha(\{\tilde{X}_p\})\, \mathrm{d}\tilde{X} \tag{2.16}$$

with the gradients of the basis functions being calculated as

$$\nabla_{\tilde{X}} S_{vp} = \frac{1}{V_p} \sum_{\alpha=1}^{4} S_v(\{\tilde{X}_c^\alpha\}) \int_{\Omega_p} \nabla_{\tilde{X}} S_\alpha(\{\tilde{X}_p\})\, \mathrm{d}\tilde{X}. \tag{2.17}$$

For a 2D MP domain using CPDI1 (thus having a parallelogram shape), the basis functions can be computed as

$$S_{vp} = \frac{1}{4}(S_v(\{\tilde{X}_c^1\}) + S_v(\{\tilde{X}_c^2\}) + S_v(\{\tilde{X}_c^3\}) + S_v(\{\tilde{X}_c^4\})) \tag{2.18}$$

with the gradient of the basis functions being dependent on the size of the MP domain. In a similar manner to CPDI1 but to take into account the more general quadrilaterial shape of the MP domain, the CPDI2 equivalent basis functions for a 2D MP domain can be obtained using (2.15) as the alternate grid basis functions such that

$$\begin{aligned} S_{vp} = \frac{1}{24V_p} \Big\{ & (1-a-b)S_v(\{\tilde{X}_c^1\}) + (1-a+b)S_v(\{\tilde{X}_c^2\}) \\ & +(1+a+b)S_v(\{\tilde{X}_c^3\}) + (1+a-b)S_v(\{\tilde{X}_c^4\}) \Big\} \end{aligned} \tag{2.19}$$

where

$$a = (x_c^4 - x_c^1)(y_c^2 - y_c^3) - (x_c^2 - x_c^3)(y_c^4 - y_c^1)$$

$$b = (x_c^3 - x_c^4)(y_c^1 - y_c^2) - (x_c^1 - x_c^2)(y_c^3 - y_c^4)$$

with (x_c^α, y_c^α) are the global x and y coordinates of the α-th corner of the MP domain. As with CPDI1, the gradient of the basis functions in (2.19) are dependent on the size of MP domain.

It was shown by Sadeghirad *et al.* [265, 266], using numerical examples based on the Method of Manufactured Solutions (MMS) manufactured solutions of Wallstedt and Guilkey [316], that the CPDI formulation produces greater accuracy over the GIMPM for both the uGIMPM and cpGIMPM formulations. Kamojjala *et al.* [170] also showed that the CPDI formulations produces more accurate results compared to the uGIMPM.

The improved accuracy of the CPDI method does come with drawbacks. Due to the fact that the MP domains are free to deform to any quadrilateral shape in 2D CPDI2, it is possible that the MP domains will invert. Brannon [30] presented in a blog post the potential for "holes" to form in the basis functions if the MP domain extends over multiple grid elements. Wang *et al.* [320] found that the CPDI2 method can become unstable for problems involving large distortion, shear and rotation displayed using multiple numerical examples.

Figure 2.4 is a graphical comparison of the 1D calculation of the standard MPM, GIMPM and CPDI basis functions for a single node for a MP with a domain half-length of l_p (for the case of GIMPM and CPDI method). The diagram shows the key differences between the calculations of the basis functions for each method. The standard MPM simply takes the value of the FE basis function based on the position of the particle. The CPDI method takes the values of FE basis functions at the corners of the MP domain, assumes a linear interpolation between the two values and integrates using this approximation over the domain. Whereas the GIMPM takes the values of the FE basis functions at the corners of the MP domain and fully integrates the FE basis functions over the length of the domain.

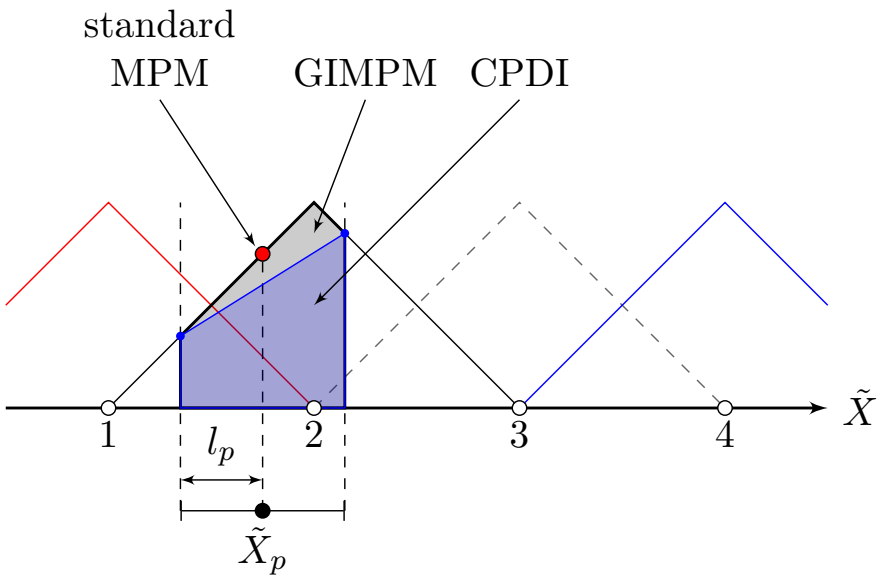

Figure 2.4: Comparison between the 1D basis function calculation for the standard MPM, GIMPM and CPDI formulations.

B-spline interpolation

Cell crossing errors occur due to the discontinuities in the basis function derivatives between elements, a way to overcome this is to use higher order basis functions. Therefore, an alternative formulation for the MPM is the B-spline MPM, developed by Steffen and co-workers [278–280], which replaces the piecewise-linear shape functions with high order B-spline basis functions. Both quadratic (order 2) or cubic (order 3) B-spline basis functions are used which means that the basis functions are once or twice continuously differentiable respectively. The gradients of the basis functions will now be continuous between elements, eliminating cell crossing errors.

B-spline basis functions are calculated based on a knot vector, $\{\Xi\} = \{\xi_1, \xi_2, \ldots, \xi_{n+p+1}\}$, which is an ordered, non-decreasing set of knot values, $\xi_i \leq \xi_{i+1}$, where n is the number of non-zero order p B-spline basis functions and p is the order of the B-spline. The Cox-de-Boor formula [248] is used to recursively calculate the B-spline basis functions, starting with the zeroth order basis function ($k = 0$) in 1D such that

$$N_{i,0}(\xi) = \begin{cases} 1 & \xi_i \leq \xi < \xi_{i+1} \\ 0 & \text{otherwise} \end{cases} \tag{2.20}$$

and for higher polynomial orders which are calculated as

$$N_{i,k}(\xi) = N_{i,k-1}(\xi)\frac{\xi - \xi_i}{\xi_{i+k} - \xi_i} + N_{i+1,k-1}(\xi)\frac{\xi_{i+k+1} - \xi}{\xi_{i+k+1} - \xi_{i+1}} \tag{2.21}$$

with a fraction of $\frac{0}{0}$ defined as zero. Elements of the mesh are defined as the non-zero knot spans in $\{\Xi\}$; boundaries of the mesh are defined using open knots where the first and last knot of $\{\Xi\}$ is repeated $p + 1$ times. The repetition of the knots at the boundary enforces the value of the basis functions to be one at the boundary node and zero elsewhere, ensuring the correct application of Dirichlet boundary conditions.

Figure 2.5 shows the 1D cubic B-spline basis functions for a uniform knot vector $\{\Xi\} = \{0, 0, 0, 0, 1, 2, 3, 4, 5, 5, 5, 5\}$, which consists of 5 knot spans (therefore represents 5 elements) and produces 8 basis functions. The smooth nature of the basis functions which span multiple elements is clear. However, it is obvious that there are too many basis functions for a mesh with 5 elements. As there are only 6 nodes, only 6 basis functions are required for the MPM in order to use the knot spans as elements in a Cartesian grid, but there are currently 8 B-spline basis functions in this example. In order to ensure partition of unity, there should be one basis function which peaks at each nodal position, which is the case for nodes 0, 2, 3 and 5 in Figure 2.5, however, nodes 1 and 4 have basis function curves either side which do not peak at the node, as shown by dashed lines. It is possible to "combine" these basis function curves either side of nodes 1 and 4 to obtain a new one dimensional B-spline basis function for the node which has a peak at said node.

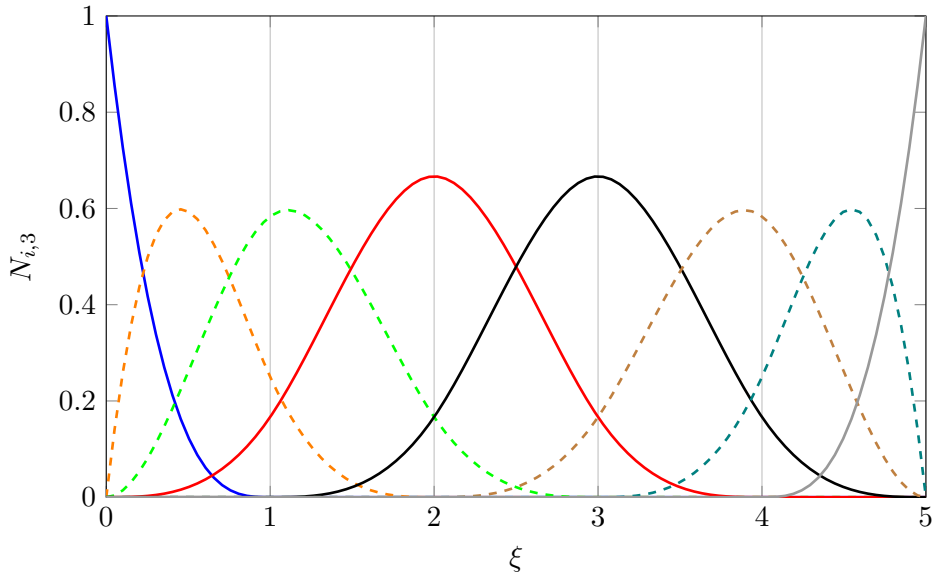

Figure 2.5: 1D cubic ($k = 3$) B-spline basis functions on a uniform knot vector $\{\Xi\} = \{0, 0, 0, 0, 1, 2, 3, 4, 5, 5, 5, 5\}$.

Assuming a uniform grid spacing, it is possible to calculate the B-spline basis function directly from the global position of a MP relative to the global position of the node in question. However, there are multiple scenarios that must be handled

based on the position of the node relative to the location of the boundary, $\tilde{X}_B$. Figure 2.6 shows the 1D B-spline MPM basis functions across 5 elements using the desired 6 basis functions. The first case is shown with a blue line where the node is located at the boundary ($\tilde{X}_v = \tilde{X}_B$) with the basis functions being calculated as

$$\begin{aligned} S_{vp} &= \frac{1}{6}x^3 - x + 1 \quad 0 \leq |x| < 1 \\ S_{vp} &= \frac{1}{6}(2-x)^3 \quad 1 \leq |x| < 2 \\ S_{vp} &= 0 \quad \text{otherwise} \end{aligned} \tag{2.22}$$

where $x = \frac{\tilde{X}_p - \tilde{X}_v}{h}$ and h is the grid spacing. The second case is when the node is one grid spacing away from the boundary to the right ($\tilde{X}_v = \tilde{X}_B + h$) and is calculated as

$$\begin{aligned} S_{vp} &= -\frac{1}{3}x^3 - x^2 + \frac{2}{3} \quad -1 \leq x < 0 \\ S_{vp} &= \frac{1}{2}x^3 - x^2 + \frac{2}{3} \quad 0 \leq x < 1 \\ S_{vp} &= -\frac{1}{6}x^3 + x^2 - 2x + \frac{4}{3} \quad 1 \leq x < 2 \\ S_{vp} &= 0 \quad \text{otherwise} \end{aligned} \tag{2.23}$$

and is shown as the green line in Figure 2.6. The third case is where the node is located at least two elements away from the boundary ($|\tilde{X}_v - \tilde{X}_B| \geq 2h$), shown as red lines, the basis functions are calculated as

$$\begin{aligned} S_{vp} &= \frac{1}{2}x^3 - x^2 + \frac{2}{3} \quad 0 \leq |x| < 1 \\ S_{vp} &= \frac{1}{6}(2-x)^3 \quad 1 \leq |x| < 2 \\ S_{vp} &= 0 \quad \text{otherwise.} \end{aligned} \tag{2.24}$$

The fourth case is the where the node is one element away from the boundary to the left side ($\tilde{X}_v = \tilde{X}_B - h$), this is shown as the black line in Figure 2.6, with the basis functions calculated as

$$\begin{aligned} S_{vp} &= \frac{1}{6}x^3 + x^2 + 2x + \frac{4}{3} \quad -2 \leq x < -1 \\ S_{vp} &= -\frac{1}{2}x^3 - x^2 + \frac{2}{3} \quad -1 \leq x < 0 \\ S_{vp} &= \frac{1}{3}x^3 - x^2 + \frac{2}{3} \quad 0 \leq x < 1 \\ S_{vp} &= 0 \quad \text{otherwise.} \end{aligned} \tag{2.25}$$

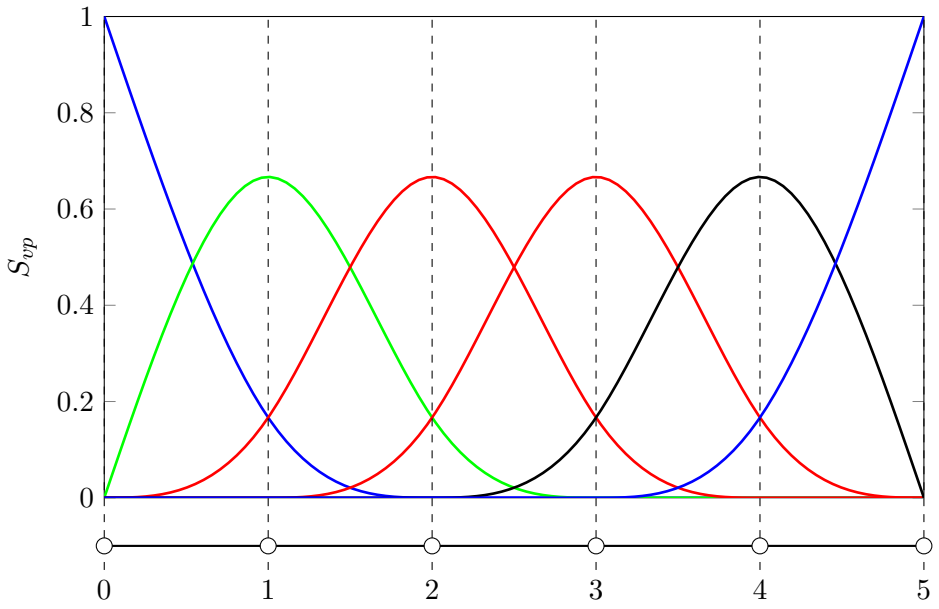

Figure 2.6: 1D cubic, B-spline MPM basis functions for 5 elements.

The use of B-spline basis functions means that it is possible to define the entire domain using a single knot vector, a concept that is akin to Isogeometric Analysis [152]. It is also simple to extend the basis functions to multiple dimensions as the product of the B-spline basis functions in each direction.

One downside to the standard B-spline MPM formulation is that it can only be used for structured rectangular grids. Yamaguchi *et al.* [334] also highlighted the fact that, due to the larger range of influence of the MP domain, small overlaps between the MP domains and the background mesh elements can occur (also called the small cut problem) where MPs have very small contributions to degrees of freedom of the background mesh which may cause ill-conditioning of the system matrix. But, being relatively new, the B-spline MPM formulation is a topic of ongoing research [5, 104, 222, 297, 334]. Further extensions to the B-spline MPM formulation have also been developed including truncated hierarchical B-splines (THB-splines) [110], locally refined splines (LR-splines) [84] as well as using Powell-Sabin splines [250] to allow the method to be used for triangular meshes [73].

Domain updating

Some variations of the MPM involve defining a domain of each MP with a given size which means that a method of updating the domain of the MP is required. For a domain defined by half-length, l_p^i, for each dimension (for $i = 1, \ldots, n_D$, where n_D is the number of dimensions), multiple options have been given to update the size of the domain. One method is to uniformly scale the domain half-lengths based on the volume change of the MP such that

$$l_p^i = l_{p_0}^i \det([F]) \tag{2.26}$$

where $l_{p_0}^i$ is the original half-length of the MP domain and $[F]$ is the deformation gradient. This method of domain updating fails for problems involving simple stretch with artificial orthogonal contraction/expansions of the domains being observed. It is possible to update the domain based on the normal components of the deformation gradient where

$$l_p^i = l_{p_0}^i F_{ii} \qquad \text{(no implied sum over } i\text{)} \tag{2.27}$$

where F_{ii} are the values of the leading diagonal of $[F]$. Updating based on just the deformation gradient values is unable to handle material rotation with the MP domains seen to vanish after seeing rotation. Charlton *et al.* [43] proposed using the material stretch tensor, $[U]$, to map the domain sizes such that

$$l_p^i = l_{p_0}^i U_{ii} \qquad \text{(no implied sum over } i\text{)} \tag{2.28}$$

where U_{ii} are the values of the leading diagonal of $[U]$. The material stretch tensor is found through the decomposition of the deformation gradient such that $[F] = [R][U]$ where $[R]$ is the rotational component of the deformation and the material stretch tensor is calculated as

$$[U] = \sqrt{[F]^T[F]} \tag{2.29}$$

which can be thought of as the deformation gradient rotated back into its original reference frame*. While the use of the material stretch tensor fixes the issue involving material rotation, it cannot correctly model simple shear and results in volume changes when isochoric deformations take place.

A fourth option for updating the domain half-lengths is a corner update procedure [59] inspired by CPDI2 where the positions of the corners of the domain are updated based on the nodal displacements, however, in order to ensure the domain remains rectangular (in 2D or cuboidal in 3D), the midpoints between the corners are found and used for the new domain half-lengths. The positions of each corner of the domain is updated using the basis functions associated with the background mesh at the position of the corner such that

$$\{x_c\} = \{\tilde{X}_c\} + \sum_{\forall v} [S_{vp}]\{u_v\} \tag{2.30}$$

where $\{\tilde{X}_c\}$ is the global coordinate of the corner at the start of the load step, $[S_{vp}]$ is a matrix containing the basis functions of the corner of the domain and $\{u_v\}$ is the background mesh nodal displacements. The midpoints of the edges formed by the new corner positions are determined in order to calculate the new domain lengths where

$$l^i_{pm} = \frac{1}{2}(\max(\{x_m\}^i) - \min(\{x_m\}^i)) \tag{2.31}$$

where $\{x_m\}^i$ are the coordinates of the updated domain edge midpoints. The GIMPM domain half lengths are then calculated as

$$l^i_p = l^i_{pm} \left(\frac{\det([F]) \prod_{j=1}^{n_D} l^j_{p0}}{\prod_{j=1}^{n_D} l^j_{pm}} \right)^{\frac{1}{n_D}} \tag{2.32}$$

which will scale the size of the GIMPM domain about the MP's location and ensures that the update is consistent with the change in volume at the MP. Figure 2.7 depicts the corner update procedure for a single GIMPM domain in 2D, the volume updating from (2.32) is not shown, only the update based on the midpoints

*The reference frame will be discussed later in this chapter when presenting the formulation of large deformation elasticity.

of the deformed corners from (2.31). In Figure 2.7, the original domain is shown by the grey-shaded region with corners shown with solid white circles and the outline of the updated GIMPM domain is depicted with a black dashed line.

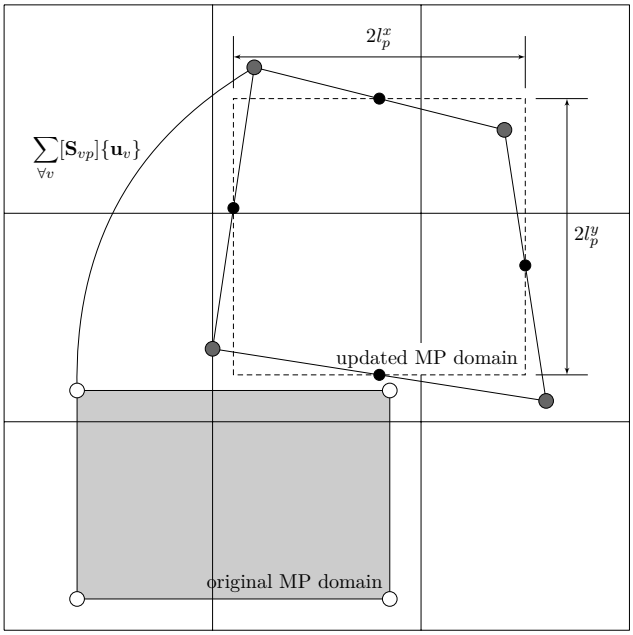

Figure 2.7: Corner update procedure (without volume update of (2.32)) for a single GIMPM domain in 2D. Adapted from Coombs *et al.* [59].

2.1.2 Other MPM formulations

The formulations presented above are the most commonly used but are not the only options that have been used in the past. Wallstedt and Guilkey developed an extension for the MPM and GIMPM which uses a Weighted Least Squares (WLS) framework [315]. This weighted least squares method displays significantly improved accuracy over the standard MPM and GIMPM formulations. However, there is a much greater complexity of the implementation compared to FEM or MPM and GIMPM due to the requirement of least squares and marching cubes routines. Zhang *et al.* proposed the Dual Domain Material Point (DDMP) method [342] which uses linear basis functions with a modified gradient form such that the gradients are continuous across element boundaries, reducing the cell crossing errors. The area of influence of each MP is also increased such that neighbouring

elements of the background grid are also influenced by a MP. The DDMP method has been widely studied. Bürg *et al.* [33] expanded the DDMP method to use second-order functions and Long *et al.* [202] used the DDMP method to model ductile damage. Dhakal and Zhang [82] compared the performance of the standard MPM, GIMPM and DDMP methods using a one-dimensional shock wave problem and found that the DDMP method produced unsatisfactory results when using a small number of MPs. The DDMP method did however converge to the solution when the number of MPs was increased, however, a very large number of MPs was needed to produce accurate results compared to the other MPM implementations.

2.1.3 Small deformation linear elasticity

Many solid materials experience only a small change in shape when forces are applied to them [277], once the applied stress is removed, the material will return to its "natural" shape (as long as the load applied is not too large that the material begins to yield). In this case, materials are said to behave elastically and assumptions such as small deformations and infinitesimal strains provide a starting point for simple analyses. A linear relationship between the stress and strain is assumed such that

$$\{\sigma\} = [D^e]\{\varepsilon\} \tag{2.33}$$

where (in the 3D Cartesian frame (x, y, z)) $\{\sigma\}$ is the Cauchy stress vector with the form,

$$\{\sigma\} = \begin{Bmatrix} \sigma_{xx} & \sigma_{yy} & \sigma_{zz} & \sigma_{xy} & \sigma_{yz} & \sigma_{zx} \end{Bmatrix}^T, \tag{2.34}$$

$[D^e]$ is the elastic material stiffness matrix given as

$$[D^e] = \frac{E}{(1+\nu)(1-2\nu)} \begin{bmatrix} (1-\nu) & \nu & \nu & 0 & 0 & 0 \\ \nu & (1-\nu) & \nu & 0 & 0 & 0 \\ \nu & \nu & (1-\nu) & 0 & 0 & 0 \\ 0 & 0 & 0 & \frac{(1-2\nu)}{2} & 0 & 0 \\ 0 & 0 & 0 & 0 & \frac{(1-2\nu)}{2} & 0 \\ 0 & 0 & 0 & 0 & 0 & \frac{(1-2\nu)}{2} \end{bmatrix}, \tag{2.35}$$

where E is the Young's modulus and ν is the Poisson's ratio, and $\{\varepsilon\}$ is the strain vector with the form

$$\{\varepsilon\} = \begin{Bmatrix} \varepsilon_{xx} \\ \varepsilon_{yy} \\ \varepsilon_{zz} \\ \gamma_{xy} \\ \gamma_{yz} \\ \gamma_{zx} \end{Bmatrix} = \begin{Bmatrix} \frac{\partial u}{\partial x} \\ \frac{\partial v}{\partial y} \\ \frac{\partial w}{\partial z} \\ \frac{\partial u}{\partial y} + \frac{\partial v}{\partial x} \\ \frac{\partial v}{\partial z} + \frac{\partial w}{\partial y} \\ \frac{\partial w}{\partial x} + \frac{\partial u}{\partial z} \end{Bmatrix} \tag{2.36}$$

where u, v and w are the components of the displacement vector, $\{u\}$, for displacements in the x, y and z directions respectively.

Using any of the basis function choices discussed above, a basis function matrix, $[S_{vp}]$, can be formed containing basis functions values associated with all nodes in the mesh for each dimension. This matrix provides the mapping between the MPs and the background mesh. Using basis functions, it is possible to calculate the current global coordinates, $\{x_p\}$, of any point within an element from the global coordinates of the element nodes where

$$\{x_p\} = [S_{vp}]\{x_v\} \tag{2.37}$$

where $\{x_v\}$ are the global coordinates of the nodes of the element. Similarly, the displacement of any point within an element, $\{u_p\}$, can be calculated from the nodal displacements, $\{u_v\}$, of said element as

$$\{u_p\} = [S_{vp}]\{u_v\}. \tag{2.38}$$

The strain-displacement matrix, $[G]$, is a matrix containing the derivatives of the basis functions with respect to the global coordinates, $[\nabla_x S_{vp}]$, and is given by

$$[G] = [L][S_{vp}] \tag{2.39}$$

where $[L]$ is the differential operator matrix with the form

$$[L] = \begin{bmatrix} \frac{\partial}{\partial x} & 0 & 0 & \frac{\partial}{\partial y} & 0 & \frac{\partial}{\partial z} \\ 0 & \frac{\partial}{\partial y} & 0 & \frac{\partial}{\partial x} & \frac{\partial}{\partial z} & 0 \\ 0 & 0 & \frac{\partial}{\partial z} & 0 & \frac{\partial}{\partial y} & \frac{\partial}{\partial x} \end{bmatrix}. \tag{2.40}$$

Using the definition of the strain vector in (2.36), the strain at any point in an element can be formulated by combining the definitions given in (2.38) and (2.39) such that

$$\{\varepsilon\} = [L]\{u_p\} = [L][S_{vp}]\{u_v\} = [G]\{u_v\} \tag{2.41}$$

meaning that the strain-displacement matrix in (2.39) can be used to calculate the strain based on the nodal displacements of the element.

From (2.5), it is possible to obtain a weak form of equilibrium in a local element-wise sense which is given by

$$\int_\Omega [G]^T [D^e][G] \, \mathrm{d}v \, \{u_v\} - \int_\Omega [S_{vp}]^T \{f_b\} \, \mathrm{d}v - \int_{\partial\Omega} [S_v]^T \{f_t\} \, \mathrm{d}s = 0 \tag{2.42}$$

where $[S_v]$ are the standard FE shape functions used to integrate the traction forces over the boundary domain. Rather than integrating over the entire domain, integration is performed on a local element-wise basis where the element stiffness matrix, $[K^E]$, is given as

$$[K^E] = \int_E [G]^T \, [D^e] \, [G] \, \mathrm{d}v. \tag{2.43}$$

The element stiffness matrix can be approximated by replacing the integration over the volume of the element with the summation over all MPs contained within the element. A MP's stiffness contribution is then given by

$$[K_p] = [G_p]^T \, [D^e] \, [G_p] \, V_p \tag{2.44}$$

where V_p is the volume of the MP. In terms of computation, it is not essential to loop over each element and subsequently loop over each MP contained within the element, knowing which element each MP is situated is enough to assemble the global stiffness matrix, $[K]$, such that

$$[K] = \underset{\forall p}{\mathcal{A}}[K_p] \tag{2.45}$$

where $\mathcal{A}$ is the standard assembly operator performed over all MPs.

The internal force vector, $\{f^{int}\}$, and external force vector, $\{f^{ext}\}$, can be formed in a similar manner through the contribution of each MP. The external force vector is made up of the point loads associated with each MP and the body forces, as well as the traction forces applied over the boundary of the domain. There is no association between the traction forces and the MPs, therefore, the traction force is simply integrated over the boundary of the domain. The contribution of force of a MP towards the external force vector is mapped from the position of the MP to the nodes of the mesh through the calculated basis functions. Therefore, the external force vector can then be assembled such that

$$\{f^{ext}\} = \underset{\forall p}{\mathcal{A}}\left(\underbrace{(\overbrace{[S_{vp}]^T\{f_p\}}^{\text{point loads}} + \overbrace{[S_{vp}]^T\{f_b\}V_p)}^{\text{body forces}}}_{\text{MP forces}}\right) + \underbrace{\int_{\partial\Omega}[S_v]^T\{f_t\}\,\mathrm{d}s}_{\text{traction forces}} \tag{2.46}$$

where $\{f_p\}$ is the point force associated with the MP. The internal nodal force vector can be determined as the integration of the stress in the domain such that

$$\{f^{int}\} = \int_\Omega [G]^T\{\sigma_p\}\,\mathrm{d}v \tag{2.47}$$

where the integration over the domain can be approximated with the assembly over all MPs, meaning that the internal force vector can be calculated using

$$\{f^{int}\} = \underset{\forall p}{\mathcal{A}}\underbrace{[G_p]^T\{\sigma_p\}V_p}_{\{f_p^{int}\}}. \tag{2.48}$$

After assembling the global stiffness matrix and the internal and external force vectors, it is possible to create the linear system

$$[K]\{u_v\} = \{f_v\} \tag{2.49}$$

where $\{f_v\}$ is the difference between the external force vector, $\{f^{ext}\}$, and the internal force vector, $\{f^{int}\}$. From (2.49), the unknown displacements of the background mesh nodes can simply be found through

$$\{u_v\} = [K]^{-1}\{f_v\}. \tag{2.50}$$

In the case of linear elasticity, equilibrium between the internal and external forces should be achieved after a single iteration over a load step. Once the unknown nodal displacements have been calculated, the strain at each MP position can be found using (2.41), and from these, the stresses for each MP can be determined using (2.33).

As mentioned previously, the MPM discretises the domain with MPs which act as the integration points for the numerical integration throughout the analysis. For simplicity in the problem setup, ideally the MPs are initially distributed evenly across each element of the background mesh with an equal distribution of MPs within an element. Based on the distribution of the MPs, each MP has a volume, V_p, which is the volume of the material domain it represents in the global frame, which is used to compute the weighting of the MP in the numerical integration procedure. For standard MPM implementations, it is assumed that the volume acts at a single point represented by the MP. For other implementations of the MPM each MP has a domain of influence which will deform with the material, therefore, this domain can be updated which will alter the associated volume of the MP. For example, for a 2D, 4-noded quad element containing 4 MPs (depicted as white circles in Figure 2.8) which are evenly distributed through the element, each MP will have a volume equal to one quarter of the total area of the element as shown by the grey areas within the element.

A key feature of the MPM is that the MPs move throughout an analysis and the mesh is reset at the end of each load step, this means that it is often the case that an MP will move from one element to another, meaning that some process of determining which element a MP is situated in is required, which can be expensive.

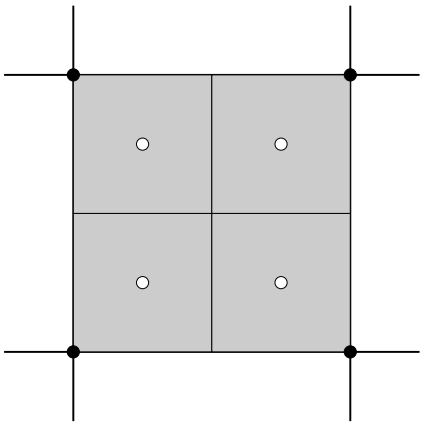

Figure 2.8: A 2D, 4-noded element containing 4 MPs. The nodes of the element are shown as black circles with each MP shown as white circles, the associated volume of each MP is shown as the grey areas.

However, if the background mesh is assembled such that the elements form a uniform grid which is aligned to the Cartesian coordinate axis (a common practice), this becomes a problem that a simple algorithm can handle. In order to determine the element which contains the MP, the global coordinates of the MP are compared with the global coordinates of the nodes of each element in each direction. If the structure of the background mesh is more complicated, other means of determining the element which contains a MP are required which will increase the expense of the analysis (see [81, 134, 252, 321]). If during a load step there are some elements that do not contain any MPs, these elements are omitted from the calculations during the load step.

The linear system in (2.49) is built for the background mesh, however, the physical domain defined by the MPs does not populate the entire mesh meaning that some elements of this mesh are not active in the analysis. This means that nodes associated with these inactive elements have no corresponding values in $[K]$ and $\{f_v\}$, therefore, the solution for displacement for the corresponding degrees of freedom should be zero. In fact, it is simpler to identify the elements that are active in the analysis, these are the elements that contain the physical domain and are influenced by the MPs. By identifying these active elements, it is possible to generate a list of active nodes and the corresponding degrees of freedom for

the analysis, these will define the rows and columns of the linear system that will be solved. Next, displacement boundary conditions must be taken into account as these will restrict the degrees of freedom that are in the linear system. Once the restricted degrees of freedom have been removed from the list, what remains are the "free degrees of freedom", these are the degrees of freedom with unknown displacements which are found using (2.50).

At the end of each load step, the positions of the MPs are updated with the displacement of each MP being calculated using (2.38). The new global coordinate of a MP for the next load step, $n+1$, is calculated by incrementing the global coordinates for the current load step, n, by the displacement of the MP over the load step such that

$$\{x_p\}_{n+1} = \{x_p\}_n + \underbrace{[S_{vp}]\{u_v\}_n}_{\{u_p\}_n}. \tag{2.51}$$

For standard MPM, the volume of each MP in the current configuration is calculated using the deformation gradient and the initial MP volume, V_p^0, or by using the MP volume in the previous configuration, V_p^n, and the increment in the deformation gradient such that

$$V_p = \det([F])\, V_p^0 = \det([\Delta F])\, V_p^n \tag{2.52}$$

where $[\Delta F]$ is the increment in the deformation gradient between the previously converged state and the current state. For other MPM formulations that include MP domains, an updating procedure is applied using the techniques discussed in Section 2.1.1.

Figure 2.9 shows the main steps of a MPM analysis, moving clockwise from top left (which represents a single load step), the steps are:

1. MP data such as stress, volume, and stiffness is mapped onto the nodes of the background mesh;

2. stiffness matrix and internal and external force vectors are assembled and the nodal displacements are calculated;

3. nodal displacements are mapped to the MP positions and MP stress, strain and global position are updated and stored;

4. background mesh is reset;

5. next load step begins (if required).

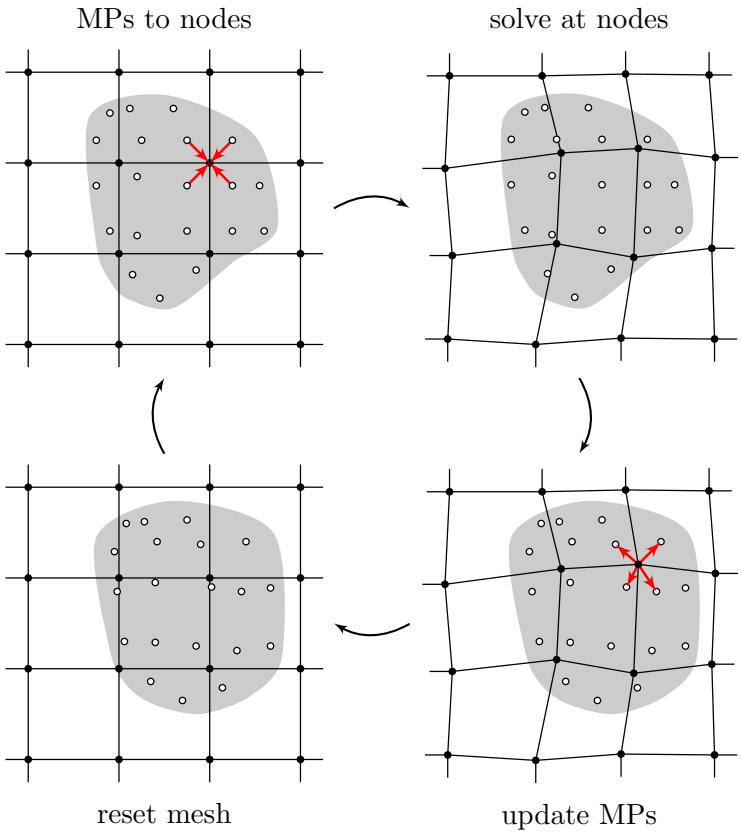

Figure 2.9: Material Point Method numerical steps.

Algorithm 2.1 provides a more in-depth description of the procedure for an implicit MPM analysis of a linear elastic problem over a single load step. For problems involving linear elasticity, it is possible to run the analysis over a single load step and produce accurate results and convergence towards an analytical solution with mesh refinement can be observed. However, if the problem is run using the procedure in Algorithm 2.1 over multiple load steps, mesh refinement will not result in convergence due to the effect of finite deformations introduced to reflect changes

in geometry at the end of each load step. The next section details the changes needed to be made to work with problems involving finite deformations.

Algorithm 2.1: Linear elastic, implicit MPM process for a single load step.

determine which element contains each MP;
determine list of active elements in analysis;
determine free degrees of freedom;
calculate external force vector, $\{f^{ext}\}$ (2.46);
for $p = 1 : n_{mp}$ **do**
  calculate strain-displacement matrix, $[G_p]$ (2.39);
  determine MP stiffness contribution, $[K_p]$ (2.44);
  determine MP internal force contribution, $\{f_p^{int}\}$ (2.48);
assemble global stiffness matrix, $[K]$ (2.45);
calculate residual force vector, $\{f_v\} = \{f^{ext}\} - \{f^{int}\}$;
solve for nodal displacements, $\{u_v\}$ (2.50);
for $p = 1 : n_{mp}$ **do**
  calculate strain-displacement matrix, $[G_p]$ (2.39);
  calculate MP displacement, $\{u_p\}$ (2.38);
  update MP coordinates, $\{x_p\}_{n+1}$ (2.51);
  calculate MP strain, $\{\varepsilon_p\}$ (2.41);
  calculate MP stress, $\{\sigma_p\}$ (2.33);

2.1.4 Large deformation elasticity

In the case of finite deformation mechanics, as the geometry of the physical domain changes through the analysis, the assumption of a linear relationship between the infinitesimal strain and small deformations does not hold. A relationship between the strain and displacements are required (as in the small deformation case), this is achieved through the use of the deformation gradient, $[F]$. The deformation gradient provides the link between the reference and deformed configurations such that

$$[F] = \frac{\partial\{x\}}{\partial\{X\}} \tag{2.53}$$

where $\{X\}$ is the vector of original (reference) coordinates and $\{x\} = \varphi(\{X\})$ are the coordinates in the updated (deformed) body where φ is the motion of the material body. In an updated Lagrangian formulation, the deformation gradient

for the current configuration can be obtained through [76]

$$[F] = [\Delta F]\,[F^n] \tag{2.54}$$

where $[F^n]$ is the deformation gradient for the previously converged state. The increment in the deformation gradient is given by [43]

$$[\Delta F] = [I] + \frac{\partial\{\Delta u\}}{\partial\{\tilde{X}\}} \tag{2.55}$$

where $[I]$ is the identity matrix, $\{\Delta u\}$ is the displacement increment over the current load step and $\{\tilde{X}\}$ is the vector of coordinates of the previously converged state or at the start of the current step. Figure 2.10 shows the reference, previous and deformed configurations of a physical domain in Euclidean space, each configuration depicted as a grey-shaded body. The physical representation of the deformation gradient from the reference configuration to the previously converged configuration can be seen as well as the increment in the deformation gradient for the shift from the previously converged state to the current deformed state. The relative displacements and displacement increments are also shown.

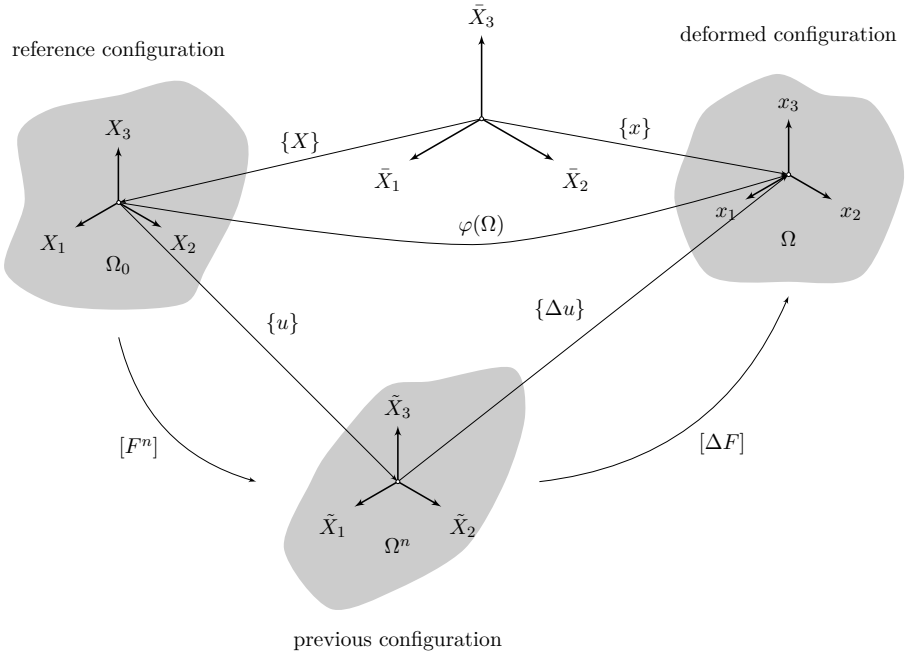

Figure 2.10: Reference, previous and deformed configurations. The physical domain is depicted by the grey-shaded bodies.

In this work the logarithmic strain and Kirchhoff stress measures are used. These measures have been chosen so that the overall framework of the work is as general as possible and can be easily adapted to various problem types. The AMPLE framework uses these stress and strain measures therefore, the work presented in this thesis will be compatible with the work done by the other members of the research group. This work mainly focusses on elasticity but some problems involving plasticity will be shown, and by adopting these measures throughout, only the constitutive model needs to be changed.

From the deformation gradient, the left and right Cauchy-Green strain tensors are calculated as

$$[B] = [F][F]^T \qquad \text{and} \qquad [C] = [F]^T[F] \tag{2.56}$$

respectively. From the left Cauchy-Green strain, the logarithmic strain is calculated as

$$\{\varepsilon\} = \frac{1}{2}\ln[B]. \tag{2.57}$$

The strain is then used to calculate the Kirchhoff stress as

$$\{\tau\} = [D^e]\{\varepsilon\} \tag{2.58}$$

where $[D^e]$ is the same linear elastic isotropic material stiffness tensor used for infinitesimal strain analysis and given in (2.35). The Cauchy stress is obtained from the Kirchhoff stress using the relationship

$$\{\sigma\} = J^{-1}\{\tau\} \tag{2.59}$$

where $J = \det([F])$ is the volume ratio between the deformed and reference configurations.

The residual force vector now takes the form of the weak statement of equilibrium in (2.42) and is given by

$$\{f^R\} = \int_\Omega [G]^T\{\sigma\}\,\mathrm{d}v - \int_\Omega [S_{vp}]^T\{f_b\}\,\mathrm{d}v - \int_{\partial\Omega} [S_v]^T\{f_t\}\,\mathrm{d}s \tag{2.60}$$

where the integration is performed over the updated domain and all basis functions and derivatives are calculated in terms of the nodal coordinates at the start of the

load step, these values do not change over the load step. The aim is to minimise the residual vector, $\{f^R\}$, therefore, an iterative approach is required within a load step as the link between the primary unknown (the nodal displacements) and the stresses in the MPs are non-linear. A Newton-Raphson (N-R) iterative approach is chosen in this work as it is well established in solid mechanics and MPM formulations as well as being a stable iterative procedure for most cases. Throughout the explanation of the N-R approach, k denotes the previous iteration and $k+1$ refers to the current iteration. The incremental displacements over a load step, $\{\Delta u\}$, are obtained by iteratively updating the nodal displacements until (2.60) is satisfied where the iterative displacement increment is given by

$$\{\delta u_{k+1}\} = [K_k]^{-1}\{f_k^R\} \tag{2.61}$$

with $\{f_k^R\}$ being the residual out-of-balance force vector at the k-th iteration and $[K_k]$ being the stiffness matrix calculated at the current displacement. The displacement increment within a load step is calculated as the sum of the incremental displacements calculated at each iteration such that

$$\{\Delta u_{k+1}\} = \sum_{i=1}^{k+1}\{\delta u_i\}. \tag{2.62}$$

The global stiffness matrix is the linearisation of the residual force vector which is assembled from the stiffness contribution of each MP using (2.45), with the particle stiffness matrix given by

$$[K_p] = [G_p]^T[A_p][G_p]\,V_p \tag{2.63}$$

where $[A_p]$ is the consistent tangent of a MP and calculated as

$$[A] = \frac{1}{2J}[D^e]^T\,[L^D]\,[B^D] - [S^D]. \tag{2.64}$$

In (2.64), $[L^D]$ is the derivative of the tensor logarithm function evaluated at the left Cauchy-Green strain, $[B^D]$ is a fourth-order tensor containing the values of the left Cauchy-Green strain and $[S^D]$ is a fourth-order tensor containing values of the

Cauchy stress and their Cartesian components are given by [43]

$$\begin{aligned} L^D_{ijkl} &= \frac{\partial \ln (B_{ij})}{\partial B_{kl}} \\ B^D_{ijkl} &= \delta_{ik} B_{jl} + \delta_{jk} B_{il} \\ S^D_{ijkl} &= \delta_{jk} \sigma_{il} \end{aligned} \tag{2.65}$$

respectively. The internal force vector is computed as in (2.48) using the current stress state of the MP and the MP basis function derivatives and volume calculated at the start of the load step.

The strain-displacement matrix, $[G]$, is generated using values contained within the derivatives of the basis functions with respect to the updated coordinates. Charlton *et al.* [43] proposed a method of generating the basis function derivatives using the chain rule and the definition in (2.53) where

$$[\nabla_x S_{vp}] = \frac{\partial ([S_{vp}])}{\partial \{x\}} = \frac{\partial ([S_{vp}])}{\partial \{\tilde{X}\}} \frac{\partial \{\tilde{X}\}}{\partial \{x\}} [\Delta F]^{-1}. \tag{2.66}$$

Figure 2.11 shows the iterative process for the N-R method. Starting at point A, the previously converged state for applied external force, $\{f^{ext}_n\}$, and converged displacement, $\{u_n\}$, the external force is incremented by $\{f^R_0\}$ to $\{f^{ext}_{n+1}\}$. The stiffness matrix is then calculated to obtain the first displacement increment, $\{\delta u_1\}$, giving an overall displacement of $\{\Delta u_1\}$ and the internal forces are recalculated. It is clear that the calculated displacement at point B^* results in internal forces that are too small with the point on the equilibrium path at point B, meaning that the equilibrium in (2.60) is not satisfied in that $\{f^R_1\}$ is greater than a prescribed tolerance, tol, therefore, another iteration is required. For the next iteration, starting at point B, the stiffness matrix is recalculated using the updated displacement state and using the residual vector, the next displacement increment, $\{\delta u_2\}$, is calculated giving an overall displacement of $\{\Delta u_2\}$ and the new out-of-balance forces, $\{f^R_2\}$, resulting in point C on the equilibrium path. The N-R iterations are repeated until the residual out-of-balance force is calculated to have a value less than the prescribed tolerance, $\{f^R_k\} < tol$, meaning that a converged state has been achieved for the prescribed external force.

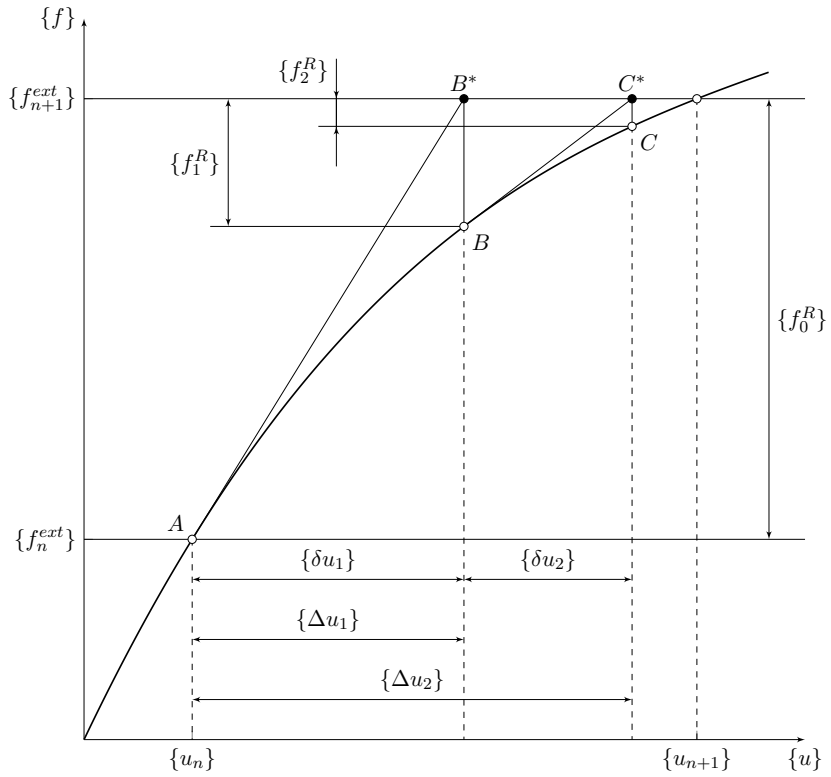

Figure 2.11: Newton-Raphson iterative method.

Algorithm 2.2 process for a simulation involving large deformation mechanics over multiple load steps. There is a clear difference compared to Algorithm 2.1 with the N-R loop where displacements and internal forces are incrementally calculated until the out-of-balance errors are withing a predetermined tolerance. The residual out-of-balance force vector is initialised at the start of each load step such that the norm of the residual is greater than the prescribed tolerance in order to enter the N-R iteration loop for the load step. The residual force vector is not used in the zeroth iteration as no stiffness matrix has been created for this load step yet, a suitable residual force vector is generated by the end of the zeroth iteration. Due to the fact that no stiffness matrix is calculate by the start of the zeroth iteration, no solution step is performed, the zeroth iteration simply generates the initial stiffness and force configuration for the load step, the solution step begins to occur in the first iteration.

Algorithm 2.2: Implicit MPM process for large deformation problems.

```
for n = 1 : lstps do
    determine which element contains each MP;
    determine list of active elements in analysis;
    determine free degrees of freedom;
    calculate external force vector, {f^ext} (2.46);
    initialise residual out-of-balance force, |{f_0^R}| > tol ⇒ f_err > tol;
    while f_err > tol do
        if k > 0 then
            solve unknown nodal displacement increment, {δu_{k+1}} (2.61);
        else
            zero nodal displacement increment, {δu_0} = {0};
        update the increment nodal displacements, {Δu_{k+1}} (2.62);
        for p = 1 : n_mp do
            calculate deformation gradient increment, [ΔF] (2.55);
            update deformation gradient, [F] (2.54);
            calculate left Cauchy-Green strain, [B_p] (2.56);
            calculate logarithmic strain, {ε_p} (2.57);
            calculate Kirchhoff stress, {τ_p} (relevant const. model eg.
            (2.58));
            calculate Cauchy stress, {σ_p} (2.59);
            calculate strain-displacement matrix, [G_p] (2.39);
            calculate consistent tangent matrix, [A_p] (2.64);
            calculate MP internal forces, {f_p^int} (2.48);
            determine MP stiffness contribution, [K_p] (2.63);
        assemble internal force vector, {f^int};
        assemble global stiffness matrix, [K];
        calculate residual out-of-balance forces, {f_{k+1}^R} = {f^ext} − {f^int};
        calculate norm of residual force, f_err = |{f_{k+1}^R}|;
    for p = 1 : n_mp do
        update MP domain lengths, l_p^i;
        calculate MP displacement, {u_p} (2.38);
        update MP coordinates, {x_p}_{n+1} (2.51);
```

2.1.5 Overcoming volumetric locking

It has been well documented that when modelling nearly incompressible solids overly stiff numerical solutions can be obtained. This is known as volumetric locking and occurs due to low order elements being used and the fact that low order interpolation polynomials are inadequate in representing volume preserving displacement fields [75]. A common approach to overcoming volumetric locking

is the F-bar approach developed by de Souza Neto and co-workers [74, 75] which was developed for the FEM. The F-bar approach involves the decomposition of the deformation gradient such that

$$[F] = [F_{dev}]\,[F_{vol}], \tag{2.67}$$

where $[F_{dev}]$ and $[F_{vol}]$ are the deviatoric and volumetric components of the deformation gradient respectively defined as

$$[F_{dev}] = \det([F])^{-1/3}\,[F] \qquad \text{and} \qquad [F_{vol}] = \det([F])^{1/3}\,[I]. \tag{2.68}$$

It is worth noting that $\det([F_{dev}]) = (\det([F])^{-1/3})^3 \det([F]) = 1$ meaning that the all of the volume change is contained within the volumetric component of the deformation gradient as expected.

A deformation gradient, $[F^0]$, is computed which results from the displacement at the centroid of the element. The modified deformation gradient, $[\bar{F}]$, is calculated as the composition of the deviatoric stress component of $[F]$ and the volumetric component of $[F^0]$ such that

$$[\bar{F}] = [F_{dev}][F^0_{vol}] = \left(\frac{\det([F^0])}{\det([F])}\right)^{-1/3} [F]. \tag{2.69}$$

The modified deformation gradient is then used to compute the stiffness matrix and internal force vector. Coombs *et al.* [57] implemented the F-bar approach in the quasi-static MPM formulation. The F-bar is a solid choice for use in the MPM as it:

- does not introduce any additional unknowns,
- is easily implemented,
- does not restrict the choice of constitutive model,
- does not require any tuning parameters,
- and does not require additional MPs to track volumetric behaviour.

2.1.6 Ghost stabilisation

The issue of cell crossing instability has been discussed already in this chapter, however, this is not the only problem that may occur within a MPM analysis. As the boundary of the physical domain will not necessarily coincide with the background mesh, there is a potential that small portions of the physical domain will occupy elements of the background mesh, these partially filled elements are susceptible to poorer integration than the elements that are completely filled by the physical domain. This "small cut" problem may lead to poor conditioning of the global system of equations and impact the stability of the MPM analysis. This problem is not confined to the MPM; similar issues can also be seen in the cut finite element method [37, 38, 282] where intersections are present between an element and the problem domain. The ill-conditioning of the global system of equations due to the presence of the partially filled elements can be quantified by the condition number of the linear system. The condition number is a measure of the the sensitivity of the solution to small perturbations in the input [80]. A problem is called ill-conditioned if the condition number is infinite. The condition number can be calculated as the the ratio of the largest and smallest eigenvalues of the global system matrix. The smallest eigenvalue of the system matrix is related to the smallest intersection between the physical domain and the background mesh. In reality, this intersection can be extremely small (much smaller than the size of the elements of the background mesh in fact) which means that there is no lower bound for the smallest eigenvalue. This means that the condition number of the system is unbounded from above (while bounded from below at zero) and this is detrimental to the solution stage of the analysis.

In order to overcome this, Burman [36] introduced the ghost stabilisation technique for a finite element framework. The ghost stabilisation involves penalising jumps in the gradient of the solution field across elements cut by the boundary of the physical domain [282]. This was done by introducing an extra term into the linear

system to improve the conditioning of the system matrix. Coombs [55] implemented the ghost stabilisation method within the MPM where the "faces" of the elements (or element edges in 2D) which are cut by the boundary of the physical domain are determined and the ghost penalty is integrated over each of these faces. The "boundary elements" are found by determining whether an element is populated by MPs and checking whether each populated element is attached to (shares a face with) any unpopulated elements. Once the boundary elements are determined, a list of boundary faces is compiled by finding which faces are between two boundary elements or a face of a boundary element which is also a face of a fully populated element.

The integration of the ghost stabilisation term is performed over each of the boundary faces, as each face is associated with two elements let $(\cdot)^+$ and $(\cdot)^-$ denote the "positive" and "negative" elements attached to the boundary face between the two elements. The ordering convention of these positive and negative faces is arbitrary but must be consistent throughout the mesh in all directions. A unit normal vector, $\{n\}$, can be determined for the boundary face, Γ, in the direction moving from the positive to the negative element for the face in question. For the case of a background mesh made up of linear finite elements, the global ghost stabilisation term is given as

$$[J_G] = \frac{h_f^3}{3} \int_\Gamma ([G_G]^T [n][n]^T [G_G]) \, \mathrm{d}\Gamma \quad \text{where} \quad [G_G] = \left[[G_G^+] \ \left(-[G_G^-] \right) \right], \tag{2.70}$$

where h_f is the size of the element face*. The $[G_G^+]$ and $[G_G^-]$ matrices contain the derivatives of the finite element shape functions for the positive and negative elements respectively. In a quasi-static analysis, the ghost stabilisation technique can be thought of as a penalty approach that introduces an extra term into the weak form of equilibrium (2.42). This can be expressed as an extra stiffness term such that

$$[K_G] = \gamma_G [J_G] \tag{2.71}$$

*The determination of the value of h_f is dependent of the number of dimensions of the analysis. In 2D, h_f is simply the length of the face, however, in 3D, the face is a 2D shape (a quadrilateral in this work), therefore, h_f is taken to be the maximum side length of the face.

where $[K_G]$ is the ghost stabilisation stiffness and γ_G is the ghost stabilisation penalty parameter. In order to integrate over each boundary face, Gauss-Legendre quadrature is chosen due to its efficiency and convenience. This approximates $[J_G]$ from (2.70) by integrating over each boundary face such that

$$[J_G] \approx \underset{\forall \Gamma}{A} \left(\frac{h_f^3}{3} \sum_{i=1}^{n_{gp}} ([G_G]_i^T [n][n]^T [G_G]_i) w_i \det([J]_i) \right) \tag{2.72}$$

where $(\cdot)_i$ denotes the quantity based on the Gauss point position, n_{gp} is the number of Gauss points used to approximate the integral over the face, w_i are the weights of the Gauss points and $\det([J])$ is the determinant of the surface Jacobian (i.e. the ratio between the global and local face sizes).

In a 2D analysis, the normal matrix and the shape function derivative matrix take the form

$$[n]^T = \begin{bmatrix} n_x & 0 & 0 & n_y \\ 0 & n_y & n_x & 0 \end{bmatrix} \quad \text{and} \quad [G_G^+] = \begin{bmatrix} \frac{\partial S_1^+}{\partial x} & 0 & \cdots & \frac{\partial S_{nen}^+}{\partial x} & 0 \\ 0 & \frac{\partial S_1^+}{\partial y} & \cdots & 0 & \frac{\partial S_{nen}^+}{\partial y} \\ 0 & \frac{\partial S_1^+}{\partial x} & \cdots & 0 & \frac{\partial S_{nen}^+}{\partial x} \\ \frac{\partial S_1^+}{\partial y} & 0 & \cdots & \frac{\partial S_{nen}^+}{\partial y} & 0 \end{bmatrix}$$

where n_{en} is the number of nodes of the element. It is worth noting that $[G_G^-]$ has the same format as $[G_G^+]$ with S_i^+ replaced by S_i^-. In 3D, the normal matrix and shape function derivative matrix take into account the extra dimension and are given by

$$[n]^T = \begin{bmatrix} n_x & 0 & 0 & n_y & 0 & n_z \\ 0 & n_y & 0 & n_x & n_z & 0 \\ 0 & 0 & n_z & 0 & n_y & n_x \end{bmatrix}$$

and

$$[G_G^+] = \begin{bmatrix} \frac{\partial S_1^+}{\partial x} & 0 & 0 & \cdots & \frac{\partial S_{nen}^+}{\partial x} & 0 & 0 \\ 0 & \frac{\partial S_1^+}{\partial y} & 0 & \cdots & 0 & \frac{\partial S_{nen}^+}{\partial y} & 0 \\ 0 & 0 & \frac{\partial S_1^+}{\partial z} & \cdots & 0 & 0 & \frac{\partial S_{nen}^+}{\partial z} \\ \frac{\partial S_1^+}{\partial y} & \frac{\partial S_1^+}{\partial x} & 0 & \cdots & \frac{\partial S_{nen}^+}{\partial y} & \frac{\partial S_1^+}{\partial x} & 0 \\ 0 & \frac{\partial S_1^+}{\partial z} & \frac{\partial S_1^+}{\partial y} & \cdots & 0 & \frac{\partial S_{nen}^+}{\partial z} & \frac{\partial S_1^+}{\partial y} \\ \frac{\partial S_1^+}{\partial z} & 0 & \frac{\partial S_1^+}{\partial x} & \cdots & \frac{\partial S_{nen}^+}{\partial z} & 0 & \frac{\partial S_1^+}{\partial x} \end{bmatrix}.$$

Including this ghost stabilisation in a MPM analysis has been shown to greatly improve the conditioning of the system which enhances the stability of the analysis. It was shown that the use of ghost stabilisation allows problems with coarse meshes and MP distributions to run to completion where there would not normally run with a standard MPM scheme [55]. Another benefit of using the ghost stabilisation is that the solution around the boundary of the physical domain is much smoother in terms of the stress fields with spurious oscillations in stresses being less frequent.

Summary

This chapter has presented the background of the MPM, discussing the applications of the MPM as well as the few times the MPM has been used in the field of biomechanical modelling. Various choices of basis functions were presented for the interpolation of the MP data to the background mesh, each with their own advantages and disadvantages. The formulation for small deformation linear elasticity with its implementation being a simple adaptation from the FEM using the MPs as the integration points. The MPM framework for finite deformation elasticity was also presented, detailing the use of the deformation gradient and the choice of the logarithmic strain and Kirchhoff stress measures used in this work. A Newton-Raphson iterative approach was chosen for the framework to calculate the deformation over a load step and the iterative process was detailed. Algorithms for the small strain and finite deformation frameworks were presented. Only linear stress-strain relationships were presented in this chapter, however, one benefit of the way that the framework has been designed, the algorithms do not need to be altered for non-linear stress-strain relationships. All that needs to be included is the desired function relating the stresses to a given strain and stiffness.

While this chapter aims to cover the main concepts of the MPM, it by no means includes everything. For more information on the formulation of the MPM, the reader is directed towards the original work of Sulsky and co-workers [287, 290]

as well as the many papers [16, 43, 226, 283] and textbooks [99, 229, 349] that cover the MPM. This chapter also does not include numerical examples as the author believes including them in this text is unnecessary as benchmark examples of the MPM have been produced in numerous instances of the past literature. If the reader is interested in seeing numerical examples of the MPM, examples of resources that the reader is directed to include [56, 77, 229, 276].

The next chapter focusses on the application of Neumann boundary conditions over the non-conforming boundary of the MPM domain using B-splines.

Chapter 3

B-spline MPM Boundary Representation

Due to the fact that MPM uses discrete points to model the problem domain, it is often the case that the boundary of the domain does not coincide with the background mesh elements. This means that it is not straightforward to apply boundary conditions directly to a domain whose boundary does not conform with the background mesh and a more involved process is required. Due to the non-conforming nature of the boundary of the domain with respect to the elements of the background mesh, inaccuracies when prescribing displacements or tractions over said boundary are often seen, therefore, a method of representing (and tracking) domain boundaries is also required. One method of applying boundary conditions is to use a moving mesh concept [169, 246] in which the background mesh is moved with every load step to ensure that the problem domain boundary always coincides with the mesh, therefore, the boundary conditions can be applied directly to the nodes of the background mesh. However, as with FEA, large deformation problems may encounter mesh distortion and remeshing is required. The moving mesh concept can only be applied if the boundary does not change shape, however, this may not be the case in the future. If a moving mesh is used in the MPM, in general, the regular structure of the background

mesh will be lost [61]. The regular background mesh is a key advantage of the MPM and losing this will result in more computational effort, especially in the MP searching process. It is also possible to apply non-conforming boundary conditions using Lagrange multipliers, the penalty method or Nitsche's method (the reader is directed towards Fernández-Méndez and Huerta [100] for more details on this). Boundary points which track the deformation of the boundary have also been used with weighting parameters to prescribe non-zero traction boundary conditions [45, 46, 131]. Mast and co-workers presented a dual-grid approach for the MPM [216] to impose boundary conditions where an additional set of elements are used to determine the essential boundaries with respect to the background mesh, however, this approach was found to be sensitive to the location of the boundaries as well as the size of the mesh [214]. Höllig and co-workers [140–142] introduced the use of weighted extended B-splines (Web-splines) as a new form of interpolation function which can be used to apply homogeneous Dirichlet boundary conditions without the need for an additional mesh. The Implicit Boundary Method (IBM) [35, 61, 177, 178, 205, 350] uses a penalty approach to apply extra penalty stiffness around the boundary of the physical domain to enforce Dirichlet boundary conditions. The IBM was applied to the MPM framework to allow for roller boundary conditions on inclined boundaries [61, 205], however, this is only feasible for straight boundaries in its current state. The weighted finite cell method [345, 346] has also been used to apply inhomogeneous Dirichlet boundary conditions without the need for mesh generation. In terms of the application of Neumann boundary conditions, Remmerswaal [258] proposed a boundary detection approach for the MPM based on level sets, similar to concepts seen in the fluid mechanics community. Yamaguchi *et al.* [334] used boundary points to represent and track the domain boundary and Nitsche's method to impose arbitrary boundary conditions. Liang *et al.* [198] imposed Neumann boundary conditions by considering the stress field at the boundary being caused by a virtual stress field positioned around the physical domain.

Bing *et al.* [24] developed a procedure of using B-spline curves to generate a representation of the boundary of a 2D domain for a MPM analysis. A series of boundary points, with zero volume so that they do not participate in the analysis, are positioned where the desired boundary of the domain should be and are used as sampling points to generate the B-spline curve. As the MPs are displaced through the background mesh, the boundary points are also displaced based on the deformation of the background mesh, therefore, representing the changing boundaries during an analysis. As a moving boundary can be represented using B-splines, without altering the background mesh, it is possible to apply homogeneous and inhomogeneous boundary conditions directly to the physical domain with increased accuracy.

Bing [25] detailed the construction of B-spline curves, including local and global interpolation of B-spline curves, which will be omitted here. This work expands on that presented by Bing and co-workers [24, 25] by developing the B-spline boundary representation for 3D problems in the MPM. Only cubic B-splines are presented in this work as the handling of 3D data and inflection points becomes simpler compared to using quadratic B-splines due to the fact that no special treatments are required, especially for the case when points of inflection are present (see [248] for more details).

When creating a B-spline curve or surface, it is often the case that a set of sampling points are used to represent the boundary, a method of fitting the B-spline to these sampling points is therefore required. There are a two methods of fitting a B-spline curve/surface to the sampling points, interpolation or approximation [248]. Interpolation constructs the B-spline curve/surface such that it will lie exactly on each sampling point, whereas with approximation, the B-spline curve/surface does not necessarily have to lie precisely on each point, often with a maximum deviation bound being prescribed. In this work, B-spline curves/surfaces are used to represent the boundary of a MPM domain and are constructed based on a set of sampling points positioned along the pseudo-boundary of the domain, therefore, it is required

that the B-spline curve/surface must lie exactly on these sampling points, so the interpolation fitting method is used. There are also two types of fitting algorithms that can be used, global or local. The global algorithm sets up a system of equations or optimisation to be solved, only the control points are unknown in this work which results in a simple linear system to be solved. The downside of a global fitting scheme is the fact that any small perturbation in the data will affect the whole system and can change the entire shape of the B-spline curve/surface. The alternative is a local scheme which is more geometrically based where the curve/surface is constructed segment-wise, using only a small proportion of the set of sampling points. This means that a perturbation in the data will only affect the curve/surface locally. Due to the segment-wise construction, local schemes also are less computationally expensive than the global scheme. For these reasons, this work utilises the local interpolation scheme to fit a B-spline curve/surface to a set of sampling points.

3.1 B-spline basis functions and their derivatives

B-spline basis functions were mentioned in Section 2.1.1 in the context of the MPM formulation. For completeness, this concept will be restated and expanded upon to include more detail on how to generate the B-spline basis functions as well as their derivatives.

The B-spline basis functions are formed from a knot vector $\{\Xi\} = \{\xi_0, \xi_1, \ldots, \xi_m\}$ where $(m+1)$ is the total number of knots and $\xi_0, \xi_1, \ldots, \xi_m$ is a sequence of non-decreasing real numbers such that $\xi_i \in \mathbb{R}$ and $\xi_i \leq \xi_{i+1}$ for $i = 0, 1, \ldots, m-1$. The type of knot vector that is used in this work is an open knot vector (or non-periodic or clamped) in which the first and last knots have a multiplicity of $p+1$, thus the knot vector takes the form

$$\{\Xi\} = \{\underbrace{a, \ldots, a}_{p+1}, \xi_{p+1}, \ldots, \xi_{m-p-1}, \underbrace{b, \ldots, b}_{p+1}\}. \tag{3.1}$$

There are a total of $n = m - p - 1$ non-zero basis functions which are calculated recursively using the Cox-de-Boor formula [64, 69, 70] such that the i-th B-spline basis function of p-degree is defined as:

- for $p = 0$

$$N_{i,0}(\xi) = \begin{cases} 1 & \text{if } \xi_i \leq \xi < \xi_{i+1} \\ 0 & \text{otherwise} \end{cases} \tag{3.2}$$

- for $p > 0$

$$N_{i,p}(\xi) = \frac{\xi - \xi_i}{\xi_{i+p} - \xi_i} N_{i,p-1}(\xi) + \frac{\xi_{i+p+1} - \xi}{\xi_{i+p+1} - \xi_{i+1}} N_{i+1,p-1}(\xi). \tag{3.3}$$

For the $p = 0$ case, (3.2) is a step function where $N_{i,0}(\xi)$ is equal to zero everywhere other than the half-open interval $\xi \in [\xi_i, \xi_{i+1})$, also called the knot span. For $p > 0$, the basis function, $N_{i,p}(\xi)$, is a linear combination of two $(p-1)$-degree basis functions. It is convention that a quotient of $\frac{0}{0}$ in (3.3) is defined as zero.

Figure 3.1 shows the non-zero zeroth-degree B-spline basis functions for the open knot vector $\{\Xi\} = \{0, 0, 0, 0, 1, 2, 3, 4, 4, 4, 4\}$ using (3.2). Only four knot spans are present in $\{\Xi\}$ which produce non-zero basis functions. These basis functions are used in the recursive formula of (3.3) to calculate the higher order basis functions which are shown in Figure 3.2 up to the cubic B-spline basis functions ($p = 3$). It is clear to see that the higher the degree of basis function that is used, the greater the number of basis functions which are produced. While the example given here uses an evenly distributed knot vector, it is entirely possible to use a non-uniformly distributed set of knots in the vector, this is not used in this work as the boundary points used to represent the boundary will initially be evenly distributed over the boundary meaning that it is reasonable to use uniformly distributed knot vectors.

The k-th derivative of the B-spline basis functions with respect to ξ are given by

$$N_{i,p}^{(k)}(\xi) = \frac{p!}{(p-k)!} \sum_{j=0}^{k} a_{k,j} N_{i+j,p-k}(\xi) \tag{3.4}$$

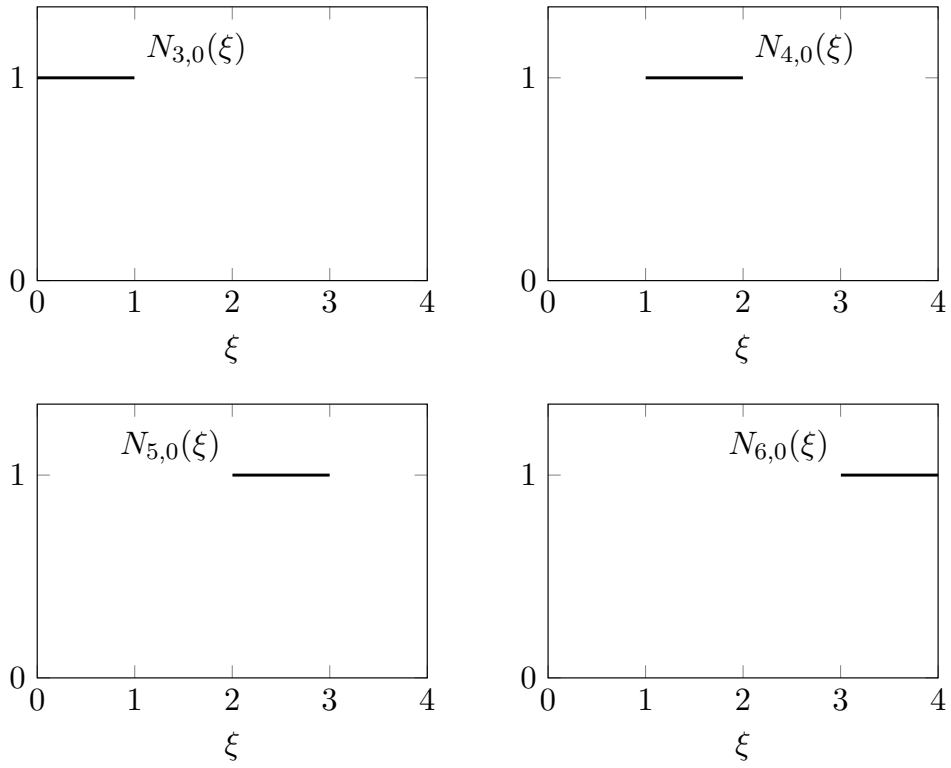

Figure 3.1: The non-zero zeroth-degree B-spline basis functions for knot vector $\{\Xi\} = \{0, 0, 0, 0, 1, 2, 3, 4, 4, 4, 4\}$.

given that

$$\begin{aligned} a_{0,0} &= 1 \\ a_{k,0} &= \frac{a_{k-1,0}}{\xi_{i+p-k+1} - \xi_i} \\ a_{k,j} &= \frac{a_{k-1,j} - a_{k-1,j-1}}{\xi_{i+p+j-k+1} - \xi_{i+j}} \quad j = 1, \ldots, k-1 \\ a_{k,k} &= \frac{-a_{k-1,k-1}}{\xi_{i+p+1} - \xi_{i+k}}. \end{aligned}$$

From (3.4), the first derivative of the B-spline basis functions are therefore defined as

$$N_{i,p}^{(1)}(\xi) = \frac{p}{\xi_{i+p} - \xi_i} N_{i,p-1}(\xi) + \frac{p}{\xi_{i+p+1} - \xi_{i+1}} N_{i+1,p-1}(\xi). \tag{3.5}$$

Using the example of the knot vector $\{\Xi\} = \{0, 0, 0, 0, 1, 2, 3, 4, 4, 4, 4\}$, the first derivative of the cubic B-spline basis functions are shown in Figure 3.3.

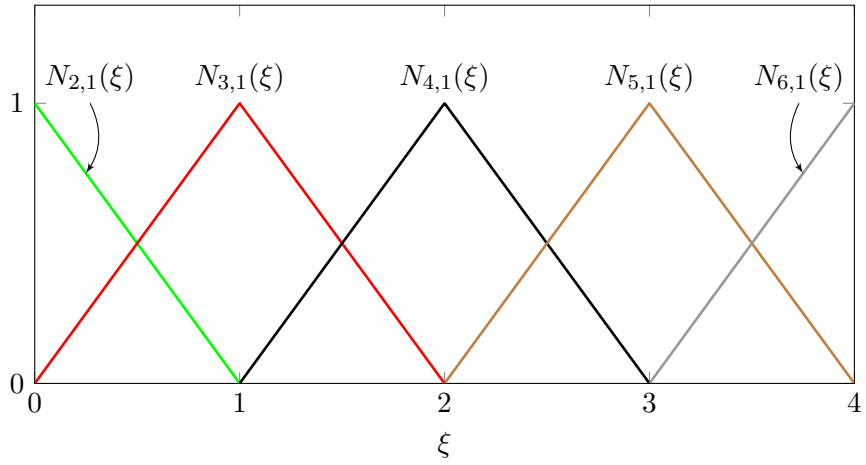

(a) linear ($p = 1$)

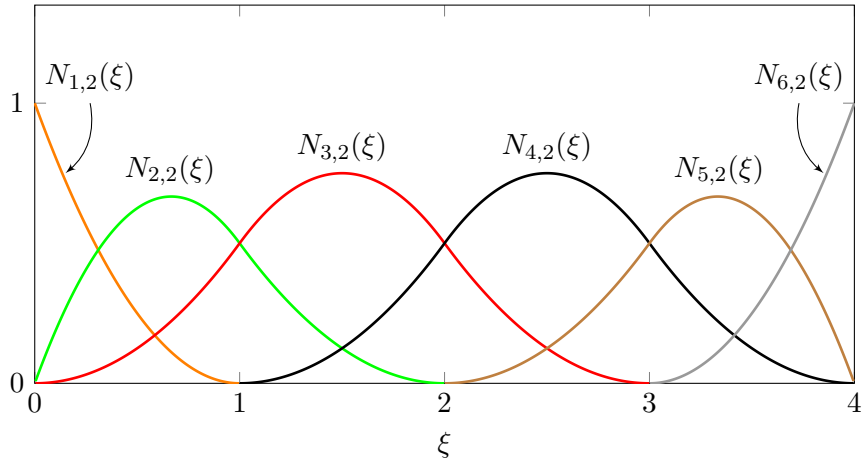

(b) quadratic ($p = 2$)

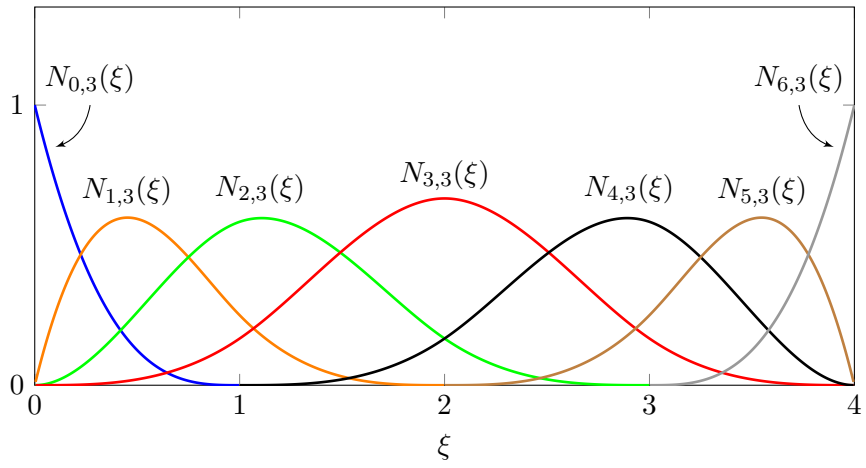

(c) cubic ($p = 3$)

Figure 3.2: The non-zero higher-degree B-spline basis functions for knot vector $\{\Xi\} = \{0, 0, 0, 0, 1, 2, 3, 4, 4, 4, 4\}$.

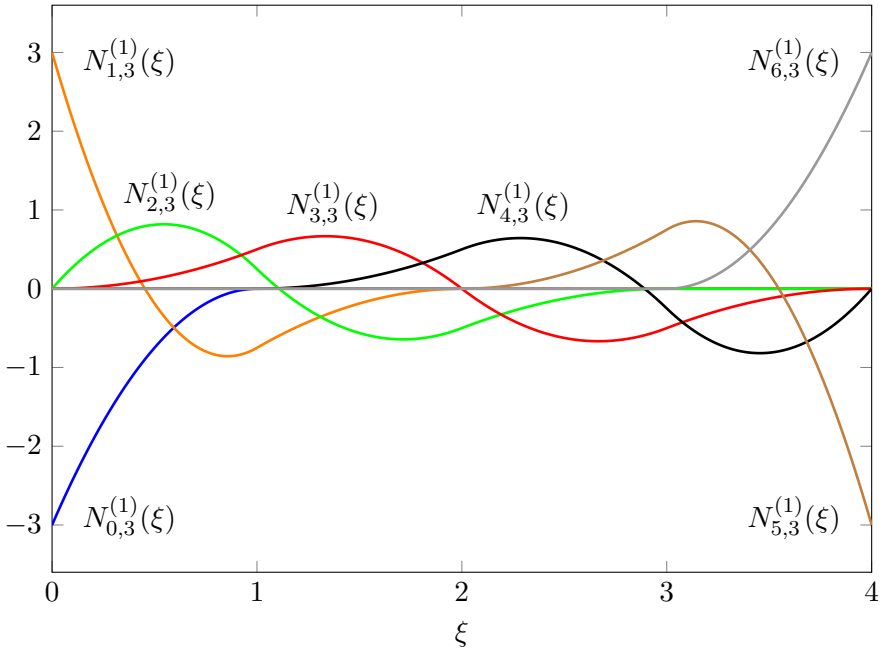

Figure 3.3: First derivative of the cubic B-spline basis functions for knot vector $\{\Xi\} = \{0, 0, 0, 0, 1, 2, 3, 4, 4, 4, 4\}$.

3.2 B-spline Curves

A p-th degree B-spline curve is defined as [248]

$$\{C(\xi)\} = \sum_{i=0}^{n_\xi} N_{i,p}(\xi)\{P_i\} \tag{3.6}$$

where ξ is the local parametric coordinate along the curve corresponding to the knot vector $\{\Xi\}$, n_ξ is the number of control points of the curve and $\{P_i\}$ is the i-th control point. The k-th derivative of a B-spline curve with respect to ξ is defined as

$$\{C^{(k)}(\xi)\} = \sum_{i=0}^{n_\xi} N^{(k)}_{i,p}\{P_i\} \tag{3.7}$$

where $N^{(k)}_{i,p}$ is the k-th derivative of the B-spline basis functions as given in (3.4). The tangent to the B-spline curve is the first derivative of the B-spline curve and is given by

$$\{C^{(1)}(\xi)\} = \sum_{i=0}^{n_\xi} N^{(1)}_{i,p}\{P_i\}. \tag{3.8}$$

3.2.1 Local interpolation

Rather than explicitly stating the positions of the control points, it is often the case that a set of sampling points are used which the B-spline curve will pass through. It is from these sampling points that the control points are determined. Using a local interpolation scheme, a polynomial Bézier curve can be generated between each pair of sampling points along the path of the boundary, this produces a set of control points and a knot vector which will preserve continuity over the entire curve. Given a set of $(n_k + 1)$ sampling points, $\{Q_k\}$, $k = 0, 1, \ldots, n_k$, to which a B-spline curve is to be fitted, a series of curve segments, $\{C_i(\xi)\}$, can be created with endpoints $\{Q_i\}$ and $\{Q_{i+1}\}$ for $i = 0, 1, \ldots, n_k - 1$. Let $\xi^\dagger$ be the local parameter at the end of $\{C_i(\xi)\}$ and the start of $\{C_{i+1}(\xi)\}$, meaning that $\{C_i(\xi)\}$ and $\{C_{i+1}(\xi)\}$ meet at $\xi^\dagger$. It is possible to achieve G^1 continuity* by ensuring that the tangent direction at the end of one curve segment coincides with the tangent direction at the start of the next curve segment such that $\{C_i^{(1)}(\xi)\} = \{C_{i+1}^{(1)}(\xi)\}$, thus ensuring that the curve is smooth along the connection between curve segments. It is worth noting that, for a cubic B-spline, the number of control points, n_ξ, can be calculated from the number of sampling points such that $n_\xi = 2n_k + 1$.

In order to create the Bézier curve segments, inner control points are required (two inner control points for cubic B-spline curves) and these control points lie of the tangents of $\{Q_k\}$. There are many methods that can be used to determine the tangent vector at each sampling point, see [27] for a survey of these methods. It is possible to categorise the methods into ones which are based on knot values at sampling points and ones which are more geometric in nature and are based on the global coordinates of the sampling points. The first option calculates the tangent,

*Here G is for geometric, G^n continuity is a measure of the how curve or surface segments meet depending on the characteristics of the curves/surfaces either side of the connection point. G^n continuity means that the n-th derivatives of the vectors of the curve/surface segments at the join are equal in direction. This is different to C^n continuity which states that the vectors must have equal direction and magnitude. For example, G^0 continuity means that the curves/surfaces simply meet at the join point. Here, G^1 continuity (or tangency continuity) means that the first derivatives must have equal directions either side of the connection point.

$\{D_k\}$, as a linear interpolation of the chord length's gradients such that

$$\{D_k\} = (1 - \alpha_k)\{d_k\} + \alpha_k\{d_{k+1}\} \tag{3.9}$$

where

$$\{d_k\} = \frac{\{q_k\}}{\Delta\xi_k} \qquad \text{given that} \qquad \Delta\xi_k = \xi_k - \xi_{k-1}$$

with $\{q_k\}$ being the vector between sampling points such that

$$\{q_k\} = \{Q_k\} - \{Q_{k-1}\}. \tag{3.10}$$

The coefficient α_k in (3.9) is calculated using the Bessel method [69]

$$\alpha_k = \frac{\Delta\xi_k}{\Delta\xi_k + \Delta\xi_{k+1}}, \tag{3.11}$$

which is a three-point method, named after the fact that three sampling points are used ($\{Q_{k-1}\}$, $\{Q_k\}$ and $\{Q_{k+1}\}$). Special treatments are needed when dealing with the end sampling points where the end tangents are calculated as

$$\{D_0\} = 2\{d_1\} - \{D_1\} \qquad \text{and} \qquad \{D_{n_k}\} = 2\{d_{n_k}\} - \{D_{n_k-1}\}. \tag{3.12}$$

The alternate approach is to determine the tangents based on the geometry of the sampling points where the tangent at each sampling point, $\{T_k\}$ is calculated as [27]

$$\{T_k\} = \frac{\{V_k\}}{|\{V_k\}|} \tag{3.13}$$

where

$$\{V_k\} = (1 - \beta_k)\{q_k\} + \beta_k\{q_{k+1}\}. \tag{3.14}$$

Equations (3.13) and (3.14) are simply geometric relations between a sampling point and its neighbouring points, the vector calculated in (3.13) only provides a measure of the direction of the tangent due to the fact that it is a unit vector. It is clear from (3.14) that $\{V_k\}$ is a linear interpolation between the two directional vectors connecting the sample points to its adjacent sampling points. The value of β_k can be found using a five-point scheme [3, 247, 259] where

$$\beta_k = \frac{|\{q_{k-1}\} \times \{q_k\}|}{|\{q_{k-1}\} \times \{q_k\}| + |\{q_{k+1}\} \times \{q_{k+2}\}|} \qquad k = 2, \ldots, n_k - 2 \tag{3.15}$$

and as with the three-point scheme, special treatments are required such that

$$\{q_0\} = 2\{q_1\} - \{q_2\} \qquad \{q_{-1}\} = 2\{q_0\} - \{q_1\}$$
$$\{q_{n_k+1}\} = 2\{q_{n_k}\} - \{q_{n_k-1}\} \quad \{q_{n_k+2}\} = 2\{q_{n_k+1}\} - \{q_{n_k}\}$$

which are substituted into (3.15) when calculating the tangent vectors $\{T_0\}$, $\{T_1\}$, $\{T_{n_k-1}\}$ and $\{T_{n_k}\}$. If three sampling points are collinear, the five-point scheme produces a tangent vector which is parallel to the line segment and generates a straight line through the points automatically, this is not the case for the three-point scheme. The additional benefit of the five-point scheme over the three-point scheme is the fact that no assignment of knot values at each sampling point is required at the start of the generation process. For these reasons, this work will utilise the five-point scheme for the creation of the B-spline curves. Figure 3.4 depicts the required components for the calculation of the tangent vector $\{T_k\}$ at sampling point $\{Q_k\}$. The black circles represent the set of five sampling points needed to calculate the tangent vector ($\{Q_{k-2}\}$, $\{Q_{k-1}\}$, $\{Q_k\}$, $\{Q_{k+1}\}$, $\{Q_{k+2}\}$), the black arrows are the vectors between each sampling points calculated using (3.10). The vectors $\{q_{k-1}\}$, $\{q_k\}$, $\{q_{k+1}\}$ and $\{q_{k+2}\}$ are then used in (3.15) to determine the interpolation value β_k which is used in (3.14) to calculate $\{V_k\}$, which is shown as the blue arrow in Figure 3.4. Finally, the red arrow is $\{T_k\}$ which is calculated as the unit vector of $\{V_k\}$ via (3.13).

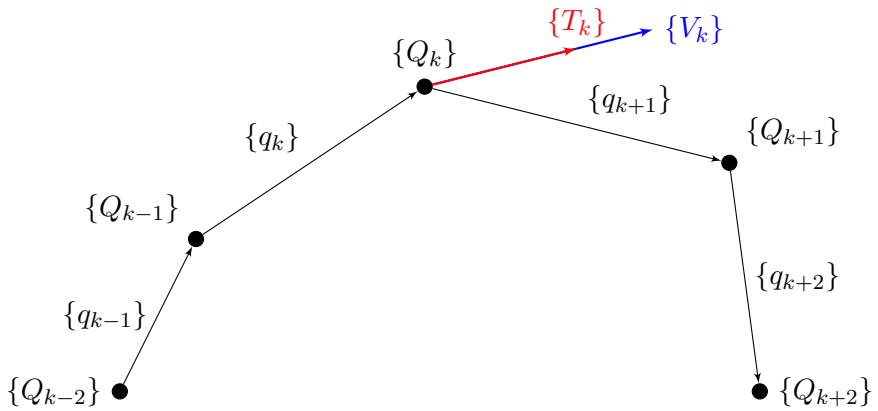

Figure 3.4: Schematic of the calculation of sampling point tangent vector $\{T_k\}$ using the five-point scheme. Recreated from Piegl and Tiller [248].

For a single Bézier curve segment with endpoints $\{P_0\}$ and $\{P_3\}$ and corresponding tangents $\{T_0\}$ and $\{T_3\}$, the inner control points are calculated as

$$\begin{aligned} \{P_1\} &= \{P_0\} + \frac{1}{3}\varsigma\{T_0\} \\ \{P_2\} &= \{P_3\} - \frac{1}{3}\varsigma\{T_3\} \end{aligned} \tag{3.16}$$

where the value of ς is determined based on the principal that the magnitudes of the derivatives of the curve segment are equal at the start, middle and end point such that

$$\varsigma = \left|\{C^{(1)}(0)\}\right| = \left|\left\{C^{(1)}\left(\frac{1}{2}\right)\right\}\right| = \left|\{C^{(1)}(1)\}\right| \tag{3.17}$$

assuming the local parametric coordinate, $\bar{\xi}$, varies between 0 and 1 along the curve segment. By applying the de Casteljau algorithm [72] at $\bar{\xi} = \frac{1}{2}$ and relations between $\{P_0\}$ and $\{P_3\}$ (see [248] for more details), a quadratic expression in terms of ς can be derived where

$$16\varsigma^2 = \varsigma^2|\{T_0\}+\{T_3\}|^2 - 12\varsigma(\{P_3\}-\{P_0\})\cdot(\{T_0\}+\{T_3\}) + 36|\{P_3\}-\{P_0\}|^2. \tag{3.18}$$

Using the standard quadratic polynomial form of

$$a\varsigma^2 + b\varsigma + c = 0, \tag{3.19}$$

the quadratic formula can be used to solve for ς using the coefficients

$$\begin{aligned} a &= 16 - |\{T_0\} + \{T_3\}|^2 \\ b &= 12(\{P_3\} - \{P_0\}) \cdot (\{T_0\} + \{T_3\}) \\ c &= -36|\{P_3\} - \{P_0\}|^2 \end{aligned} \tag{3.20}$$

which will give two real solutions, one positive and one negative. In order to ensure that the control points are positioned between the two sampling points for the curve segment, the positive solution is taken and used in (3.16) to calculate $\{P_1\}$ and $\{P_2\}$. For each Bézier curve segment, four points are obtained and denoted as

$$\{P_{k,0}\} = \{Q_k\}, \{P_{k,1}\}, \{P_{k,2}\}, \{P_{k,3}\} = \{Q_{k+1}\} \tag{3.21}$$

which are arranged with the other Bézier curve segment points to create an overall control polygon to generate a curve over the full set of sampling points and ensure a

fit with C^1 continuity. The control polygon is formed from the first sampling point, $\{Q_0\}$, the inner control points, $\{P_{k,1}\}$ and $\{P_{k,2}\}$, for each Bézier curve segment, $k = 0, \ldots, n_k - 1$, and the end sampling point, $\{Q_{n_k}\}$, to produce

$$\{Q_0\}, \{P_{0,1}\}, \{P_{0,2}\}, \{P_{1,1}\}, \{P_{1,2}\}, \ldots, \{P_{n_k-1,1}\}, \{P_{n_k-1,2}\}, \{Q_{n_k}\}. \tag{3.22}$$

The next step is to create the knot vector, $\{\Xi\}$, by calculating the interior knot values such that

$$\xi_0 = 0\,, \qquad \xi_{k+1} = \xi_k + 3|\{P_{k,1}\} - \{P_{k,0}\}|, \tag{3.23}$$

which populate the open knot vector

$$\{\Xi\} = \left\{0, 0, 0, 0, \frac{\xi_1}{\xi_{n_k}}, \frac{\xi_1}{\xi_{n_k}}, \frac{\xi_2}{\xi_{n_k}}, \frac{\xi_2}{\xi_{n_k}}, \ldots, \frac{\xi_{n_k-1}}{\xi_{n_k}}, \frac{\xi_{n_k-1}}{\xi_{n_k}}, 1, 1, 1, 1\right\}. \tag{3.24}$$

Algorithm 3.1 shows the procedure of creating a B-spline curve using local interpolation using the five-point scheme when calculating the tangent vectors at each sampling point. Initially, the tangent vectors are calculated for each sampling point, then the inner control points are determined for each Bézier curve segment between the sampling points. Once the inner control points are found, the list of control points is formed which is used to determine the knot vector. The global coordinates for points on the curve are then calculated for the range of local parametric coordinates within the range of the knot vector values, where the B-spline basis functions are calculated for each parametric coordinate.

Figure 3.5 shows the generation of a B-spline curve fitted to a set of sampling points which are shown as red circles. At each sampling point, the tangent is calculated using (3.13) and shown as blue dashed lines. The control point positions are calculated based on the tangent vectors at each sampling point using (3.16) and are shown by blue squares. Parametric coordinates are chosen at regular intervals in the range $[0, 1]$ in order to build the B-spline curve using (3.6), shown by the black line.

It is also possible to produce closed B-spline curves by extending an open curve (where the end points of the curve are not coincident, as in Figure 3.6a) with an

Algorithm 3.1: Pseudocode for the creation of a B-spline curve using local interpolation with the five-point scheme.

for *each sampling point* $\{Q_k\}$ **do**
  determine neighbouring points, $\{Q_{k-2}\}$, $\{Q_{k-1}\}$, $\{Q_{k+1}\}$, $\{Q_{k+2}\}$;
  calculate direction vectors, $\{q_{k-1}\}$, $\{q_k\}$, $\{q_{k+1}\}$, $\{q_{k+2}\}$ (3.10);
  calculate interpolation parameter, β_k (3.15);
  calculate tangent vector, $\{V_k\}$ (3.14);
  calculate normalised tangent vector, $\{T_k\}$ (3.13);

for *each Bézier curve segment* $\{C_i(\xi)\}$ **do**
  solve quadratic equation in (3.18) for interpolation parameter α;
  calculate inner control points, $\{P_1\}$, $\{P_2\}$ (3.16);
  form curve segment control point list (3.21);

form complete control point list, $\{P_i\}$ (3.22);
compute interior knot values, ξ_k (3.23);
form knot vector, $\{\Xi\}$ (3.24);
for $\xi \in [0, 1]$ **do**
  determine the knot span, $\xi \in [\xi_i, \xi_{i+1})$;
  calculate B-spline basis functions, $N_{i,p}(\xi)$ using (3.2) and (3.3);
  calculate global coordinate on B-spline curve, $\{C(\xi)\}$ (3.6);

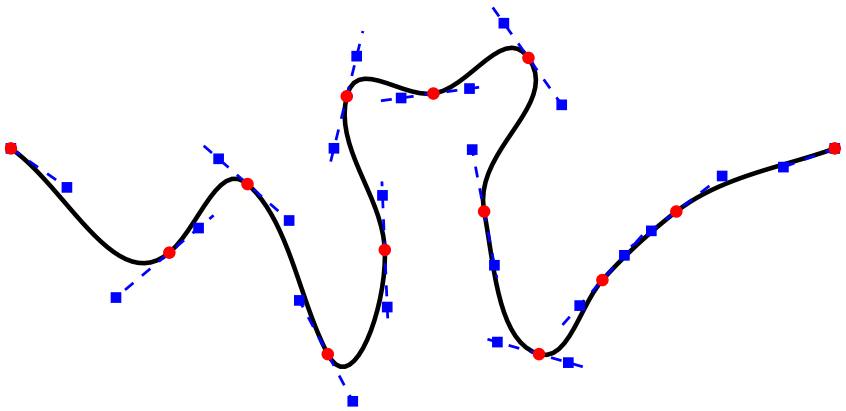

Figure 3.5: Fitting a cubic B-spline curve to a set of sampling points (red circles) showing calculated tangents at each sampling point (blue dashed lines), the positions of the control points (blue squares) and the fitted curve (black line).

extra sampling point at the end point which is coincident with the first sampling point of the curve. The gradients of the end points can be set to be equal in order to ensure that the closed curve is C^1 continuous across this connection point between the two ends. An example of a closed curve is shown in Figure 3.6b where the closing point (the start and end of the curve) is circled in green.

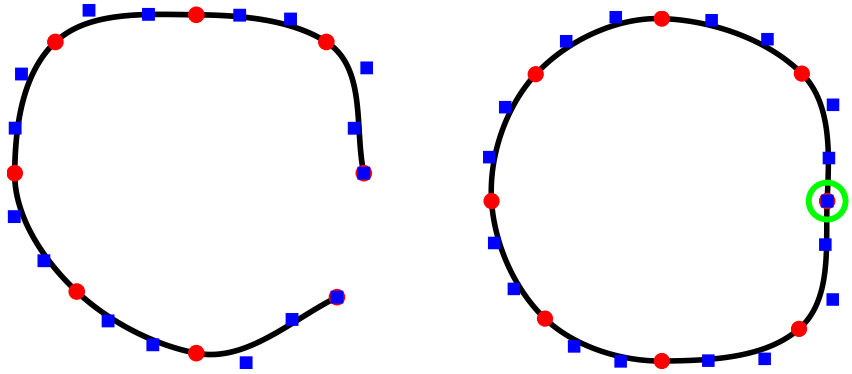

(a) open curve (b) closed curve

Figure 3.6: Open and closed cubic B-spline curves (black lines) given a set of sampling points (red circles) and the computed control points (blue squares). The closing point of the closed curve is also circled in green.

3.2.2 Validation

In order to validate the fitting of a B-spline curve to a set of sampling points, a test case is presented in the form of a smooth star shape as this is a closed shape which is mathematically defined. The smooth star is given as a level set with equation [2]

$$\phi^0 = (x^2 + y^2) - \left(1 + 0.2\sin\left(6\arctan\left(\frac{y}{x}\right)\right)\right). \tag{3.25}$$

Given the relationship between Cartesian and polar coordinates

$$\theta = \arctan\left(\frac{y}{x}\right), \qquad R = \sqrt{x^2 + y^2}, \tag{3.26}$$

substituting into (3.25) and setting the value of ϕ^0 to zero, the radius, R, at angle θ is found to be

$$R = \sqrt{1 - 0.2\sin(6\theta)}. \tag{3.27}$$

Points around the smooth star shape were generated at regular angular intervals, shown as red circles inset in Figure 3.7, which were used as the sampling points to fit a closed cubic B-spline curve. In order to validate the ability to fit a B-spline curve to a given shape, the relative error between the position on the fitted curve and the mathematical shape is calculated as

$$\epsilon_c^i = \frac{\|(x_i^h, y_i^h) - (x_i^a, y_i^a)\|_2}{\|(x_i^a, y_i^a)\|_2} \tag{3.28}$$

where (x_i^h, y_i^h) are the coordinates on the B-spline curve and (x_i^a, y_i^a) are the analytical coordinates where the analytical radius is calculated using (3.27) based on the angular position of (x_i^h, y_i^h), from this the analytical coordinates are calculated using the standard trigonometric identities, $x = R\cos\theta$ and $y = R\sin\theta$. Taking 10^4 equally spaced points along the generated B-spline curve*, the overall error was determined using the trapezium rule to numerically integrate over the length of the B-spline curve. Figure 3.7 shows the total error along the generated B-spline curve for a varying number of sampling points. A quadratic rate of convergence can be seen as the number of sampling points is increased. This makes sense as the B-spline curve is generated by positioning control points along the tangents at each sampling point, these tangents are representative of the derivatives along the B-spline curve at each of the corresponding sampling point positions. Therefore, the rate of convergence should be one degree lower than the degree of the B-spline curve, as a cubic B-spline is used, the rate of convergence would be expected to be quadratic.

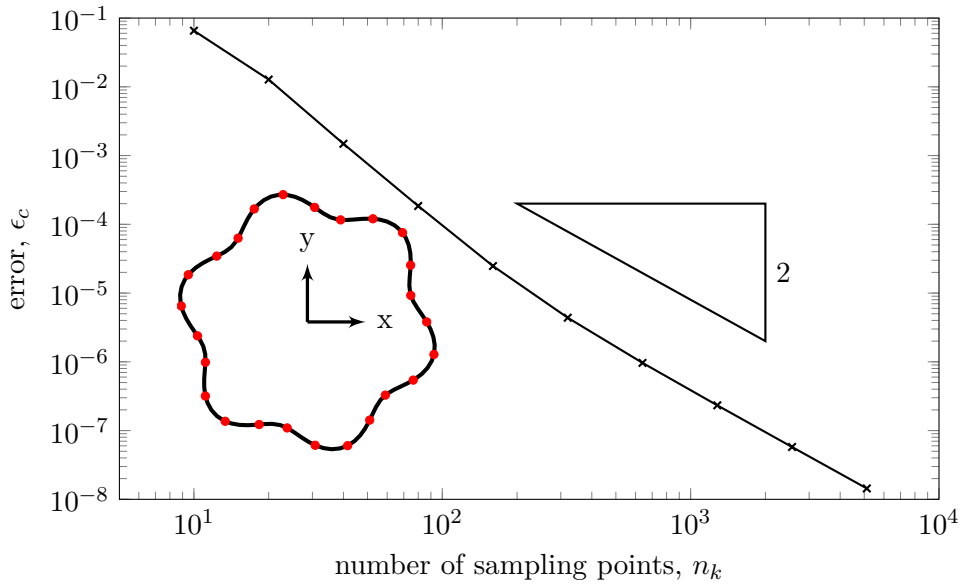

Figure 3.7: B-spline curve fitting errors for increasing number of sampling points. Inset: smooth star sampling points and fitted curve.

*This number was chosen to be sufficiently large to accurately calculate the error as it is larger than the number of sampling points used to generate the B-spline curve.

3.3 B-spline Surfaces

The work performed by Bing and co-workers [24, 25] is extended here to the creation of B-spline surfaces based on the procedures presented by Piegl and Tiller [248]. The initial steps in the creation of a B-spline surface is similar to the work presented above for B-spline curves in order to obtain the tangents at each sampling points. However, two parametric directions are now required, therefore, the tangents in each directions are needed.

A B-spline surface is defined as [248]

$$\{S(\xi,\eta)\} = \sum_{i=0}^{n_\xi}\sum_{j=0}^{n_\eta} N_{i,p}(\xi)N_{j,q}(\eta)\{P_{i,j}\} \tag{3.29}$$

where ξ is the parametric coordinate corresponding to the knot vector $\{\Xi\}$, η is the parametric coordinate corresponding to the knot vector $\{H\}$, p is the degree of the B-spline surface in the ξ direction and q is the degree of the B-spline surface in the η direction. The number of control points in the ξ direction is given by n_ξ while n_η is the number of control points in the η direction. $N_{i,p}(\xi)$ is the p-th degree B-spline basis function for the i-th control point at position ξ and $N_{j,q}(\eta)$ is the q-th degree B-spline basis function for the j-th control point at position η, both calculated using (3.2) and (3.3).

A B-spline surface can be generated by constructing $n_k \times n_l$ Bézier patches, $\{B_{k,l}(\xi,\eta)\}$ for $k = 0, 1, \ldots, n_k$ and $l = 0, 1, \ldots, n_l$, where each patch has corner points $\{Q_{k,l}\}$, $\{Q_{k+1,l}\}$, $\{Q_{k,l+1}\}$ and $\{Q_{k+1,l+1}\}$. There will also be $C^{1,1}$ continuity between each patch. A single patch, as shown in Figure 3.8, has 16 control points (shown as blue squares) in total, 12 along the boundary of the patch and 4 internal control points. As the B-spline surface will be locally 2D, for each corner point, the tangents in ξ and η directions must be calculated. These tangents can be found using the same method as for a B-spline curve by treating each direction separately and using (3.13), (3.14) and (3.15). Assuming the sampling points are arranged

in a grid, B-spline curves can be created along each row and column of sampling points to generate these tangent vectors.

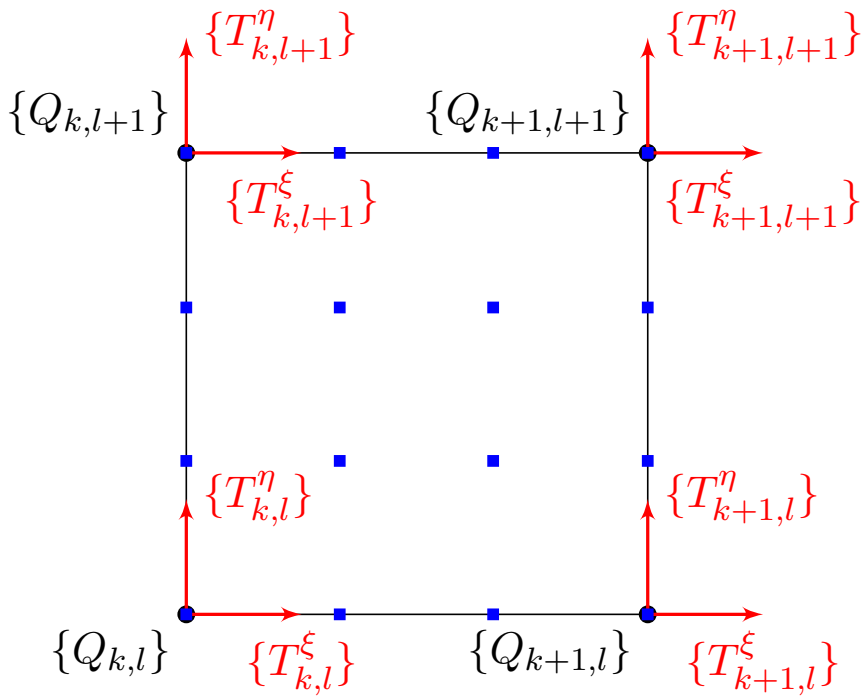

Figure 3.8: Single Bézier patch to generate B-spline surface based on sampling points (black circles) with sampling points tangents (red arrows) and 16 control points (blue squares) shown.

For each Bézier patch, the 16 control points must be calculated in order to create the entire B-spline surface. The control points $\{P_{0,0}\}$, $\{P_{3,0}\}$, $\{P_{0,3}\}$ and $\{P_{3,3}\}$ correspond to the four corner points of the patch, $\{Q_{k,l}\}$, $\{Q_{k+1,l}\}$, $\{Q_{k,l+1}\}$ and $\{Q_{k+1,l+1}\}$ respectively. The 12 control points around the boundary of the patch are given by

- bottom boundary:

$$\begin{aligned} \{P_{1,0}\} &= \{P_{0,0}\} + \varsigma_l\{T^{\xi}_{k,l}\} \\ \{P_{2,0}\} &= \{P_{3,0}\} - \varsigma_l\{T^{\xi}_{k+1,l}\} \end{aligned} \tag{3.30}$$

- top boundary:

$$\begin{aligned} \{P_{1,3}\} &= \{P_{0,3}\} + \varsigma_{l+1}\{T^{\xi}_{k,l+1}\} \\ \{P_{2,3}\} &= \{P_{3,3}\} - \varsigma_{l+1}\{T^{\xi}_{k+1,l+1}\} \end{aligned} \tag{3.31}$$

- left boundary:

$$\begin{aligned} \{P_{0,1}\} &= \{P_{0,0}\} + \varsigma_k\{T^{\eta}_{k,l}\} \\ \{P_{0,2}\} &= \{P_{0,3}\} - \varsigma_k\{T^{\xi}_{k,l+1}\} \end{aligned} \tag{3.32}$$

- right boundary:

$$\begin{aligned} \{P_{3,1}\} &= \{P_{3,0}\} + \varsigma_{k+1}\{T^{\eta}_{k+1,l}\} \\ \{P_{3,2}\} &= \{P_{0,0}\} - \varsigma_{k+1}\{T^{\xi}_{k+1,l+1}\} \end{aligned} \tag{3.33}$$

where $\{T^{\xi}_{k,l}\}$ and $\{T^{\eta}_{k,l}\}$ denote the tangents in the ξ and η directions respectively and the values of ς_l and ς_k are calculated as

$$\varsigma_l = \frac{r_l(\xi_{k+1} - \xi_k)}{3} \qquad \text{and} \qquad \varsigma_k = \frac{s_k(\eta_{l+1} - \eta_l)}{3} \tag{3.34}$$

with r_l being the chord length of the row of sampling points in the ξ direction and s_k being the chord length of the column of sampling points in the η direction.

The location of the four internal control points are calculated as

$$\begin{aligned} \{P_{1,1}\} &= \varsigma_s\{D^{\xi\eta}_{k,l}\} + \{P_{0,1}\} + \{P_{1,0}\} - \{P_{0,0}\} \\ \{P_{2,1}\} &= -\varsigma_s\{D^{\xi\eta}_{k+1,l}\} + \{P_{3,1}\} + \{P_{3,0}\} - \{P_{2,0}\} \\ \{P_{1,2}\} &= -\varsigma_s\{D^{\xi\eta}_{k,l+1}\} + \{P_{1,3}\} + \{P_{0,3}\} - \{P_{0,2}\} \\ \{P_{2,2}\} &= \varsigma_s\{D^{\xi\eta}_{k+1,l+1}\} + \{P_{2,3}\} + \{P_{3,2}\} - \{P_{3,3}\} \end{aligned} \tag{3.35}$$

where the coefficient ς_s is given by

$$\varsigma_s = \frac{\Delta\xi_{k+1} - \Delta\eta_{l+1}}{9}. \tag{3.36}$$

It is possible to create B-spline curves along the rows and columns of the grid of data points meaning that it is possible to calculate the tangent vectors at each sampling point in the ξ and η directions. Also, from the B-spline curves along each row and column, knot values in each direction can be directly assigned to each sampling point position. Because of this, the three-point Bessel method [69] can be used to determine $\{D^{\xi\eta}_{k,l}\}$ such that

$$\{D^{\xi\eta}_{k,l}\} = \frac{\varsigma_k\{d^{\xi\eta}_{k,l}\} + \varsigma_l\{d^{\eta\xi}_{k,l}\}}{\varsigma_k + \varsigma_l} \tag{3.37}$$

where ς_k is calculated using (3.11) and ς_l is the equivalent calculation for the η direction such that

$$\varsigma_l = \frac{\Delta\eta_l}{\Delta\eta_l + \Delta\eta_{l+1}}. \tag{3.38}$$

Given that

$$\{D^{\xi}_{k,l}\} = r_l\{T^{\xi}_{k,l}\} \qquad \text{and} \qquad \{D^{\eta}_{k,l}\} = s_k\{T^{\eta}_{k,l}\}, \tag{3.39}$$

the final two undefined terms in (3.37) are given by

$$\begin{aligned}
\{d^{\eta\xi}_{k,l}\} &= (1-\varsigma_k)\frac{\{D^{\eta}_{k,l}\} - \{D^{\eta}_{k-1,l}\}}{\Delta\xi_k} + \varsigma_k\frac{\{D^{\eta}_{k+1,l}\} - \{D^{\eta}_{k,l}\}}{\Delta\xi_{k+1}} \\
\{d^{\xi\eta}_{k,l}\} &= (1-\varsigma_l)\frac{\{D^{\xi}_{k,l}\} - \{D^{\xi}_{k,l-1}\}}{\Delta\eta_l} + \varsigma_l\frac{\{D^{\xi}_{k,l+1}\} - \{D^{\xi}_{k,l}\}}{\Delta\eta_{l+1}}.
\end{aligned} \tag{3.40}$$

Other than for the open edges of the surface (ie. around the border of the grid of control points), all rows and columns of control points which contain the sampling points are removed, leaving $(2n_k + 2) \times (2n_l + 2)$ control points in total. This is the same as what is done in (3.22) and ensures the $C^{1,1}$ continuity across the boundaries between each Bézier patch which makes up the B-spline surface. Figure 3.9 shows an arrangement of sampling points (shown as red circles) in a grid and the set of control points that have been computed (shown as blue squares). It is clear to see the rows and columns from which the control points have been removed to produce the B-spline surface control point net.

The first derivatives of a B-spline surface with respect to the ξ and η directions are given by

$$\begin{aligned}
\{S^{(1,0)}(\xi,\eta)\} &= \sum_{i=0}^{n_\xi-1}\sum_{j=0}^{n_\eta} N_{i,p-1}(\xi)N_{j,q}(\eta)\{P^{(1,0)}_{i,j}\} \\
\{S^{(0,1)}(\xi,\eta)\} &= \sum_{i=0}^{n_\xi}\sum_{j=0}^{n_\eta-1} N_{i,p}(\xi)N_{j,q-1}(\eta)\{P^{(0,1)}_{i,j}\}
\end{aligned} \tag{3.41}$$

respectively, where

$$\begin{aligned}
\{P^{(1,0)}_{i,j}\} &= p\frac{\{P_{i+1,j}\} - \{P_{i,j}\}}{\xi_{i+p+1} - \xi_{i+1}} \\
\{P^{(0,1)}_{i,j}\} &= q\frac{\{P_{i,j+1}\} - \{P_{i,j}\}}{\eta_{j+q+1} - \eta_{j+1}}.
\end{aligned} \tag{3.42}$$

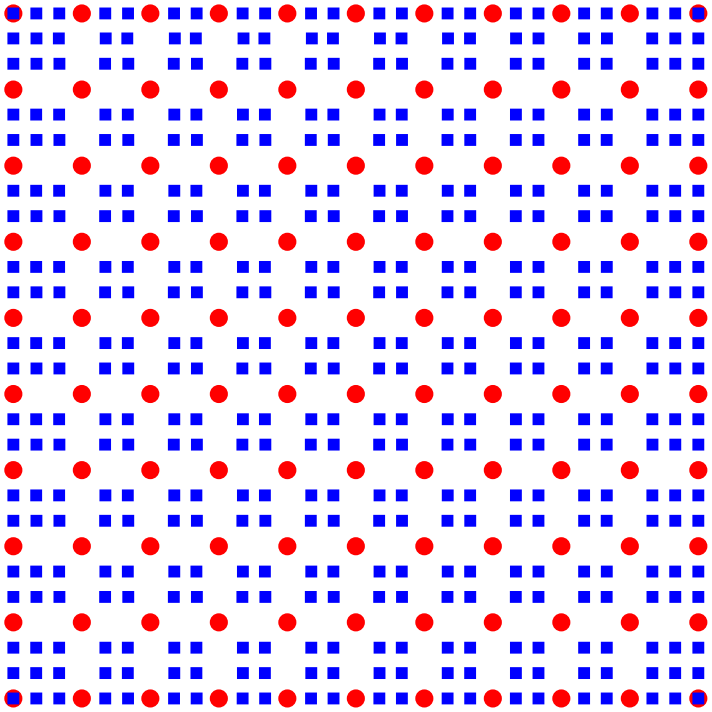

Figure 3.9: Grid of sampling points (red circles) and computed control point arrangement (blue squares). The control points have been removed in the rows and columns of the grid which contain the sampling points (except for the open edges of the surface).

For completeness, the derivatives of a B-spline surface with respect to ξ and η are given by

$$\{S^{(k,l)}(\xi,\eta)\} = \sum_{i=0}^{n_\xi - k} \sum_{j=0}^{n_\eta - l} N_{i,p-k}(\xi) N_{j,q-l}(\eta) \{P_{i,j}^{(k,l)}\} \tag{3.43}$$

where $P_{i,j}^{(k,l)}$ is defined as

$$\{P_{i,j}^{(k,l)}\} = (q-l+1)\frac{\{P_{i,j+1}^{(k,l-1)}\} - \{P_{i,j}^{(k,l-1)}\}}{\eta_{j+q+1} - \eta_{j+l}} \tag{3.44}$$

Figure 3.10 shows two examples of generated B-spline surfaces with Figure 3.10a showing an open surface with equation $z = \sin^2(x) + \sqrt{\cos(y)}$. As the B-spline surface is generated from a series of B-spline curves, it is possible to create a closed surface, as shown in Figure 3.10b which depicts the surface of an extrusion of the smooth star shape described by (3.25). The colour of each surface in Figure 3.10 is related to the z position on the surface.

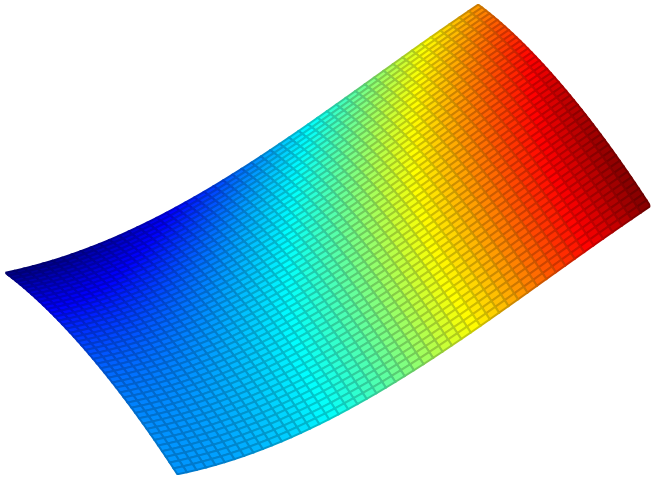

(a) open B-spline surface
($z = \sin^2(x) + \sqrt{cos(y)}$)

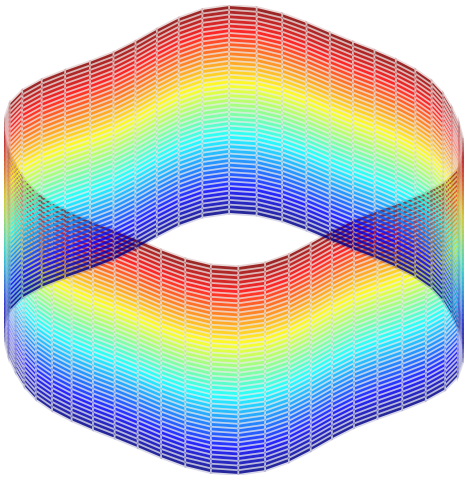

(b) closed B-spline surface
(Extruded smooth star from (3.25))

Figure 3.10: Fitting B-spline surfaces to open and closed sets of 3D sampling points.

3.4 Handling unstructured data

It has been shown how to generate B-spline curves and surfaces where sampling points can be manually placed along the pseudo-boundary of a physical domain. However, when producing models based on real world problems, the geometry is often given by scanned data or from a set of unstructured data points. Due to the digital nature of the scans, the data points which represent the boundary are often artificially stepped based on the pixel resolution of the image. A method

of smoothing out the data to create a smooth boundary is required. In the case of an unstructured set of data, there is no prescribed order to the points and it is not clear how to connect the points in a way which can be used to generate a B-spline boundary, the global coordinates of the data points are given with no extra information on how each would connect to the neighbouring points. A significant pre-processing effort would be required to structure the set of data points to determine the correct "order" for the points such that the B-spline boundary could be generated. This work uses a least squares fitting method to manipulate a B-spline curve to suitably represent a set of data points such that the total distance between the B-spline curve and the data points is minimised. The ordering of the unstructured set of data points is also not required when using the least squares fitting procedure. The control points of the B-spline boundary are manipulated in order to minimise the overall distance between the data points and the B-spline boundary, therefore, only the global coordinates of the data points are required. This work only considers the least squares fitting of B-spline curves to a set of data points as a B-spline surface can easily be created based on the B-spline curves that have been fitted to rows or columns of data points.

In order to perform the least squares fitting procedure, the closest point on the B-spline curve to a given data point (also known as the foot point) must be determined.

3.4.1 Foot point determination

The foot point of a data point, $\{X_d\}$, is the point on a B-spline curve/surface which is the closest, this typically means that the data point lies on the normal to the foot point on the curve/surface. The general framework for finding the foot point starts with a subdivision algorithm to obtain a good initial guess for the foot point followed by an iterative point inversion stage in order to determine a more accurate position. This section describes the process of accurately finding the foot point on a B-spline curve for a given data point. As will be discussed in Chapter

6 for the model generation, data points are generated for each slice in a segmented image stack through the length of the Left Ventricle (LV). This means that B-spline curves will be generated using the least squares fitting procedure for each slice of the image stack, with each fitted B-spline curves being used to generate a B-spline surface representation of the LV model. For this reason, an accurate calculation of the foot point is only required for a B-spline curve. The exact foot point on a B-spline surface is not required in any part of this work, only an estimate of the foot point would be required in order to determine the position of a MP relative to a B-spline surface, therefore, only the subdivision step is needed, which will be briefly presented also.

B-spline curve

As mentioned above, the first step of finding the foot point of a data point on a B-spline curve is to obtain a good initial guess, this is found using a subdivision algorithm (which was initially developed for stress integration over B-spline yield surfaces within computational plasticity, see [58]). Algorithm 3.2 shows the process of obtaining an initial guess for the foot point of a data point on a B-spline curve. The global positions of all knots in the knot vector are determined and the distance to the data point is calculated. The knot with is situated closest to the data point is selected and the subdivision routine is implemented. An interval of parametric coordinates is calculated around the closest knot over a series of n_s increments, with smaller intervals each time, up to a set number of intervals. It was found that a value of $n_s = 5$ was found to be reasonable to find a good initial guess. Figure 3.11 shows a visual representation of the subdivision routine given in Algorithm 3.2.

Once an appropriate initial guess for ξ_{ck} is found, a point inversion scheme [248] is implemented to minimise the distance between the data point and the B-spline

Algorithm 3.2: B-spline curve foot point initial guess subdivision procedure.

for $\xi_i \in \{\Xi\}$ **do**
  calculate global position on B-spline curve, $\{C(\xi_i)\}$ (3.6);
  calculate distance to data point;
select closest knot location, ξ_{ck};
for $a = 1 : n_s$ **do**
  calculate knot interval, $\xi \in \left[\frac{\xi_{ck-1}-\xi_{ck}}{2^a}\ ,\ \xi_{ck}\ ,\ \xi_{ck}+\frac{\xi_{ck+1}-\xi_{ck}}{2^a}\right]$;
  calculate global position for each parametric coordinate, $\{C(\xi)\}$ (3.6);
  calculate distance to data point for each parametric coordinate;
  select new ξ_{ck} as point with the minimum distance to the data point;

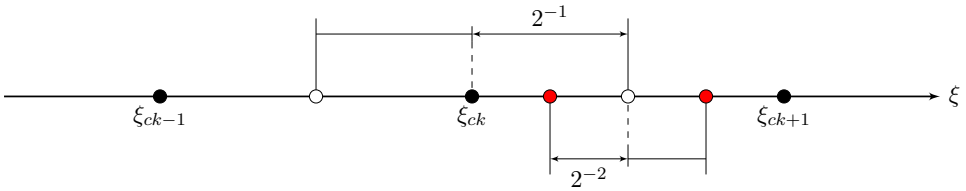

Figure 3.11: Subdivision algorithm to obtain a good initial guess for a foot point of a data point on a B-spline curve.

curve where the residual is defined as

$$f(\xi) = \{C^{(1)}(\xi)\} \cdot (\{C(\xi)\} - \{X_d\}) \tag{3.45}$$

where the distance between the data point and the B-spline curve is minimum when $f(\xi) = 0$. Equation (3.45) takes into account both the distance between the data point and the current guess of the foot point on the curve, $|\{C(\xi)\} - \{X_k\}|$, as well as the angle between this vector and the tangent to the curve at the current guess of the foot point. Using a Newton-Raphson iterative approach, an improved estimate for the foot point can be found to update the local parametric coordinate of the foot point on the B-spline curve such that

$$\xi_{i+1} = \xi_i - \frac{f(\xi_i)}{f'(\xi_i)} = \xi_i - \frac{\{C^{(1)}(\xi_i)\} \cdot (\{C(\xi_i\} - \{X_d\})}{\{C^{(2)}(\xi_i)\} \cdot (\{C(\xi_i\} - \{X_d\}) + |\{C^{(1)}(\xi_i)\}|^2} \tag{3.46}$$

where $\xi_0 = \xi_{ck}$ is the initial guess obtained from the subdivision algorithm. A series of criteria are defined to check for convergence, firstly, checking whether the data point lies on the B-spline curve

$$|\{C(\xi_i)\} - \{X_d\}| \leq tol \tag{3.47}$$

where the tolerance is typically set at 1×10^{-9}. If the data point is found to lie on the curve, the process is halted, as this is clearly the closest point to the curve. However, if the data point is found not to lie on the curve, a check for a zero cosine value is performed to determine whether the data point lies on the normal to curve for the current foot point estimation. The zero cosine criteria is given by

$$\frac{|\{C^{(1)}(\xi_i)\} \cdot (\{C(\xi_i)\} - \{X_d\})|}{|\{C^{(1)}(\xi_i)\}||\{C(\xi_i)\} - \{X_d\}|} \leq tol. \tag{3.48}$$

If (3.47) and (3.48) are not satisfied, an updated local parametric coordinate for the foot point, ξ_{i+1}, is found using (3.46). After the new parametric coordinate is calculated, a check is performed to ensure that the value lies within the range of the B-spline curve's parametric coordinates, $\xi_{i+1} \in [a, b]$. This check is dependent on whether the curve is open or closed:

- for an open curve:

$$\text{if } (\xi_{i+1} < a) \rightarrow \xi_{i+1} = a$$

$$\text{if } (\xi_{i+1} > b) \rightarrow \xi_{i+1} = b$$

- for an closed curve:

$$\text{if } (\xi_{i+1} < a) \rightarrow \xi_{i+1} = b - (a - \xi_{i+1})$$

$$\text{if } (\xi_{i+1} > b) \rightarrow \xi_{i+1} = a + (\xi_{i+1} - b).$$

The Newton-Raphson iterative procedure is repeated until a value of ξ_i is found which satisfies the convergence criteria or the number of iterations reaches a prescribed maximum number, which is typically set as 10.

B-spline surface

A foot point on a B-spline surface can also by found for a data point by extending the process for a B-spline curve. However, for this work, only an estimate of the foot point on a B-spline surface is required to determine the position of a MP relative to the B-spline surface. Therefore, a subdivision algorithm is suitable to obtain a good approximation of the foot point. The steps of the algorithm can

be followed as above with the inclusion of the second parametric coordinate, η, where the initial closest knot is the global position based on the local parametric coordinates (ξ_{ck}, η_{ck}) which is the minimum distance from the data point. The knot intervals are then calculated as

$$\xi \in \left[\frac{\xi_{ck-1} - \xi_{ck}}{2^a} \, , \; \xi_{ck} \, , \; \xi_{ck} + \frac{\xi_{ck+1} - \xi_{ck}}{2^a} \right]$$
$$\eta \in \left[\frac{\eta_{ck-1} - \eta_{ck}}{2^a} \, , \; \eta_{ck} \, , \; \eta_{ck} + \frac{\eta_{ck+1} - \eta_{ck}}{2^a} \right]$$

giving nine points on the B-spline surface which are checked to find a new estimate of the foot point. Figure 3.12 is a visual representation of the subdivision algorithm to find an estimate of the foot point of a data point on a B-spline surface.

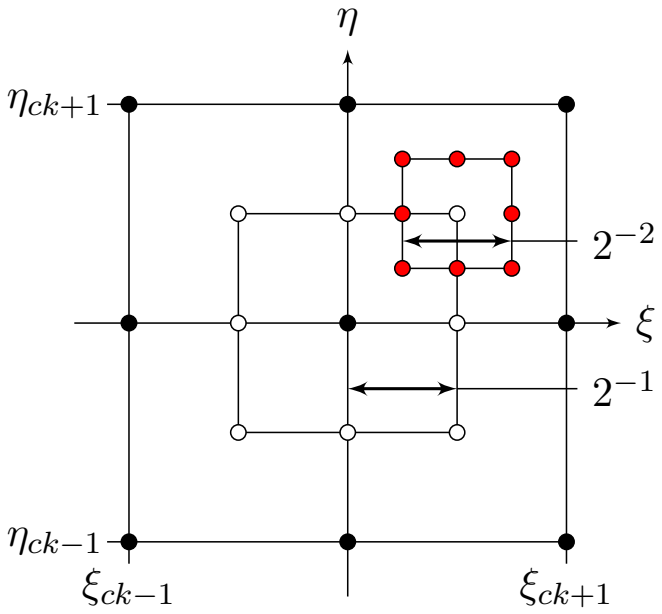

Figure 3.12: Subdivision algorithm to find an approximation of the foot point of a data point on a B-spline surface. Reproduced from Coombs *et al.* [58].

3.4.2 Least squares fitting

When generating a boundary representation for a set of data points, it is often the case that there is no structure to the set and just the global coordinates of the data points are given. An expensive pre-processing step would be required to order the data points to determine the path of the B-spline curve. Given that this

pre-processing is performed to order the set of data points, it is not ideal to just use these data points as the sampling point to create B-spline curve as described in Section 3.2 as the curve will be forced to pass through every data point, potentially producing an unrealistic boundary, especially if the data is artificially stepped due to pixelation due to the data points being taken from images. Therefore, a B-spline curve can be made which roughly matches the shape* of the data points and a least squares fitting procedure can be performed to acquire a reasonable curve to represent the boundary. This section describes the process for the least squares fitting of a B-spline curve to a set of data points drawing on information from Section 3.2 for the B-spline curve definition and Section 3.4.1 for the foot point calculations.

Given a set of data points, $\{X_d\}$ with $d = 0, 1, \ldots, n_{dp}$, a B-spline curve can be fitted using a least squares approximation by updating the global positions of the control points of the B-spline curve. The least squares fitting is a minimisation problem in which the least squares error is given by [26]

$$\text{minimise } f = \sum_{d=0}^{n_{dp}} \|\{X_d\} - \{C(\xi_d)\}\|_2^2 \tag{3.49}$$

where $\{C(\xi_d)\}$ is the foot point of the data point on the B-spline curve with the local parametric coordinate ξ_d and $\|\cdot\|_2$ is the L2-norm. Substituting (3.7) into (3.49), the residual becomes

$$f = \sum_{d=0}^{n_{dp}} \|\{X_d\} - \sum_{i=0}^{n_{ls}} N_{i,p}(\xi_d)\{P_i\}\|_2^2 \tag{3.50}$$

where n_{ls} is the number of control points used in this least squares fitting procedure to create the B-spline curve. Expanding (3.50) results in the expression

$$\begin{aligned} f = \sum_{d=0}^{n_{dp}} \Bigg[\{X_d\} \cdot \{X_d\} - 2 \sum_{i=0}^{n_{ls}} N_{i,p}(\xi_d)(\{X_d\} \cdot \{P_i\}) \\ + \left(\sum_{i=0}^{n_{ls}} N_{i,p}(\xi_d)\{P_i\} \right) \cdot \left(\sum_{i=0}^{n_{ls}} N_{i,p}(\xi_d)\{P_i\} \right) \Bigg] . \end{aligned} \tag{3.51}$$

*It is recognised by the author that a set of data points does not technically have any physical shape, however, this work uses data points taken from objects for which there is a recognisable shape.

The minimum of the residual in (3.51) is found by setting the derivative of f with respect to a control point, $\{P_l\}$, to be zero such that

$$\frac{\partial f}{\partial \{P_l\}} = \sum_{d=0}^{n_{dp}} \left[-2N_{l,p}(\xi_d)\{X_d\} + 2N_{l,p}(\xi_d) \left(\sum_{i=0}^{n_{ls}} N_{i,p}(\xi_d)\{P_i\} \right) \right] = 0. \tag{3.52}$$

This can be simplified to

$$\sum_{i=0}^{n_{ls}} \left(\sum_{d=0}^{n_{dp}} N_{l,p}(\xi_d) N_{i,p}(\xi_d) \right) \{P_i\} = \sum_{d=0}^{n_{dp}} N_{l,p}(\xi_d)\{X_d\} \tag{3.53}$$

which, written in matrix form, becomes

$$[[N^{ls}]^T [N^{ls}]]\{P^{ls}\} = \{r^{ls}\} \tag{3.54}$$

where

$$[N^{ls}] = \begin{bmatrix} N_{0,p}(\xi_0) & N_{1,p}(\xi_0) & \cdots & N_{n_{ls},p}(\xi_0) \\ N_{0,p}(\xi_1) & N_{1,p}(\xi_1) & \cdots & N_{n_{ls},p}(\xi_1) \\ \vdots & \vdots & \ddots & \vdots \\ N_{0,p}(\xi_{n_{dp}}) & N_{1,p}(\xi_{n_{dp}}) & \cdots & N_{n_{ls},p}(\xi_{n_{dp}}) \end{bmatrix}$$

$$\{r^{ls}\} = \begin{Bmatrix} \sum_{\forall d} N_{0,p}(\xi_d)\{X_d\} \\ \sum_{\forall d} N_{1,p}(\xi_d)\{X_d\} \\ \vdots \\ \sum_{\forall d} N_{n_{ls},p}(\xi_d)\{X_d\} \end{Bmatrix}$$

$$\{P^{ls}\} = \Big\{ \{P_0\} \quad \{P_1\} \quad \dots \quad \{P_{n_{ls}}\} \Big\}^T.$$

The updated control point positions are determined by solving the linear system

$$\{P^{ls}\} = [[N^{ls}]^T [N^{ls}]]^{-1} \{r^{ls}\}. \tag{3.55}$$

This is performed over a single iteration even though the fitting is a non-linear process due to the fact that a new B-spline curve is generated each time meaning that a new set of foot points are calculated for each data point. This means that the system matrix, $[[N^{ls}]^T [N^{ls}]]$, which comprises of the B-spline basis functions, will change for each fitting step and generates the non-linearity in the problem. Through

numerical experimentation of test problems in the development of this work, it was found that after the first fitting step, there is no significant improvement in the fitting of the B-spline curve and any further fitting steps result in unnecessary computational expense.

In theory, there is no limit to the number of control points used to create the B-spline curve, however, to allow for greater control in the model generation stage, a maximum number of control points is determined such that the number of control points must be at least half the number of data points. As the number of control points is based on the number of sampling points ($n_\xi = 2n_k + 1$), the number of sampling points that can be used to create the initial B-spline curve (which is to be fitted) should follow the rule $n_{dp} > 4n_k + 2$. However, it is not always necessary to use the maximum value of n_k for the fitting, an open B-spline curve can be created using only two sampling points ($n_k = 2$) while a closed B-spline curve requires a minimum of three sampling points ($n_k = 3$). For simplicity in implementation, a minimum value of $n_k = 3$ is used for both open and closed curves. This means that a range for n_k is present. Therefore, a new variable is introduced, $\zeta \in [0, 1]$, which is the fitting strength which determines the value of n_k using a linear interpolation between the minimum and maximum allowed values of the number of least squares fitting control points.

The least squares fitting error, ϵ_f, is calculated as the sum of the distances between the data points and the corresponding foot points on the B-spline curve which is then normalised by the number of data points (and enclosed area of the B-spline curve if a closed curve is used). The fitting error is calculated as

$$\epsilon_f = \begin{cases} \frac{1}{n_{dp}+1} \sum\limits_{\forall d} \|\{X_d\} - \{C(\xi_d)\}\|_2^2 & \text{for an open curve} \\ \frac{1}{n_{dp}+1} \frac{1}{A} \sum\limits_{\forall d} \|\{X_d\} - \{C(\xi_d)\}\|_2^2 & \text{for an closed curve} \end{cases} \tag{3.56}$$

where A is the area enclosed by the closed B-spline curve.

In order to demonstrate the least squares fitting, two examples of a B-spline curve fitting is shown, for an open and closed curve. For each example, six sets of data

points were generated using 2^5 to 2^{10} data points, increasing by a factor of 2 each time, to show the effect on the fitting error based on the number of data points. For each data set, the least squares fitting is performed for 100 different values of the fitting strength parameter, ζ, ranging from 0 to 1.

Firstly, for the open curve case, the set of data points is generated based on the equation

$$y = 1.25 \sin(2x) + 0.45 \cos(6x)$$

for values of $x \in [0, 1]$. B-spline sampling points are positioned at the first and last data point, the corresponding control points at the ends of the B-spline curve are fixed during the fitting process to ensure the start and end of the fitted B-spline curve coincides with the first and last data points. An example of a least squares fitting is shown in Figure 3.13 with 2^6 data points (shown as red circles) where an initial B-spline curve (blue line) from sampling points (blue crosses) linearly distributed between the first and last data point. The B-spline curve is fitted to the data points using a fitting strength of $\zeta = 1$ and is shown by the black line in Figure 3.13 and curve points are shown as black circles.

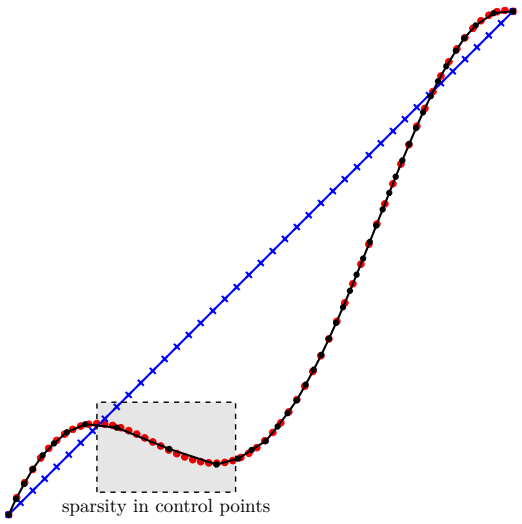

Figure 3.13: Open curve least squares fitting data points (red circles), initial B-spline curve and sampling points (blue line and crosses) and fitted B-spline curve (black line and circles) for 2^6 data points and a fitting strength of $\zeta = 1$.

The least squares fitting errors from (3.56) is given in Figure 3.14 for the different

sets of data points and fitting strengths. It is clear to see from Figure 3.14 that as the fitting strength is increased, there is a general trend that the fitting error decreases. There seems to be an exception when 2^8 data points are used for fitting strengths greater than 0.9. This may be due to distribution of the data points and the choice of distribution of the initial B-spline curve sampling points. A choice was made to distribute the sampling points linearly between the start and end data points, this was chosen such that the approach is robust and can be used for all problems regardless of the distribution of the data points for an open curve. It can be seen in Figure 3.13 that there is a portion of the data points that is only covered by a small number of control points in the fitting, contained within the shaded box (it is worth reiterating that the diagram in Figure 3.13 shows 2^6 data points for clarity as using 2^8 data points becomes difficult to visualise clearly due to the large number of data points). This is because this set of data points will all have foot points all relatively close to each other meaning that only a few control points will be manipulated to shift the curve towards that area. For lower values of fitting strength, this effect is less prominent as there are a small number of control points in general and the distribution of control points is more even across the data points. At the higher fitting strengths, having the sparsity of control points around this area will be detrimental to the fitting error, while the fitted curve will match the data points very well elsewhere, the curve around this area will be less free to be manipulated to match the data points. For lower number of data points, plateaus in the fitting errors for increasing fitting strengths can be seen, this is simply because of the discrete number of sampling points that can be used to generate the B-spline curves. As discussed, the number of sampling points ranges from 3 to a quarter of the number of data points, only integer values between these values can be used meaning that the same number of sampling points may be used for varying ζ. Another clear trend seen in Figure 3.14 is that as the number of data points is increased, the fitting error decreases for all values of the fitting strength, this is obvious as there is a greater amount of data that informs the least squares

fitting system of equations. There will also be more degrees of freedom in the system as more control points can be used to fit to the data producing a stronger fit to the set of data points.

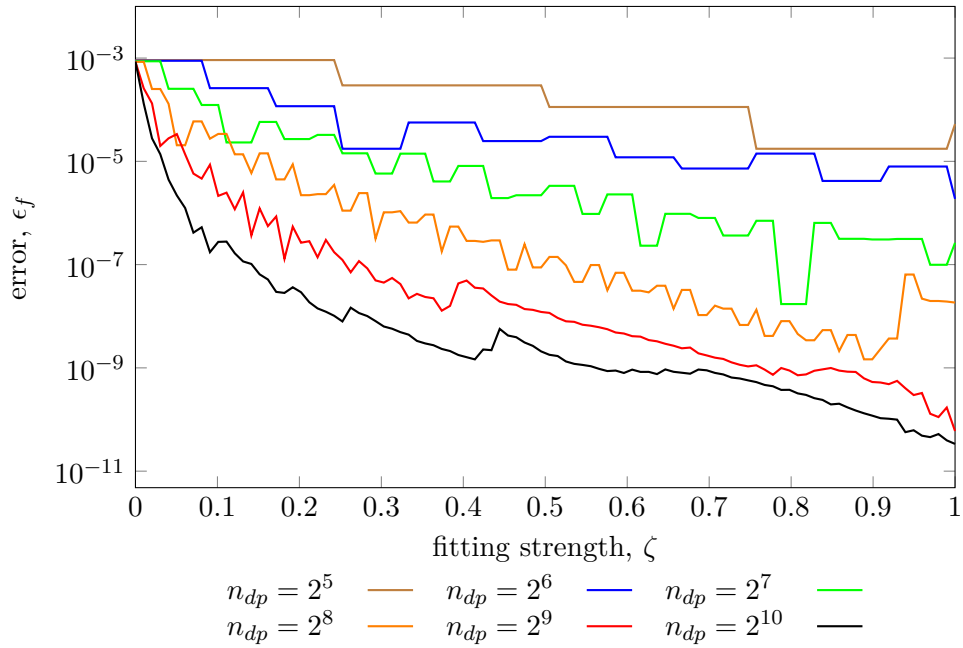

Figure 3.14: Open curve least squares fitting errors for varying fitting strength, ζ, and varying number of data points.

The least squares fitting of a closed B-spline curve to a set of data points is also examined. The data points for this example are generated using the smooth star shape given in (3.25) for the various number of data points. As with the open curve case, a B-spline curve is fit to the data points for 100 different values of the fitting strength parameter. For a closed curve case, rather than fixing the positions of the first and last control points* with the corresponding data point, the continuity of the curve is preserved by setting the position of these control points to the average position of the control points either side of the join such that

$$\{P_0\} = \{P_{n_\xi}\} = \frac{1}{2}\left(\{P_1\} + \{P_{n_\xi - 1}\}\right).$$

Figure 3.15 shows the least squares fitting errors for the closed B-spline curve to the smooth star shape data points for varying numbers of data points and varying

*For the closed B-spline curve, the first and last control point will be coincident.

fitting strengths. It is worth emphasising that the B-spline curve is not created in the same way as the previous example which used the smooth star shape (in Section 3.2.2), it is the data points used for the least squares fitting which are positioned around the smooth star shape based on (3.25), the sampling points for the initial B-spline curve are then seeded at equal angular intervals around the average centre of the data points. The control points are then manipulated based on the foot points on the B-spline curve to approximate the shape of the data points. The smooth star shape is used due the fact it is mathematically defined and the error between the fitted B-spline curve and the target shape can be easily determined. Similar trends to the open curve case can be seen in the fitting errors here. A general decrease in the fitting errors can be seen as the fitting strength is increased, more control points are being used to fit the curve means more degrees of freedom for the curve to be manipulated to fit to the data points. Compared to the open curve case, there seems to be a smoother decrease in errors as ζ is increased with much less fluctuation in the errors. This may be due to the example that is being shown, using a more regular shape to generate the data points means that the foot points of the data points will be more evenly distributed along the B-spline curve so there will be more even fitting for each part of the curve. As well as seeing the decrease in error with fitting strength, as the number of data points is increased, the fitting error decreased. Initially the error decreases at an even rate as the number of data points is increased, however, the cases of 2^9 and 2^{10} seem to converge to a similar error for higher fitting strengths. Again, this may be due to the choice of using the smooth star shape to demonstrate the least squares fitting and after a certain point, no further improvements in the fit can be made.

For a set of 50 data points, the fitted B-spline curves for 6 different values of ζ are shown in Figure 3.16. For each value of ζ, the number of sampling points used to generate the initial B-spline curve is also reported. It is clear from Figure 3.16 that as the fitting strength is increased, the fitted B-spline matches the data points more closely. A very loose fit is achieved for $\zeta = 0$ (Figure 3.16a) where none of the

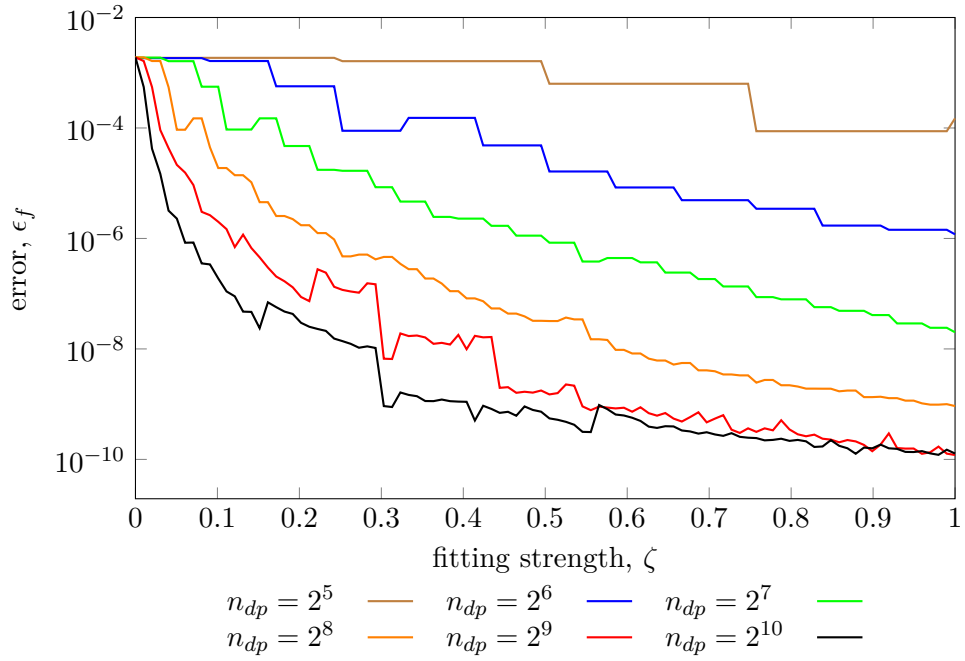

Figure 3.15: Closed curve least squares fitting errors for varying fitting strength, ζ, and varying number of data points.

features of the smooth star are obtained and the curve remains relatively circular. As the fitting strength is increased, more of the smooth star shape can be recognised from the B-spline curve as the higher number of degrees of freedom allows the curve to be manipulated by the data points. By using a fitting strength of 0.4 (Figure 3.16c), the B-spline curve has a relatively good fit to the data points but is not able to fully fit to the high curvature of the smooth star. Using the maximum fitting strength (Figure 3.16f) provides a B-spline curve that is almost indistinguishable from the data points with a very close fit. Depending on the properties of the desired boundary and the quality of the data points used, a decision on the value of the fitting strength parameter can be made. For example, if the boundary of the physical domain must match very closely to the data points, a higher value of ζ would be required. However, if there is a lot of noise in the data points and a rough estimate of the boundary is suitable, a lower value of ζ could be used, which also reduces computational cost as the least squares fitting system will be smaller as a smaller number of control points will be used to fit to the data points. The choice

of ζ is problem dependent based on the importance of how accurate the B-spline boundary should represent the set of data points, this will be explored further in the context of setting up the LV model in Chapter 6.

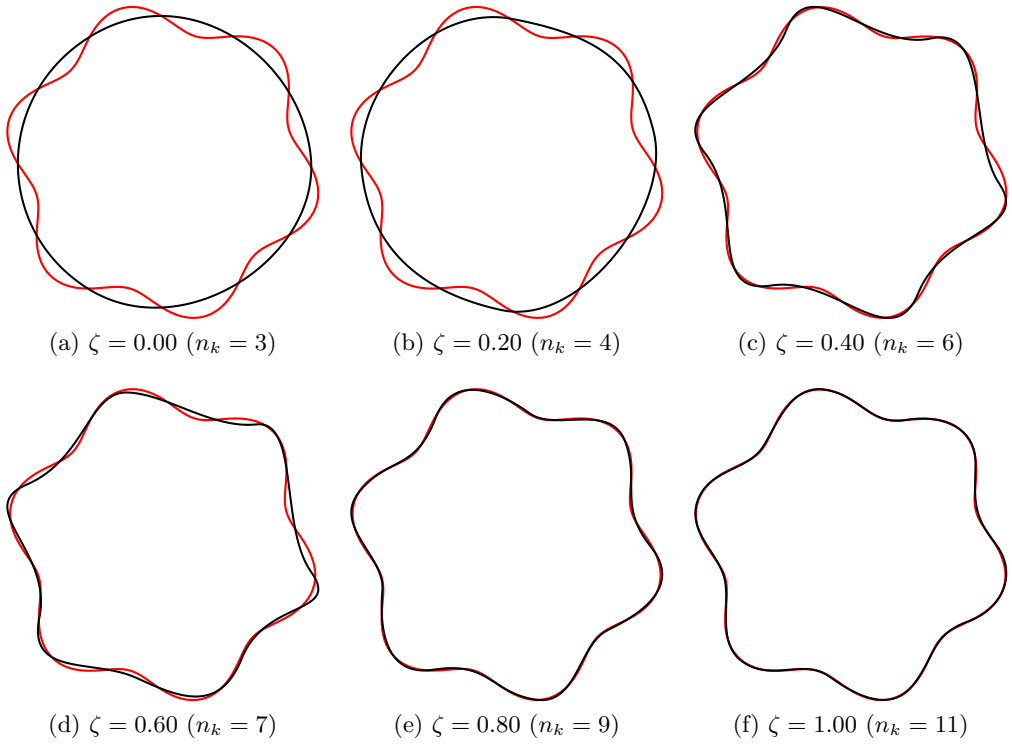

(a) $\zeta = 0.00$ ($n_k = 3$) (b) $\zeta = 0.20$ ($n_k = 4$) (c) $\zeta = 0.40$ ($n_k = 6$)

(d) $\zeta = 0.60$ ($n_k = 7$) (e) $\zeta = 0.80$ ($n_k = 9$) (f) $\zeta = 1.00$ ($n_k = 11$)

Figure 3.16: Least squares fitting of a closed B-spline curve for 50 data points for various fitting strengths.

3.5 Imposing inhomogeneous Neumann boundary conditions

Now that the process of creating a B-spline curve and surface has been described, it is possible to use these as a boundary of a physical domain in a MPM analysis. As the boundary of the physical domain will often not coincide with the background mesh, it is not possible to simply impose boundary conditions on the background mesh, the B-spline MPM boundary representation overcomes this issue as boundary conditions can be applied over the B-spline curve or surface. This work only considers the imposition of Neumann boundary conditions, however, Dirichlet

boundary conditions can also be applied to the B-spline boundary. See [24, 25] for further details on the imposition of Dirichlet boundary conditions to B-spline MPM boundaries.

In order to integrate a traction (or pressure) boundary condition over a B-spline, a numerical integration scheme can be employed, Gauss quadrature is used in this work, in which the integration takes place over local coordinates ranging from -1 to 1 in 1D for a B-spline curve and 2D for a B-spline surface.

For clarity in demonstration, the example of applying a traction boundary condition over a B-spline curve is presented, the formulation for B-spline surfaces is also given but not shown illustratively. Based on the work of Bing [24], the curve is split into segments for each knot span of $\{\Xi\}$ and Gauss points are used to integrate over each segment. As the local parametric coordinates of the B-spline curve range between 0 and 1, multiple spaces are defined: the physical (global) space, the parametric space and the integration space. The three spaces are shown in Figure 3.17. The physical space (Figure 3.17a) contains the background mesh and the B-spline curve, $\{C(\xi)\}$, using the global coordinate system. The parametric space (Figure 3.17b) contains the B-spline curve using the local B-spline parametric coordinate, ξ, defining the points along the curve. The integration space (Figure 3.17b) is the space over a knot span over which Gauss quadrature is performed using local parameter $\tilde{\xi} \in [-1, 1]$. The way that the integration is performed in this work is different to the work of Bing [24, 25] who determines the intersection points between the B-spline curve and elements of the background mesh, with the integration taking place over each segment of the curve between the intersection points. While this is a "simple" process for a 2D analysis using a B-spline curve, it becomes much more difficult for a 3D analysis using B-spline surfaces, hence the integration between knot spans in this work to unify the integration approach for 2D and 3D analyses. A trade off will be required in this work where more Gauss points should be used over each segment of the B-spline boundary between the knot spans compared to number of Gauss points used by Bing *et al.* in order to achieve a similar error. This is due to

the discontinuous nature of the shape functions of the background mesh over the integration length which do not coincide with the element boundaries.

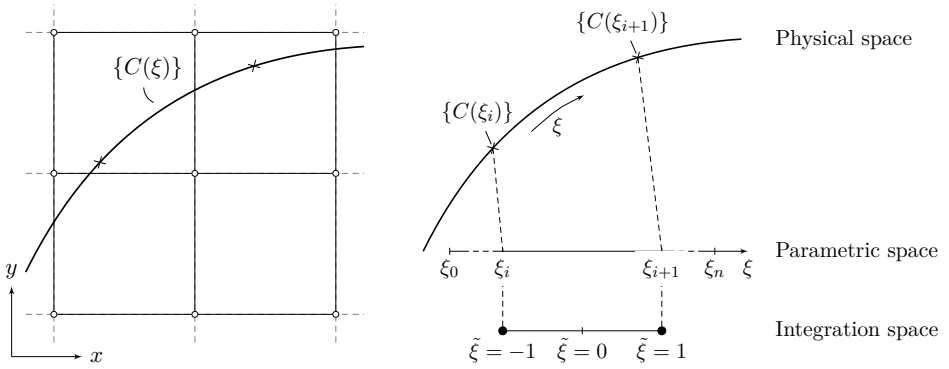

(a) physical (global) space

(b) mapping between physical, parametric and integration spaces

Figure 3.17: Spaces used in the integration over a B-spline curve. Reproduced from [24].

The mapping from the integration space, $\tilde{\xi} \in [-1, 1]$, to the parametric space, $[\xi_i, \xi_{i+1}]$, is a linear transformation, by inspection

$$\xi = \xi_i + \frac{(\tilde{\xi} + 1)(\xi_{i+1} - \xi_i)}{2}. \tag{3.57}$$

For integration over B-spline surfaces, both the ξ and η directions are used independently where the spaces seen in Figure 3.17b are equivalent for the η direction. The mapping in the η direction is given by

$$\eta = \eta_j + \frac{(\tilde{\eta} + 1)(\eta_{j+1} - \eta_j)}{2} \tag{3.58}$$

where $\tilde{\eta} \in [-1, 1]$ is the integration space and $[\eta_j, \eta_{j+1}]$ is the range of local parametric coordinates of the B-spline surface in the η direction.

A traction is integrated over a boundary, $\partial\Omega$, such that [17, 24, 77]

$$\{f_t\} = \int_{\partial\Omega} [S_v]^T \{t\} \, \mathrm{d}s \tag{3.59}$$

where $\{f_t\}$ is the resultant nodal force due to traction, $[S_v]$ are the standard FE shape functions and $\{t\}$ is the prescribed traction. Using Gauss quadrature to evaluate (3.59), the resultant nodal traction force vector becomes

$$\{f_t\} = \sum_{i=1}^{n_{gp}} [S_v]_i^T \{t\} \det([J_B]_i) w_i \tag{3.60}$$

where n_{gp} is the number of Gauss points used to approximate the integration over the boundary, w_i is the weight associated with the i-th Gauss point and $[J_B]$ is the Jacobian matrix of the i-th Gauss point. The Jacobian matrix is the transformation between the integration space and the physical space, as there is the intermediate parametric space for the B-spline curve and surface, two mapping are required, from the physical space to the parametric space and then from the parametric space to the integration space. A B-spline curve is essentially a 1D line in 2D space, therefore, the Jacobian is vector which is formed using the chain rule such that

$$\{J_B\} = \left\{ \frac{\mathrm{d}\{C\}}{\mathrm{d}\tilde{\xi}} \right\} = \{C^{(1)}(\xi)\} \frac{\mathrm{d}\xi}{\mathrm{d}\tilde{\xi}} = \begin{Bmatrix} \frac{\mathrm{d}x}{\mathrm{d}\tilde{\xi}} \\ \frac{\mathrm{d}y}{\mathrm{d}\tilde{\xi}} \end{Bmatrix} \tag{3.61}$$

where

$$\frac{\mathrm{d}\xi}{\mathrm{d}\tilde{\xi}} = \frac{\xi_{i+1} - \xi_i}{2}. \tag{3.62}$$

The same principle can be applied for B-spline surfaces, which are 2D surfaces in a 3D space, producing the rectangular Jacobian matrix given by

$$[J_B] = \begin{bmatrix} \frac{\mathrm{d}\{S\}}{\mathrm{d}\tilde{\xi}} \\ \frac{\mathrm{d}\{S\}}{\mathrm{d}\tilde{\eta}} \end{bmatrix} = \begin{bmatrix} \{S^{(1,0)}(\xi,\eta)\} & 0 \\ 0 & \{S^{(0,1)}(\xi,\eta)\} \end{bmatrix} \begin{Bmatrix} \frac{\mathrm{d}\xi}{\mathrm{d}\tilde{\xi}} \\ \frac{\mathrm{d}\eta}{\mathrm{d}\tilde{\eta}} \end{Bmatrix} = \begin{bmatrix} \frac{\mathrm{d}x}{\mathrm{d}\tilde{\xi}} & \frac{\mathrm{d}y}{\mathrm{d}\tilde{\xi}} & \frac{\mathrm{d}z}{\mathrm{d}\tilde{\xi}} \\ \frac{\mathrm{d}x}{\mathrm{d}\tilde{\eta}} & \frac{\mathrm{d}y}{\mathrm{d}\tilde{\eta}} & \frac{\mathrm{d}z}{\mathrm{d}\tilde{\eta}} \end{bmatrix} \tag{3.63}$$

where

$$\frac{\mathrm{d}\eta}{\mathrm{d}\tilde{\eta}} = \frac{\eta_{j+1} - \eta_j}{2}. \tag{3.64}$$

In (3.60), the determinant of the Jacobian matrix is required, it is well known that it is not possible to calculate the determinant of a non-square matrix in the traditional way. As the Jacobian matrices in (3.61) and (3.63) are non-square, an alternate approach is required. The determinant of the Jacobian vector for a B-spline curve is simply the L2-norm of the vector

$$\det(\{J_B\}) = \|\{J_B\}\|_2. \tag{3.65}$$

There is no concept to find the determinant of a rectangular matrix, however, one can be approximated such that [306]

$$\det([J_B]) = \sqrt{v_x^2 + v_y^2 + v_z^2} \tag{3.66}$$

where

$$v_x = \det\left(\begin{bmatrix} \frac{\mathrm{d}z}{\mathrm{d}\bar{\xi}} & \frac{\mathrm{d}y}{\mathrm{d}\bar{\xi}} \\ \frac{\mathrm{d}z}{\mathrm{d}\bar{\eta}} & \frac{\mathrm{d}y}{\mathrm{d}\bar{\eta}} \end{bmatrix}\right),\ v_y = \det\left(\begin{bmatrix} \frac{\mathrm{d}x}{\mathrm{d}\bar{\xi}} & \frac{\mathrm{d}z}{\mathrm{d}\bar{\xi}} \\ \frac{\mathrm{d}x}{\mathrm{d}\bar{\eta}} & \frac{\mathrm{d}z}{\mathrm{d}\bar{\eta}} \end{bmatrix}\right),\ v_z = \det\left(\begin{bmatrix} \frac{\mathrm{d}y}{\mathrm{d}\bar{\xi}} & \frac{\mathrm{d}x}{\mathrm{d}\bar{\xi}} \\ \frac{\mathrm{d}y}{\mathrm{d}\bar{\eta}} & \frac{\mathrm{d}x}{\mathrm{d}\bar{\eta}} \end{bmatrix}\right).$$

While the applied traction vector, $\{t\}$, can be applied in any direction, it is often the case that a pressure is applied over a boundary. For a pressure boundary condition, the traction vector is the vector normal to the boundary scaled by the magnitude of the pressure imposed. It is straightforward to obtain the normal vector when using a B-spline boundary representation as the first derivatives of the B-spline curve/surface can be found anywhere on the curve/surface. And, as the Gauss points are positioned on the B-spline curve/surface based on the local parametric coordinates the first derivatives can be determined using (3.7) for a B-spline curve (setting $k = 1$) and (3.43) for a B-spline surface (setting $k = 1$, $l = 0$ for the derivative in the ξ direction and $k = 0$, $l = 1$ for the derivative in the η direction, these first derivatives are given in (3.41)). The normal to the B-spline curve is then the cross product between the derivative of the curve with the out of plane vector such that

$$\{C^{\perp}(\xi)\} = \{C^{(1)}(\xi)\} \times \{0, 0, 1\}^T \tag{3.67}$$

while the normal to the B-spline surface is the cross product between the two derivative vectors

$$\{S^{\perp}(\xi, \eta)\} = \{S^{(1,0)}(\xi, \eta)\} \times \{S^{(0,1)}(\xi, \eta)\}. \tag{3.68}$$

3.5.1 Validation of traction imposition

The application of a traction boundary condition to the physical domain using the B-spline boundary representation in a MPM analysis is validated using a series of problems. Each problem is run over a single load step using a small strain, linear elastic material.

2D Elastic cylinder under internal pressure

The first example is that of a 2D, plane strain analysis of a thick walled elastic cylinder under internal pressure. Due to symmetry, only a quarter of the cylinder is modelled, the problem and boundary conditions are depicted in Figure 3.18a where the cylinder has an inner radius, R_i, of 1 m and an outer radius, R_o, of 5 m. The material has a Young's modulus of $E = 1\,\text{MPa}$ and a Poisson's ratio of $\nu = 0.25$. Using the analytical solution [298], an internal pressure of 0.75 MPa is required to double the inner radius of the cylinder, this is the pressure, P, applied over the inner boundary of the cylinder over a single load step in this analysis. No pressure is applied over the outer boundary. Roller boundary conditions are also applied over the sides of the background mesh at $x = 0\,\text{m}$ and $y = 0\,\text{m}$.

The problem domain is discretised by distributing MPs evenly in the circumferential and radial directions between the inner and outer radius of the cylinder, the distribution of 10×10 MPs can be seen as black crosses in Figure 3.18b on a mesh of size $h = 1\,\text{m}$. It is worth noting that this MPs distribution is for illustrative purposes only as there is not enough MPs to adequately represent the physical domain and produce reliable results. In fact, the physical domain is discretised by 512×512 MPs for all analyses in this example. It is also worth noting that the MPs are positioned within the problem domain and not positioned at points along the boundaries of the problem domain in the way this problem was presented by Bing *et al.* [24]. Boundary sampling points are positioned along the desired inner and outer boundaries of the physical domain at regular angular intervals, as depicted by the red circles in Figure 3.18b. The number of boundary points over each boundary is dependent on the size of the background mesh in order to ensure that the integration over each boundary is sufficient and has captured all intersections between the boundary and the elements of the background mesh. As regular B-splines are used (as opposed to Non-Uniform Rational B-Splines (NURBS)), the number of boundary sampling points must also be increased in order to achieve

a good approximation of the circular boundary, regular B-splines are simply unable to fully capture a true circular shape [248]. The pressure boundary condition is applied using Gaussian quadrature over each B-spline curve segment between the boundary points. For each curve segment, two Gauss points are used to integrate the pressure over the boundary. Using two Gauss points for each curve segment was determined to be a reasonable value as it positioned several integration points within each element of the background mesh which contain the boundary while also not significantly increasing the computational cost of the external force calculation.

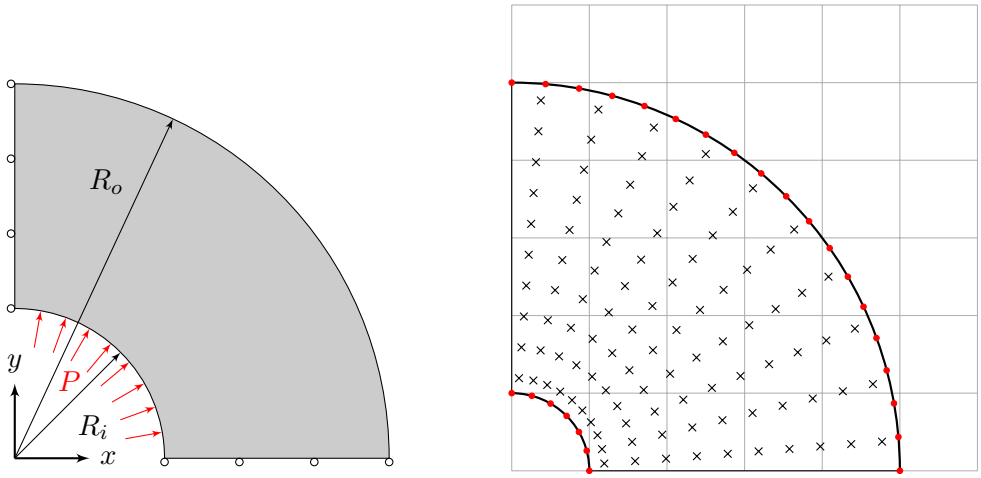

(a) (b)

Figure 3.18: 2D thick walled cylinder: (a) problem geometry and (b) discretisation (right).

The problem is run for multiple meshes with sizes $h = 1\,\text{m}$, 2^{-1} m, 2^{-3} m and 2^{-4} m, all using a 512×512 standard interpolation MPs to discretise the physical domain. Although the pressure boundary condition is only applied over the inner boundary of the cylinder, the outer boundary is also represented with a separate B-spline curve. Table 3.1 displays the number of boundary sampling points used to generate the inner and outer B-spline boundary representations, where n^i_{bp} and n^o_{bp} are the number of boundary sampling points for the inner and outer boundary respectively.

For each analysis, the deformed inner radius is determined by taking 1000 points

Mesh size, h (m)	n_{bp}^{i}	n_{bp}^{o}
1	7	27
2^{-1}	12	52
2^{-2}	22	103
2^{-3}	42	205
2^{-4}	83	409

Table 3.1: Number of boundary sampling points for the inner and outer boundaries for the elastic cylinder problem for different background mesh sizes.

along the deformed inner boundary and calculating the radial position of each point (the distance between the point on the boundary and the origin) and taking the mean average of these points. The relative average inner radius error, ϵ_r, is determined as

$$\epsilon_r = \frac{|r^h - r^a|}{r^a} \tag{3.69}$$

where r^h is the average deformed inner radius and r^a is the analytical deformed inner radius [298].

Figure 3.19 shows the average relative inner radius error as the background mesh is refined where a good convergence rate can be seen. Up to a mesh size of $h = 2^{-3}$ m, there is a quadratic convergence rate which is similar to the results of Bing *et al.* [24]. This may be due to the high curvature of the inner boundary which will not be best captured at large mesh sizes with the linear basis functions. As the mesh is refined, the section of the boundary contained within an element will have much lower curvature so can be more accurately captured and the deformation field across the boundary will be smoother. This effect can be seen in Figure 3.20 where the initial (solid black lines) and deformed (dashed black lines) boundaries are shown for a coarse mesh ($h = 1\,\text{m}$, Figure 3.20a) and a relatively finer mesh ($h = 2^{-2}\,\text{m}$, Figure 3.20b). It can be seen in Figure 3.20a that the deformed inner boundary is not realistic in terms of what would be expected for a cylinder under internal pressure. In comparison, the deformed boundary when modelled with a mesh size of $2^{-2}\,\text{m}$ in Figure 3.20b where the boundary seems to have maintained its circular shape. The deformation of the outer boundary does not seem to be affected by using a coarser mesh as the curvature of the boundary is

much lower compared to the inner boundary. For a mesh size of $h = 2^{-4}$ m, the rate of convergence decreases, this may be because of the fact that the curvature of the inner boundary is well captured using a mesh size of $h = 2^{-3}$ m so refining the mesh further will not significantly improve the results of the analysis any further. The stagnation in the error as the mesh is refined may also be due to the fact that the total number of MPs is kept constant for each mesh, which will limit the accuracy of the integration of the physical material for finer meshes. The results presented in this work differ from those presented by Bing *et al.* [24], this may be due to the method of applying the Neumann boundary condition over the inner boundary of the cylinder, with a secondary effect due to the differences in the setup of the problem. Increasing the number of Gauss points used to integrate over each curve segment may produce results closer to those of Bing *et al.* As mentioned when discussing how the problem is set up, this work does not position MPs over the boundary of the problem domain, instead the MPs are fully contained within the problem domain. This will mean that the traction boundary will not be applied directly to the positions of some MPs in the problem. The fact that the traction is applied using numerical integration over the curve segments between sampling points rather than segments of the curve contained within each element of the background mesh may also cause the difference in error values, this will be discussed further in the next numerical example.

3D Elastic cylinder under internal pressure

The second numerical example is an extension of the example above into 3D, a cylinder with an inner radius, R_i, of 1 m and an outer radius, R_o, of 5 m and a length, $L = 1$ m, the cross section of the problem is shown in Figure 3.18a. The material has a Young's modulus of $E = 1$ MPa and a Poisson's ratio of $\nu = 0.25$. A pressure $P = 0.75$ MPa is applied over the inner boundary of the cylinder over a single load step (the pressure required to double the inner radius as per the analytical solution [298]). Roller boundary conditions are applied over the sides of

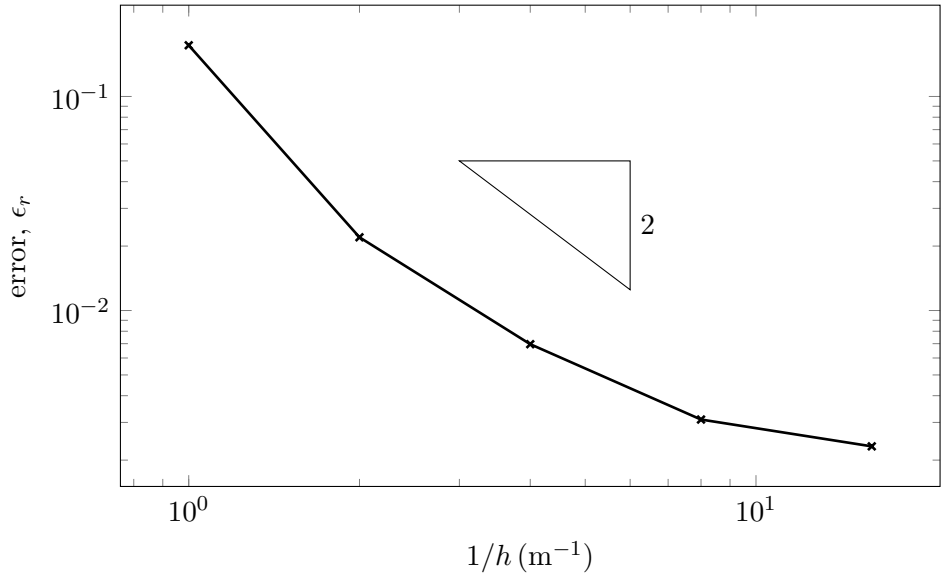

Figure 3.19: Convergence plot of the average relative error of the calculated inner radius of the 2D elastic cylinder analysis as the background mesh is refined.

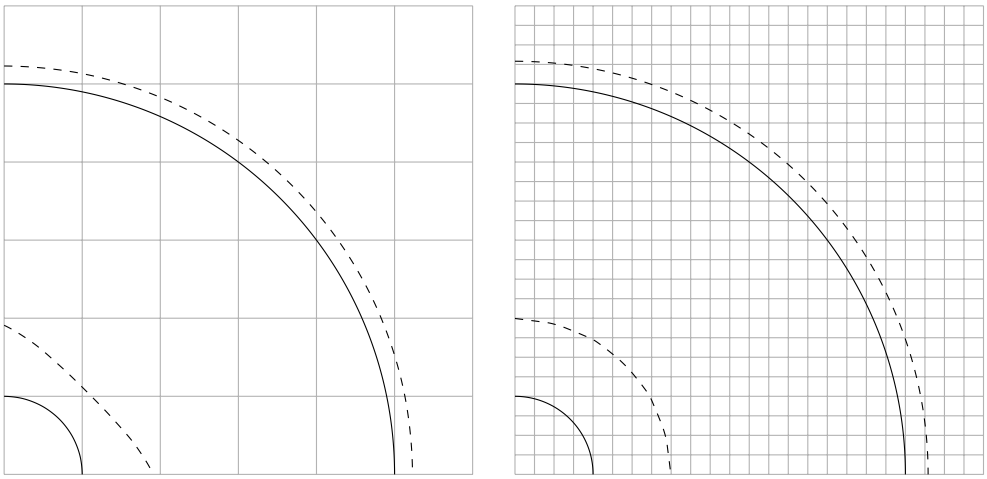

(a) $h = 1\,\mathrm{m}$ (b) $h = 2^{-2}\,\mathrm{m}$

Figure 3.20: Initial (solid black line) and deformed (dashed black line) inner and outer boundaries of the 2D elastic cylinder for different mesh sizes.

the background mesh at $x = 0\,\mathrm{m}$, $y = 0\,\mathrm{m}$, $z = 0\,\mathrm{m}$ and $z = 1\,\mathrm{m}$.

The inner and outer boundaries of the cylinder are represented as two B-spline surfaces. Weightless boundary points are applied over the boundary of the physical domain to generate the B-spline surfaces, the ξ direction is taken to be the curved aspect of the boundary (as seen in the xy-plane) and the η direction is taken to be along the length of the cylinder (parallel to the z axis). Boundary points are

positioned along the ξ direction for the inner and outer boundaries in the same manner as the 2D case above with the number of boundary points in this direction is given in Table 3.1 for each level of mesh refinement. A total of $2n_{el}^{z}+1$ boundary points in the η direction are positioned at even intervals along the length of the cylinder, where n_{el}^{z} is the number of elements of the background mesh in the z direction. Fewer boundary points are required in the η direction compared to the ξ direction as this aspect of the boundary is essentially a straight line. Therefore, it does not have the same issue in truly representing the boundary compared to the circular aspect of the boundary, as per the discussion in the previous example. The number of boundary points in the η direction are still increased at the same rate as in the ξ direction as the mesh is refined to ensure that the integration patches over the B-spline surface are made smaller with mesh refinement.

The problem is run for mesh sizes ranging from 1 m to 2^{-3} m with the size of the elements reducing by a factor of 2 each time. However, the MP distribution used for the 2D problem (displayed in Figure 3.18b) is not used, this is because it is not practical to use so many MPs through the length of the cylinder. Instead, each element of the background mesh is populated with evenly distributed standard interpolation MPs and those which are not contained within the physical domain of the cylinder are removed. The MPs which have a global position such that $R_i \leq \sqrt{x_p^2 + y_p^2} \leq R_o$ are kept, where (x_p, y_p, z_p) is the global position of the MP. The analysis for each mesh size is run using using an initial MP distribution of 2^3, 3^3, 4^3 and 5^3 MPs per element in the background mesh. Overall, the total number of MPs used in the analyses ranges from 152 ($h = 1$ m and 2^3 MPs) to 1 206 520 ($h = 2^{-3}$ m and 5^3 MPs) after the MPs outside of the cylinder domain have been removed.

For each analysis, the relative average inner radius error, ϵ_r, is calculated using (3.69) where the average deformed inner radius, r^h, is determined as the average radial position of 1000 points over the inner B-spline surface boundary using 100 points over the ξ direction and 10 points over the η direction. The analytical

deformed inner radius, r^a, is determined using the analytical solution [298]. Figure 3.21 shows the relative average inner radius error as the mesh is refined for various initial MP distributions. There is predominantly a linear convergence rate as the mesh is refined for all MP distributions, this is strongest when using an initial MP distribution of 3^3 MPs per background mesh element. Interestingly, the other three MP distributions sees an initial quadratic convergence rate (as seen in Figure 3.19 for the 2D case) which degrades to a linear rate at finer meshes. The relative average inner radius error seems to plateau as the mesh is refined when using an initial MP distribution of 2^3 MPs, this may be due to the fact that there are not enough MPs positioned in the space around the boundary to accurately model the deformation around the boundary. The MPM is also susceptible to larger errors around the boundary of the domain, especially when the boundary conditions are applied to the boundary of the physical domain, see Bing *et al.* [24] for evidence of this.

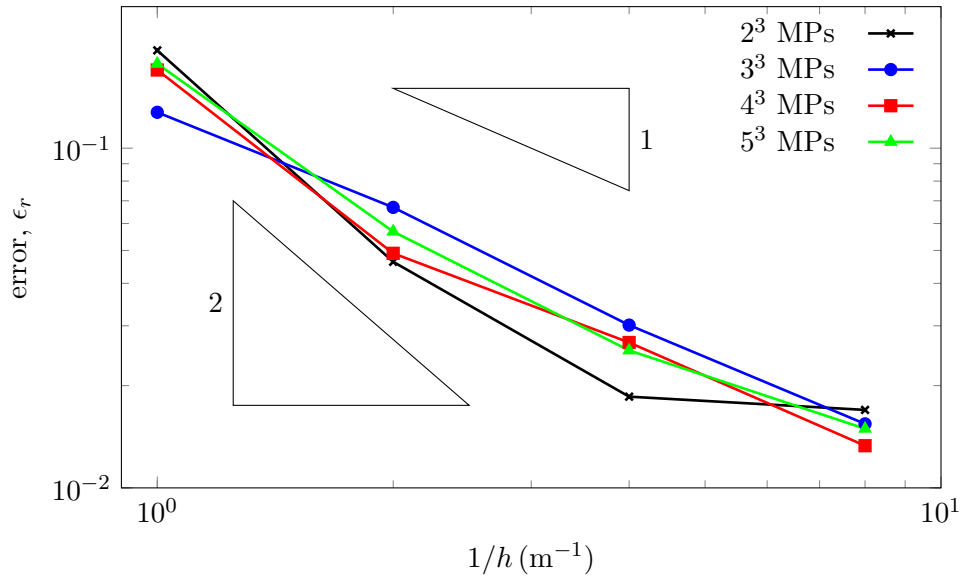

Figure 3.21: Convergence of the average relative error of the calculated inner radius of the 3D elastic cylinder analysis as the background mesh is refined for various initial MP distributions.

Infinite plate with circular hole

The final example is that of a plane stress analysis of an infinite plate with a circular hole under a far field stress in the x direction. The circular hole of the plate has a radius, R_i, of 0.5 m and a far field stress of $S = 10\,\text{MPa}$ is applied in the x direction. The material is modelled as an elastic material with a Young's modulus of $E = 10\,\text{MPa}$ and a Poisson's ratio of $\nu = 0.25$. Due to symmetry, one quarter of the problem is modelled with the problem domain truncated and represented by a B-spline boundary with roller boundary conditions applied directly to the sides of the background mesh at $x = 0\,\text{m}$ and $y = 0\,\text{m}$. Figure 3.22 shows a diagram of the problem for a mesh size of $h = 2^{-3}\,\text{m}$. The boundary is defined using 11 sampling points with the global coordinates

$$\begin{bmatrix} \{x_p\}^T \\ \{y_p\}^T \end{bmatrix} = \begin{bmatrix} 0.00 & 0.10 & 0.35 & 0.60 & 0.73 & 1.00 & 1.50 & 1.75 & 2.00 & 1.78 & 1.50 \\ 1.50 & 1.75 & 1.95 & 1.80 & 1.31 & 1.15 & 1.35 & 1.30 & 0.75 & 0.21 & 0.00 \end{bmatrix} \text{m}$$

which are used to generate the B-spline boundary. These sampling points are shown as red circles in Figure 3.22 with the calculated control points shown as blue squares. To generate the initial physical domain of the plate, the background mesh is fully populated with each element containing 8×8 evenly spaced standard interpolation MPs (the diagram in Figure 3.22 only shows a 2×2 distribution of MPs per element for illustrative purposes). The MPs with a radial distance from the origin of less than 0.5 m are removed as well as those MPs which are positioned outside of the B-spline boundary.

A traction boundary condition is applied over the B-spline boundary based on the analytical stress states at the positions of the integration points along the boundary. The analytical stress solution in the Cartesian coordinate system is given by [298]

$$\sigma_{xx} = S - S\left(\frac{R_i^2}{r^2}\right)\left(\frac{3}{2}\cos(2\theta) + \cos(4\theta)\right) + S\left(\frac{3R_i^4}{2r^4}\right)\cos(4\theta) \tag{3.70a}$$

$$\sigma_{yy} = -S\left(\frac{R_i^2}{r^2}\right)\left(\frac{1}{2}\cos(2\theta) + \cos(4\theta)\right) - S\left(\frac{3R_i^4}{2r^4}\right)\cos(4\theta) \tag{3.70b}$$

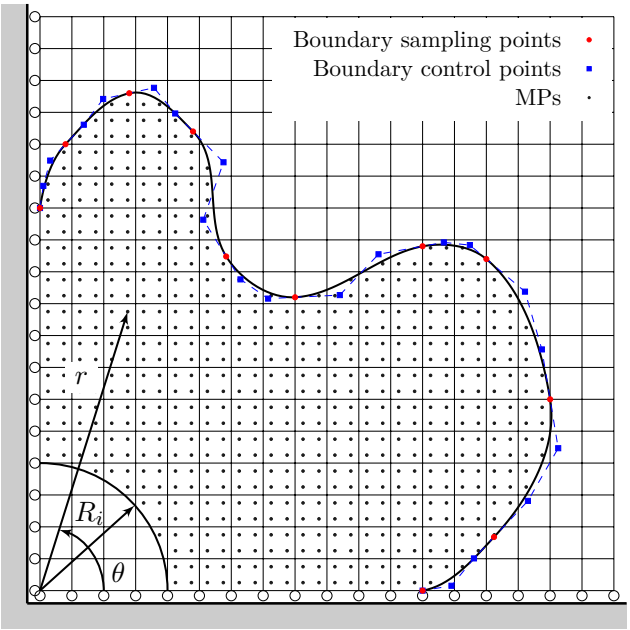

Figure 3.22: Infinite plate with circular hole problem diagram with boundary sampling points (red circles) and control points (blue squares) shown.

$$\sigma_{xy} = -S\left(\frac{R_i^2}{r^2}\right)\left(\frac{1}{2}\sin(2\theta) + \sin(4\theta)\right) - S\left(\frac{3R_i^4}{2r^4}\right)\sin(4\theta) \tag{3.70c}$$

where S is the far field applied stress, r is the radial distance from the origin to the point in question and θ is the angular position of the point from the positive x direction, as shown in Figure 3.22. Due to the method of integrating the traction boundary condition in this work, simply using the 11 sampling points as the boundary points is not feasible, therefore, the sampling points are used to generate an initial B-spline boundary representation and $\frac{22}{h}$ boundary points are evenly spaced across the B-spline curve. This is to ensure that there are enough boundary points such that every element in the background mesh is accounted for when applying the traction load. The traction boundary condition is applied using Gaussian quadrature over each B-spline curve segment between the boundary points, 3 Gauss points are used for each curve segment. The normal vector to the B-spline boundary, $\{n\}$, is determined at the integration point from the derivative of the curve (tangent vector) using (3.8) and (3.67) which is then used to calculate

the traction force given by

$$\{t\} = [\sigma]\{n\} = \begin{bmatrix} \sigma_{xx} & \sigma_{xy} \\ \sigma_{xy} & \sigma_{yy} \end{bmatrix} \begin{Bmatrix} n_x \\ n_y \end{Bmatrix} \tag{3.71}$$

with the stress values calculated based on (3.70). The analytical displacement of a point in the plate is given by [298]

$$u_x = \frac{SR_i}{8\mu}\left(\frac{r}{R_i}(\kappa+1)\cos(\theta) + \frac{2R_i}{r}((1+\kappa)\cos(\theta)+\cos(3\theta)) - \frac{2R_i^3}{r^3}\cos(3\theta)\right) \tag{3.72a}$$

$$u_y = \frac{SR_i}{8\mu}\left(\frac{r}{R_i}(\kappa-3)\sin(\theta) + \frac{2R_i}{r}((1-\kappa)\sin(\theta)+\sin(3\theta)) - \frac{2R_i^3}{r^3}\sin(3\theta)\right) \tag{3.72b}$$

where $\mu = \frac{E}{2(1+\nu)}$ and $\kappa = \frac{(3-\nu)}{(1+\nu)}$ for a plane stress analysis.

The problem is run for mesh sizes ranging from $h = 2^{-1}\,\text{m}$ to $2^{-7}\,\text{m}$, reducing the size of the mesh by a factor of 2 each time. For each analysis, the relative stress error, ϵ_σ, and displacement error, ϵ_u, are computed based on the stress and displacements of each MP such that

$$\epsilon_{\sigma_{ij}} = \frac{1}{V_0}\sum_{\forall p}\left(\frac{\|\sigma_{ij}^p - \sigma_{ij}^a\|V_p^0}{\|\sigma_{ij}^a\|}\right) \text{ and } \epsilon_{u_i} = \frac{1}{V_0}\sum_{\forall p}\left(\frac{\|u_i^p - u_i^a\|V_p^0}{\|u_i^a\|}\right) \tag{3.73}$$

where σ_{ij}^p and u_i^p are the calculated stresses and displacements at the MP position respectively, σ_{ij}^a and u_i^a are the analytical stresses and displacements at the MP position respectively, V_p^0 is the initial volume of the MP and $V_0 = \sum_{\forall p} V_p^0$ is the initial volume of the physical domain. The $\epsilon_{\sigma_{ij}}$ errors are computed for σ_{xx}, σ_{yy} and σ_{xy} and the ϵ_{u_i} errors are computed for u_x and u_y. The calculated relative stress and displacement errors are shown in Figure 3.23 where the stress errors are shown with solid lines and the displacement errors are shown with dashed lines.

Looking at the errors in Figure 3.23, a linear convergence rate can be seen for all the stress errors and a quadratic convergence rate is seen for the displacement errors as the mesh is refined. This follows what was seen by Bing *et al.* [24], however, there are many differences between the results in this work and those of Bing *et al.* Most

notably is the fact that there is a difference in the u_x and u_y displacement errors values in this work where Bing and co-workers saw that these errors are very similar for each mesh size throughout the convergence study. Another difference is seen in the stress errors, Bing and co-workers saw three distinct lines for each stress error, in this work the σ_{yy} and σ_{xy} stresses are similar for each mesh size but still see the linear convergence rate. The error lines in Figure 3.23 also appear to be more erratic compared to Bing *et al.* All of these reasons may be due to the differences in approach to solving the problem. As discussed in the previous numerical example, there is a difference between this work and that of Bing *et al.* in the application of the traction boundary conditions, which may impact the results. Bing *et al.* [24] used Gaussian quadrature to integrate over each curve segment contained within an element whereas this work performs the numerical integration over curve segments between boundary points. In order to reduce any issues with this approach, this work uses a large number of boundary points to ensure that the every element that is cut by the B-spline curve boundary is affected by the imposition of the traction boundary condition, that is the external force vector includes entries for the nodes of all of these elements.

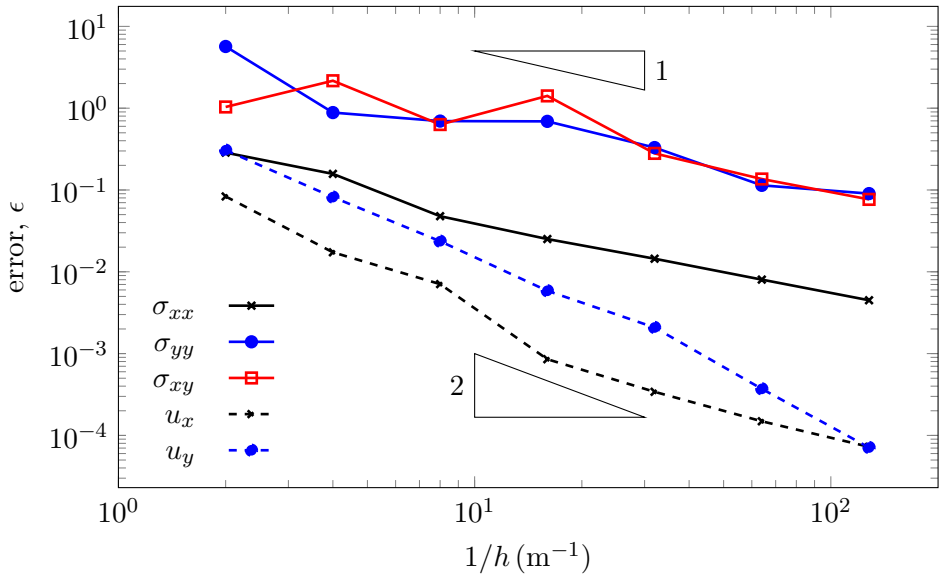

Figure 3.23: Stress and displacement error convergence under mesh refinement for the infinite plate with circular hole problem.

Summary

This chapter presented the method of representing a non-conforming boundary of the physical domain in the MPM, initially based on the work by Bing *et al.* [24] for 2D analyses and extended here into 3D. The principles of B-spline basis functions and their derivatives have been presented and how to calculate these using the recursive formula for higher degree B-splines. This was followed by a discussion on B-spline curves and surfaces including how to generate a B-spline curve or surface from a set of data points using a local interpolation scheme. It is not always the case that the data points are positioned by the analyst, instead, the data points may be an unstructured set of points. In this case a least squares fitting procedure was chosen to generate a B-spline boundary representation. For this, the process of determining the foot point of a data point on a B-spline curve/surface is presented using a subdivision algorithm to determine an adequate initial guess before a point inversion scheme is used to find the foot point. It is worth noting that only the subdivision algorithm is used to determine the foot point on a B-spline surface due to the complexity of the calculation to account for the multiple local dimensions over the B-spline surface as well as the fact that the true foot point on the surface will not be required at any point in this work, thus a sufficiently good estimate is reasonable. The process of fitting a B-spline curve to a set of unstructured data points using the least squares fitting procedure is presented where a fitting strength parameter is introduced to set the number of control points of the B-spline curve which affects how closely the fitted curve represents the data. Ultimately, the B-spline boundary will be used to apply Neumann boundary conditions to the physical domain in a MPM analysis, therefore, a means of integrating traction (or pressure) forces over the B-spline boundary is given for 2D and 3D analyses and validated using a small strain, linear elastic MPM code. Three validation cases were shown where Neumann boundary conditions were applied over a B-spline boundary representation of a physical domain with the resulting deformation and stress fields

compared to analytical results. The analysis of a thick walled cylinder subjected to an internal pressure was shown in 2D and 3D where the inner and outer boundaries of the cylinder was represented using B-spline curves (in 2D) and surfaces (in 3D). In both cases, the deformed inner radius was compared to the analytical solution as the background mesh is refined where convergence in the numerical solution to the analytical solution was seen. An irregular boundary was also modelled for the case of an 2D infinite plate under a far field stress, the analytical stress state was applied as a traction over a B-spline curve representation of the boundary. Again, the numerical stress field and displacements of the MPs were compared to the analytical solution and convergence was seen through mesh refinement.

Given that boundary conditions can now be applied directly to the non-conforming boundaries in a MPM analysis, the next chapter covers the implementation of the arc-length method in the MPM which is able to analyse problems involving non-linear load-displacement responses. As the aim of this work is to model the LV as a hyperelastic material, it is possible that a highly non-linear load-displacement response may be seen or a restriction of the total displacement over a single load may be required to improve the stability of the numerical simulation.

Chapter 4

The Arc-Length Method

For a quasi-static, implicit, non-linear problem in the Finite Element Method (FEM), a prescribed load (or displacement) is applied incrementally at the start of each load step with a Newton-Raphson (N-R) iterative scheme often used to determine the corresponding displacement (or load) such that the out-of-balance forces are minimised over a load step. However, this procedure will only work if the incremented load (or displacement) is strictly increasing throughout the analysis of the problem in order to accurately trace the equilibrium path. Figure 4.1a shows an increasing equilibrium path in which a single value of force corresponds to a single value of displacement. It is possible to determine a solution on the equilibrium path for each load step as the load (or displacement) is incremented. On the other hand, it is not guaranteed that the equilibrium path will be strictly increasing, problems involving large deformations [66] and/or non-linear material behaviour [76] can see critical points along the equilibrium path where it is not possible to increment a variable further and obtain a solution. A snap-through response is shown in Figure 4.1b where an increase is displacement is seen for a decrease in load. In this case, a single force value can correspond to multiple displacement states, therefore, it is not possible to use a load controlled scheme to model a snap-through problem after the critical point. As the snap-through equilibrium path is still an increasing path in terms of displacements, these problems may still be modelled using a displacement controlled scheme. It is worth noting that

this changes the physical problem being modelled depending on the nature of the imposed boundary conditions. A snap-back response displays a decrease in displacement after a snap-through response, an example of which is shown in Figure 4.1c. It is not possible to use either a load controlled or displacement controlled scheme to model a problem involving a snap-back response due to the multiple displacement states for a given force as well as multiple load states for a given displacement. There are two common options for the solution of these non-linear responses, the first option uses a perturbation method [50, 175, 261, 296] while the other uses a predictor-corrector method [6, 227, 314]. Refer to [260] for a discussion on these two methods. Another path following method was proposed by Eriksson and is named the generalised path following method [91]. This work focusses on the second option, the predictor-corrector method, namely the arc-length method [260, 262, 326], which is the most common path following technique.

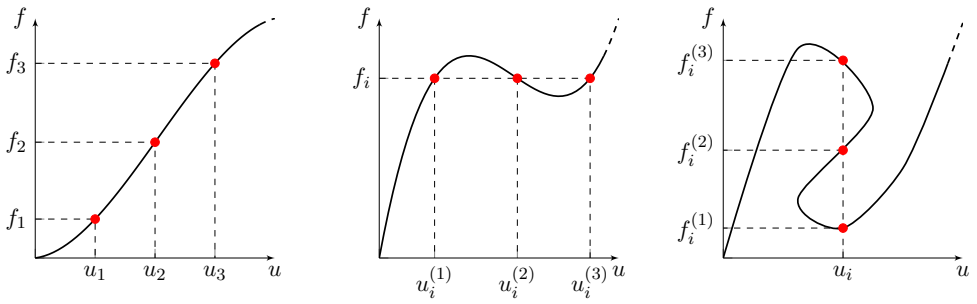

Figure 4.1: Equilibrium paths of (a) increasing response, (b) snap-through response and (c) snap-back response.

The arc-length method was independently developed by Riks [260, 262] and Wempner [326] in the 1970s and is one of the main techniques used in Finite Element Analysis (FEA) to overcome the issues associated with the solving of snap-through and snap-back equilibrium paths [218]. Crisfield [65] adapted the method proposed by Riks such that the arc-length method is more suited for use in the FEM when used with the modified Newton-Raphson method. Since its conception, many variations of the arc-length method have been proposed to solve complex equilibrium paths including (but not limited to): handling

structural instabilities using the current stiffness parameter and identifying the limit points [18], linearising the solution to solve over a hyperplane rather than a hypersphere [254], decomposing the out-of-balance forces into parallel and orthogonal components with respect to the applied external force [180], combining the Crisfield and Ramm arc-length approaches using a geometrical interpretation [94], augmenting the stiffness matrix (stiff arc-length method) [230] and a displacement controlled arc-length method [251]. The essence of the arc-length method comes from the constraint equation, or arc-length equation, which is included in the non-linear equations of the problem and solved to give an incremental load factor and corresponding incremental displacements. The displacement solution is constrained by the arc-length equation and determined based on this allowed displacement, this means that the issues which may arise in traditional load/displacement controlled schemes due to snap-through or snap-back responses are mitigated. The arc-length method has been used to solve a variety of non-linear problems including buckling of cylindrical shells [166, 179, 233, 329], structural analysis [256], modelling of crack propagation [101, 323] and failure of brittle materials [4, 39].

While the arc-length method is well established in its use with the FEM, to the author's knowledge, no literature had published prior to the implementation presented in [106] which presents the implementation of a Material Point-Based Arc-Length Method (MP-BALM). The referenced paper [106] forms the basis of this chapter which describes the first implementation of a MP-BALM, which expands the applicability of the MPM to model load controlled problems involving snap-through responses. The arc-length method in it current form for FEA will be presented followed by an explanation of the adaptations needed for the arc-length method to be successfully used with the MPM. The MP-BALM will be demonstrated for various problems involving linear elastic, linear elastic-perfectly plastic and linear elastic-plastic softening material behaviours under large deformations. The arc-length method presented in this chapter is

able to analyse problems involving both snap-through and snap-back responses, however, the MPM is a continuum method for which there are no known physically meaningful problems involving global snap-back responses. This means that only problems involving snap-through responses will be shown in the chapter.

The main aim of this work is to develop a large deformation model of the left ventricle with a non-linear hyperelastic constitutive model, this means that there is the potential that a snap-through response can be encountered. The arc-length method can also be used as a means of restricting the displacement of the domain over a single load step in order to improve stability of an analysis. These are the main reasons for the implementation of the MP-BALM in this work. This chapter uses the MP-BALM to model large deformation problems with snap-through behaviour, it will also be used in Chapter 5 to validate the hyperelastic, isotropic Ogden material model for a problem which sees snap-through behaviour.

4.1 The arc-length method for FEA

An arc-length solver (or Riks solver) solves for both load and displacement based on the converged state of the previous load step and a specified arc length. The equilibrium path is formed of load factor-displacement pairs, $(\lambda, \{u\})$, where λ is the load factor and $\{u\}$ are the nodal displacements. The load factor acts as a scalar multiplier of the external force vector applied to the problem domain such that

$$\{f^{ext}\} = \lambda\{f_0^{ext}\} \tag{4.1}$$

where $\{f_0^{ext}\}$ is the initial applied external force vector and $\{f^{ext}\}$ is the external force vector corresponding to the current load factor. A key feature of the arc-length method is that the distance from the current converged state to the next state along the equilibrium path is limited by a specified arc length, Δl. The most general form of the arc-length constraint is the spherical arc-length constraint [76] which is given

by

$$\{\Delta u\}^T\{\Delta u\} + \Delta\lambda^2\psi^2\{f_0^{ext}\}^T\{f_0^{ext}\} = \Delta l^2 \tag{4.2}$$

where $\{\Delta u\}$ and $\Delta\lambda$ are the converged values of the change in nodal displacements and the change in the load factor respectively for the current load step and ψ is a prescribed scaling parameter which determines the involvement of the applied external force in the satisfaction of the arc-length constraint. This work utilises the more widely used version of the arc-length constrain by setting the scaling parameter ψ to be zero, ensuring that only the Euclidean norm of the change in nodal displacements is equal to the prescribed arc-length [76], this version is called the cylindrical arc-length method. The cylindrical arc-length constraint is given by

$$\{\Delta u\}^T\{\Delta u\} = \Delta l^2. \tag{4.3}$$

Figure 4.2 shows the use of the cylindrical arc-length method to track through the equilibrium path for a simple two degree of freedom system. Given a converged state, $(\lambda_n, \{u_n\})$, when visualised in terms of two displacement components, $\{u_1\}$ and $\{u_2\}$, the constraint equation (4.3) creates a cylindrical zone around the converged point. The equilibrium path will intersect the cylinder at two points, A and B. These are the two points on the equilibrium path which satisfy the arc-length constraint based on the change in nodal displacements from the converged state. Using an appropriate selection method, either point A or point B is chosen to be the next converged state and the process is repeated for the next load step.

The arc-length method is often paired with a N-R iterative scheme to find a solution such that the equilibrium of forces is achieved as well satisfying the arc-length constraint. In each iteration of a load step, the load factor increment, $\delta\lambda$, is found by substituting the incremental forms of displacement and load factor (which will be introduced later in this section) into (4.3) and solving the resulting quadratic equation [65]

$$\alpha_1\delta\lambda^2 + \alpha_2\delta\lambda + \alpha_3 = 0 \tag{4.4}$$

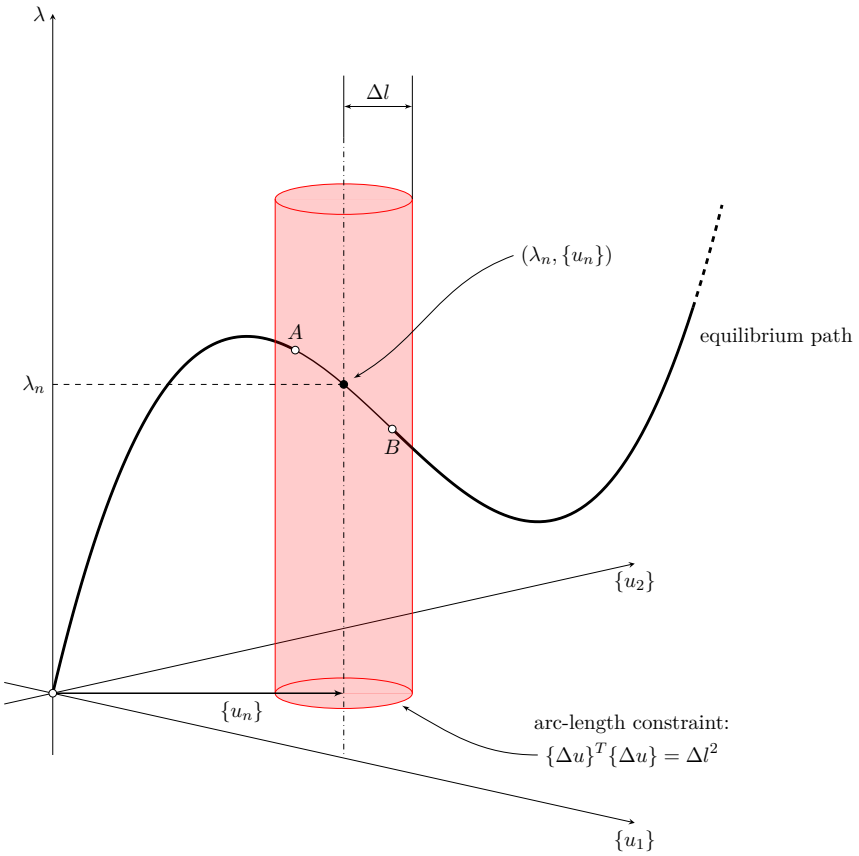

Figure 4.2: The cylindrical arc-length method. Reproduced from de Souza Neto *et al.* [76].

with the coefficients of the quadratic equation given by

$$\begin{aligned} \alpha_1 &= \{\delta\bar{u}\}^T\{\delta\bar{u}\} \\ \alpha_2 &= 2\{\delta\bar{u}\}^T\{\{\Delta u_k\} + \{\delta u^*\}\} \\ \alpha_3 &= \{\{\Delta u_k\} + \{\delta u^*\}\}^T\{\{\Delta u_k\} + \{\delta u^*\}\} - \Delta l^2 \end{aligned} \tag{4.5}$$

where subscript k denotes values from the previous N-R iteration and $\{\Delta u_k\}$ is the change in nodal displacements calculated so far in the load step. The tangential displacement, $\{\delta\bar{u}\}$, and the N-R displacement*, $\{\delta u^*\}$, are given by

$$\{\delta\bar{u}\} = [K]^{-1}\{f_0^{ext}\} \tag{4.6a}$$

$$\{\delta u^*\} = [K]^{-1}\{f^R\} \tag{4.6b}$$

*Naming convention taken from the literature, see Crisfield [65]. The N-R displacement is the vector resulting from the elimination of the out-of-balance forces, while the tangential displacement is the vector tangential to the N-R displacement on the load-displacement curve.

where $\{f^R\}$ is the residual force vector from (2.60).

As the form of (4.4) is a quadratic equation, there are two possible solutions for $\delta\lambda$, one root will progress along the equilibrium path and the other root will track back along the path. These two roots correspond to the two points of intersection between the equilibrium path and the arc-length constraint and can be seen in Figure 4.2 as points A and B. The selection of the appropriate root is required to ensure that the analysis progresses in the desired direction. One option is to utilise the "angle criteria" [76] which minimises the angle between the change in nodal displacements so far in the load step and the newly calculated change in nodal displacements. This is done by maximising the dot product of the two vectors in question, the value of $\delta\lambda$ is chosen such that

$$\delta\lambda^{(k+1)} = \arg\left[\max_{\delta\tilde{\lambda}}\left(\left\{\{\Delta u_k\} + \{\delta u^*\} + \delta\tilde{\lambda}\{\delta\bar{u}\}\right\}^T \{\Delta u_k\}\right)\right]. \tag{4.7}$$

An alternative for the root selection was proposed by Hellweg and Crisfield [138] which sought to overcome issues when using the angle criterion with problems involving sharp snap-back responses. The two roots for $\delta\lambda^{(k+1)}$ are calculated as standard, however, the total displacements, stresses and internal forces are computed for each root and the root which produces the smallest residual is chosen. Hellweg and Crisfield stated that this method is only required when modelling material failure with sharp snap-back responses. However, this work does not consider snap-back responses and thus no further consideration of this method is taken, the choice of appropriate root of $\delta\lambda^{(k+1)}$ is found using (4.7). Complex roots are a well documented occurrence when solving (4.4), this may happen when the value of Δl is too large and it is difficult to determine the intersection with the load-displacement curve [40, 94]. Methods to overcome the issue of complex roots have been proposed, see [71, 76, 180, 263, 271].

The incremental change in nodal displacements, $\{\delta u\}$, is then calculated as a combination of the N-R displacement and the tangential displacement (which is

scaled by the load factor increment determined by (4.4) and (4.7)) such that

$$\{\delta u_{k+1}\} = \{\delta u^*\} + \delta\lambda^{(k+1)}\{\delta\bar{u}\}. \tag{4.8}$$

At the start of the simulation, an initial arc length is required. It is possible to simply prescribe this value, however, this is not easy for the user to determine a reasonable initial arc length as it is dependent on the mesh size. Instead, the initial arc length can be calculated as the Euclidean norm of the iterative increment of the tangential displacement at the start of the problem, that is

$$\Delta l_0 = \sqrt{\{\delta\bar{u}\}^T\{\delta\bar{u}\}}, \tag{4.9}$$

where the $\{\delta\bar{u}\}$ used is the initial tangential displacement based on the reference load with a prescribed initial iterative load factor increment of 1 to produce an initial arc length value. A choice can be made to set this initial arc length value from (4.9) to be the maximum allowed arc length throughout the simulation, however, this choice is not a requirement of the arc-length method. In principle, the arc length can take any value but there may be cases where the arc length becomes too large and causes issues in the analysis, so imposing an upper limit for this value is often the best action. Depending on the number of N-R iterations needed in a load step, the arc length in the following load step is adjusted accordingly. Given a prescribed desired number of iterations, if the number of N-R iterations exceed this value, the arc length is reduced for the following load step, reducing the distance away from the current converged state to the next converged state. Conversely, if the number of N-R iterations needed is below the desired value, the arc length is able to increase (up to a user prescribed maximum value) for the subsequent load step. The arc length for the following load step is calculated at the end of each load step such that

$$\Delta l_n = \max\left[\min\left[\left(\frac{k_{des}}{k_n}\right)^{\alpha_{al}}\Delta l_0, \Delta l_0\right], \frac{\Delta l_0}{\gamma_{al}}\right] \tag{4.10}$$

where k_{des} and k_n are the desired and actual number of N-R iterations needed in the load step respectively and α_{al} and γ_{al} are positive scalars. In the literature,

α_{al} is taken to be 1 [65] or 0.5 [180], however, Ramm [254] explains that when $\alpha_{al} = 1$, oscillations in the number of N-R iterations needed in each load step can be seen and therefore taking $\alpha_{al} = 0.5$ is a more stable approach. The value of γ_{al} controls the minimum allowed arc length through the entire simulation such that Δl_n is a value in the interval $\left[\frac{\Delta l_0}{\gamma_{al}}, \Delta l_0\right]$, this ensures that if the required N-R process continues to exceed the desired number of iterations, the arc length will not continue to decrease so much that the tracing of the equilibrium path begins to halt as the allowed displacement increment becomes very small. There is no theory on the choice of value of γ_{al}, therefore $\gamma_{al} = 4$ is chosen here based on Pretti *et al.* [251].

In the first iteration of each load step, there is clearly no information as to the change in nodal displacements, $\{\Delta u_0\} = \{0\}$. In this case, solving (4.4) produces the solutions for the initial load factor increment of

$$\delta\lambda^{(1)} = \pm \frac{\Delta l}{\sqrt{\{\delta\bar{u}\}^T\{\delta\bar{u}\}}} \tag{4.11}$$

giving a magnitude of the initial increment. However, it is not possible to use (4.7) to determine which solution to choose and a predictor is required. It is important to choose the correct value of the predictor solution as one will progress the simulation along the equilibrium path and the other will track back along the path [66]. Multiple options of predictor solution criteria have been presented in the literature to choose the correct sign for $\delta\lambda^{(1)}$ to progress along the path, including:

1. Stiffness determinant [19] - sign determined by the determinant of the current stiffness matrix:

$$sign\left(\delta\lambda^{(1)}\right) = sign(|[K]\{u_0\}|) \tag{4.12}$$

2. Incremental work [249] - sign determined by predictor work increment:

$$sign\left(\delta\lambda^{(1)}\right) = sign\left(\{\delta\bar{u}\}^T\{f^{ext}\}\right) \tag{4.13}$$

3. Secant path [97, 98] - sign determined by deformation of the previous load step, $\{\Delta u_n\}$:

$$sign\Big(\delta\lambda^{(1)}\Big) = sign\Big(\{\Delta u_n\}^T\{\delta\bar{u}\}\Big) \tag{4.14}$$

Option 1 is widely used and is easily implemented as the stiffness matrix will be known, however, issues may arise if the stiffness matrix is close to singular [65] or in the presence of bifurcations where the solution will oscillate around the bifurcation point [76]. Option 2 is able to trace an equilibrium path through a bifurcation point but is not able to effectively trace snap-back responses [76]. Both options 1 and 2 use information based on the current equilibrium state and nothing about the history of the equilibrium path. Option 3 involves the use of $\{\Delta u_n\}$ which takes the deformation of the mesh in the previous load step into account when determining the deformation of the current load step. The secant path predictor is able to overcome the issues seen with the stiffness determinant and incremental work predictor schemes. An alternative predictor solution was proposed by Kadapa [166] where an extrapolation operator uses the solution from two previous converged load steps to determine the change in nodal displacements and load factor increment in the first iteration for each load step. These incremental values are calculated as a linear combination of the respective nodal displacements and load factor of the previous two load steps such that change in nodal displacements and load factor increment in the predictor step are given by

$$\left.\begin{aligned} \{\delta u_1\}_{n+1} &= \alpha_{pr}\{\Delta u_n\} \\ \delta\lambda^{(1)}_{n+1} &= \alpha_{pr}\Delta\lambda_n \end{aligned}\right\} \quad \text{where} \quad \alpha_{pr} = \frac{\Delta l_0}{\Delta l_n} > 0. \tag{4.15}$$

It is worth noting that this approach is not used in the first load step as there is no change in nodal displacement or load factor at the start of the analysis and an alternative prediction must be made, Kadapa found that a value of $\Delta\lambda^{(1)}_0$ which produces a noticeable deformation is sufficient for this first predictor value. This is a simpler and less expensive predictor solution which does not require any additional

computation to determine the direction of the progression along the equilibrium path in the predictor step. This work adopts the secant path predictor.

Figure 4.3 shows the process of the arc-length solver through the iterations of a single load step. From the previously converged point, $(\lambda_n, \{u_n\})$, the predictor iteration determines the initial load factor increment (with direction determined by the secant path predictor) which is used to calculate an initial change in nodal displacement in order to satisfy the arc-length constraint. In subsequent iterations, the load factor increment is calculated using (4.4) and then the change in nodal displacements are calculated using (4.8). These steps are repeated until the N-R error is below an allowed tolerance to give the next converged point, $(\lambda_{n+1}, \{u_{n+1}\})$.

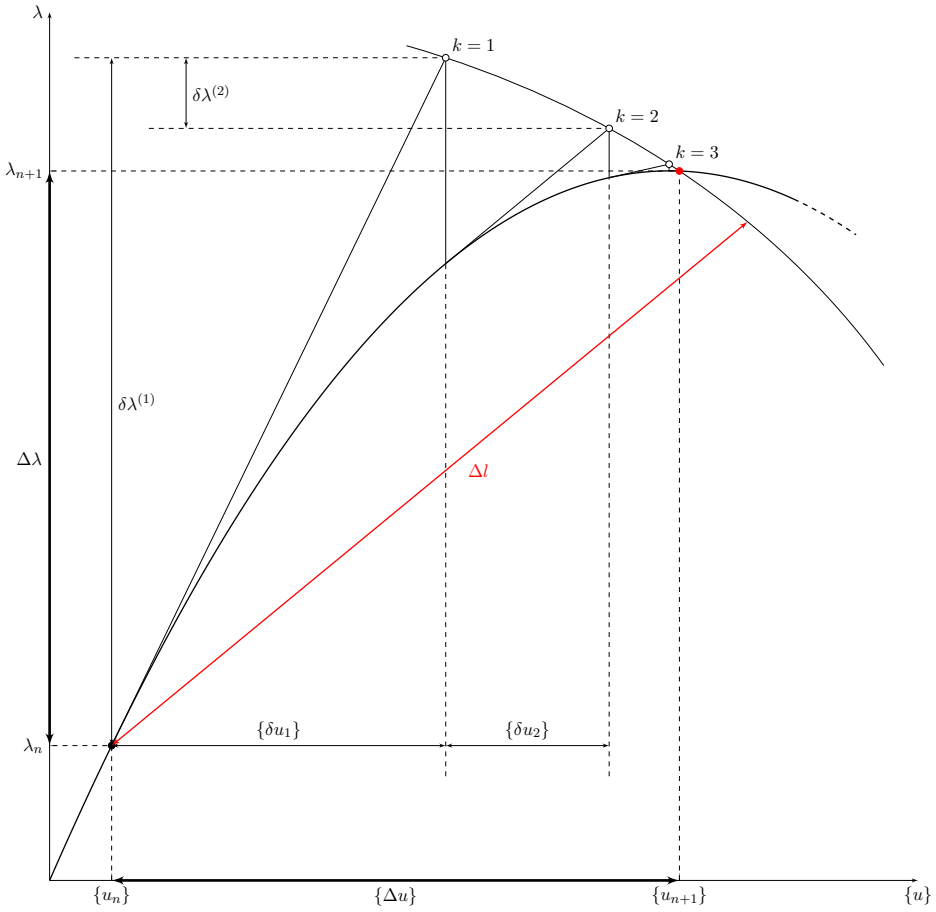

Figure 4.3: The arc-length method using the N-R iterative scheme over a single load step.

This section has covered the form of the FEM-based arc-length method to solve

problems involving snap-through or snap-back responses. However, some changes must be made to the arc-length formulation in order for robust analysis when using the arc-length method with the MPM. These changes will be covered in the following section.

4.2 The arc-length method for the MPM

As discussed in Chapter 2, the MPM allows the Material Points (MPs) to move through the background mesh, which means that it is possible that the MPs will populate small portions of an element around the boundary of the physical domain. This causes issues with elements that participate in the analysis having very small stiffnesses, resulting in extremely large nodal displacements relative to the applied external load. This means that if an arc-length solver is implemented into the MPM in its FEM form, the large nodal displacements will account for the majority of the allowed nodal displacements of the arc-length constraint, manifesting in very small increments of the load factor and an inefficient tracing of the equilibrium path. In order to overcome this issue, it is proposed that the arc-length constraint is reformulated based on the change in MP displacements rather than the nodal displacements. The change in MP displacement, $\{\Delta u_p\}$, is calculated by mapping the change in nodal displacements to the location of the MP such that

$$\{\Delta u_p\} = \sum_{v=1}^{n_v} S_{vp}\left(\{x_p\}\right)\{\Delta u\} = [S_{vp}]\{\Delta u\} \tag{4.16}$$

where n_v is the number of nodes in the background mesh, $S_{vp}\left(\{x_p\}\right)$ is the basis function of node (or vertex) v based on the position of the MP and $[S_{vp}]$ is a $3\times 3n_v$ matrix containing the basis functions associated with the MP for all nodes in the background mesh. As the $[S_{vp}]$ matrix can be seen as a measure of the influence each node in the background mesh has on single MP, by summing all of the shape functions associated with each node of the background mesh for each MP, the total influence of each node on the physical domain can be estimated. The summation of shape functions over each MP for each node (repeating for each dimension) can

be used to form a diagonal matrix, $[\bar{N}]$, of size $(n_D * n_v) \times (n_D * n_v)$. For a 3D analysis, this matrix takes the form

$$[\bar{N}] = \begin{bmatrix} \sum_{\forall p} S_{1p} & 0 & 0 & \cdots & 0 & 0 & 0 \\ 0 & \sum_{\forall p} S_{1p} & 0 & \cdots & 0 & 0 & 0 \\ 0 & 0 & \sum_{\forall p} S_{1p} & \cdots & 0 & 0 & 0 \\ \vdots & \vdots & \vdots & \ddots & \vdots & \vdots & \vdots \\ 0 & 0 & 0 & \cdots & \sum_{\forall p} S_{n_v p} & 0 & 0 \\ 0 & 0 & 0 & \cdots & 0 & \sum_{\forall p} S_{n_v p} & 0 \\ 0 & 0 & 0 & \cdots & 0 & 0 & \sum_{\forall p} S_{n_v p} \end{bmatrix}. \tag{4.17}$$

The values within $[\bar{N}]$ are scaled by the maximum diagonal value such that the matrix contains values between 0 and 1. The values in $[\bar{N}]$ are representative of the influence of the change in nodal displacements on the physical body, where nodes surrounded by fully populated elements have a value equal or close to 1 and the nodes associated with less physical material have a value of less than 1. Due to the nature of the MPM, the displacements of the MPs have more of a physical meaning compared to the displacements of the nodes of the mesh as it is the MPs that represent the deformation of the physical domain in a MPM analysis. Therefore, in a similar fashion to the MP displacement calculation in (4.16), a vector of scaled nodal displacements, $\{\Delta u_s\}$, is calculated as

$$\{\Delta u_s\} = [\bar{N}]\{\Delta u\}. \tag{4.18}$$

The arc-length constraint in (4.3) can then be modified using the scaled nodal displacements giving

$$\begin{aligned} \{\Delta u_s\}^T\{\Delta u_s\} &= \left([\bar{N}]\{\Delta u\}\right)^T \left([\bar{N}]\{\Delta u\}\right) \\ &= \{\Delta u\}^T \left([\bar{N}]^T[\bar{N}]\right)\{\Delta u\} \\ &= \{\Delta u\}^T[\tilde{N}]\{\Delta u\} \end{aligned} \tag{4.19}$$

where $[\tilde{N}] = [\bar{N}]^T[\bar{N}]$ is a diagonal matrix with values between 0 and 1. The result of the modification in (4.19) is that the nodes associated with partially filled

elements will not take up as much of the allowed change in nodal displacements, improving the performance of the arc-length solver in tracing the equilibrium path with more uniform increments. This will be demonstrated with numerical examples in Section 4.3. The values in $[\bar{N}]$ are scaled in order to ensure that changing the number of MPs used in the analysis does not have a significant effect on the progression of tracing along the equilibrium path. For example, if no scaling is present, increasing the number of MPs will increase the values on the diagonal of $[\bar{N}]$ thus increasing the left hand side of (4.19) and resulting in smaller displacements per load step and a slower progression through the analysis. The $[\bar{N}]$ matrix scales the nodal displacements in the arc-length condition based on a node's influence on the physical domain, however, as the values in the matrix are rescaled such that they are between 0 and 1, $[\bar{N}]$ has no physical meaning in terms of the problem. The reason for the use of $[\bar{N}]$ is to reduce the impact of the large nodal displacements of the partially filled elements around the boundary of the domain (as the corresponding values in $[\bar{N}]$ will be close to zero) while maintaining the displacements of the nodes which have more influence on the physical domain. The author made the decision that the values on the diagonal of the $[\bar{N}]$ matrix are between 0 and 1 rather than ensuring that the norm of the matrix is equal to 1, this decision was made such that the displacements of the nodes of fully populated elements are minimally affected by the scaling matrix as the value in $[\bar{N}]$ which corresponds to these nodes will be very close to 1. If the scaling of $[\bar{N}]$ is performed such that the norm of the matrix is equal to 1, all values on the diagonal of the scaled matrix will be smaller that 1 which will result in significantly slower progression through the analysis as the material is unable to deform as much through each load step. Refining the mesh will also have a detrimental effect with scaling $[\bar{N}]$ such that the norm is equal to 1 as the matrix will increase in size meaning that the values on the diagonal must decrease which will slow the progression even further. By scaling the values such that they are between 0 and 1, this issue is mitigated.

The addition of the $[\tilde{N}]$ matrix in (4.19) is incorporated throughout the MP-BALM

formulation to calculate the load factor increment where the new coefficients of (4.4) become

$$\begin{aligned} \alpha_1 &= \{\delta\bar{u}\}^T[\tilde{N}]\{\delta\bar{u}\} \\ \alpha_2 &= \{\delta\bar{u}\}^T[\tilde{N}]\left\{\{\Delta u_k\} + \{\delta u^*\}\right\} \\ \alpha_3 &= \left\{\{\Delta u_k\} + \{\delta u^*\}\right\}^T[\tilde{N}]\left\{\{\Delta u_k\} + \{\delta u^*\}\right\} - \Delta l^2. \end{aligned} \tag{4.20}$$

The initial arc-length calculation in (4.9) also includes $[\tilde{N}]$ such that

$$\Delta l_0 = \sqrt{\{\delta\bar{u}\}^T[\tilde{N}]\{\delta\bar{u}\}} \tag{4.21}$$

as well as for the predictor solution where the initial load factor increment is calculated as

$$\delta\lambda^{(1)} = sign\Big(\{\Delta u_n\}^T[\tilde{N}]\{\delta\bar{u}\}\Big)\frac{\Delta l}{\sqrt{\{\delta\bar{u}\}^T[\tilde{N}]\{\delta\bar{u}\}}}. \tag{4.22}$$

It is still important to include the scaling matrix in (4.22), as $\{\delta\bar{u}\}$ is calculated from the assembled stiffness matrix for the MPs in the current state meaning that the partially filled elements at the boundary of the MP domain may still see large nodal displacements. The large nodal displacements may also be seen within $\{\Delta u_n\}$ as these are simply the calculated nodal displacements from the previous load step where the large nodal displacements may have also occurred.

4.2.1 Nodal displacement reconstruction

This work uses the secant path predictor in (4.22) (the scaled form of (4.14)) for the determination of the direction of the equilibrium path in the first iteration of a load step where the converged nodal displacement of the previous load step is required. However, since a key feature of the MPM is that the background mesh is reset at the end of every load step, obtaining these nodal displacements is not trivial. Using the nodal displacement vector at the end of the previous load step is not feasible as the body has deformed and the MPs have changed position, meaning that the domain is not influenced by the mesh nodes in the same way as in the

previous load step. A method of reconstructing the nodal displacement field based on the MP displacements of the previous load step and the updated MP positions is therefore needed. This is done using a least squares weighted residual technique based on the approach of [24]

$$\int_{\Omega} [S_{vp}]^T \{ [S_{vp}] \{\Delta u_n\} - \{\Delta u_p^a\} \} \, \mathrm{d}v = \{0\} \tag{4.23}$$

where $\{\Delta u_p^a\}$ are the known MP displacements from the previous load step and $\{\Delta u_n\}$ are the unknown nodal displacements which are to be solved for. Rearranging for the unknown nodal displacements, an expression can be obtained such that

$$\{\Delta u_n\} = \left[\int_{\Omega} [S_{vp}]^T [S_{vp}] \, \mathrm{d}v \right]^{-1} \left\{ \int_{\Omega} [S_{vp}]^T \{\Delta u_p^a\} \, \mathrm{d}v \right\}. \tag{4.24}$$

It is worth noting that $\{\Delta u_n\}$ is evaluated globally in order to minimise the residual error across the whole domain meaning that the integrals in Equation (4.24) must be assembled into a global matrix and vector respectively. This means that $\{\Delta u_n\}$ is calculated as

$$\{\Delta u_n\} = \left[\mathop{\mathcal{A}}_{\forall p} \left([S_{vp}]^T [S_{vp}] V_p \right) \right]^{-1} \left\{ \mathop{\mathcal{A}}_{\forall p} \left([S_{vp}]^T \{\Delta u_p^a\} V_p \right) \right\}. \tag{4.25}$$

As the nodal displacements of the previous load step are reconstructed based on the MPs' position in the current state, there may still be cases where large nodal displacements are calculated for partially filled elements around the boundary of the MP domain, therefore, the scaling matrix is needed in the predictor meaning (4.22) should be used over (4.14) in order to mitigate issues involving large nodal displacements.

Algorithm 4.1 shows the standard solution procedure for the MP-BALM. It is worth pointing out that a zeroth load step is analysed to generate the initial state of the domain and the arc-length solver is not used in this load step. The nodal displacement reconstruction takes place at the start of each load step before entering the N-R iteration loop. The arc-length solver itself requires multiple if

statements in order to determine how to find the load factor increment and the arc length needs to be updated at the end of each load step based on the iterative performance of said load step. Some control is needed in terms of how many load steps are allowed to be performed over the analysis, this is due to the fact that there is no longer control on how many load steps it will take to apply the full prescribed load. Therefore, it is wise to prescribe a maximum number of load steps, n_{max}, which will halt the analysis once this number of load steps has been reached. This algorithm is used to solve the numerical examples presented in Section 4.3.

4.3 Numerical examples

A series of numerical examples are now presented to demonstrate the capability of the new, scaled approach to the arc-length solver within the MPM formulation. The first example presented does not show a snap-through response, however, it is included to show that the arc-length solver can be implemented into a MPM code and produce correct results for simple problems with an analytical solution. Further examples show the capabilities of the MP-BALM with problems which encounter snap-through responses.

4.3.1 2D column under self weight

A simple benchmark test is utilised to demonstrate the the functionality of the implemented arc-length solver within a MPM framework, namely the 1D compression of an elastic column with an initial height of $L_0 = 50\,\text{m}$ under self weight. Although this example is a 1D problem in essence, a 2D plane strain implementation is used. The column is modelled as a Hencky material with a Young's modulus of 10 kPa and a Poisson's ratio of zero. The background mesh is generated using square elements with roller boundary conditions applied over the base and sides of the mesh. The column is discretised using 2×2 evenly distributed generalised interpolation MPs in each populated element of the background mesh.

Algorithm 4.1: MP-BALM procedure.

```
for n = 0 : n_max do
    initialise change in nodal displacement, {Δu^(0)} = 0;
    determine material point data in current state;
    calculate scaling matrix, [N̄] (4.17);
    determine list of active elements in analysis;
    determine free degrees of freedom;
    calculate external force vector, {f_0^ext};
    nodal displacement reconstruction, {Δu_n} (4.25);
    initialise residual out-of-balance force, |{f_0^R}| > tol ⇒ f_err > tol;
    start iteration counter, k = 0;
    while f_err > tol do
        if n > 0 then
            if k > 0 then
                if i = 1 and k = 1 then
                    calculate initial arc length (4.21);
                calculate tangential displacement, {δū} (4.6a);
                if k = 1 then
                    determine δλ^(1) using predictor solution (4.22);
                else
                    calculate Newton-Raphson displacement, {δu*} (4.6b);
                    determine δλ^(k+1) by solving quadratic equation (4.4)
                    with (4.20);
                calculate incremental change in nodal displacement, {δu_k+1}
                (4.8);
            else
                zero incremental displacement in zeroth iteration, {δu_0} = 0;
        increment change in nodal displacements,
        {Δu_k+1} = {Δu_k} + {δu_k+1};
        assemble global stiffness matrix, [K];
        assemble internal force vector, {f^int};
        calculate residual out-of-balance forces, {f_k+1^R} = {f^ext} − {f^int};
        calculate norm of residual force, f_err = |{f_k+1^R}|;
    update material point information;
    update Δl (4.10);
```

A diagram of the column compression problem is shown inset in Figure 4.4, the background mesh and MP distribution are not shown but populate the full space of the initial domain of the column. A target body load of $800\,\mathrm{N\,m^{-2}}$ (corresponding to a gravitational acceleration of $g = 10\,\mathrm{m\,s^{-2}}$ and a density of $\rho_0 = 80\,\mathrm{kg\,m^{-3}}$) is applied. As the load at any point in the analysis is determined by the initial

applied load and the load factor (as per (4.1)), an initial gravitational acceleration is prescribed and the problem is run until the load at the end of a load step exceeds the target body load. In an arc-length analysis, the body forces are increased by increasing the value of the gravitational acceleration. Selecting a smaller initial gravitational acceleration means that more load steps are required to reach the target load.

To study convergence, the number of elements along the height of the column (y direction) is varied between 2^2 and 2^{13} (between 4 and 8192) while a single element is used through the width of the column (x direction). As the background mesh elements are square elements, this means that the width of the column will vary based on the number of elements used along the height of the column. The MP to background mesh element ratio is also maintained throughout. The problem is run with the MP-BALM for three different initial body loads, $8\,\mathrm{N\,m^{-2}}$, $4\,\mathrm{N\,m^{-2}}$ and $2\,\mathrm{N\,m^{-2}}$ which results in the simulations running over 17, 33 and 67 load steps respectively.

The analytical solution for the normal stress in the y direction at the end of the analysis is

$$\sigma^a_{yy}(Y) = \rho_0 g_n (L_0 - Y) \tag{4.26}$$

where Y is the original vertical position of the point in the body, L_0 is the initial height of the column and g_n is the gravitational acceleration due to the load factor at the end of the simulation. Figure 4.4 shows the numerical results for the column under self weight using a mesh of 2^6 elements and an initial body load of $2\,\mathrm{N\,m^{-2}}$ where the calculated vertical stress is plotted against the original vertical position of each MP. The solid line in Figure 4.4 is the analytical solution in (4.26).

The error between the numerical stress results and the analytical solution is calculated as

$$\epsilon_\sigma = \sum_{\forall p} \frac{\|\sigma^p_{yy} - \sigma^a_{yy}(Y)\| V^0_p}{g_n \rho_0 L_0 V_0} \tag{4.27}$$

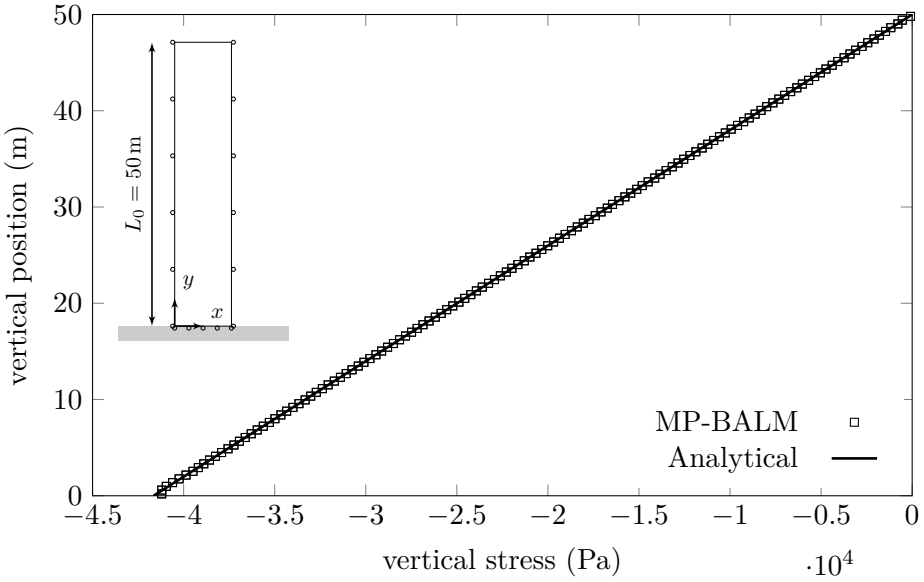

Figure 4.4: 2D column compression under self weight. Plot: numerical results of vertical stress against initial vertical position (squares) compared to the analytical solution (solid line). Inset: diagram of column compression problem showing roller boundary conditions applied over base and sides of domain.

where σ_{yy}^p is the vertical stress at each MP position, V_p^0 is the initial volume associated with the MP and $V_0 = \sum_{\forall p} V_p^0$ is the initial volume of the column. As the arc-length method will not perfectly achieve the target body load and the simulation will simply run until the body load first exceeds the target body load, each run will have a different value for g_n which needs to be taken into account when calculating the errors. For the three initial body loads used, running over 17, 33 and 67 load steps gives final g_n values of $12.9\,\mathrm{m\,s^{-2}}$, $11.7\,\mathrm{m\,s^{-2}}$ and $10.2\,\mathrm{m\,s^{-2}}$ respectively, which correspond to body loads of $1032\,\mathrm{N\,m^{-2}}$, $936\,\mathrm{N\,m^{-2}}$ and $816\,\mathrm{N\,m^{-2}}$. Figure 4.5 shows the convergence of the solution as the mesh is refined, with h being the size of the mesh elements and its inverse on the horizontal axis and the error being shown on the vertical axis. It is clear that the rates of convergence for the three MP-BALM simulations match the rate of convergence when running the same problem with a linear solver. It is also clear to see that the error value of the MP-BALM compared to the linear solver depends on the total number of load steps required to reach the target body force. This is due to the fact that the linear solver is run over 40 evenly spaced load steps whereas in

the arc-length solver, the load increment is not evenly distributed throughout the simulation. As the number of load steps used to run the simulation is increased, the convergence behaviour of the MP-BALM tends towards that of the linear solver. By looking at the final body loads, it is clear that the all MP-BALM analyses have a final body load which is greater than that of the linear solver analysis, while the error calculation for each analysis is adjusted according to the final gravitational acceleration, the larger deformations seen by the MP-BALM analyses may also be the reason that greater errors are seen.

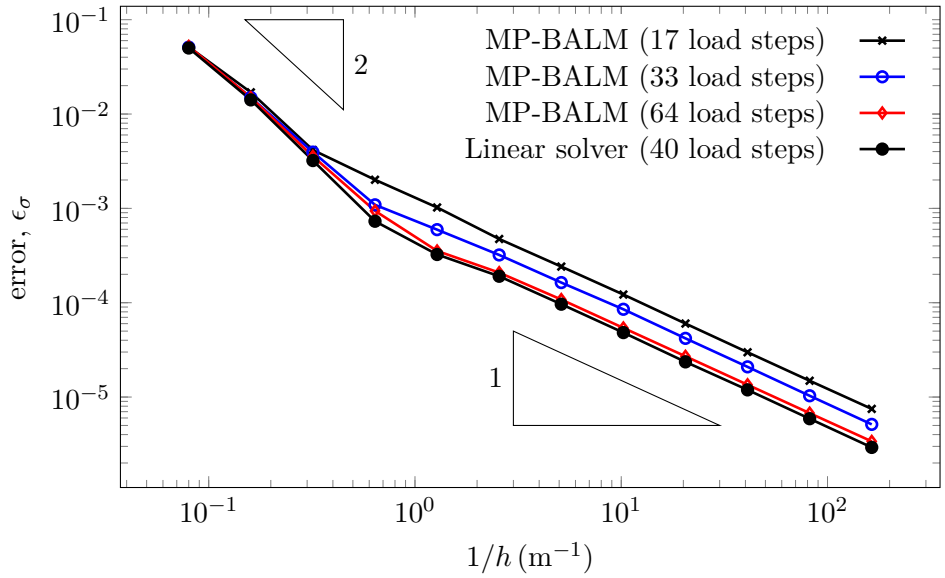

Figure 4.5: Convergence of the MP-BALM simulations of the column compression problem for various initial body loads compared to a linear solver simulation run over 40 load steps.

4.3.2 Double notched plate under tension

The next numerical example is the plane strain, elasto-plastic analysis of a deep double-edge-notched plate under tensile load to demonstrate the ability of the MP-BALM implementation to track a snap-through response. This problem was initially presented by Nagtegaal *et al.* [224]. The specimen has a overall width, $2W$, of 10 m and length, $2L$, of 30 m. Two deep notches are made along the horizontal midline of the plate creating a ligament with a width, $2B$, of 2 m. The geometry of

the plate is shown in Figure 4.6a, which also shows a pressure, P, applied along the top and bottom edges of the plate. Due to the symmetry of the problem, only one quarter of the geometry is modelled which is depicted as the grey area in Figure 4.6a. The computational setup of the problem is shown in Figure 4.6b with roller boundary conditions applied along the side of the mesh (vertical line of symmetry) where $x = 0\,\text{m}$ and the base of the mesh (horizontal line of symmetry) but only the portion of the mesh which corresponds to where the ligament of the plate is situated, $y = 0\,\text{m}$ and $x \leq 1\,\text{m}$. The physical domain is discretised using 2×2 evenly spaced generalised interpolation MPs within each background mesh element. The background mesh is extended in the vertical and horizontal directions to allow for the deformation of the physical domain. The problem is analysed using an F-bar implementation [57] in order to reduce the effect of volumetric locking. The plate material is modelled as a Hencky material with a von Mises plastic model using a Young's modulus of $E = 206.9\,\text{GPa}$, a Poisson's ratio of $\nu = 0.29$ and a uniaxial yield stress of $\sigma_y = 0.45\,\text{GPa}$. A B-spline boundary is generated along the top edge of the physical domain by positioning weightless boundary points at regular intervals over the top edge of the plate. The number of boundary points, n_{bp}, is determined by the mesh size such that $n_{bp} = \frac{2}{h} + 1$, where h is the size of the mesh. An initial pressure of $50\,\text{MPa}$ is applied over the top edge by integrating the traction over the B-spline boundary and the simulation is run until a top edge displacement of $0.2\,\text{m}$ is achieved.

The simulation is run four times for multiple stages of mesh refinement, starting at a mesh size of $2^{-1}\,\text{m}$ and down to a mesh size of $2^{-4}\,\text{m}$, with the mesh size reducing by a factor of 2 each time. In order to maintain the same approach presented by de Souza Neto *et al.* [76], throughout each analysis, the reaction force of the nodes which are situated along the ligament of the plate (i.e. where the roller boundary conditions are applied along the bottom of the mesh) are calculated as the top edge of the plate is displaced due to the applied pressure. Letting F_R denote the total reaction force of the restrained bottom edge, the net vertical stress through the

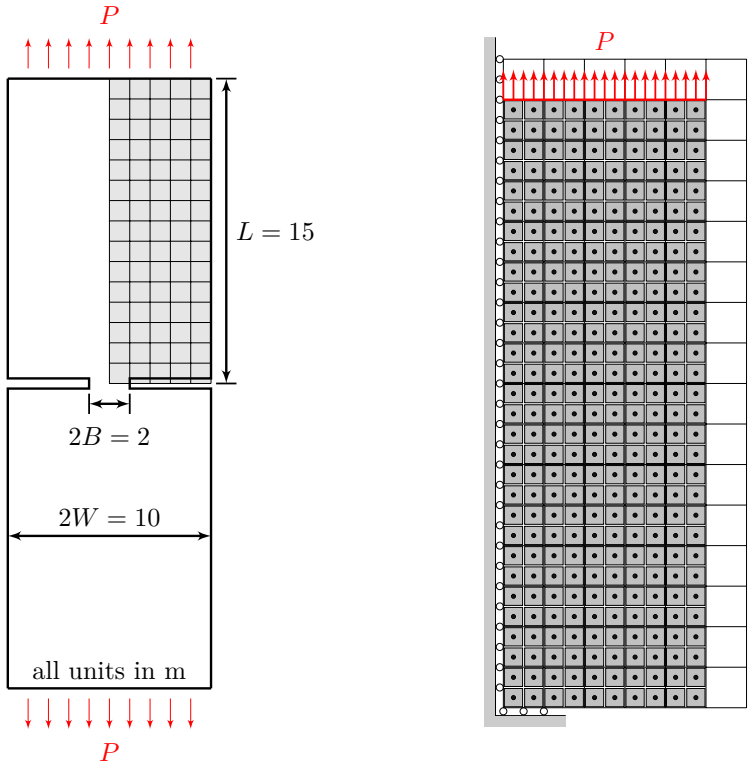

(a) (b)

Figure 4.6: Double notched plate: (a) problem geometry and (b) computational mesh and MP distribution.

ligament is given by

$$\bar{\sigma} = \frac{F_R}{B}. \tag{4.28}$$

The normalised load-displacement response for this problem is shown in Figure 4.7. The snap-through behaviour is clearly shown for all mesh sizes with varying intensities, with only a slight snap-through response seen for the coarsest mesh. Also shown in Figure 4.7 is the Prandtl limit load [224] which is the analytical small strain limit load for this problem which is controlled by the stress at the ligament in which $\sigma_{lim} \approx 2.97\sigma_y$. It is not until the mesh is refined to a size of 2^{-3} m that the load does not exceed the theoretical small strain limit load. As the mesh is refined, the effect of the large deformations of the necking of the ligament is increased and the analysis begins to predict an understiff response with a greater effect.

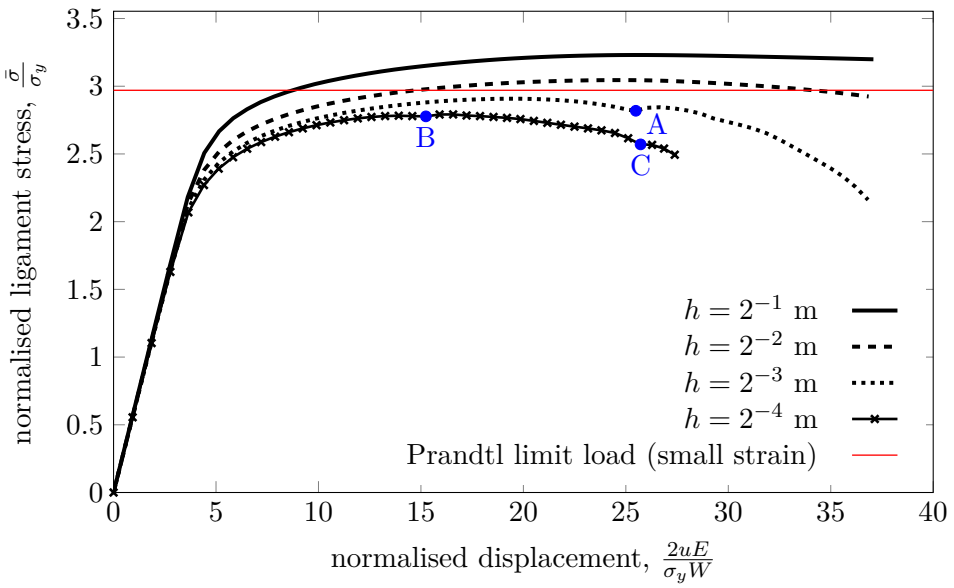

Figure 4.7: Double notched plate normalised load-displacement curves for various mesh sizes.

Due to the geometry of the problem, a singularity is formed at the end of the notch which is difficult to accurately model. As the mesh is refined, this singularity is amplified and causes the issue of MPs separating from the base. These points of separation can be seen in Figure 4.7 by the sudden change in the load-displacement response for mesh sizes 2^{-3} m (point A) and 2^{-4} m (points B and C). This is especially prominent for the mesh size of 2^{-4} m as the analysis fails at a displacement of 0.15 m. Figure 4.8 shows the MP positions for the final load step of each analysis as well as the vertical stress, σ_{yy}, at each MP. It is clear from Figures 4.8a and 4.8b that the singularity does not have much of an effect for the coarser meshes as there is a smooth change in the MPs' vertical positions moving away from the end of the ligament. In Figure 4.8c, the separation of the MPs away from the base is clear as well as the separation between the MPs around the singularity. Figure 4.8d shows the MP distribution for the end displacement of 0.15 m as this is the point where the analysis fails, it is clear that there is a large stress concentration at the end of the ligament as well as the disordering of the MPs around the singularity.

To demonstrate the need for the scaling matrix, $[\bar{N}]$, in the MP-BALM, the double

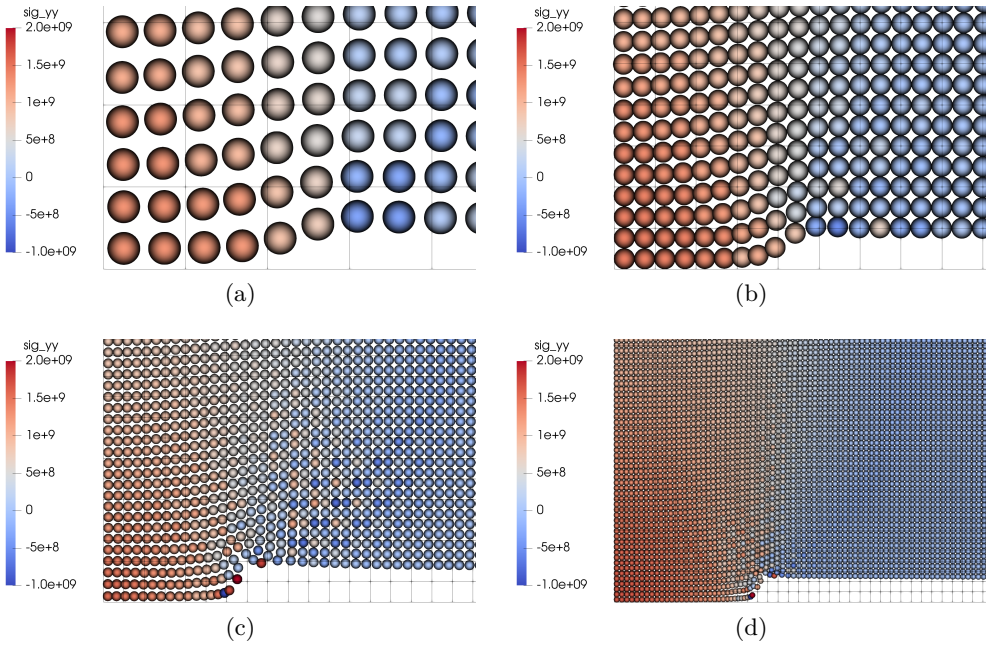

Figure 4.8: MP positions and stress distribution around the notch singularity at the end of the simulation for mesh sizes of (a) 2^{-1} m, (b) 2^{-2} m, (c) 2^{-3} m and (d) 2^{-4} m.

notched plate problem is re run with a mesh size of 2^{-1} m and an initial pressure of 10 MPa over the top edge of the physical domain. The problem is run twice, once using the traditional arc-length constraint in (4.3) where there is no scaling of the nodal displacements and once with the new approach to the arc-length constraint in (4.19), where the nodal displacements are scaled based on the influence of the nodes of the background mesh on the physical domain through the use of the $[\bar{N}]$ matrix. Figure 4.9 shows the normalised load-displacement curves for the traditional (unscaled) and new (scaled) arc-length approaches for the first 100 load steps of the analysis. It is clear that the traditional arc-length approach begins to stall at a vertical displacement of approximately 0.02 m. After this point, the progression along the equilibrium path slows such that the physical material of the plate shows only slight deformation over each load step. This is due to the fact that there are partially filled elements and large nodal displacements are calculated for nodes that only have a weak influence on the MPs. Referring to (4.3), these large nodal displacements mean that the load factor increment must be very small

in order to satisfy the arc-length constraint. On the other hand, by weighting the calculated nodal displacements based on the strength of the node's association with the physical domain, using (4.19), the effect of these large nodal displacements are mitigated. This allows the simulation to progress along the equilibrium path much further and at a more even rate that the unscaled case. For this problem, no ghost stabilisation is utilised in order to solely demonstrate the effect of the scaling matrix with the new arc-length method.

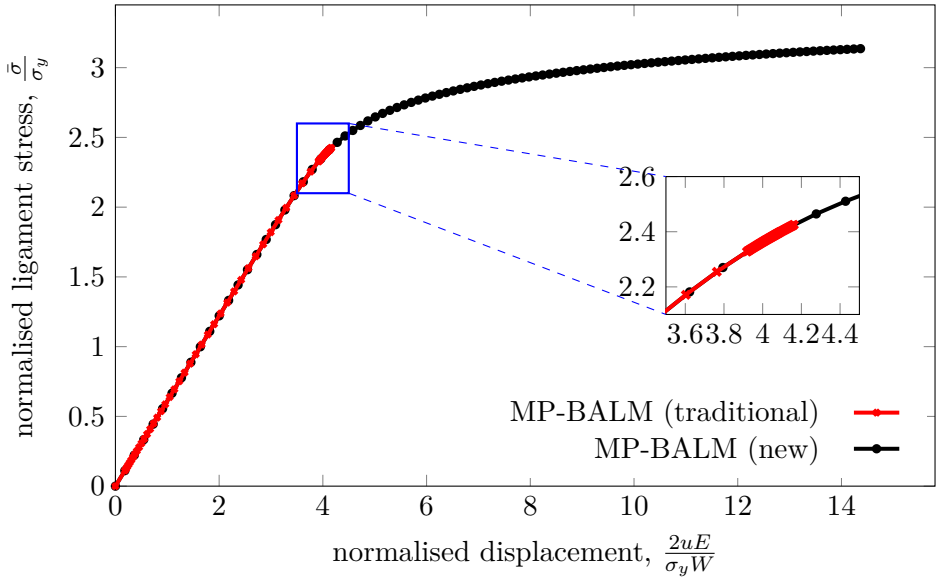

Figure 4.9: Normalised load-displacement responses over 100 load steps using the traditional (unscaled) and new (scaled) arc-length approaches.

The double notched plate problem is run for the same problem setup as above for varying mesh sizes and MP distributions. In order to improve the stability of the analyses, ghost stabilisation is used with a stabilisation parameter of $\gamma_G = 2.069\,\text{MPa}$ (5 orders of magnitude less that the Young's modulus of the material). As ghost stabilisation restricts the gradient of solution around the boundary of the domain, the solution of the unknown nodal displacements is improved and a reduction in the large nodal displacements is seen. This means that the stalling seen in Figure 4.9 is less frequent. Figure 4.10 shows the normalised top edge displacement of the double notched plate after 100 load steps to compare the traditional and new arc-length approaches for varying mesh sizes and MP

distributions. The results shown in Figure 4.10 does not represent a plot of accuracy and is not representative of the convergence of the analyses to an exact solution. By reporting the top edge displacement after 100 load steps, it is possible to see the sensitivity of the arc-length approaches to the discretisation of the problem. It is clear that the new (scaled) approach displays much less sensitivity to mesh refinement and changes in MP distribution compared to the traditional (unscaled) approach. Even when ghost stabilisation is applied which dampens the large nodal displacements, the new arc-length approach results in a more efficient analysis with further progression along the equilibrium path for all mesh sizes and MP distributions compared to the traditional approach. It is not until a mesh size of 2^{-4} m that the traditional and new arc-length approaches produce the same displacement after 100 load steps. Using the new arc-length approach produces more consistent results for the top edge displacement after 100 load steps when varying the MP distribution meaning that it is reasonable to reduce the overall number of MPs needed for the analysis compared to the traditional approach as well as having the option to increase the mesh size to reduce the overall runtime is desired.

4.3.3 Shallow arch under point load

The third numerical example is a 2D shallow arch with a plane strain assumption subjected to a point load to demonstrate the ability of the MP-BALM to track the equilibrium path of a snap-through behaviour for a problem involving large deformations. This problem is akin to the Crisfield arch [66], which was also presented by Hrinda [148]. The problem is adapted so that it can be modelled by continuum elements. A schematic of the problem geometry and mesh setup is given in Figure 4.11 in which the arch is formed with an inner length, L_i, and outer length, L_o, from the origin of 9.5 m and 10 m respectively. The height of the inner arch wall, H_i, and outer arch wall, H_o, are set as 4.09 m and 4.45 m respectively. The inner and outer radius of the curves formed by the arch are

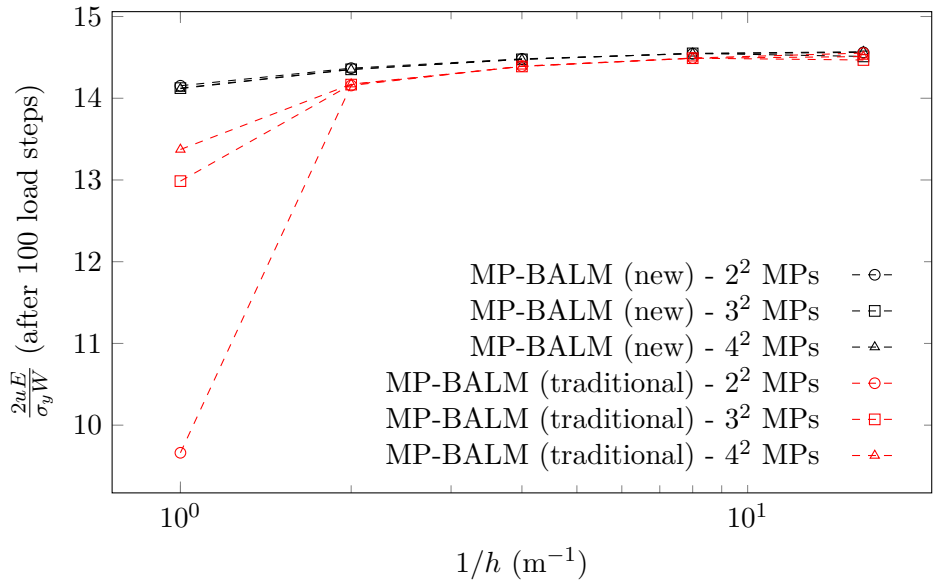

Figure 4.10: Comparison of top edge displacement after 100 load steps using the traditional (unscaled) and new (scaled) arc-length approaches for varying mesh sizes and MP distributions. All analyses have a ghost stabilisation parameter of $\gamma_G = 2.069\,\text{MPa}$ applied.

13.09 m and 13.45 m respectively. The mesh is generated such that the nodes of the mesh align with the base of the arch in order to apply the fully fixed boundary conditions to the nodes coincident with the base of the arch. The mesh is also extended below the line of the base of the arch to allow for further displacement past the initial height of the arch. The arch is modelled as a Hencky material with a Young's modulus of 100 kPa and a Poission's ratio of 0.25. To generate the initial physical domain of the arch, the background mesh is fully populated with each element containing 4×4 evenly spaced generalised interpolation MPs. The MPs which are not contained within the boundaries of the arch are discarded to leave the desired physical domain, resulting in a total of 8226 MPs used to discretise the domain of the arch. A background mesh of square elements with size $h = 2^{-3}\,\text{m}$ is used for this analysis. A ghost stabilisation parameter of $\gamma_G = 1\,\text{Pa}$ (6 orders of magnitude less that the Young's modulus of the material) is used to improve the stability of the analysis. It is worth noting that the scale factor by which the stabilisation parameter is reduced is different to that used in the previous example, there is no set rule for what value to use [55], it is however more beneficial to use

as small a value for γ_G as possible as to reduce the effect of this stabilisation on the results of the analysis.

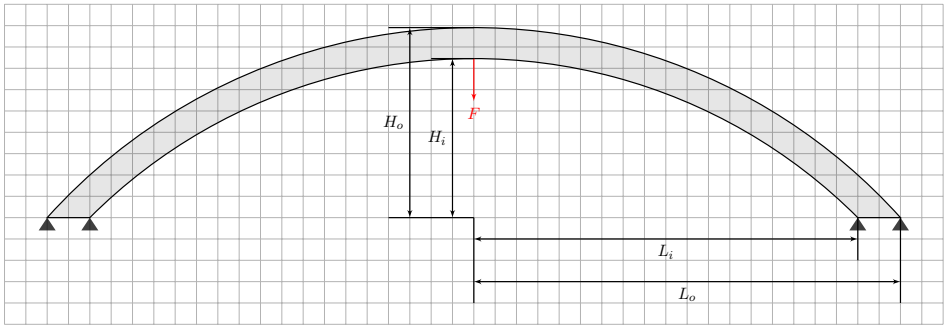

Figure 4.11: Geometry and basic mesh schematic of shallow arch problem.

An initial point load of 100 N is applied at the centre of the inner edge of the arch (indicated by the red arrow in Figure 4.11), this load is applied evenly between the bottom-most MPs in the arch, one either side of the centreline. The simulation is run until the MPs which have the load applied to them have displacement by 8.2 m, taking a total of 139 load steps to complete. Figure 4.12 shows the load-displacement response at the MPs at which the load is applied. Four stages of the analysis are highlighted along the equilibrium path, the unscaled MP deformations at each stage are shown in Figure 4.13.

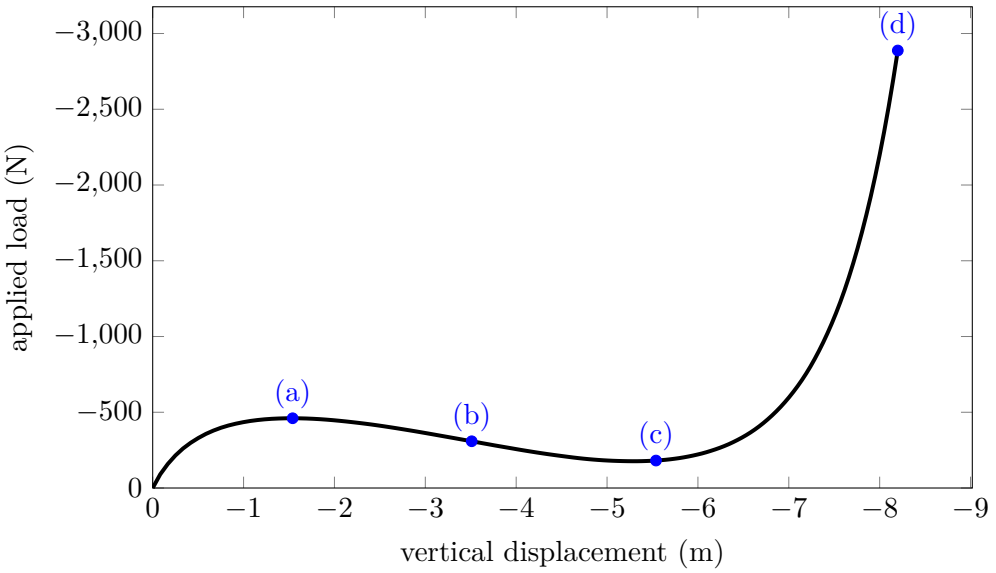

Figure 4.12: Load-displacement response of the shallow arch under applied load.

It is clear to see from Figure 4.12 that there is a clear snap-through response as the arch is pulled down and through the base of the arch. A critical point is reached at point (a) (at load step 19) where the centre of the arch has been pulled down and bulging can be seen on the left and right sides of the arch. After the critical point, the snap-through response can be observed as the material softens and deforms through point (b) (at load step 48), the arch is then pulled past the base of the arch until the next stationary point at point (c) (at load step 84). After point (c), the material begins to stiffen again as the load required to further deform the arch begins to increase until the centre of the arch has displaced through a distance of 8.2 m at point (d) (at load step 139).

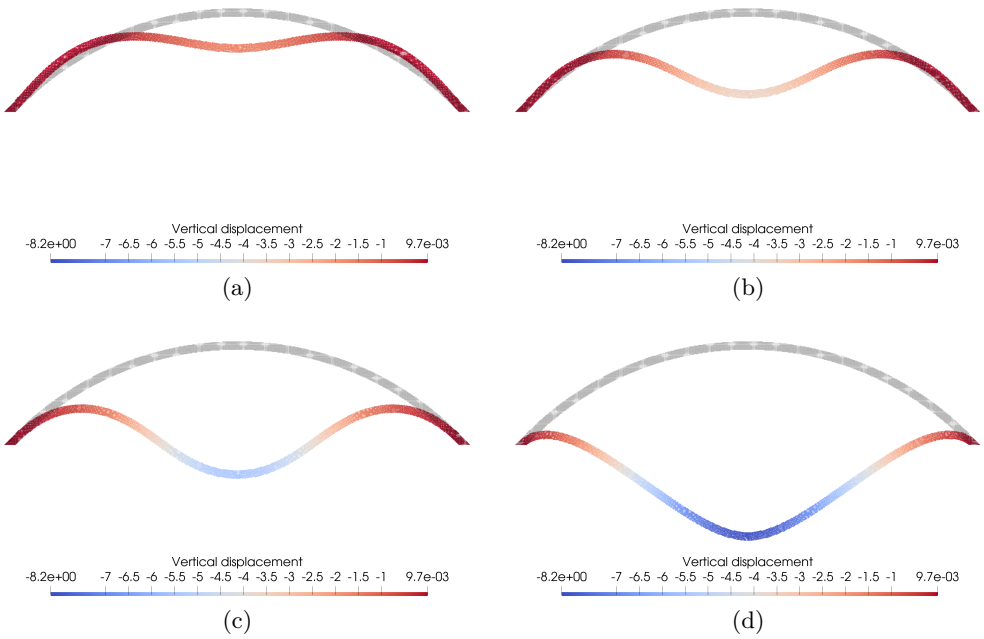

Figure 4.13: Unscaled MP deformation for shallow arch problem at stages (a) load step 19, (b) load step 48, (c) load step 84 and (d) load step 139 (see Figure 4.12 for position along equilibrium path).

4.3.4 2D elasto-plastic slope collapse

The final numerical example examines the deformation of a 45° elasto-plastic, plane strain slope collapse due to gravitational loading. The geometry of the slope is shown in Figure 4.14 where roller boundary conditions are applied over the left

edge of the domain and the bottom of the domain is fully fixed. The domain of the slope is generated by fully populating the background mesh (with a mesh size of $h = 2^{-2}$ m) with 4×4 evenly spaced generalised interpolation MPs per element and removing the MPs which are not contained within the desired area, giving a total of 16 040 MPs.

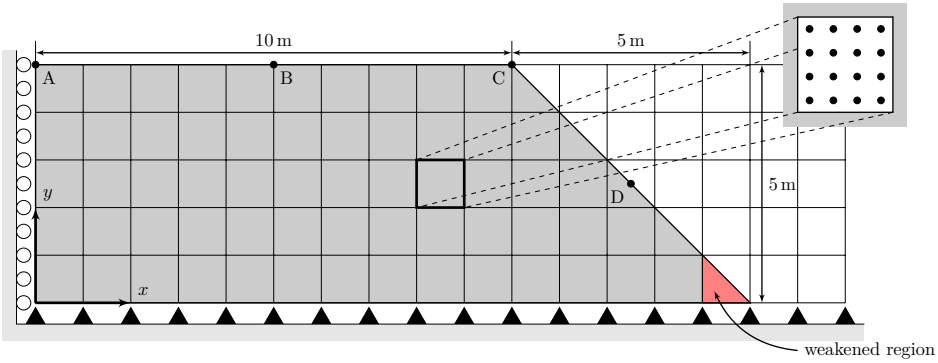

Figure 4.14: Slope geometry and boundary conditions (note that background mesh is for illustrative purposes only and does not represent the actual size of the mesh used in the analysis).

The material is represented using a von Mises yield criterion with softening behaviour with a Young's modulus of $E = 1$ MPa, a Poisson's ratio of $\nu = 0.33$ and an initial von Mises yield stress of $\sigma_y^0 = 20$ kPa. The yield function is defined as

$$f = \sqrt{3J_2} - \sigma_y(\bar{\varepsilon}^{\mathrm{p}}) = 0, \tag{4.29}$$

where $\sigma_y(\bar{\varepsilon}^{\mathrm{p}}) = \sigma_y^0 + H^{\mathrm{p}}\,\bar{\varepsilon}^{\mathrm{p}}$ is the current yield stress of the material, $\bar{\varepsilon}^{\mathrm{p}} = \sqrt{\frac{2}{3}\mathrm{tr}([\varepsilon^{\mathrm{p}}][\varepsilon^{\mathrm{p}}])}$ is the magnitude of the accumulated plastic strains, H^{p} is the plastic hardening (or softening) modulus, J_2 is the second invariant of the deviatoric stress

$$J_2 = \frac{1}{2}\mathrm{tr}([s][s]), \qquad \text{where} \qquad [s] = [\tau] - \frac{1}{3}\mathrm{tr}([\tau]) \tag{4.30}$$

and $[\tau]$ is the Kirchhoff stress. A strain softening modulus of $H^{\mathrm{p}} = -50$ kPa* is used and a minimum von Mises yield stress of 13.3 kPa is set (the initial yield stress reduced by a factor of 1.5). A weaker region ($x \in [14.5, 15]$ m) at the toe of the slope is introduced, as shown by the red area in Figure 4.14, where the initial yield

*A negative H^{p} value represents a softening behaviour.

stress is reduced to $\sigma_y^0 = 18\,\text{kPa}$. The material has a uniform initial density of $2400\,\text{kg}\,\text{m}^{-3}$. It is worth noting that this problem is provided for the purpose of demonstrating the MP-BALM and is not representative of any real-life slope due to only using the J_2 yield criterion as the basis of the material failure behaviour.

The problem is run with both load control and the MP-BALM schemes with gravitational loading of $g = 9.81\,\text{m}\,\text{s}^{-2}$. For both cases, the deformation of four positions on the slope are tracked through the analysis, the points A $= (0, 5)\,\text{m}$, B $= (5, 5)\,\text{m}$, C $= (10, 5)\,\text{m}$ and D $= (12.5, 2.5)\,\text{m}$ are shown in Figure 4.14. Ghost stabilisation is utilised for both cases with a ghost stabilisation parameter set to $\gamma_G = 1\,\text{Pa}$ (6 orders of magnitude less than the Young's modulus of the material). The problem is analysed using an F-bar implementation in order to reduce the effect of volumetric locking.

For the load controlled scheme, the gravitational load is applied over 160 equal load steps and the problem is run until convergence over a load step is not achieved after 10 N-R iterations. This occurs after 79 load steps with no convergence seen in load step 80. Figure 4.15 shows the displacement magnitude of positions A, B, C and D as gravity is increasingly applied up to load step 79 and are shown as red crosses in each plot.

The problem is also run with the MP-BALM with an initial gravitational acceleration of $g_0 = \frac{9.81}{160}\,\text{m}\,\text{s}^{-2}$, which is equivalent to the initial gravitational load for the load controlled case. The analysis is run until position C sees a displacement magnitude of $0.5\,\text{m}$, a significant increase from the maximum displacement magnitude seen in the load controlled case, which fails at a position C displacement magnitude of approximately $0.19\,\text{m}$. The MP-BALM analysis took a total of 477 load steps to achieve this target displacement magnitude. The load-displacement curves of each position for the MP-BALM analysis are shown in Figure 4.15 and are depicted as solid black lines in each plot.

In terms of local deformation, it is clear that positions A and B display local

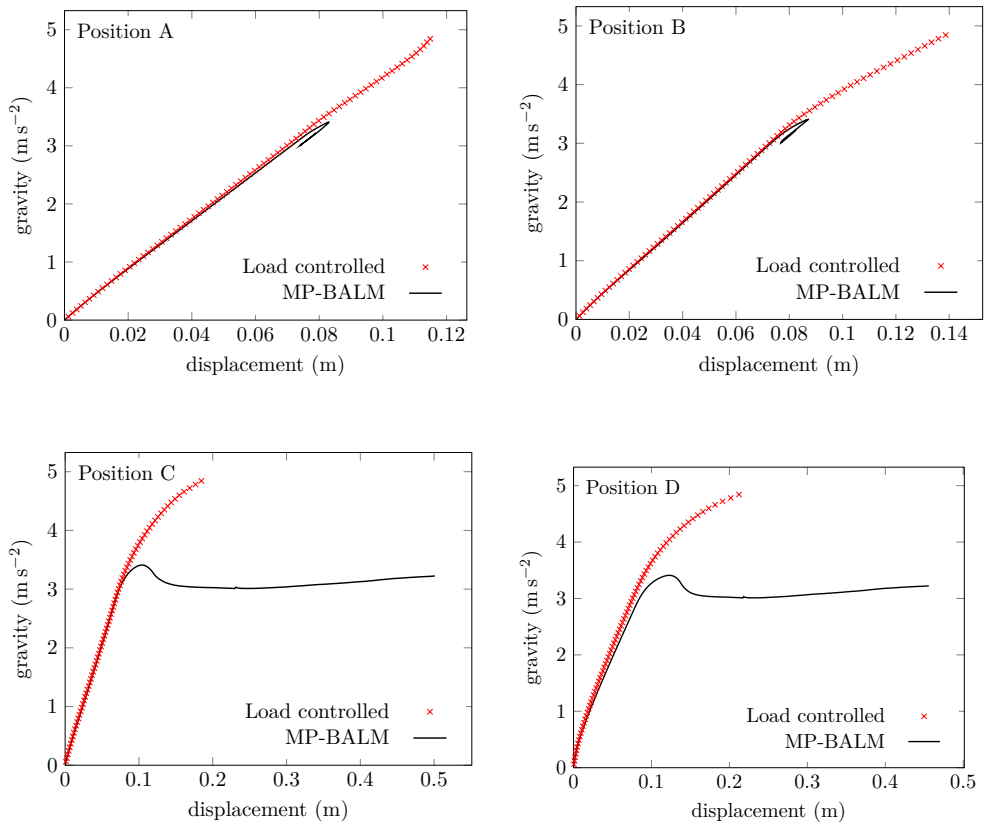

Figure 4.15: Load-displacement responses at specified positions around edge of slope domain throughout elasto-plastic collapse.

snap-back responses and positions C and D undergo snap-through responses. The difference in the load-displacement response between the arc-length and load controlled cases are stark and can be explained that at the point at which the paths begin to diverge that the material points will continue to displace with smaller increases in gravity than imposed by the load controlled case. Implicit MPMs satisfy equilibrium using the state of the MPs at the end of the current load step, where the stress carried by the MPs at their deformed positions are in equilibrium with the externally applied load. Once this equilibrium point has been found the points are then advected (displaced) through the mesh based on the incremental nodal displacements associated with the current step. However, once the MP positions are updated there is no guarantee that the stresses at the MPs are still in equilibrium with the externally applied loads; this is the case

for all MPMs, not just implicit MPMs or the implementation considered in this chapter. This can be clearly seen by considering Equation (2.42) where the body forces are transferred to the nodes using the basis functions whereas the stress in the material is transferred using the derivatives of the basis functions. Once the MPs have changed position within the element it is likely, apart from for trivial cases, that there will be a non-zero residual at the start of the next step without increasing the imposed load. This non-zero residual will lead to additional material displacement in order to satisfy (2.42) without any increase in load. Increasing the load will lead to a different equilibrium path, as seen in Figure 4.15. The use of the MP-BALM ensures that the unbounded displacements seen by the load controlled schemes are contained due to the fact that the displacements of the domain are limited within each load step, this means that the simulation is stabilised around the critical point where the unbounded displacements begin.

Figure 4.16 shows the deformed configurations of the slope collapse analysis using a load controlled scheme (left column) and the MP-BALM (right column). For each analysis the final shear stress (top) and yield stress (bottom) states are shown. It is clear from Figure 4.16 that the MP-BALM results in far greater overall displacement with a larger failure band being seen in the material and importantly at a lower load compared to the load controlled case, identifying a more critical failure mode for the slope.

Summary

This chapter has presented a new arc-length method of the MPM framework to expand the physical problems and loading scenarios that the MPM can solve, notably those involving snap-through responses. It has been shown that simply implementing the arc-length method in the MPM as it is given in the FEM approach is not suitable due to the presence of partially filled element around the boundary of a physical domain, a common feature in a MPM simulation. These partially

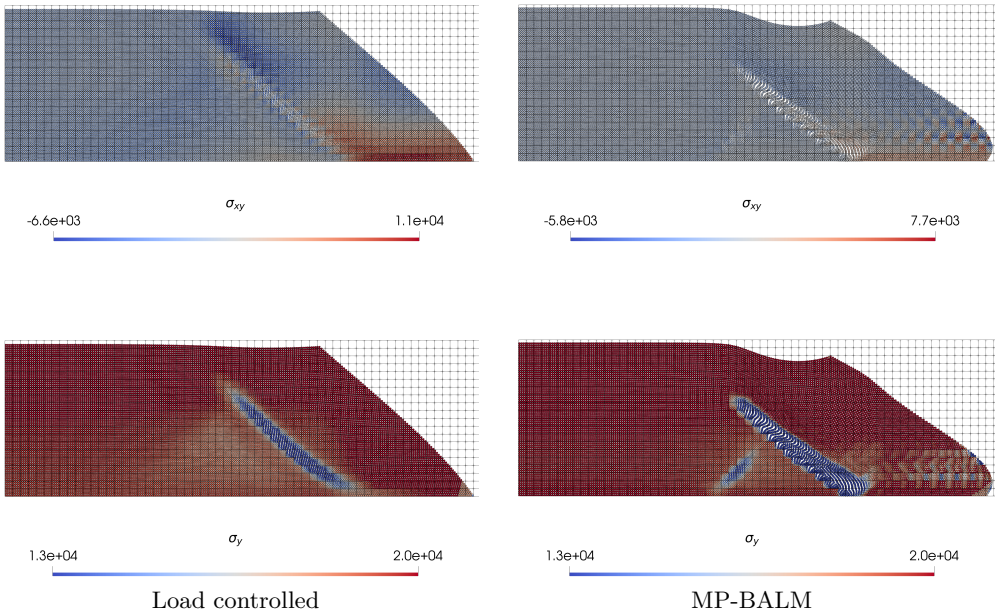

Figure 4.16: Final deformed configurations of the slope collapse problem for the load controlled analysis (left column) and MP-BALM analysis (right column). For each analysis, the shear stress (top row) and yield stress (bottom row) is shown.

filled elements will be poorly integrated, understiff and potentially experience extremely large nodal displacements. While mapping the large nodal displacements to the MP positions reduces their effect, they are prominent within the arc-length constraint as these large nodal displacements account for the majority of the allowed displacement based on the prescribed arc length. Therefore, the arc-length constraint is reformulated such that it is based on the MP displacements, scaling the nodal displacements based on the node's influence on the physical domain. The use of the secant path predictor solution requires the nodal displacements of the previous load step, however, as the MPM involves resetting the background mesh at the end of each load step and nodal displacement information is lost due to the fact that the MPs have moved positions. The nodal displacements cannot simply be carried over from the previous load step so an estimate of the nodal displacements for the previous load step based on the current MP positions is needed. This nodal displacement reconstruction is carried out at the start of each load step and uses a least squares weighted residual technique.

A simple benchmark test of a 2D column under self weight was given to show that the MP-BALM is able to model standard problems that the MPM with a linear solver has been proven to solve. More complex examples were shown to demonstrate that the MP-BALM can model problems with more complex deformation and model snap-through responses with problems of a double notched plate under tension, the deflection of a shallow arch and collapse of a slope including material softening. The double notched plate problem was analysed using the traditional (unscaled) and new (scaled) arc-length approaches and it is clear that through scaling the nodal displacement increments, a more robust and efficient analysis is achieved. The final case demonstrated the ability of the method to control the displacement response of a gravity-driven problem with unbounded deformation, typically of geotechnical slope collapse, which is not possible with conventional load controlled quasi-static methods.

In the next chapter, hyperelastic constitutive models are presented for both the isotropic and anisotropic cases. The formulation of each model will be given and numerical examples will be shown to validate each model.

Chapter 5

Constitutive Modelling

The tissue of the Left Ventricle (LV) is often modelled as a hyperelastic material [11, 109, 122, 123] (also called a Green elastic material) which is an elastic material for which the stress-strain relationship is determined from a strain-energy function [237]. It is well documented that the myocardium is not isotropic and should be modelled as an anisotropic material [63, 79, 122, 185, 269] due to the fact that the heart is made of tissue containing muscle fibres [335]. The actual structure of the heart is still not fully understood [112], both in terms of the construction of the heart tissue and the true level of anisotropy present in the myocardium. Torrent-Guasp and co-workers [300, 301] proposed that the ventricular myocardium is constructed from a band of myocardial fibres which are helically wound to form the shape of the heart. Others suggest that the ventricular walls are comprised of laminar sheets of muscle fibres, which is an approach often used in modelling [9, 145, 240]. Many examinations of ventricular tissues have been performed [183, 184, 267, 337] which concluded that ventricular myocardium is a complex structure with approximately 70% of the volume made up of layers of myocytes (the main type of muscle fibres) with the interconnections between the myocytes made of collagen fibres. Another stream of literature proposed that there are no distinguishable layers in the myocardium at all and that the ventricular tissue can simply be modelled as a continuum [118, 187, 285]. This work uses the assumption that the myocardium is composed of laminar sheets of muscle fibres that are distributed

through the thickness of the ventricular tissue based on the results of studies of LeGrice and co-workers [183, 184] which experimentally determined this.

This chapter begins with the implementation of an isotropic hyperelastic model, whilst this will not be used in the final simulations of the LV, it is used as an exercise to develop the skills of implementing a relatively simple (compared to the inclusion of anisotropic behaviour) non-linear constitutive model before moving onto the relatively more complex anisotropic model. The isotropic model is implemented in a Finite Element Analysis (FEA) code for initial validation before being implemented into the MPM framework. A separate validation test is performed for a large deformation problem with a snap-through response requiring the MP-BALM presented in the previous chapter. The formulation of an anisotropic constitutive model is then presented with the model being validated using a MPM implementation against experimental data of ventricular tissue in various simple shear problems.

5.1 Isotropic Ogden model

In 1972, Ogden proposed a method of modelling rubber-like solids using isotropic elasticity through a strain-energy function based on the principal stretches of the material, $\bar{\lambda}_i$ (for $i = 1, 2, 3$) [236]. The general form of the Ogden model strain-energy function is given by [76]

$$\Psi(\bar{\lambda}_1, \bar{\lambda}_2, \bar{\lambda}_3) = \sum_{r=1}^{N} \frac{\mu_r}{\alpha_r}(\bar{\lambda}_1^{\alpha_r} + \bar{\lambda}_2^{\alpha_r} + \bar{\lambda}_3^{\alpha_r} - 3) \tag{5.1}$$

where N is the total number of terms in the series and μ_r and α_r are the corresponding pairs of material parameters. The principal stretches can be calculated from the left Cauchy-Green strain, $[B]$, via the deformation gradient (see (2.56)). The left Cauchy-Green strain matrix can undergo eigendecomposition

such that

$$[B] = [\bar{t}][b][\bar{t}]^{-1} = \begin{bmatrix} \{\bar{t}_1\} & \{\bar{t}_2\} & \{\bar{t}_3\} \end{bmatrix} \begin{bmatrix} b_1 & 0 & 0 \\ 0 & b_2 & 0 \\ 0 & 0 & b_3 \end{bmatrix} \begin{bmatrix} \{\bar{t}_1\} & \{\bar{t}_2\} & \{\bar{t}_3\} \end{bmatrix}^T \tag{5.2}$$

where b_i are the eigenvalues and $\{\bar{t}_i\}$ are the eigenvectors of $[B]$ for $i = 1, 2, 3$. Here we denote the elements of the eigenvector matrix as

$$[\bar{t}] = \begin{bmatrix} t_1 & t_4 & t_7 \\ t_2 & t_5 & t_8 \\ t_3 & t_6 & t_9 \end{bmatrix}.$$

The principal stretches are calculated as the square root of the eigenvalues of the left Cauchy-Green strain matrix such that

$$\bar{\lambda}_i = \sqrt{b_i}. \tag{5.3}$$

It is worth noting that the conventional shear modulus, μ, is related to the pairs of material parameters, where [236]

$$2\mu = \sum_{r=1}^{N} \mu_r \alpha_r. \tag{5.4}$$

The Ogden model has two special cases, the neo-Hookean model can be obtained when $N = 1$, $\mu_1 = 2C_1$ and $\alpha_1 = 2$, where C_1 is a material constant representing half the shear modulus. The Mooney-Rivlin model can be also be obtained when $N = 2$, $\mu_1 = 2C_1$, $\mu_2 = -2C_2$, $\alpha_1 = 2$ and $\alpha_2 = -2$, where C_1 and C_2 are empirically determined material constants representing contributions to the shear modulus.

This work uses the regularised, compressible formulation of the Ogden model due to the fact that myocardium is often considered a nearly incompressible material but not fully incompressible [232]. Therefore, using the regularised version of the Ogden model allows more freedom in the modelling process. The inclusion of compressibility in the material model also avoids other issues relating

to ill-conditioning of the stiffness matrix [102], spurious stress fields [292] as well as volumetric and shear locking [57, 76, 167, 168]. The strain-energy function of the regularised Ogden model can be written using the principal isochoric stretches, $\bar{\lambda}_i^*$, which are calculated from the isochoric form of the left Cauchy-Green strain such that

$$\bar{\lambda}_i^* = \frac{\bar{\lambda}_i}{J^{\frac{1}{3}}} = \frac{\bar{\lambda}_i}{(\bar{\lambda}_1\bar{\lambda}_2\bar{\lambda}_3)^{\frac{1}{3}}} \tag{5.5}$$

where J is the volume ratio. The inclusion of the volume ratio in (5.5) means that this formulation can represent a compressible material, therefore, the compressible Ogden model can be described using the strain-energy function [76]

$$\Psi^*(\bar{\lambda}_1^*, \bar{\lambda}_2^*, \bar{\lambda}_3^*, J) = \sum_{r=1}^{N} \frac{\mu_r}{\alpha_r}\left[(\bar{\lambda}_1^*)^{\alpha_r} + (\bar{\lambda}_2^*)^{\alpha_r} + (\bar{\lambda}_3^*)^{\alpha_r} - 3\right] + \frac{1}{2}K(\ln J)^2 \tag{5.6}$$

where K is the bulk modulus of the material. It will be seen in a numerical example later in this section that a nearly incompressible material model can be achieved by scaling up the value of the bulk modulus.

The principal Kirchhoff stresses, τ_i, are obtained based on the derivative of the strain-energy function with respect to the principal stretches where [76]

$$\tau_i = \bar{\lambda}_i \frac{\partial \Psi^*}{\partial \bar{\lambda}_i} = \bar{\lambda}_i \frac{\partial \Psi^*}{\partial \bar{\lambda}_i^*}\frac{\partial \bar{\lambda}_i^*}{\partial \bar{\lambda}_i}. \tag{5.7}$$

Using the chain rule with (5.7) for each principal stretch (and considering that J is also a function of the principal stretches), the principal Kirchhoff stresses are given as

$$\tau_i = \sum_{r=1}^{N} \mu_r J^{-\frac{\alpha_r}{3}}\left(\bar{\lambda}_i^{\alpha_r} - \frac{1}{3}\left(\bar{\lambda}_1^{\alpha_r} + \bar{\lambda}_2^{\alpha_r} + \bar{\lambda}_3^{\alpha_r}\right)\right) + K\ln J. \tag{5.8}$$

Once the principal Kirchhoff stresses are calculated, it is necessary to map the stresses such that the stresses align with the Cartesian axis*. This is done through a six component mapping matrix, $[Q]$, using the eigenvectors of the left Cauchy-Green

*If a Cartesian reference frame is used, which is the case in this work.

strain such that [60]

$$[Q] = \begin{bmatrix} (t_1)^2 & (t_2)^2 & (t_3)^2 & t_1t_2 & t_2t_3 & t_3t_1 \\ (t_4)^2 & (t_5)^2 & (t_6)^2 & t_4t_5 & t_5t_6 & t_6t_4 \\ (t_7)^2 & (t_8)^2 & (t_9)^2 & t_7t_8 & t_8t_9 & t_9t_7 \\ 2t_1t_4 & 2t_2t_5 & 2t_3t_6 & t_1t_5 + t_4t_2 & t_2t_6 + t_5t_3 & t_3t_4 + t_6t_1 \\ 2t_4t_7 & 2t_5t_8 & 2t_6t_9 & t_4t_8 + t_7t_5 & t_5t_9 + t_8t_6 & t_6t_7 + t_9t_4 \\ 2t_7t_1 & 2t_8t_2 & 2t_9t_3 & t_7t_2 + t_1t_8 & t_8t_3 + t_2t_9 & t_9t_1 + t_3t_7 \end{bmatrix}. \tag{5.9}$$

The Kirchhoff stress vector can be calculated as

$$\{\tau\} = [Q]^T \begin{Bmatrix} \tau_1 & \tau_2 & \tau_3 & 0 & 0 & 0 \end{Bmatrix}^T \tag{5.10}$$

which contains the Kirchhoff stresses in the coordinate frame used in the analysis. As per (2.59), it is simple to compute the Cauchy stress vector once the mapping in (5.10) is performed as the volume ratio, J, is also used in the calculation of the Kirchhoff stress. It is worth noting that for an incompressible material, $J = 1$, meaning that the Cauchy stress vector is equivalent to the Kirchhoff stress vector.

The consistent tangent matrix, $[A]$, can be expressed in a similar fashion to that seen in (2.64), however, the formulation in this case includes the derivative of the Kirchhoff stresses with respect to the left Cauchy-Green strain, $\frac{\partial[\tau]}{\partial[B]}$, such that

$$[A] = \frac{1}{J}\frac{\partial[\tau]}{\partial[B]}[B^D] - [S^D] \tag{5.11}$$

where $[B^D]$ and $[S^D]$ take the same form as presented in (2.65). Based on the strain-energy function and the fact that it is solely dependent on the principal stretches, it is clear that Kirchhoff stress matrix is a function of the left Cauchy-Green strain and in fact can be written as a function of the eigenvalues of the left Cauchy-Green strain. This means that it is possible to generate $\frac{\partial[\tau]}{\partial[B]}$ from the derivatives of the principal Kirchhoff stresses with respect to the eigenvalues of the left Cauchy-Green strains

$$\frac{\partial \tau_i}{\partial b_j} \qquad \text{for } i, j = 1, 2, 3.$$

This derivative is calculated using the chain rule, taking advantage of the link between the principal stretches and the left Cauchy-Green strain, such that

$$\begin{aligned}\frac{\partial \tau_i}{\partial b_j} &= \frac{\partial \tau_i}{\partial \bar{\lambda}_j}\frac{\partial \bar{\lambda}_j}{\partial b_j} \\ &= \sum_{r=1}^{N} \frac{\mu_r \alpha_r J^{-\frac{\alpha_r}{3}}}{6\bar{\lambda}_j^2}\left[\frac{1}{3}\left(\bar{\lambda}_1^{\alpha_r} + \bar{\lambda}_2^{\alpha_r} + \bar{\lambda}_3^{\alpha_r}\right) - \bar{\lambda}_i^{\alpha_r} - \bar{\lambda}_j^{\alpha_r} + 3\bar{\lambda}_i^{\alpha_r}\delta_{ij}\right] + \frac{K}{2\bar{\lambda}_j^2}\end{aligned} \tag{5.12}$$

which are used to assemble the derivative of the Kirchhoff stress with respect to the left Cauchy-Green strain, following the procedure of Miehe [219]. It is not as simple as assembling the derivative matrix directly from those calculated in (5.12), consideration is needed for the eigenvalues of the left Cauchy-Green strain matrix. If there are three unique eigenvalues of $[B]$, the derivative matrix is given as

$$\begin{aligned}\frac{\partial [\tau]}{\partial [B]} =& \sum_{i=1}^{3}\sum_{j=1}^{3} \frac{\partial \tau_i}{\partial b_j}\left(\{\bar{t}_i\} \otimes \{\bar{t}_i\} \otimes \{\bar{t}_j\} \otimes \{\bar{t}_j\}\right) \\ &+ \sum_{i=1}^{3}\sum_{j\neq i}^{3} \frac{1}{2}\frac{\tau_i - \tau_j}{b_i - b_j}\left(\{\bar{t}_i\} \otimes \{\bar{t}_j\} \otimes \left(\{\bar{t}_i\} \otimes \{\bar{t}_j\} + \{\bar{t}_j\} \otimes \{\bar{t}_i\}\right)\right)\end{aligned} \tag{5.13}$$

where $\otimes$ denotes the tensor product. In the case that there are two repeated eigenvalues and a third, unique eigenvalue, the closed form solution from Chadwick and Ogden [42] is utilised. The calculation to generate the derivative matrix is the same as in (5.13), however, for the repeated eigenvalues, the $\frac{\tau_i - \tau_j}{b_i - b_j}$ becomes $\frac{\partial}{\partial b_j}(\tau_i - \tau_j)$. The final case is when $[B]$ has three repeated eigenvalues, in this case, the derivative matrix is give as [76]

$$\frac{\partial [\tau]}{\partial [B]} = \left(\frac{\partial \tau_1}{\partial b_1} - \frac{\partial \tau_1}{\partial b_2}\right)[I_s] + \frac{\partial \tau_1}{\partial b_2}[I] \otimes [I] \tag{5.14}$$

where $[I]$ is the identity matrix and $[I_s]$ is the fourth order symmetric identity tensor with components calculated as

$$(I_s)_{ijkl} = \frac{1}{2}\left(\delta_{ik}\delta_{jl} + \delta_{il}\delta_{jk}\right).$$

5.1.1 Numerical examples

It is appropriate to validate this isotropic Ogden model by comparing this work's implementation of the model to results presented in previously published literature.

Before implementing the isotropic Ogden model in the MPM, the model was implemented into a large deformation FEA code. This is the first numerical example shown in this section. Once the model is validated with FEA, the Ogden model is implemented in the MPM framework and subsequently validated.

Stretching of square perforated sheet

The Ogden model is first validated using a 3D, F-bar FEA code as this is a simple means of ensuring that the implementation of the Ogden model is correct before implementing the model in the MPM. This decision was made due to the fact that most numerical examples of the Ogden model are presented with FEA results. The problem used to validate the Ogden model with FEA is that of the stretching of a perforated, square rubber sheet as presented by de Souza Neto *et al.* [76]. A diagram of the problem is shown in Figure 5.1 where the plate has an overall side length of $2L = 20\,\text{m}$ and a thickness of $T = 0.1\,\text{m}$. The circular hole is positioned at the centre of the sheet and has a diameter of $D = 6\,\text{m}$. Due to symmetry, one eighth of the plate is modelled using a mesh of 8-noded linear hexahedral elements, the computational mesh shown in red in Figure 5.1. The mesh shown is for illustrative purposes, the actual mesh is finer. The initial mesh is made up of a single element through the thickness of the plate and 10 elements along each of the radial and circumferential directions. Numerical integration is performed using Gauss quadrature with $2 \times 2 \times 2$ Gauss points per element. Roller boundary conditions are applied over the surfaces corresponding to the planes $x = 0$, $y = 0$ and $z = 0$ allowing movement of the domain in the direction tangent to the planes. A prescribed displacement, U, is applied over the top surface ($y = L$) of the mesh such that the top surface of the plate is displaced by $10\,\text{m}$ in the y direction over 40 load steps with the top surface of the plate free to deform in the x and z directions. The material of the plate is modelled using the isotropic, regularised Ogden model with material parameters

$$\alpha_1 = 2 \qquad \alpha_2 = -2$$
$$\mu_1 = 50\,\text{MPa} \quad \mu_2 = -14\,\text{MPa}$$

which corresponds to the reduction of the Ogden model into the Mooney-Rivlin model, as previously mentioned. Using (5.4), these material parameters equate to a shear modulus of $\mu = 64\,\text{MPa}$. The presentation of this problem by de Souza Neto *et al.* [76] uses the incompressible, plane stress Ogden model, however, this work uses the compressible formulation of the Ogden model meaning that a bulk modulus must be specified. Therefore, a estimate of the bulk modulus of rubber was taken to be 1.5 GPa [12].

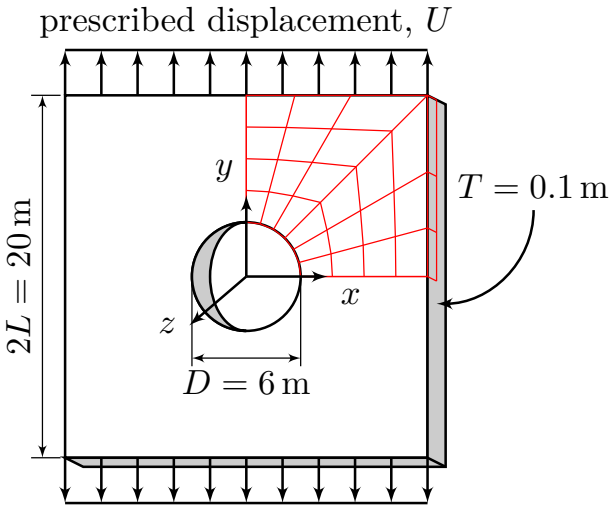

Figure 5.1: Initial geometry and computational mesh of the perforated rubber sheet. Reproduced from de Souza Neto *et al.* [76].

The end reaction load over the top surface of the plate is calculated by summing the vertical reaction forces of the nodes over the top surface. Figure 5.2 shows the end reaction force of the plate as the top surface is displaced, plotted with a black line. This is also compared with the results of de Souza Neto *et al.* [76] (plotted with a red line), which were validated compared to the numerical results of Parisch [244] and Oden [235]. It is clear from Figure 5.2 that there is a large difference between the results from this work and those presented by de Souza Neto *et al.* .

In order to determine the effect of the compressibility, the problem is run for eight different values for the bulk modulus, starting at 1.5 GPa and increasing to

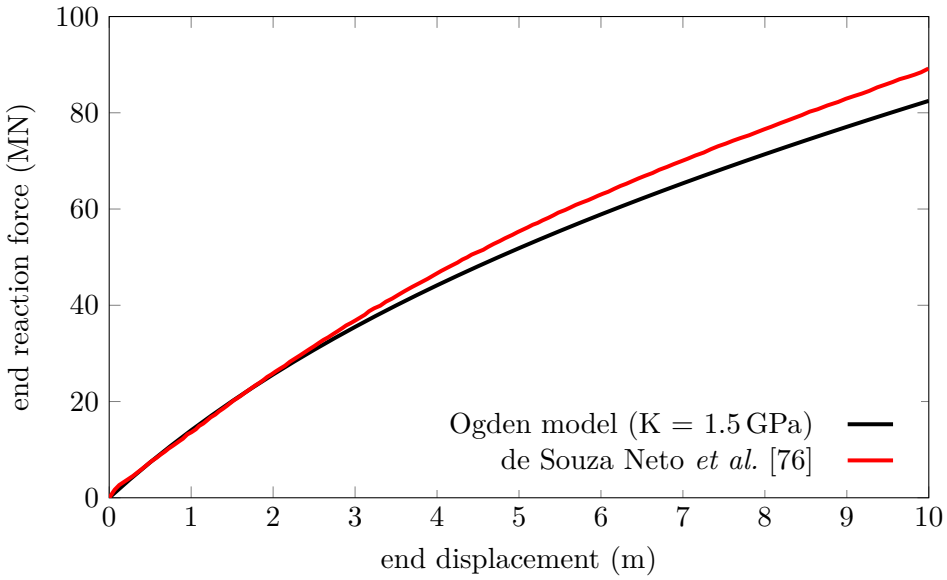

Figure 5.2: Perforated rubber sheet: end reaction force against displacement using the compressible Ogden model with a bulk modulus of 1.5 GPa (black line) compared to incompressible results from de Souza Neto *et al.* [76] (red line).

192 GPa, where the bulk modulus is increased by a factor of 2 each time. The end reaction force achieved at the end of each analysis for each bulk modulus value is shown in Figure 5.3 as well as the end reaction load presented by de Souza Neto *et al.* as the red line at the top of the plot at an end reaction force of 89.2 MN. As the bulk modulus increases, the end reaction force increases until a bulk modulus of 48 GPa. After this point, the end reaction force begins to plateau which implies that a nearly incompressible model is achieved and increasing the bulk modulus any further will not have much more of an impact on the compressibility of the material (the Poisson's ratio is already very near 0.5). This can be checked using the formula

$$\nu = \frac{3K - 2\mu}{2(3K + \mu)} \tag{5.15}$$

for various values of the bulk modulus and a shear modulus of $\mu = 64$ MPa. Table 5.1 contains the Poisson's ratios for the bulk modulus values used in Figure 5.3. As the bulk modulus increases, the Poisson's ratio tends towards a value of 0.5. When smaller bulk modulii are increased, there is a relatively large increase in Poisson's ratio compared to when the larger bulk modulii are increased. After a

bulk modulus of 48 GPa, there is only a small increase in the Poisson's ratio when the bulk modulus increases which confirms the results in Figure 5.3 as there is only a small change in the end reaction force after this point.

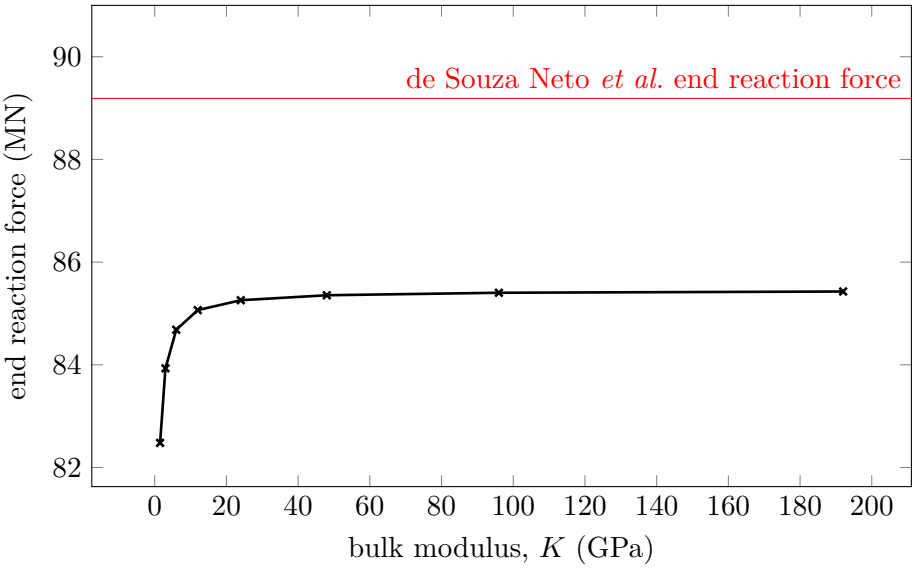

Figure 5.3: Calculated end reaction force at an end displacement of 10 m as the bulk modulus of the rubber sheet is increased compared to the end reaction force presented by de Souza Neto *et al.* [76] (red line).

Bulk modulus, K (GPa)	Poisson's ratio, ν
1.5	0.478966
3.0	0.489409
6.0	0.494686
12.0	0.497338
24.0	0.498668
48.0	0.499334
96.0	0.499667
192.0	0.499833

Table 5.1: Poisson's ratios based on bulk modulus value using a shear modulus of $\mu = 64$ MPa.

The problem is run again with the same setup as before, now using a bulk modulus of $K = 192$ GPa to model the rubber sheet as a nearly incompressible material. Figure 5.4 shows the end reaction force against displacement for the nearly incompressible case, shown as the blue, dashed line. For comparison, the compressible case results (black line) and the de Souza Neto *et al.* results (red line) are also shown. It is clear to see that the nearly incompressible case produces

results closer to the de Souza neto *et al.* results compared to the compressible case, however, there is still a discrepancy in the results. The difference in results between this work and those seen by de Souza Neto *et al.* will be due to the different types of meshes used, this work uses 100 8-noded hexahedral elements with de Souza Neto *et al.* using 528 3-noded triangular elements. The combination of different shaped elements and the difference in how fine the meshes are will also contribute to the difference in final end reaction force. It is also worth noting that, for this problem, a reduction in force will be seen with mesh refinement, which may close the gap between the two results with enough mesh refinement.

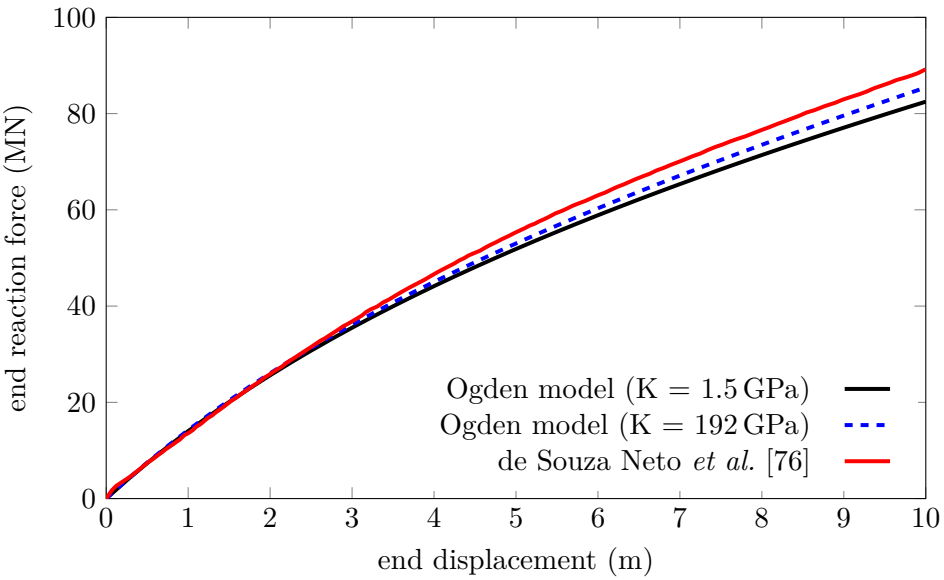

Figure 5.4: Perforated rubber sheet: end reaction force against displacement using the compressible Ogden model with a bulk modulus of 1.5 GPa (black line) and a bulk modulus of 192 GPa (dashed, blue line) compared to incompressible results from de Souza Neto *et al.* [76] (red line).

A convergence study is performed by maintaining a single element through the thickness of the plate and increasing the number of elements in the radial and circumferential directions by a factor of 2 for each stage of mesh refinement. Figure 5.5 shows the end reaction force for a displacement of 10 m as the mesh is refined. The problem is run with a bulk modulus of 1.5 GPa to ensure that no locking occurs with the finer meshes caused by the near incompressibility. As expected, the end reaction forces converges to a solution from above when a displacement is

prescribed as the problem is becoming less stiff as the mesh is refined.

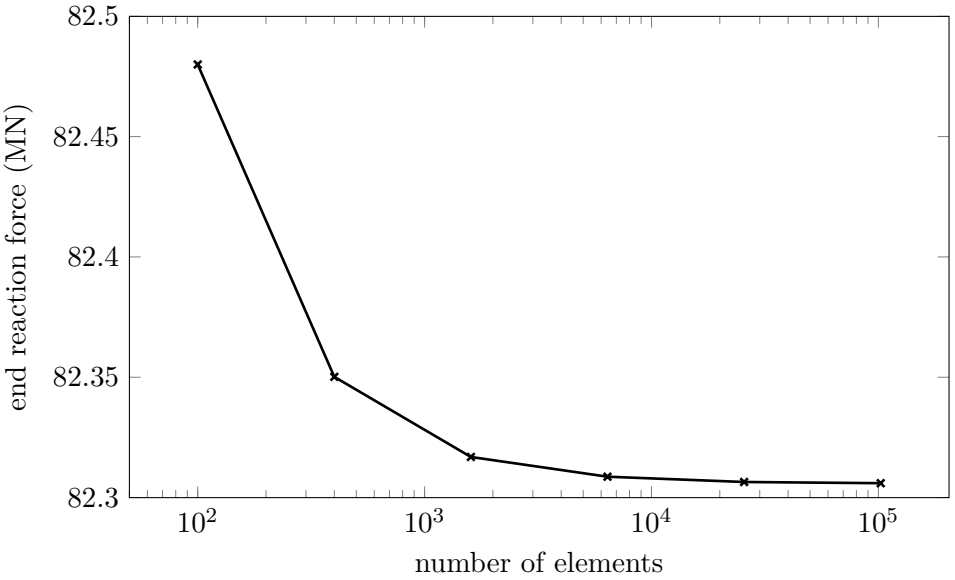

Figure 5.5: Convergence of numerical end reaction force through mesh refinement for various bulk modulus values.

For completeness, the perforated sheet problem is run using the isotropic, compressible Ogden model and a compressible neo-Hookean model to compare the results. The strain-energy function of the neo-Hookean material model is

$$\Psi(I_1) = \frac{\mu}{2}(I_1 - 3) \tag{5.16}$$

where I_1 is the first invariant of the left Cauchy-Green strain (the trace of $[B]$). The problem geometry is the same as before but the material is modelled with different material parameters. Both models are run with a bulk modulus of $K = 1.5\,\text{GPa}$ and a shear modulus of $\mu = 100\,\text{kPa}$. This corresponds to Ogden material parameters of $\mu_1 = 100\,\text{kPa}$ and $\alpha_1 = 2$. The problem is run over 40 load steps as before and the end reaction force as the top edge of the rubber sheet is displaced is shown in Figure 5.6, the results of the Ogden model are plotted as a black line while the results of the neo-Hookean model are shown as red circles. Both models produce near-identical results, with the end reaction force calculated at each load step within 1×10^{-9} of each other.

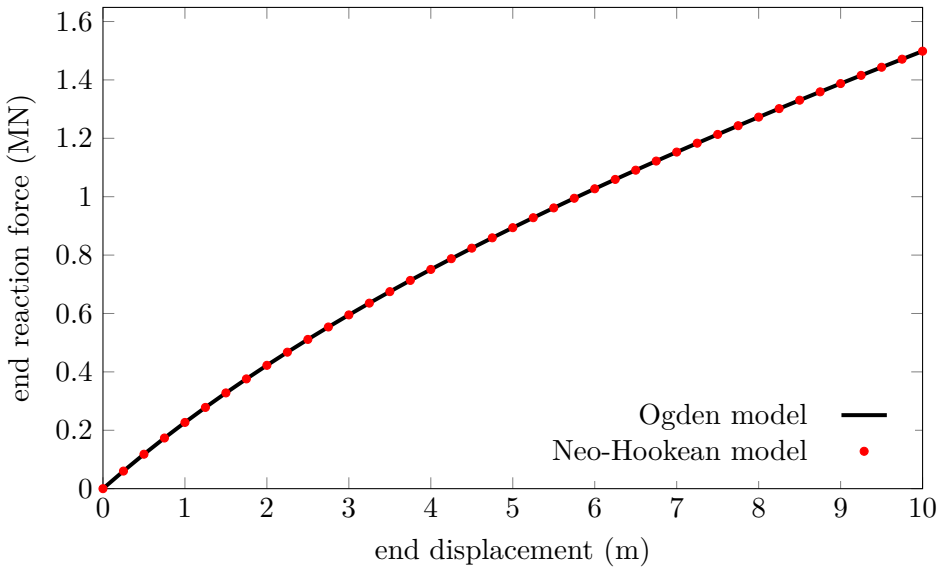

Figure 5.6: Comparison of numerical results using the isotropic Ogden model (black line) with a neo-Hookean model (red circles) using equivalent material parameters.

2D cylinder under internal pressure

The next example is that of a 2D incompressible, hyperelastic cylinder under internal pressure. The cylinder has an inner radius $R_i = 1\,\text{m}$ with the outer radius, R_o, set such that the ratio $\frac{R_i}{R_o} = 0.85$. The material parameters are defined as [136]

$$\alpha_1 = 1.3 \qquad \alpha_2 = 5.0 \qquad \alpha_3 = -2.0$$
$$\mu_1^* = 1.491 \quad \mu_2^* = 0.003 \quad \mu_3^* = -0.023$$

where $\mu_i^* = \frac{\mu_i}{\mu}$ and μ is the shear modulus of the material. The shear modulus is chosen arbitrarily as 0.375 MPa, which is the equivalent shear modulus based on a Young's modulus of 1 MPa and a Poisson's ratio of 0.3. It is worth noting that due to the fact the cylinder is incompressible, it is assumed that $J \approx 1$, however, this is not strictly enforced, therefore, incompressibility is ensured through a suitably large value for the bulk modulus. For this example, the bulk modulus is set as $K = 99.8\,\text{MPa}$. This value is two orders of magnitude higher than the bulk modulus calculated using the relation between the bulk modulus, Young's modulus

and Poisson's ratio

$$K = \frac{E}{3(1-2\nu)}. \tag{5.17}$$

Based on the results from Figure 5.3, it would seem that the scaling the bulk modulus up by two orders of magnitude would ensure that a nearly incompressible material behaviour is obtained. In fact, it was found to that this bulk modulus is close to the upper limit that the bulk modulus can be, when the problem is run using a bulk modulus of 100 MPa, the analysis fails. The author believes that this is due to the large difference between the bulk modulus value and the other material parameters, this was discovered in the initial implementation stage of the Ogden model. As the ratio of the bulk modulus to the shear modulus is increased, the level of near incompressibility also increases, meaning that the stiffness matrix becomes further ill-conditioned, resulting in such instability in the analysis that it fails.

Due to symmetry, one quarter of the cylinder cross section is modelled with a plane strain assumption. A diagram of the problem is shown in Figure 5.7. The background mesh is generated with an overall width and height of 3.5 m in order to provide enough space for the domain to deform up to a final inner stretch of 3, in other words, until the deformed inner radius is three times the initial inner radius. Each element in the background mesh is a square with size $h = 0.05$ m. In order to generate the initial domain of the cylinder, the entire mesh is filled with MPs where each element contains 8×8 evenly spaced generalised interpolation MPs. It is important to ensure that there is a large number of MPs initially populating the mesh to ensure sufficient coverage over the domain to allow for good integration and avoid ill-conditioning of the stiffness matrix. The MPs which do not lie within the boundaries of the cylinder are then removed, leaving the desired physical domain made up of a total of 7722 MPs. This check is performed at the centre of the MP domain, determining whether the centre of the domain is within the boundaries of the cylinder meaning that some portions of the Generalised Interpolation Material Point (GIMP) domains may exist outside of the cylinder

boundary. Roller boundary conditions are applied over each edge of the background mesh. The problem is run using the ghost stabilisation technique [55], which was covered in Chapter 2, in order to reduce errors and improve the stability of the simulation due to partially filled background elements. The ghost stabilisation parameter is set to $\gamma_G = 1\,\text{MPa}$.

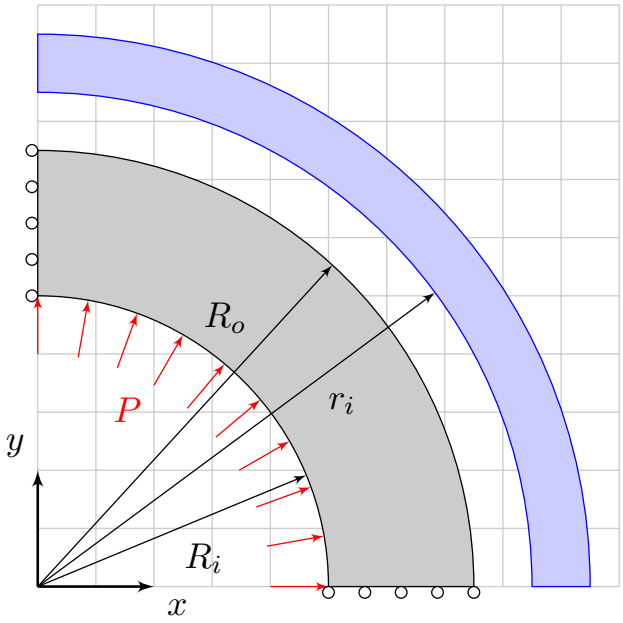

Figure 5.7: 2D hyperelastic cylinder initial and deformed diagram.

An analytical solution of the internal pressure required to inflate an incompressible hyperelastic cylinder is given as [136]

$$P = \int_{\bar{\lambda}_a}^{\bar{\lambda}_b} \frac{\hat{\Psi}_{\bar{\lambda}}\, \mathrm{d}\bar{\lambda}}{(\bar{\lambda}^2 \bar{\lambda}_z - 1)} \tag{5.18}$$

where $\hat{\Psi}(\bar{\lambda}, \bar{\lambda}_z) = \Psi(\bar{\lambda}, \bar{\lambda}_z, (\bar{\lambda}\bar{\lambda}_z)^{-1}, 1)$ and $\hat{\Psi}_{\bar{\lambda}}$ is the derivative of $\hat{\Psi}$ with respect to the stretch, $\bar{\lambda}$, and the integration is performed between the radial stretch at the inner radius, $\bar{\lambda}_a$, and the radial stretch at the outer radius, $\bar{\lambda}_b$. As the problem in question is run using the plane strain assumption, there is zero stretch in the axial (z) direction meaning $\bar{\lambda}_z = 1$ throughout the analysis. Given that the problem is run until an inner stretch of 3 is achieved, the analytical solution shows that there is a snap-through response. As mentioned in Chapter 4, this cannot be modelled using the standard load controlled scheme, therefore, the MP-BALM is used to

analyse this problem. An initial normalised pressure, $P^* = \frac{P}{\mu}$, of 5×10^{-3} is applied over the inner boundary of the cylinder using a B-spline boundary representation [24]. To anticipate the length of the boundary near to the end of the analysis, 304 boundary points were used represent the inner boundary with 5 Gauss points used to integrate the traction over each segment of the B-spline curve. These number are very high, but this is to ensure that every element cut by the boundary is accounted for in the integration at every step in the analysis. No pressure is applied over the outer radius of the cylinder. The pressure applied over the inner boundary of the cylinder evolves through the analysis as it is scaled based on the calculated load factor in each load step.

Figure 5.8 shows the calculated inner stretch against applied internal pressure (normalised with the shear modulus) for the analysis. There is a clear snap-through behaviour displayed with the maximum in pressure seen at an inner stretch of 1.9. Comparing the calculated load-displacement curve with the analytical solution calculated using (5.18), the calculated load-displacement response using the isotropic Ogden model (using the MP-BALM) matches the analytical solution very closely throughout the simulation.

At large displacements, small fluctuations can be seen in the calculated load-displacement curve, this may be due to the fact that the physical domain does not have a defined boundary in the MPM with the use of the B-spline boundary being used as an approximation for the boundary. This means that the pressure will not be applied perfectly to the true boundary of the domain. Also, at large deformations, the incompressible cylinder is stretched by a large distance and the thickness of the cylinder is reduced, potentially meaning that a small number background elements are active through the thickness of the cylinder thus the integration over the physical domain is sub-optimal, especially over the boundaries. Figure 5.9 shows the undeformed and deformed configurations of the cylinder where it can be seen that at least two background elements span the thickness of the cylinder in the undeformed configuration whereas only a single

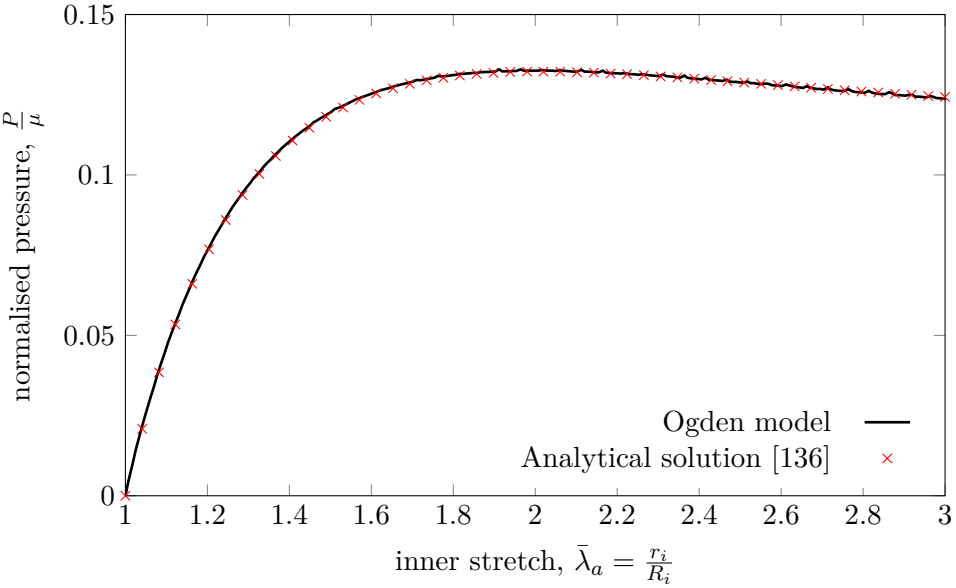

Figure 5.8: 2D hyperelastic cylinder inner stretch against normalised applied internal pressure comparing calculated results (solid black line) and analytical solution (red crosses).

element contains the full thickness of the cylinder in the deformed configuration for this problem setup.

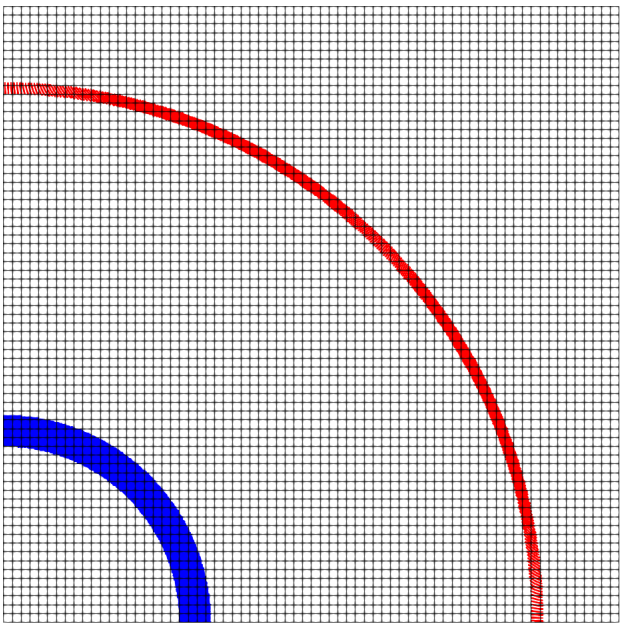

Figure 5.9: 2D hyperelastic cylinder under internal pressure in the undeformed (blue) and deformed (red) configurations.

5.2 Holzapfel-Ogden model

The implementation of the isotropic Ogden model was a good exercise on how to implement a hyperelastic model in the MPM. However, as discussed at the start of this chapter, the ventricular myocardium is in fact anisotropic due to the presence of the muscle fibres and sheets. Therefore, an anisotropic model is required, of which there are numerous. Some examples of the use of transversely isotropic models include: Humphrey and Yin [155]; Humphrey *et al.* [153]; Guccione and co-workers [122, 123]; Usyk *et al.* [305]; Quarteroni *et al.* [253]; Klepach *et al.* [174]; Costa *et al.* [62]; Taber [293] and Horgan and Saccomandi [147]. However, LeGrice *et al.* determined that myocardium is not a transversely isotropic material [184], therefore, an orthotropic material model would be more appropriate such as the models proposed by Hunter *et al.* [156], Costa *et al.* [63] and Schmid *et al.* [268] which is based on a Fung type model [103]. This work uses the structurally based model proposed by Holzapfel and Ogden [145] (referred to as the Holzapfel-Ogden (H-O) model) due to the fact that it takes into account the directions of the muscle fibres and sheets (which will vary throughout the material) using invariants found from the deformation gradient. This material model has been widely used to model ventricular tissue, see [105, 115, 221, 241, 319, 332, 347] for a small number of examples where the H-O model is used.

Throughout this section, f denotes terms associated with the fibre direction, s denotes terms associated with the sheet direction and n denotes terms associated with the normal direction to the fibre and sheet directions. This can be seen in Figure 5.10 where a cube of myocardium is shown with the fibre, sheet and normal direction aligned with the Cartesian axes. The muscle fibres are depicted as the red lines on the top of block and the muscle sheets are shown as the grey and white bands on the side of the block. For this example, it is assumed that the fibre, sheet and normal directions do not change throughout the block. This cube of myocardium will be used later in this section to validate the H-O model.

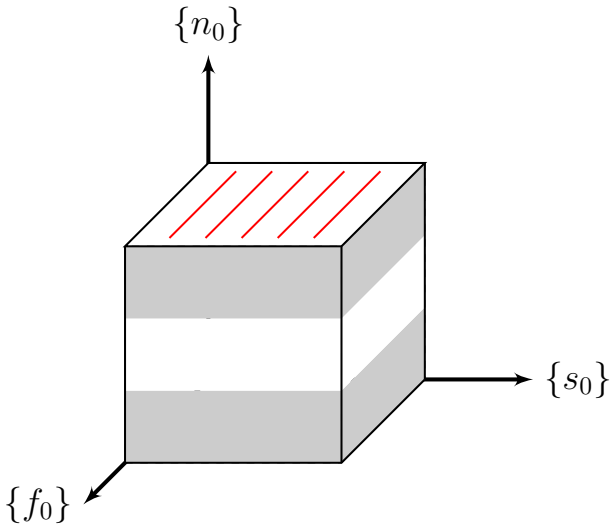

Figure 5.10: Diagram of myocardium block showing muscle fibres (red lines) and muscle sheets (grey and white bands) with the fibre, sheet and normal directions shown.

5.2.1 Invariants

Before the H-O is presented, it is necessary to cover the calculation of the required invariants. As discussed in previous chapters, the deformation gradient, $[F]$, is the description of the local kinematics of the material. The volume ratio, $J = \det([F]) > 0$, is a measure of the change in volume of the material. The left and right Cauchy-Green strain matrices, $[B]$ and $[C]$ respectively, are calculated from the deformation gradient (see (2.56)). The principal invariants (or isotropic invariants) of $[C]$ (or $[B]$) are defined by

$$I_1 = \mathrm{tr}([C])\,, \quad I_2 = \frac{1}{2}\left(I_1^2 - \mathrm{tr}([C]^2)\right) \quad \text{and} \quad I_3 = \det([C]) \tag{5.19}$$

where $I_3 = J^2 = 1$ for incompressible materials. Given that the myocardium has a muscle fibre and sheet direction, it is possible to define invariants based on the anisotropy of the material. Defining the unit vectors of the fibre and sheet directions as $\{f_0\}$ and $\{s_0\}$ respectively, the additional invariants are defined as

$$I_{4f} = \{f_0\}^T([C]\{f_0\}) \qquad \text{and} \qquad I_{4s} = \{s_0\}^T([C]\{s_0\}) \tag{5.20}$$

which are the transversely isotropic invariants. If the direction of $\{f_0\}$ or $\{s_0\}$ is reversed, the invariants in (5.20) do not change. There is a coupling invariant between the fibre and sheet invariants such that

$$I_{8fs} = \{f_0\}^T([C]\{s_0\}) = \{s_0\}^T([C]\{f_0\}). \tag{5.21}$$

It is worth noting that if the direction of either $\{f_0\}$ or $\{s_0\}$ is reversed, I_{8fs} will change sign, so it is not a true invariant. However, the formulation of the H-O model uses I_{8fs}^2 which removes this issue.

There is also a direction normal to fibre and sheet directions with a unit vector $\{n_0\}$. Similar invariants to those in (5.20) and (5.21) can be formed but are unused in this work so will not be covered.

5.2.2 Formulation

The strain-energy function of the H-O model is defined as [145]

$$\begin{aligned}\Psi(I_1, I_{4f}, I_{4s}, I_{8fs}) = \underbrace{\frac{a}{2b}e^{b(I_1-3)}}_{\text{isotropic}} + \underbrace{\sum_{i=f,s}\frac{a_i}{2b_i}\left(e^{b_i(I_{4i}-1)^2}-1\right)}_{\text{transversely isotropic}} \\ + \underbrace{\frac{a_{fs}}{2b_{fs}}\left(e^{b_{fs}I_{8fs}^2}-1\right)}_{\text{orthotropic}}\end{aligned} \tag{5.22}$$

in terms of eight non-negative material parameters a, b, a_f, b_f, a_s, b_s, a_{fs} and b_{fs} and the invariants I_1, I_{4f}, I_{4s} and I_{8fs}. The first term is the Fung-type portion used to model the isotropic component of the material. The second set of terms (the summation for the fibre and sheet terms) correspond to the transversely isotropic behaviour due to the muscle fibres and sheets. The final term corresponds to the orthotropic material behaviour due to the coupling between the muscle fibres and sheets. Given that there is no contribution of the normal direction in (5.22), it is assumed that the material behaves solely in an isotropic manner when considering the normal direction.

For a compressible material, the Kirchhoff stress can be obtained from the strain-energy function such that

$$[\tau] = J[\sigma] = [F] \sum_i \Psi_i \frac{\partial I_i}{\partial [F]} \qquad \text{for} \qquad i = 1, 4f, 4s, 8fs \tag{5.23}$$

where this section uses the notation

$$\Psi_i = \frac{\partial \Psi}{\partial I_i} \qquad \text{for} \qquad i = 1, 4f, 4s, 8fs \tag{5.24}$$

throughout description of the formulation of the H-O model. The Kirchhoff stress can be obtained for an incompressible material such that

$$[\tau] = J[\sigma] = [F] \sum_i \Psi_i \frac{\partial I_i}{\partial [F]} - \bar{p}[I] \qquad \text{for} \qquad i = 1, 4f, 4s, 8fs \tag{5.25}$$

where $\bar{p}$ is a Lagrange multiplier used to enforce the incompressibility constraint.

There does not seem to be a general consensus in published literature on the incompressibility of myocardium due to the presence of the vascular network in the ventricular wall [115], which may result in between 5% and 10% volume change during experimental testing. Based on the approach of Göktepe *et al.* [115], the Kirchhoff stress is calculated using the decoupled volumetric-isochoric formulation of finite elasticity. This begins by decomposing the deformation gradient into the volumetric, $[F_{vol}]$, and isochoric, $[F_{iso}]$, parts such that

$$[F] = [F_{iso}]\,[F_{vol}] \quad \text{where} \quad [F_{vol}] = J^{1/3}[I] \quad \text{and} \quad [F_{iso}] = J^{-1/3}[F]. \tag{5.26}$$

It is worth noting that this is a similar starting approach to the F-bar formulation in Section 2.1.5, however, the notation has been altered here to distinguish between the two applications. The isochoric components of the left and right Cauchy-Green strains, $[\bar{B}]$ and $[\bar{C}]$ respectively, are calculated as

$$[\bar{B}] = [F_{iso}][F_{iso}]^T \qquad \text{and} \qquad [\bar{C}] = [F_{iso}]^T[F_{iso}]. \tag{5.27}$$

The strain-energy function in (5.22) can be decomposed such that

$$\Psi = U(J) + \bar{\Psi}(\bar{I}_1, \bar{I}_{4f}, \bar{I}_{4s}, \bar{I}_{8fs}) \tag{5.28}$$

where $U(J)$ is the volumetric part and $\bar{\Psi}$ is the isochoric part calculated using the isochoric invariants such that

$$\begin{aligned} \bar{I}_1 = \mathrm{tr}([\bar{C}])\,,\ \bar{I}_{4f} = \{f_0\}\cdot([\bar{C}]\{f_0\}) \\ \bar{I}_{4s} = \{s_0\}\cdot([\bar{C}]\{s_0\})\,,\ \bar{I}_{8fs} = \{f_0\}\cdot([\bar{C}]\{s_0\}). \end{aligned} \tag{5.29}$$

The isochoric part of the strain-energy function is then given by

$$\begin{aligned} \bar{\Psi}(\bar{I}_1, \bar{I}_{4f}, \bar{I}_{4s}, \bar{I}_{8fs}) = \frac{a}{2b} e^{b(\bar{I}_1 - 3)} + \sum_{i=f,s} \frac{a_i}{2b_i} \left(e^{b_i(\bar{I}_{4i}-1)^2} - 1 \right) \\ + \frac{a_{fs}}{2b_{fs}} \left(e^{b_{fs}\bar{I}_{8fs}^2} - 1 \right). \end{aligned} \tag{5.30}$$

For the volumetric component of the strain-energy function, this work uses [133, 275]

$$U(J) = \frac{1}{4} K \left(J^2 - 1 - 2\log(J) \right). \tag{5.31}$$

Using the decoupled strain-energy function, the decoupled Kirchhoff stress is found using the Doyle-Ericksen formula [89]

$$[\tau] = [\tau_{vol}] + [\tau_{iso}] = J\hat{p}[I] + [\bar{\tau}] : \mathbb{P} \tag{5.32}$$

where $\hat{p} = U'(J)$, $\mathbb{P} = [I_s] - \frac{1}{3}([I] \otimes [I])$ is the isochoric projection tensor and $[\bar{\tau}]$ is given by

$$\begin{aligned} [\bar{\tau}] = 2\bar{\Psi}_1[\bar{B}] + 2\bar{\Psi}_{4f}(\{\bar{f}\} \otimes \{\bar{f}\}) + 2\bar{\Psi}_{4s}(\{\bar{s}\} \otimes \{\bar{s}\}) \\ + \bar{\Psi}_{8fs}(\{\bar{f}\} \otimes \{\bar{s}\} + \{\bar{s}\} \otimes \{\bar{f}\}) \end{aligned} \tag{5.33}$$

where $\{\bar{f}\} = [F_{iso}]\{f_0\}$, $\{\bar{s}\} = [F_{iso}]\{s_0\}$ and the scalar coefficients $\bar{\Psi}_1$, $\bar{\Psi}_{4f}$, $\bar{\Psi}_{4s}$ and $\bar{\Psi}_{8fs}$ are calculated using (5.24) using the isochoric invariants given in (5.29). Once the Kirchhoff stress is determined using (5.32), the Cauchy stress can then simply be found using (2.59).

As with the isotropic model, a tangent representing the sensitivity of the stresses with respect to the associated deformation is required, in this case, it is the spatial tangent matrix, $[A^s]$, which is computed by decoupling the volumetric and isochoric

components (as with the Kirchhoff stress above) and takes the form [115]

$$\begin{aligned}[A^s] = [A^s_{vol}] + [A^s_{iso}] =& J(\hat{p} + J\hat{k})([I] \otimes [I]) - 2J\hat{p}[I_s] \\ &+ \mathbb{P} : \left([\bar{A}^s] + \frac{2}{3}\mathrm{tr}([\bar{\tau}][I])[I_s]\right) : \mathbb{P} \\ &- \frac{2}{3}\left(\mathbb{P} : ([\bar{\tau}] \otimes [I]) + ([I] \otimes [\bar{\tau}]) : \mathbb{P}\right)\end{aligned} \tag{5.34}$$

where $\hat{k} = U''(J)$. For passive myocardium, $[\bar{A}^s]$ is based on the derivative of the isochoric Kirchhoff stress and is given by

$$\begin{aligned}[\bar{A}^s] =& 4\bar{\Psi}'_1([\bar{B}] \otimes [\bar{B}]) \\ &+ 4\bar{\Psi}'_{4f}(\{\bar{f}\} \otimes \{\bar{f}\} \otimes \{\bar{f}\} \otimes \{\bar{f}\}) + 4\bar{\Psi}'_{4s}(\{\bar{s}\} \otimes \{\bar{s}\} \otimes \{\bar{s}\} \otimes \{\bar{s}\}) \\ &+ \bar{\Psi}'_{8fs}(\{\bar{f}\} \otimes \{\bar{s}\} + \{\bar{s}\} \otimes \{\bar{f}\}) \otimes (\{\bar{f}\} \otimes \{\bar{s}\} + \{\bar{s}\} \otimes \{\bar{f}\})\end{aligned} \tag{5.35}$$

with the scalar coefficients being the second derivatives of $\bar{\Psi}$ with respect to the isochoric invariants

$$\bar{\Psi}'_1 = \frac{\partial \bar{\Psi}_1}{\partial \bar{I}_1}, \quad \bar{\Psi}'_{4f} = \frac{\partial \bar{\Psi}_{4f}}{\partial \bar{I}_{4f}}, \quad \bar{\Psi}'_{4s} = \frac{\partial \bar{\Psi}_{4s}}{\partial \bar{I}_{4s}}, \quad \bar{\Psi}'_{8fs} = \frac{\partial \bar{\Psi}_{8fs}}{\partial \bar{I}_{8fs}}. \tag{5.36}$$

For the implementation of the H-O model in the MPM formulation, it is possible to track the evolution of the orientation of the fibre, sheet and normal direction vectors through the analysis based on the local deformation of each MP. This work does not consider changing orientation, the initial fibre, sheet and normal directions are stored at the start of the analysis and are assumed to be unchanged throughout.

5.2.3 Validation

In order to validate the H-O model, the behaviour of a unit cube block of myocardium is analysed under applied simple shear. The block of myocardium can be seen in Figure 5.11 under the six different ways the block can be sheared due to the anisotropy of the myocardium. The muscle fibre direction, $\{f_0\}$, is depicted with the red lines on the block, the sheet direction, $\{s_0\}$, is depicted as the light grey and white bands on the block and the the normal direction, $\{n_0\}$, is the unit vector orthogonal to the fibre and sheet directions. The mode of each

shear is assigned a code (ij), for $i, j \in \{\text{f,s,n}\}$, based on the the shear in the ij plane and the shear applied in the j direction. For example, (fs) refers to shear in the fibre-sheet plane with the shear applied in the direction of the sheet axis.

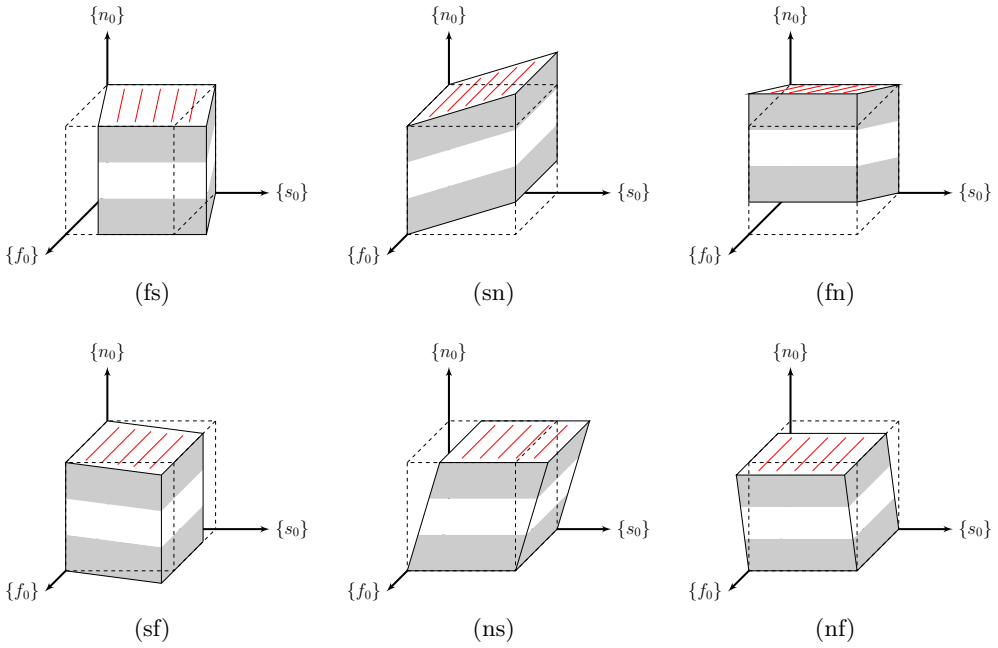

Figure 5.11: The six possible modes of simple shear applied to a myocardium black with respect to the muscle fibre axis $\{f_0\}$, sheet axis $\{s_0\}$, and normal axis $\{n_0\}$.

Holzapfel and Ogden [145] validated the proposed model using the experimental shear test results on a cube of porcine myocardium presented by Dokos *et al.* [85]. This data has also been used as a validation tool in many examples of published literature including, but by no means limited to, [115, 223, 232, 234, 268, 319]. This work will also use these experimental shear test results to validate the implementation of the H-O model. It is worth noting that due to the form of the strain-energy function in (5.22) (and subsequent representations of the strain-energy function in this section), there is no inclusion of the normal fibre direction or any coupling with this direction and the fibre or sheet directions. This means that the shear modes (ns) and (nf) are essentially the same, meaning that the results for these shear modes will be equal. This is also the case in the experimental data used to validate the problem.

This work will use the three separate sets of material parameters presented by Holzapfel and Ogden [145], Göktepe *et al.* [115] and Wang *et al.* [319] to validate the model. Each of these sets of material parameters were presented as being fit to the experimental data from Dokos *et al.* [85]. The material parameters given by Holzapfel and Ogden (referred to from this point forwards at the H-O parameters) are [145]

$$a = 0.059\,\text{kPa} \quad a_f = 18.472\,\text{kPa} \quad a_s = 2.481\,\text{kPa} \quad a_{fs} = 0.216\,\text{kPa}$$
$$b = 8.023 \qquad b_f = 16.026 \qquad b_s = 11.120 \qquad b_{fs} = 11.436.$$

Göktepe *et al.* also proposed a set of material parameter for passive myocardium (which will be referred to as G-K parameters from this point forward) with the values [115]

$$a = 0.496\,\text{kPa} \quad a_f = 15.193\,\text{kPa} \quad a_s = 3.283\,\text{kPa} \quad a_{fs} = 0.662\,\text{kPa}$$
$$b = 7.209 \qquad b_f = 20.417 \qquad b_s = 11.176 \qquad b_{fs} = 9.466.$$

The third set of material parameters used in the this work was presented by Wang *et al.* (denoted as W-W for the remainder of this work) which take the values [319]

$$a = 0.2362\,\text{kPa} \quad a_f = 20.037\,\text{kPa} \quad a_s = 3.7245\,\text{kPa} \quad a_{fs} = 0.4108\,\text{kPa}$$
$$b = 10.810 \qquad b_f = 14.154 \qquad b_s = 5.1645 \qquad b_{fs} = 11.300.$$

For all sets of material parameters, the bulk modulus, K, is set seven orders of magnitude greater than the value of the a parameter to enforce some level of near incompressibility. This scaling of the bulk modulus is considerably higher than the scale factors which were seen for the isotropic Ogden model, this may be due to the simplicity of the problems seen in this validation case. The first validation will simply calculate the shear stresses directly from the strain-energy function and no solution of a linear system is requires, therefore, there is no need to consider the conditioning of the system matrix. The second and third validation cases model the myocardium cube using the MPM, however, the mesh will be very coarse with enough MPs used to ensure a well conditioned stiffness matrix.

The first validation case does not specifically model the myocardium block, instead, the corresponding forms of the deformation gradient, $[F]$, for each shear case in Figure 5.11 is generated (see [145] for each deformation gradient) and used directly with the strain-energy function in (5.28) to calculate the Cauchy stress from (5.32). A total of 100 deformation gradients were used, ranging from zero strain to a strain of 0.5, for each shear mode. The calculated shear stresses against the applied shear strain is shown in Figure 5.12 for each shear mode and each set of material parameters. The H-O parameters are shown as a green line, the G-K parameters are shown with the red line and the W-W parameters are shown with the blue line. The experimental data from Dokos *et al.* [85] is also plotted as black circles for each shear mode. Given the sparsity of experimental data points in Figure 5.12, it is not simple to obtain a true error measure for each set of material parameters. Instead, an error estimate is calculated for each data point such that

$$\epsilon_{\sigma}^{i} = \frac{|\sigma_i^h - \sigma_i^a|}{|\sigma_i^a|} \qquad \text{for} \qquad i = 1, \ldots, n_{dp} \tag{5.37}$$

where σ_i^h is the calculated shear stress for the given level of shear of the data point and σ_i^a is the shear stress from the experimental data. The mean average error (the error estimate is summed over all data points and normalised by the number of data points) for each set of material parameters for each shear mode is given in Table 5.2. The first observation that can be made from Figure 5.12 is that the H-O material parameters do not provide any adequate fit for the (nf) and (ns) shear modes, greatly underestimating the shear stresses at all values of shear strain. In fact, the H-O parameters do not provide good fits for the majority of the shear modes, it only seems that the (fs) and (fn) modes have a near fit to the experimental data but still not as close as the other two sets of parameters. This point is backed up by the fact that the average errors for the H-O parameters for all shear modes are considerably greater than for the other two parameter sets for all shear modes. The discrepancies in the shear stress values for the H-O parameters may stem from the altered formulation of the strain-energy function with the decoupling of the volumetric and isochoric components that is present in the work by Göktepe

et al. and Wang *et al.* but not Holzapfel and Ogden. In fact, this discrepancy was shown by Wang *et al.* [319] for the (fs) shear mode but no others, the same discrepancy can be seen for the (fs) mode in this work in Figure 5.12. For this reason, the H-O parameters will no longer be considered in the validation of the H-O model, just the G-K and W-W parameters will be used. Considering the G-K and W-W parameters, the fitting of the model to the experimental data is much better with both producing similar curves for each shear mode. By eye, it appears that the W-W parameters match the experimental data slightly better than the G-K parameters but both produce reasonable results. However, it seems that across the range of shear applied to the block, the G-K parameters demonstrate a lower average error for all shear modes except the (sf) shear mode.

Shear mode	H-O error	G-K error	W-W error
(fs)	2.99×10^{-1}	1.51×10^{-1}	1.60×10^{-1}
(sf)	5.72×10^{-1}	3.57×10^{-1}	2.49×10^{-1}
(fn)	3.00×10^{-1}	1.91×10^{-1}	2.23×10^{-1}
(nf)	8.94×10^{-1}	3.42×10^{-1}	3.78×10^{-1}
(sn)	6.84×10^{-1}	3.45×10^{-1}	3.81×10^{-1}
(ns)	8.94×10^{-1}	3.42×10^{-1}	3.78×10^{-1}

Table 5.2: Average errors between shear stresses and experimental data from Dokos *et al.* [85] for H-O, G-K and W-W material parameters based on results in Figure 5.12.

The second validation case is to model the shear of the myocardium block using the MPM. The physical domain of a $1\,\mathrm{m} \times 1\,\mathrm{m} \times 1\,\mathrm{m}$ myocardium block is immersed in a $2\,\mathrm{m} \times 2\,\mathrm{m} \times 2\,\mathrm{m}$ background mesh with a mesh size of $h = 0.5\,\mathrm{m}$. The physical domain is discretised using $5 \times 5 \times 5$ evenly spaced generalised interpolation MPs within each background mesh element, any MPs which are not contained within the physical domain are removed. To reduce the effect of any volumetric locking, the F-bar implementation of the MPM is used for the analysis. Also, the ghost stabilisation technique is employed with a ghost stabilisation parameter six orders below the value of the bulk modulus, the analyses run with the G-K parameters have to a ghost stabilisation parameter of $\gamma_G = 4.96\,\mathrm{kPa}$, while the simulations using the W-W parameters have a ghost stabilisation parameter of $\gamma_G = 2.37\,\mathrm{kPa}$.

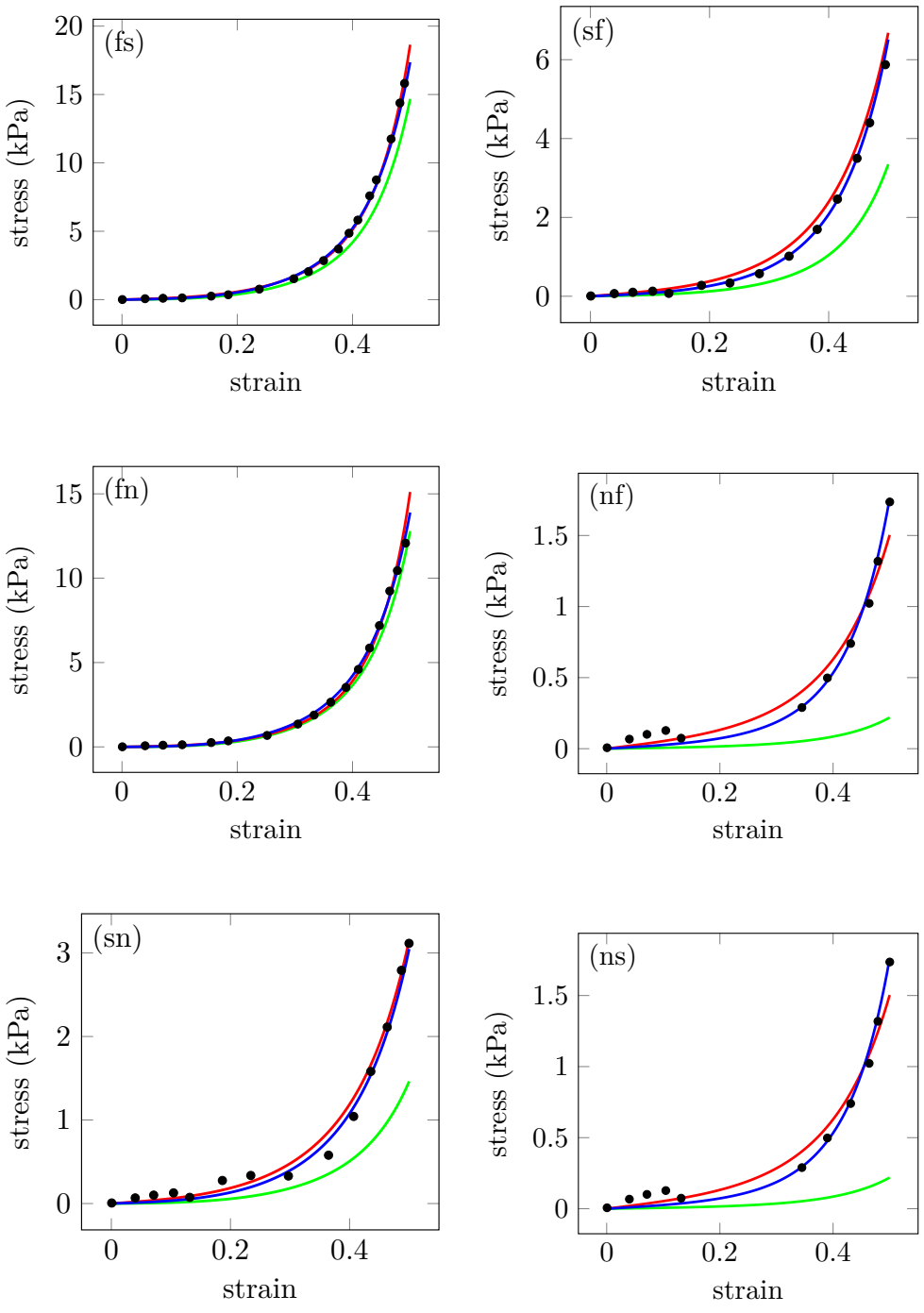

Figure 5.12: Shear stresses directly calculated from the strain-energy function (5.28) for the H-O parameters (green lines), G-K parameters (red lines) and W-W parameters (blue lines) compared to the experimental data from Dokos *et al.* [85] (black circles).

For each shear mode, a B-spline surface is generated over the corresponding plane in which the shear will be applied. For example, for the (fs) shear mode, a B-spline surface is constructed for $x = 1$, and $y, z \in [0, 1]$.* Each B-spline surface is generated using 3×3 boundary points with a traction applied in the corresponding direction over 100 equal load steps. The applied traction varies based on the shear modes, which makes logical sense due to the anisotropy of the material meaning that it will be stronger or weaker based on the direction that it is deformed. These tractions were determined empirically to provide the stress-strain plots which would cover the range of the experimental data for each shear mode, the tractions are presented in Table 5.3. Depending on the direction that the shear traction is applied, the block is constrained in all other directions and at the base of the block parallel to the plane in which the traction is applied, the block is free to move in that direction the traction is applied at any other point in the block. Using the (fs) example, the traction is applied in the y direction, therefore the fixed boundary conditions are applied in the y and z directions throughout the background mesh and fixed at $x = 0$.

Shear mode	Applied traction (kPa)
(fs)	18.64
(sf)	6.68
(fn)	15.11
(nf)	2.26
(sn)	3.15
(ns)	2.26

Table 5.3: Applied tractions over the B-spline surface boundary for each shear mode in the MPM analysis.

The shear stresses and strains calculated throughout each MPM analysis for each shear mode for the G-K and W-W material parameters are shown in Figure 5.13. As with the case when the shear stresses were calculated directly from the deformation gradient, both sets of material parameters display a very good fit with the experimental data, especially for the (fs), (sf), (fn) and (sn) shear modes. The

*This problem is set up such that the fibre direction, $\{f_0\}$, the sheet direction, $\{s_0\}$, and the normal direction, $\{n_0\}$, are aligned with the x, y and z axes respectively.

same error estimates as in (5.37) is calculated for each set of material parameters and shear modes, as before, the average errors are given in Table 5.4. It could be said that the W-W material parameters produce stress-strain results that are closer to the experimental data for all shear modes compared to the G-K parameters. The W-W does seem to match the data for the (nf) and (ns) shear modes very well considering that the normal direction does not feature in the strain-energy function. That being said, the G-K parameters produce stress-strain results for these shear modes with a lower average error value compared to the W-W parameters. This may be due to the fact that the G-K parameters predict greater shear stresses at low shear values (< 0.1) compared to the W-W parameters, giving shear stresses closer to that of the experimental data. However, the W-W parameters do produce shear behaviour much closer to the experimental data at the higher shears (> 0.3), it is not clear at this point in the thesis which range of shears will have the most effect on the LV model.

Shear mode	G-K error	W-W error
(fs)	1.48×10^{-1}	1.24×10^{-1}
(sf)	3.55×10^{-1}	2.42×10^{-1}
(fn)	1.34×10^{-1}	1.43×10^{-1}
(nf)	3.42×10^{-1}	3.75×10^{-1}
(sn)	3.43×10^{-1}	3.72×10^{-1}
(ns)	3.42×10^{-1}	3.75×10^{-1}

Table 5.4: Average errors between shear stresses and experimental data from Dokos *et al.* [85] for G-K and W-W material parameters based on results in Figure 5.13.

The final validation case still involves the MPM analysis of the myocardium block, however, rather than changing the boundary conditions of the block (ie. the surface to which the traction is applied and the direction the traction is applied), the analyses are run maintaining the B-spline boundary positioned at $x = 1$, and $y, z \in [0, 1]$ with the traction being applied in the x direction. Fixed boundary conditions are in place for $x = 0$ and for all y and z. Each shear mode is then tested by altering the fibre, sheet and normal directions to model the desired shear. Table 5.5 presents the alignments of the fibre, sheet and normal directions with the x, y

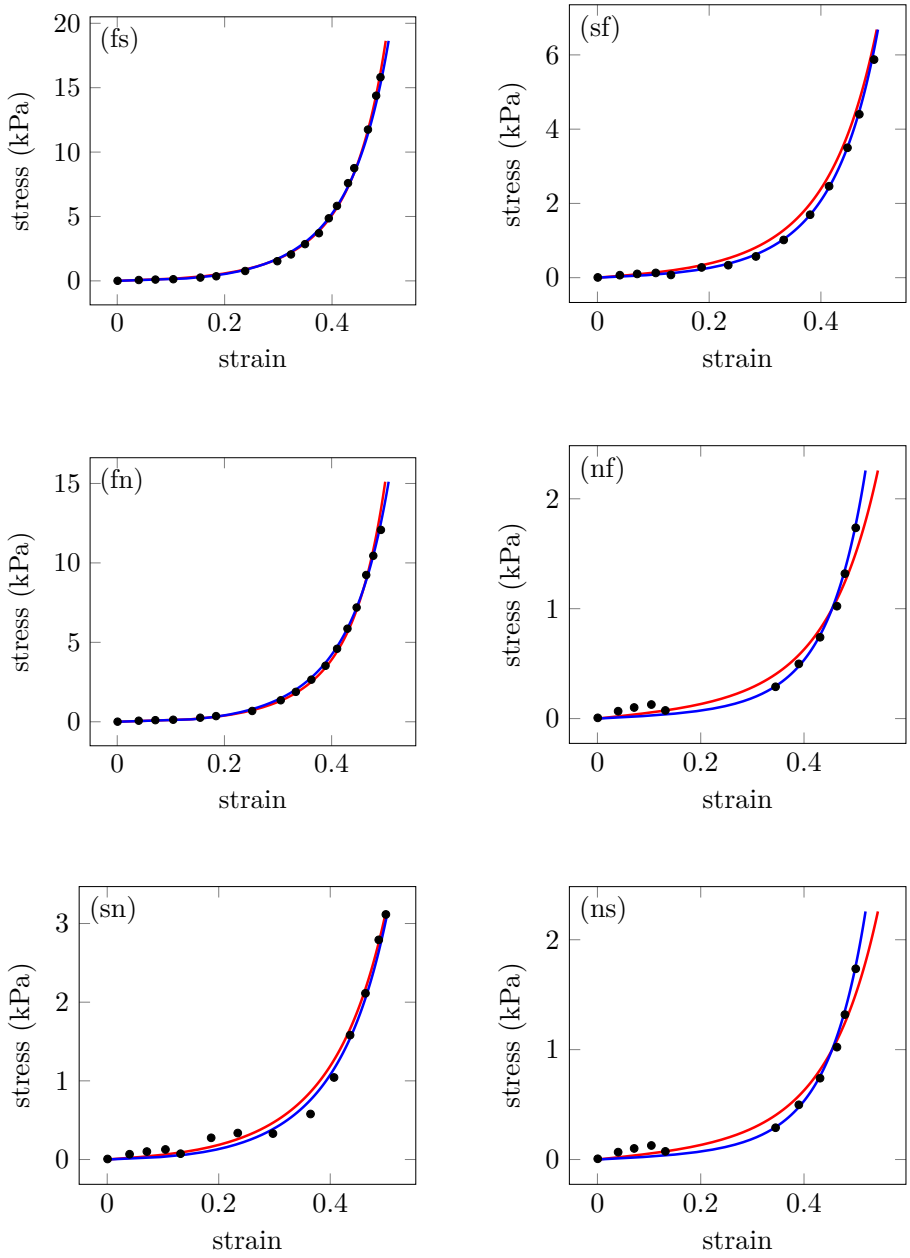

Figure 5.13: Shear stresses and strains calculated using a MPM analysis applying tractions over varying planes and directions for the G-K (red lines) and W-W (blue lines) material parameters compared to the experimental data from Dokos *et al.* [85] (black circles).

and z axes for each shear mode. Other than the change in boundary conditions and material orientation, the problem set up is the same as above with the magnitude of the tractions for each shear mode used given in Table 5.3.

Shear mode	x axis	y axis	z axis
(fs)	$\{s_0\}$	$\{f_0\}$	$\{n_0\}$
(sf)	$\{f_0\}$	$\{s_0\}$	$\{n_0\}$
(fn)	$\{n_0\}$	$\{f_0\}$	$\{s_0\}$
(nf)	$\{f_0\}$	$\{n_0\}$	$\{s_0\}$
(sn)	$\{n_0\}$	$\{s_0\}$	$\{f_0\}$
(ns)	$\{s_0\}$	$\{s_0\}$	$\{f_0\}$

Table 5.5: Orientation of fibre, sheet and normal directions aligned with the x, y and z axes when modelling shear modes through rotation of the myocardium block.

Figure 5.14 shows the calculated shear stresses against shear strains for each of the six shear modes. As expected, these results are identical to the ones shown in Figure 5.13. The average errors of the shear stresses for each set of material parameters for each shear mode compared to the experimental data is given in Table 5.6. Like the curves in Figure 5.14, these error values are identical to those in Table 5.4. This improves the confidence that the implementation of the H-O model within the MPM framework is correct and that the G-K and W-W material parameters seem to be a good fit for modelling passive myocardium.

Shear mode	G-K error	W-W error
(fs)	1.48×10^{-1}	1.24×10^{-1}
(sf)	3.55×10^{-1}	2.42×10^{-1}
(fn)	1.34×10^{-1}	1.43×10^{-1}
(nf)	3.42×10^{-1}	3.75×10^{-1}
(sn)	3.43×10^{-1}	3.72×10^{-1}
(ns)	3.42×10^{-1}	3.75×10^{-1}

Table 5.6: Average errors between shear stresses and experimental data from Dokos *et al.* [85] for G-K and W-W material parameters based on results in Figure 5.14.

Summary

Due to the fact that myocardium is modelled as a hyperelastic material, this chapter has presented two hyperelastic material models, the isotropic Ogden model and the anisotropic H-O model. The isotropic model was used as an exercise in the implementation of a non-linear material model in the MPM. The formulation was presented and the model was validated with numerical examples. Firstly with

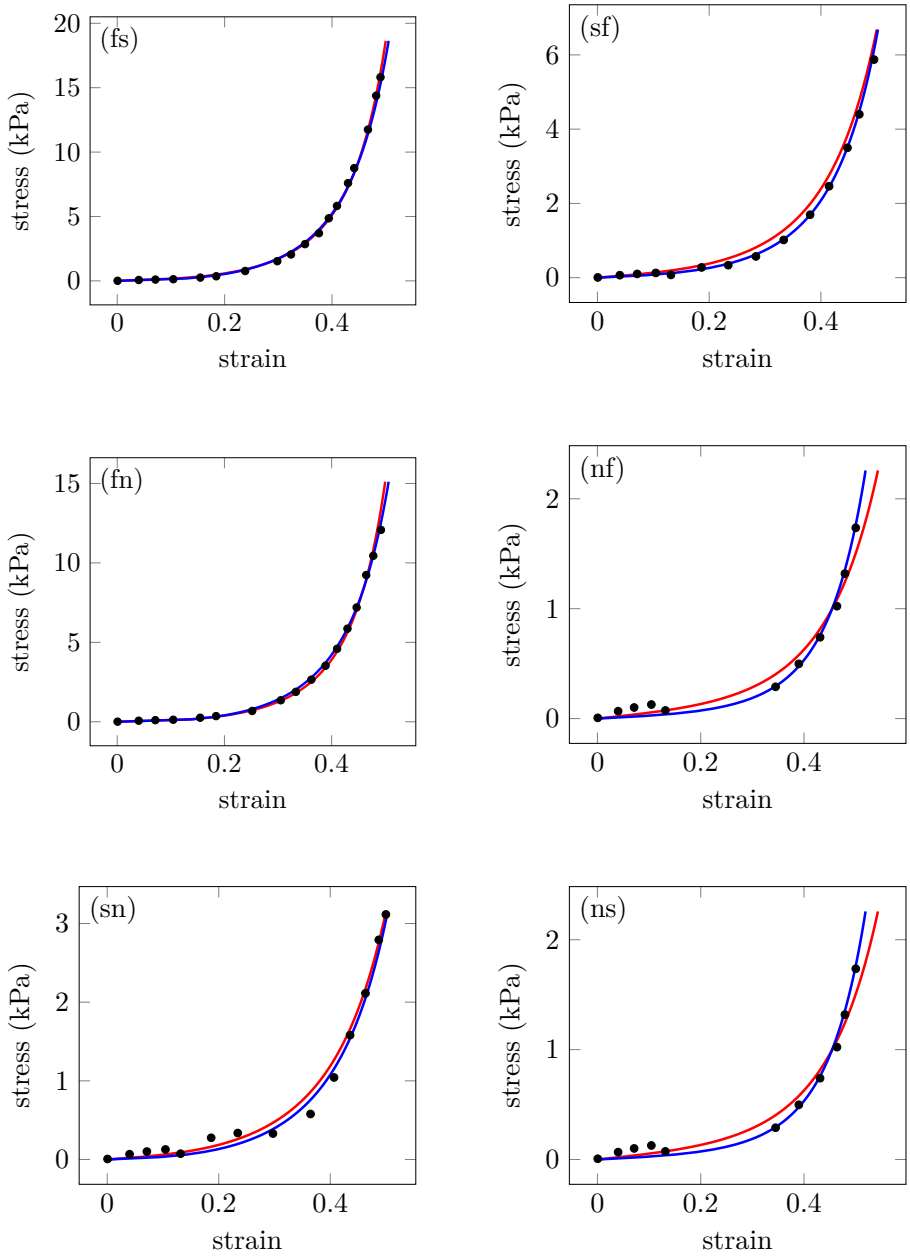

Figure 5.14: Shear stresses and strains calculated using a MPM analysis maintaining the position of the B-spline surface boundary and direction of the applied tractions and swapping the directions of the fibre, sheet and normal unit vectors. Comparing the G-K (red lines) and W-W (blue lines) material parameters to the experimental data from Dokos *et al.* [85] (black circles).

the stretching of a perforated rubber sheet using a FEA analysis. This showed the effect of the inclusion of compressibility of the material model and how it is

possible to model a nearly incompressible material by increasing the value of the bulk modulus to simulate the incompressibility of the material. The Ogden model was then validated with the MPM through the example of a cylinder under internal pressure. Due to the non-linear behaviour that this problem sees, the MP-BALM from Chapter 4 was used. The numerical results from this analysis closely matched the analytical results. Myocardium is not an isotropic material, therefore, the H-O model was chosen as the anisotropic material model for this work. The formulation of the H-O model was presented and the model was validated using experimental data of the shearing of a myocardium block. Shear stress-strain results were calculated directly from the strain-energy function as well as through MPM analyses using multiple sets of material parameters. Two sets of parameters were found to produce results which sufficiently match the experimental data, these parameters will be used for the LV models that will be analysed.

Now that all of the "tools" required to analyse a LV model have been presented, the next chapter covers the process of generating the initial MPM model of a left ventricle from the medical imaging data.

Chapter 6

Left Ventricular Modelling - Model Creation

The previous chapters have presented all of the tools needed to generate and analyse a model of a Left Ventricle (LV) using the Material Point Method (MPM):

- Chapter 2 - the MPM formulation used to analyse the model,
- Chapter 3 - B-spline boundary representations to handle non-conforming boundaries,
- Chapter 4 - the arc-length solver implemented in the MPM formulation for highly non-linear responses,
- and Chapter 5 - the anisotropic, hyperelastic H-O model to simulate the material behaviour of the LV myocardium.

The overall aim of this work is to produce a patient-specific model of the LV. The added aim is to generate the model in a manner which requires as little user input as possible. There are three main components that need to be considered for the LV model generation: the geometry, the orientation of the muscle fibre, sheet and normal directions in the myocardium and the boundary conditions which can be applied to the physical domain. The automation of the model generation is a key

feature of this work, which is possible due to the non-conforming nature of the MPM so that the physical domain can simply be immersed into a regular background mesh. Thus, the intensive meshing process that is required for Finite Element Analysis (FEA) is not needed for the MPM. Instead, a relatively simple method of generating the LV geometry can be used to populate the physical domain with MPs. This chapter begins with the generation of the geometry of the endocardial (inner) and epicardial (outer) surfaces of the LV using B-spline surfaces, based on the work in Chapter 3. The B-spline surfaces are not discarded after the initial model generation, as they are then used as the boundary representations of the endocardial and epicardial surfaces throughout the MPM analysis. The physical domain between these two surfaces is then discretised with MPs through the creation of a temporary mesh between the two surfaces used to position the MPs in the domain. The orientation of the muscle fibres and sheets are determined for each MP based on their position relative to the endocardial and epicardial surfaces. The steps of creating the B-splines and determining the orientation of each MP can be performed without any human input, which greatly improves the pre-processing time for each model. Finally, this chapter presents the boundary conditions which are applied to the physical domain throughout the analysis.

There are multiple ways to approximate the LV geometry. For example, several studies have used a prolate spheroid approximation of the shape of the LV [123, 156, 157, 304]. Alternatively, the geometry can be extracted from medical images using segmentation [54, 108, 109, 220, 232, 322]. This work employs the latter method, therefore, fulfilling the aim of making a patient-specific model of the LV. Magnetic Resonance Imaging (MRI) scans were utilised from a healthy ageing study at the Newcastle Magnetic Resonance Centre (NMRC). The data set used in this work has also been used in other medical studies, for example [41, 130, 143, 144, 162, 243]. The images were acquired using a 3.0 T Philips Intera Achieva scanner (Philips, Best, The Netherlands) where 14 images were taken in the short axis view through the longitudinal direction of the heart. Each image represents

a slice thickness of 8 mm with a 0 mm skip between slices. Each image has a resolution of 256 × 256 pixels with each pixel of the image representing an area of 1.367 19 mm × 1.367 19 mm. The images were taken over 25 phases of the cardiac cycle, from End-Diastole (ED) of one cycle to ED of the next. Each stack of patient medical images include a series of slices showing the cross section of the heart, as shown in Figure 6.1 moving longitudinally (from head to toe) through the patient. To aid in the reader's understanding of what is shown in the image in Figure 6.1, key anatomical features have been highlighted with red numbers. The part of the anatomy for each number is given in Table 6.1.

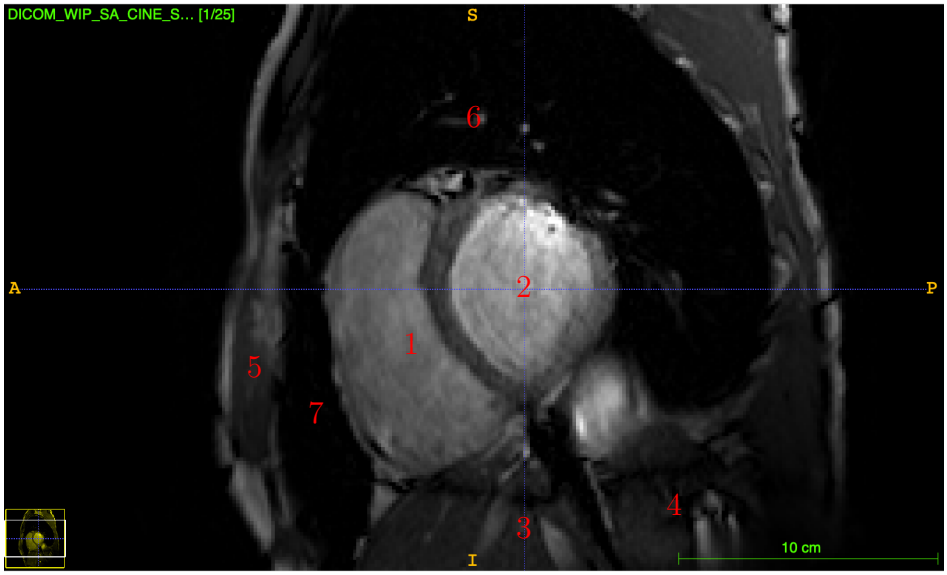

Figure 6.1: Slice of MRI image stack with key positions labelled (see Table 6.1 for labels).

Figure 6.1 label	Anatomical feature
1	right ventricle
2	left ventricle
3	liver
4	stomach
5	chest wall
6	left lung
7	right lung

Table 6.1: Key anatomical identifiers labelled in Figure 6.1.

6.1 Generation of left ventricular geometry

The first stage of generating the LV model is to create the geometry of the physical domain (the volume of the myocardium tissue that surrounds the LV cavity). This section demonstrates the process of generating a B-spline representation of the endocardial surface of the LV, from segmentation to the generation of the physical domain and the MP discretisation.

In this work, the step in the model setup which requires significant user effort is the segmentation of the stack of medical images. The process of generating the LV model geometry following segmentation has been designed to be fully automated. The inputs for the model are the segmentation data, the fitting strength parameter (see Section 3.4.2 for an explanation of the fitting strength parameter, ζ), the desired number of MPs for the model and the material properties.

6.1.1 Segmentation

For the segmentation, the stack of medical images is loaded into ITK-Snap* [340] to analyse each slice as seen in Figure 6.2a. This work focusses on the ED stage of the cardiac cycle. Therefore, the stack of images were segmented where the LV appears to be at its largest volume. The segmentation of the endocardial surface for a single slice of the stack of medical images is shown in Figure 6.2b, where the red patch is the segmented area.

Each image slice is an image made up of 256×256 pixels, therefore, for each segmented slice, a mask is generated where each pixel of the slice image is assigned a value based on the its position relative to the segmented area in Figure 6.2b. If the pixel is outside of the red area, then the pixel is assigned a value of 0, conversely, if the pixel is situated in the red area, it takes a value of 1. The mask of the segmentation in Figure 6.2b is shown in Figure 6.3a where the black area

*ITK-Snap is an open-source software which can be used to segment 3D and 4D medical images.

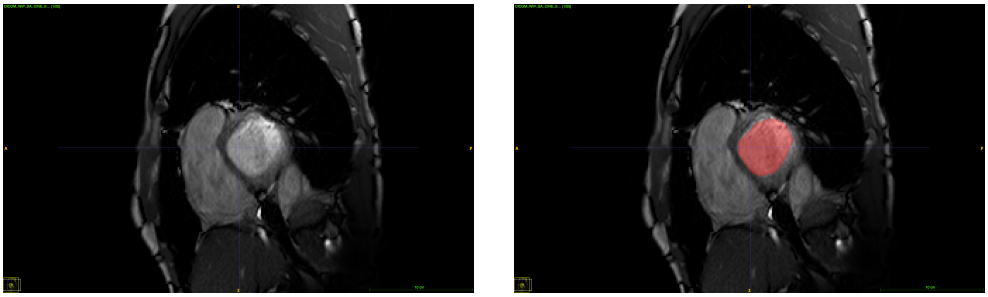

(a) (b)

Figure 6.2: Single slice of patient MRI scan (a) unsegmented slice (b) segmented slice of the endocardial surface shown in red.

represents a 0 value and the white area has a value of 1 (the segmented area). The outline of the mask is then determined (shown as the red points in Figure 6.3b) to generate a set of data points for the slice. As the slices are taken through the longitudinal direction of the heart, a z coordinate can be assigned based on the index of the slice and the slice thickness of the imaging procedure (in this case it is 8 mm per slice with 0 mm skip between slices). It is assumed that there is no movement of the patient as the images were taken as no corrections will be made to the global positions of the slice data points to account for any patient movement.

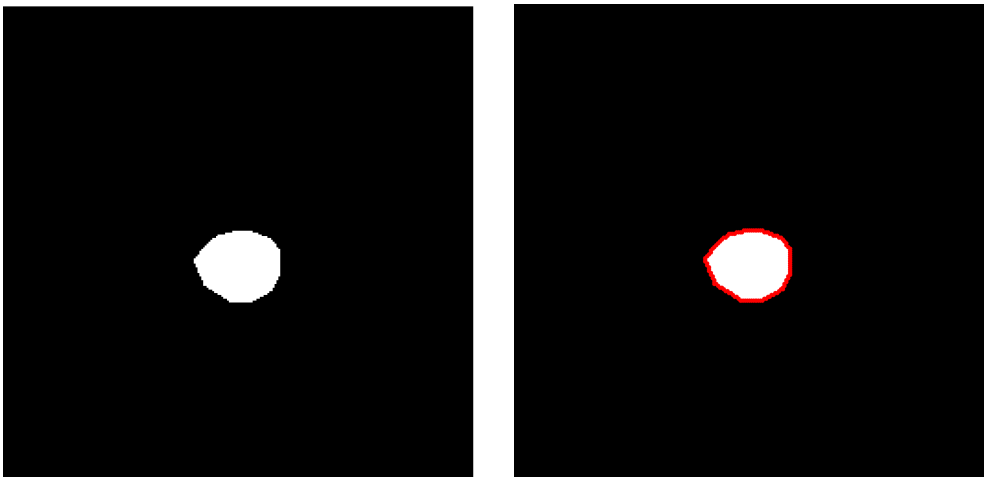

(a) (b)

Figure 6.3: Output of segmentation of a slice of the medical image stack (a) mask of data (b) outline of mask shown in red.

6.1.2 Least squares fitting

An unstructured set of data points is obtained from the outline of the segmentation mask in Figure 6.3b. For the slice used in this example, the segmentation produces a total of 105 data points, which are shown in Figure 6.4a. It is not appropriate to use the data points from each slice of the medical image stack to directly generate the B-spline surface representation of the endocardial surface. This is due to multiple factors, the first issue is the pixelated nature of the data points. If a B-spline was generated through the local interpolation method of B-spline curve generation, the resulting curve would include the sharp corners from the pixels of the image, as seen in Figure 6.4b. This is not representative of the shape of a human LV as it does not appear to be a natural shape and some means of reducing the sharp corners is required. Using the local interpolation method, the data points must be ordered to determine the "path" of the B-spline through the set of points, which requires extra computational effort. This task involves determining the angular positions of each data point from the centre (the average x and y coordinate of the data points) relative to the positive x direction. Issues in the ordering may arise for more complex geometries where multiple points lie along the same angular direction and user interference would be required to manually sort these points. Another issue is faced when it comes to the generation of the B-spline surface. The method of surface generation used in this work requires the same number of sampling points along each row and column of the sampling point grid (see Figure 3.9). The number of data points generated from each segmented slice is dependent on the size of the segmented area, the larger the segmented area, the more data points are produced and vice versa. This means that a method of generating the same number of B-spline surface sampling points is required. To do this, a B-spline curve is created for each segmented slice using the least squares fitting procedure described in Section 3.4.2 and a set of sampling points is produced from each B-spline curve to generate the grid of sampling points around the LV surface.

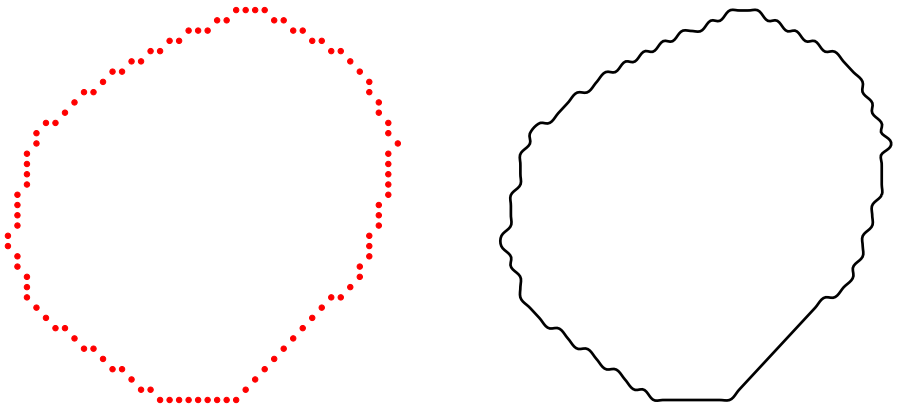

(a) (b)

Figure 6.4: Slice segmentation (a) data points (b) direct B-spline curve generated through local interpolation.

As in Section 3.4.2, the fitting strength parameter, ζ, is used in this least squares fitting procedure as a means to control the closeness of the B-spline curve fit to the data points so that the presence of sharp corners in the curve is reduced. The first step in the least squares fitting process is to generate an initial B-spline curve. Sampling points are positioned at evenly spaced angular positions around the centre of the data points (mean global x and y coordinates of the data points) with the radial distance based on the radial positions of the data points around that angular position. A B-spline curve is generated using a local interpolation scheme through these sampling points. The number of sampling points, n_k, is calculated based on the number of data points and the value of ζ. The initial B-spline curves using $\zeta \in [0.00, 0.20, 0.40, 0.60, 0.80, 1.00]$ are shown as blue, dashed lines in Figure 6.5.

The control points of the initial B-spline curve are then manipulated using the least squares fitting using (3.55) to produce the fitted B-spline curve which are shown as the black lines in Figure 6.5. It is clear that as the value of ζ increases, the fitted B-spline curve begins to match the shape of the data points more closely. The fitted curve when using $\zeta = 1$ (Figure 6.5f) almost recreates the B-spline curve in Figure 6.4b as there are some sections of the curve that are straight lines (the bottom and bottom left of the curve). This fitted curve does not have as many sharp corners

as the curve in Figure 6.4b as the stepping of the pixels is slightly reduced but the unnatural shape of the data points is still present. As discussed above, the aim of this least squares fitting procedure is to remove the sharp corners and produce a more natural shaped B-spline curve as an approximation of the cross section of the LV. Examining the fitted curves in Figure 6.5, it appears that the curves produced when $\zeta = 0.20$ (Figure 6.5b), $\zeta = 0.40$ (Figure 6.5c), $\zeta = 0.60$ (Figure 6.5d), $\zeta = 0.80$ (Figure 6.5e) and $\zeta = 1.00$ (Figure 6.5f) all exhibit a straight line segment at the bottom left of the data points. Referring to the slice in Figure 6.2, this is a portion of the septum wall, however, a straight line will not typically be seen in the heart so should be put down as an artefact due to the low resolution of the medical imaging procedure. This signifies that the value of ζ should at least be lower than 0.20 to smooth out this area and produce a more natural shape. Therefore, to ensure the maximum amount of smoothing, a value of $\zeta = 0.00$ is used for the least squares fitting of the B-spline curves for all sets of data points. This also means that the least squares fitting will use the same number of sampling points for all sets of data points irrespective of the number of data points in the set.

6.1.3 Surface generation

To generate the B-spline surface, a grid of sampling points is required, these are the sampling points over each fitted B-spline curve for each segmented slice through the longitudinal direction of the LV. Every slice must have the same number of sampling points, therefore, 100 sampling points are positioned at regular angular intervals around the fitted B-spline curve. The sampling points are shown as black circles in Figure 6.6. Through numerical experimentation during the development of the LV model, it was found that using a total of 100 sampling points to produce the B-spline curve for each slice was suitable to represent the fitted B-spline curve. For the medical image stack used in this section, the maximum number of data points for a single slice is 127 with the fitted B-spline curve having a length of

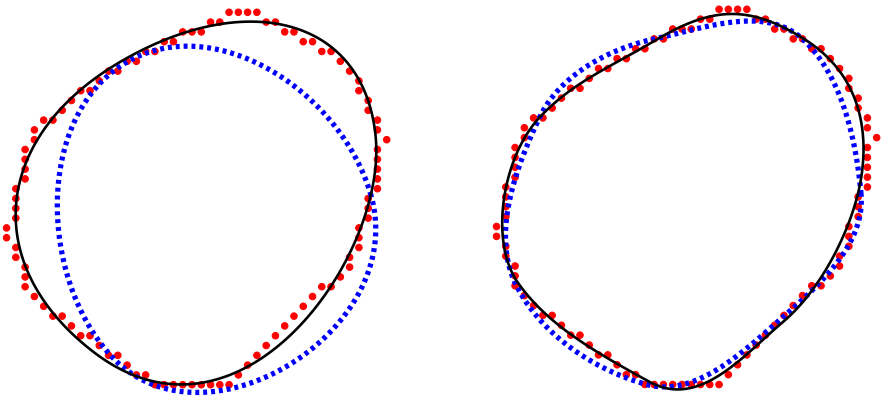

(a) $\zeta = 0.00$ ($n_k = 3$)

(b) $\zeta = 0.20$ ($n_k = 7$)

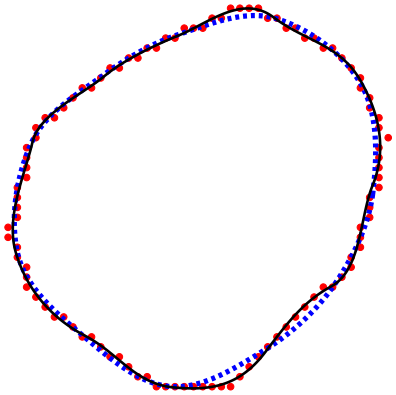

(c) $\zeta = 0.40$ ($n_k = 11$)

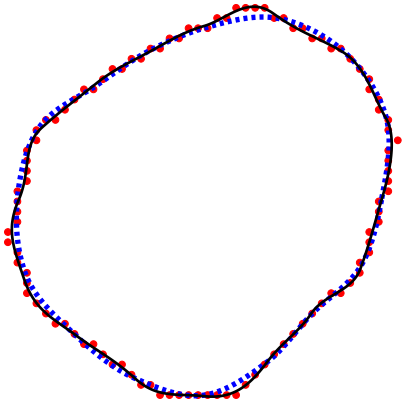

(d) $\zeta = 0.60$ ($n_k = 16$)

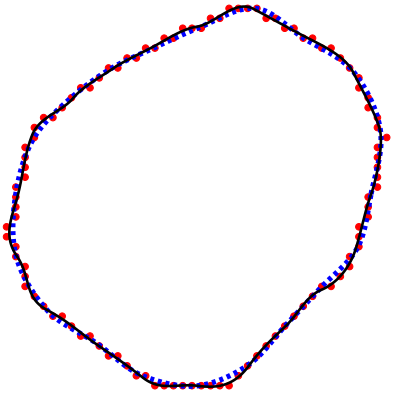

(e) $\zeta = 0.80$ ($n_k = 20$)

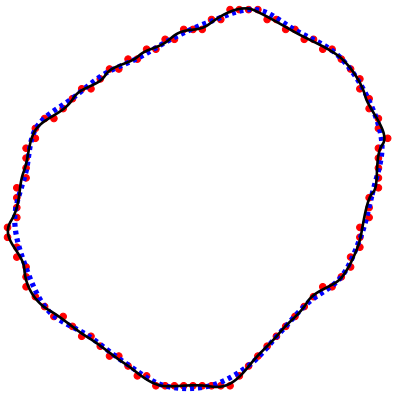

(f) $\zeta = 1.00$ ($n_k = 25$)

Figure 6.5: Least squares fitting of a closed B-spline curve to slice data points (red circles) for various fitting strengths. Both the initial B-spline curve (blue, dashed line) and fitted B-spline curve (black line) are shown.

193 mm, therefore, using 100 sampling points means that each curve segment of the B-spline curve will have a length approximately equal to the resolution of the image from the stack for the largest slice curve. Obviously, the slices with shorter B-spline curves will have curve segments with lengths much smaller than the image resolution, this is the reason that 100 sampling points was deemed the most reasonable as increasing this number would increase the computational effort whilst not significantly improving the quality of the B-spline curve for these smaller slice curves.

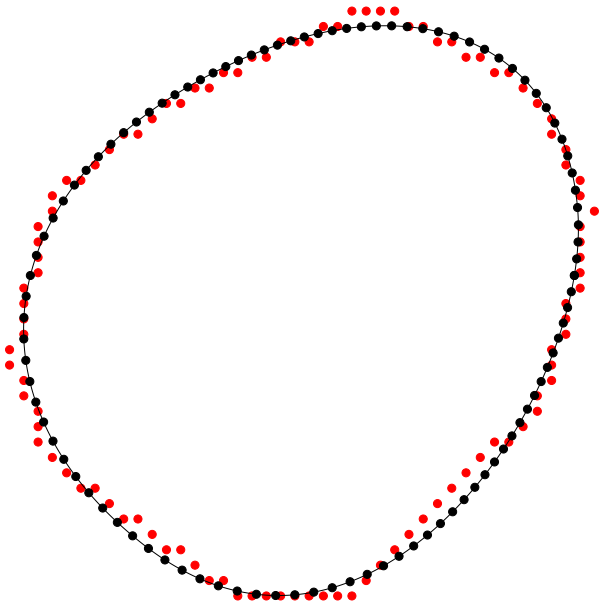

Figure 6.6: B-spline curve generated using a fitting strength of $\zeta = 0$ (black line) and the even, angular distribution of 100 B-spline surface sampling points along the B-spline curve (black circles) from the data points obtained from segmented slice (red circles).

Having created the B-spline curves for all segmented slices, the curves are positioned in 3D space as shown in Figure 6.7. The global coordinated of all of the fitted B-spline curves are shifted such that the centre of the upper most slice is positioned at the origin with the positive z direction along the longitudinal direction and the x and y axes acting in the plane of the upper most slice. Given that the MRI scanning procedure means that 8 mm of the LV is accounted for in each slice, it is

likely that a lot of geometric information will be lost between slices, such as the apex of the LV. In this work, the apex is not considered due to the high uncertainty in its position.

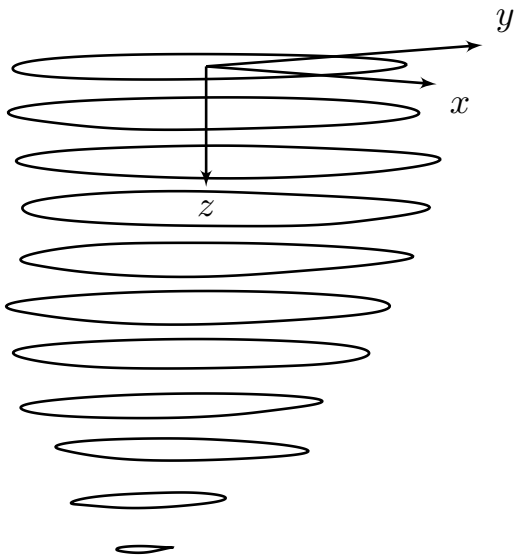

Figure 6.7: Fitted B-spline curves for all segmented slices.

Once the B-spline curves are created for all segmented slices, the 100 sampling points of each fitted B-spline curve are used to generate the grid of sampling points for the B-spline surface. The B-spline surface representation of the endocardial surface is then produced as shown in Figure 6.8a. The epicardial surface is generated using the same procedure as described above, where the epicardial surface is segmented with points around the outer surface of the LV and the septum wall between the LV and the Right Ventricle (RV). The generated B-spline representation of the epicardial surface is shown in Figure 6.8b.

This work only focusses on the stress in the free wall of the LV and the septum wall between the LV and RV. The apex will not have a significant effect on the stresses in these walls, so there is no need to include the apex within the model. The fitted endocardial surface (red surface) and epicardial surface (blue surface) used for the LV model are shown in Figure 6.9. The free wall and septum wall are also labelled on the side view of the surfaces. It is not a trivial task to determine

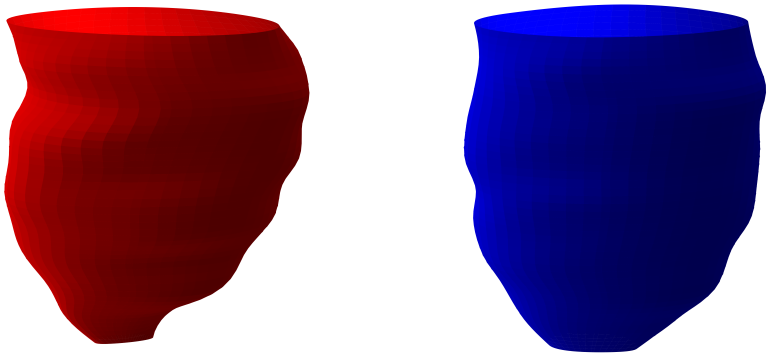

(a) (b)

Figure 6.8: Fitted B-spline representation of the LV (a) endocardial and (b) epicardial surfaces.

the true position of the basal plane from the stack of medical images and the fitted surfaces. Therefore, the basal plane is taken to be situated in the plane of the upper most segmented slice of the endocardial surface. Any segmented slices of the epicardial surface which have a z coordinate greater than the basal plane are simply discarded. Generating the B-spline surfaces from solely the rings of the segmented slices means that there are flat cuts across the top and bottom of the model domain, which can be more easily aligned with the edges of the background mesh for easier application of boundary conditions.

The resulting model for this work is similar to other studies which model the equatorial region of the LV as a thick walled cylinder [54, 122, 154]. This work simply expands the scope from looking at the equatorial region and instead looks from the basal plane down to near the apex of the LV, assuming that it is essentially a thick walled cylinder with an irregular cross section. Therefore, the MP domain is created between the basal plane and the lowest segmented slice as this provides the best approximation of the patient geometry based on the segmentation of the MRI.

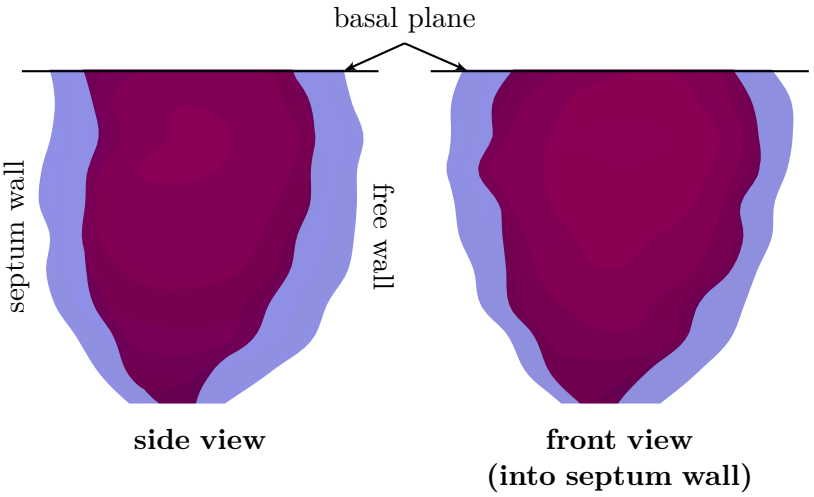

Figure 6.9: Side and front views of the fitted B-spline representation of the LV endocardial surface (red surface) and epicardial surface (blue surface) which are used for the LV model. The top of the model is aligned with the upper most segmented slice (basal plane) and the bottom of the model is aligned with the lower most segmented slice.

6.1.4 Material Point generation

Two methods of discretising the physical domain with MPs have been used in this work. The first method is the "flood-and-remove" method where the entire background mesh is filled with MPs by populating each element with evenly distributed MPs, the MPs which are not situated within the desired domain are then removed. The second option is to generate a temporary volumetric mesh over the desired domain which is populated with MPs. However, if the geometry of the physical domain is complex, a substantial amount of work is required to produce the mesh for this second approach. The first method has the advantage that a second mesh generation step is not required, but, if a large number of MPs are used, a considerable amount of computational time is required to determine whether each MP is within the physical domain. It is possible to do this by determining the foot point for each MP on the two surfaces and comparing the two directional vectors to the foot points. If the dot product of the two vectors is negative, the two vectors are pointing in opposite directions which would likely mean that the MP is between the surfaces. Using B-splines to represent the endocardial and epicardial surfaces

means that it is possible to distribute points over each surfaces which can be used to generate a volumetric mesh between the two surfaces by connecting points on each surface to achieve the second method for MP placement. This is the method used in this work, as it is less computationally expensive than the flood-and-remove method and provides more control on the number of MPs used in the physical domain as a number of MPs can be prescribed. With the first method, only the number of MPs per element of the background mesh is given and there is no direct means of controlling how may MPs will be located within the physical domain.

This work requires the analyst to prescribe the total number of MPs which are situated through the thickness of the LV wall, the number of elements of the mesh through the thickness of the wall and a target number of MPs, n_{mp}^{tar}, in order to produce the MP mesh. These are used to determine the number of elements in the circumferential and longitudinal directions of the LV. The total number of MPs is calculated as

$$n_{mp} = n_{el}^{c}\ n_{el}^{l}\ n_{el}^{r}\ (n_{mp}^{e})^{3} \tag{6.1}$$

where n_{el}^{c}, n_{el}^{l} and n_{el}^{r} are the number of elements in the circumferential, longitudinal and radial directions respectively and n_{mp}^{e} is the number of MPs per dimension in each element. Given the prescribed number of MPs through the thickness of the LV wall and the number of elements through the radial direction, the value of n_{mp}^{e} can be easily found as the ratio of the number of MPs to the number of elements. In order to determine n_{el}^{c} and n_{el}^{l}, the ratio between the largest circumferential length of the epicardial surface and the longitudinal length is determined and the product of the two values is calculated based on (6.1) such that

$$n_{el}^{c}\, n_{el}^{l} = \frac{n_{mp}^{tar}}{n_{el}^{r}\,(n_{mp}^{e})^{3}}. \tag{6.2}$$

The number of elements in the circumferential and longitudinal directions are calculated in this fashion to ensure that the MP mesh is generated based on the geometry of the endocardial and epicardial surfaces as well as to reduce the possibility of highly distorted elements.

Once the number of elements in the circumferential and longitudinal directions are determined, local parametric coordinates, (ξ, η), are calculated for each surface which correspond to the nodes of the MP mesh on the endocardial and epicardial surfaces, $S^{endo}(\xi, \eta)$ and $S^{epi}(\xi, \eta)$ respectively. These local coordinates are a distribution between 0 and 1 based on the number of elements in each direction where ξ generates the points in the circumferential direction and η gives the points in the longitudinal direction. For cases where multiple elements are used in the radial direction, the intermediate points through the thickness are found using a linear interpolation between the points on the endocardial and epicardial surfaces with the same local parametric coordinates. An example of a generated MP mesh is shown in Figure 6.10. For illustrative purposes, 2D views of the circumferential elements (Figure 6.10a) and longitudinal elements (Figure 6.10b) are shown. For each diagram, the endocardial surface is shown in red and the epicardial surface is shown in blue with the MP mesh shown in black. Only one element is used in the radial direction for clarity. For this example, 20 elements are used in the circumferential direction ($n^c_{el} = 20$) and 10 elements are used in the longitudinal direction ($n^l_{el} = 10$), which would suggest that the circumferential length is twice that of the longitudinal length*. The element distribution in the circumferential direction seems to reflect the shape of the surfaces fairly well. Small areas are present between the edges of the mesh and the epicardial surface (as seen in the upper portion of Figure 6.10a), which will be reduced by increasing the value of n^c_{el} as well as using more elements through the thickness of the LV wall. In contrast, there is more irregularity in the shape of the endocardial wall in the longitudinal direction. It is clear from Figure 6.10b that 10 elements is not suitable to capture the shape of the model geometry, meaning that more elements will be required in this case. Care must be taken when choosing values for n^{tar}_{mp} and n^r_{el} to account for this.

*This is not actually the case for this patient geometry, the values used for n^c_{el} and n^l_{el} here have been chosen for illustrative purposes. The values used for the actual models are presented in Chapter 7.

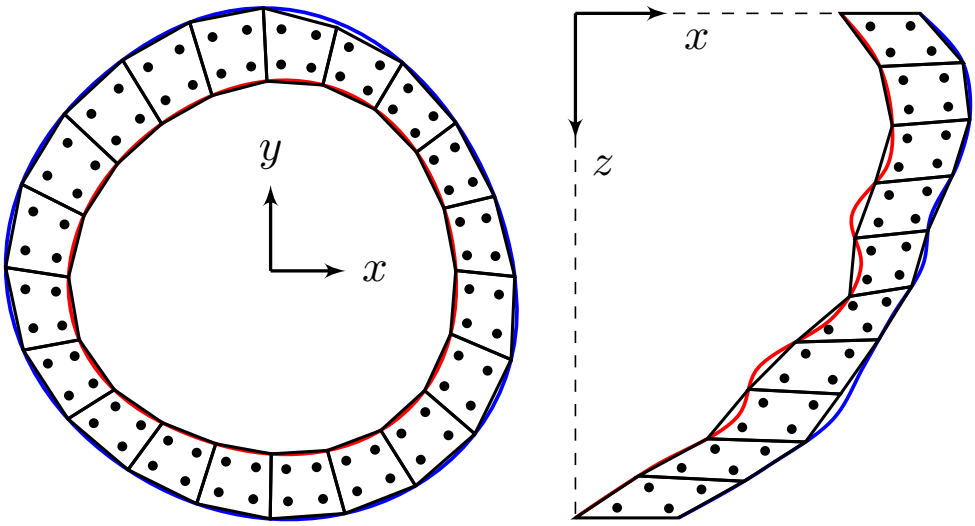

(a) circumferential (b) longitudinal

Figure 6.10: 2D diagram of MP mesh (black lines) generated between endocardial (red line) and epicardial (blue line) surface with 2×2 MPs (black circles) evenly distributed in each element. For illustrative purposes, one element is used in the radial direction.

Once the MP mesh is created, MPs are evenly distributed within each element, as shown in Figure 6.10 where 2×2 MPs are distributed in each element. As this work uses a 3D model, each element will contain $n^e_{mp} \times n^e_{mp} \times n^e_{mp}$ MPs per element. This work uses generalised interpolation MPs, this means that the domain half lengths for each MP are required. Unlike previous numerical examples which generated the MPs in a regular mesh, this MP mesh is highly irregular meaning that the l^i_p values cannot be found by simply dividing the size of the element based on how many MPs are contained within the element. Instead, the volume associated with each MP is calculated which is then used to determine the domain half length. Firstly, the Jacobian matrix is calculated such that

$$[J] = \left[\frac{\partial N}{\partial \xi}\right] \{x_v\} \tag{6.3}$$

where $\left[\frac{\partial N}{\partial \xi}\right]$ is a matrix containing the derivatives of the linear hexahedral element shape functions of a MP with respect to the local coordinates of the MP* and $\{x_v\}$ is the global coordinates of the nodes of the element. The initial volume associated

*Here the local coordinates (ξ, η, ζ) are the local coordinates of the MP within the element and should not be mistaken for the local parametric coordinate of the B-spline curve/surface.

with the MP is then calculated as

$$V_p^0 = \det([J])\, w_p \tag{6.4}$$

where w_p is the weight associated with the MP. As the MPs are evenly distributed within each element, the value of w_p is simply 8 divided by the number of MPs in the element. For simplicity, the MP domain is then assumed to be cubic in shape meaning that the domain half lengths are computed such that

$$l_{p_0}^i = \frac{1}{2}\sqrt[3]{V_p^0}. \tag{6.5}$$

While the assumption of the initial MP domain being cubic may cause large overlaps in the MP domains for the coarse meshes (such as the ones seen in Figure 6.10), using finer meshes will mean that the shape of the elements will be more regular and less overlaps between the MP domains will be seen.

As will be seen in Chapter 7, this work uses a target of 250 000 MPs for the initial LV models with 16 MPs positioned through the transmural direction, which was empirically determined through experimentation when generating the LV model.

6.2 Orientation of muscle fibres

As discussed in Chapter 5 (specifically Section 5.2), myocardium is an anisotropic material, this work models the LV tissue as a series of laminar sheets distributed through the thickness of the LV wall which contain muscle fibres. The direction of these muscle fibres and sheets will vary through the radial (or transmural) direction. A diagram of the local fibre and local sheet directions relative to the circumferential, longitudinal and radial axes are shown in Figure 6.11. The local fibre direction is considered as a rotation of the local circumferential axis about the local radial axis and the local sheet direction is the rotation of the local radial axis about the local circumferential axis. The rotation angles for the local fibre and local sheet directions are denoted as θ_f and θ_s respectively. The local circumferential

and radial axes will vary based on the position of the MP. It is assumed that the longitudinal axis will always be aligned with the z axis.

To find the local radial axis, a directional vector between the MP and a centre point is found. Due to the irregular shape of the endocardial and epicardial surfaces, it is not suitable to simply draw a straight line from the centre of the top edge of the model to the bottom edge of the model. Instead, centre points through the longitudinal direction are found based on the average x, y and z coordinates of the points for each circumferential ring of nodes on the endocardial and epicardial surfaces which are used to create the MP mesh. The position on the centreline for a MP is calculated as a linear interpolation between the centre points above and below the MP position and based on the z coordinate of the MP. A directional vector is calculated between this centre point and the MP, once normalised, this vector is taken to be the basis vector for the local radial axis. As the three local axes are orthogonal, the local circumferential axis is found through the cross product of the local radial and longitudinal axes.

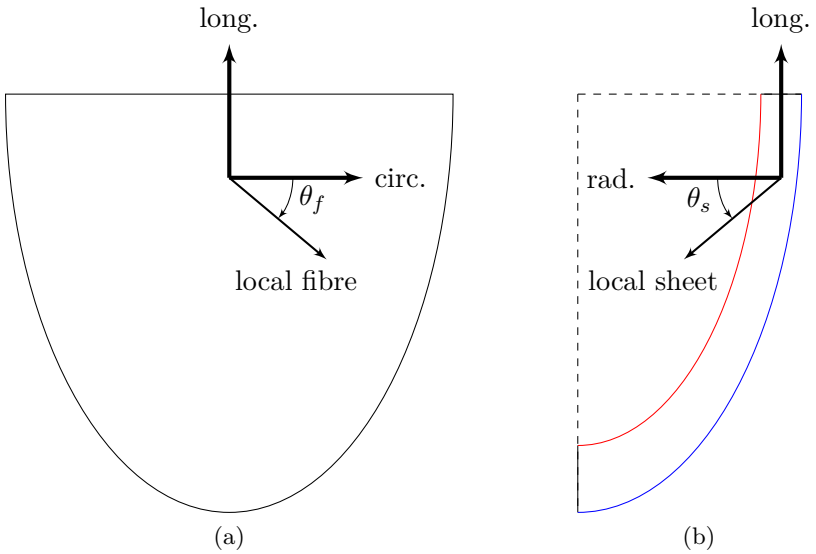

Figure 6.11: Negatively oriented (a) local fibre direction and (b) local sheet direction relative to the circumferential, longitudinal and radial directions.

This work calculates the directions of the local muscle fibre, sheet and normal

vectors through a series of two counterclockwise* rotations such that

$$\begin{bmatrix}\{f_0\} & \{s_0\} & \{n_0\}\end{bmatrix} = [R_s][R_f]\begin{bmatrix}\{u_c\} & \{u_r\} & \{u_l\}\end{bmatrix} \tag{6.6}$$

where $\{f_0\}$, $\{s_0\}$ and $\{n_0\}$ are the vectors of the local fibre, sheet and normal directions respectively, $\{u_c\} = \{u_c, v_c, w_c\}^T$, $\{u_r\} = \{u_r, v_r, w_r\}^T$ and $\{u_l\}$ are the vectors of the local circumferential, radial and longitudinal axes respectively. The rotation matrices, $[R_f]$ and $[R_s]$, are used to rotate the local circumferential, radial and longitudinal axes into the fibre, sheet and normal direction, the rotation matrices are calculated as [217]

$$[R_f] = \cos(\theta_f)[I] + \sin(\theta_f)[W_f] + (1 - \cos(\theta_f))(\{u_r\} \otimes \{u_r\}) \tag{6.7a}$$

$$[R_s] = \cos(\theta_s)[I] + \sin(\theta_s)[W_s] + (1 - \cos(\theta_s))(\{u_c\} \otimes \{u_c\}) \tag{6.7b}$$

where $\otimes$ denoted the outer (tensor) product of the two vectors and

$$[W_f] = \begin{bmatrix} 0 & -w_r & v_r \\ w_r & 0 & -u_r \\ -v_r & u_r & 0 \end{bmatrix} \quad \text{and} \quad [W_s] = \begin{bmatrix} 0 & -w_c & v_c \\ w_c & 0 & -u_c \\ -v_c & u_c & 0 \end{bmatrix}. \tag{6.8}$$

The first rotation matrix, $[R_f]$, rotates the local circumferential, radial and longitudinal axes about the local radial axis through an angle of θ_f. This is followed by a further rotation of the rotated axes through an angle of θ_s about the undeformed local circumferential axis.

The local fibre angle for a MP is calculated as a linear interpolation between the fibre angle at the endocardial surface and the epicardial surface such that

$$\theta_f = (1 - d_r)\,\theta_f^{endo} + d_r\,\theta_f^{epi} \tag{6.9}$$

where θ_f^{endo} and θ_f^{epi} are the fibre angles at the endocardial and epicardial surfaces respectively and d_r is the transmural depth ratio, which is the distance between the MP and the endocardial surface normalised between 0 and 1. The foot points of the

*It is a simple procedure to apply a clockwise rotation by prescribing a negative angle through which the rotation should occur.

MP on the B-spline surfaces representing the endocardial and epicardial surfaces, denoted as $\{S_p^{endo}\}$ and $\{S_p^{epi}\}$ respectively, are used to calculate the value of d_r such that

$$d_r = \frac{|\{x_p\} - \{S_p^{endo}\}|}{|\{S_p^{epi}\} - \{S_p^{endo}\}|}. \tag{6.10}$$

The same procedure is performed to determine the sheet angle where

$$\theta_s = (1 - d_r)\,\theta_s^{endo} + d_r\,\theta_s^{epi} \tag{6.11}$$

given that θ_s^{endo} and θ_s^{epi} are the sheet angles at the endocardial and epicardial surfaces respectively and d_r is the same transmural depth ratio as calculated in (6.10).

There is no consensus in the published literature on the true value of the fibre and sheet angles in the myocardium. There have been multiple experimental studies, including those by LeGrice and co-workers [184, 185] which propose that the fibre angles have a transmural distribution starting at around -90° at the endocardial surface and transitioning to between 30° and 60° at the epicardial surface. Other experimental investigations have stated other ranges of fibre angle distributions, a selection of which are presented in Table 6.2. It is clear that there is a large variation in the experimental findings and there is no set value for these fibre angles which should be used in the LV model for this work. As mentioned by Greenbaum *et al.* [119], this variation may be due to taking samples of the LV tissue at different positions around the LV wall which will have an effect on the results. This may be due to the heart having a helical structure in terms of the muscle tissue [300] where the fibre orientation sees variations not only in the transmural direction but the longitudinal and circumferential directions also. When comparing the fibre angles proposed by Streeter Jr. *et al.* [286] and Greenbaum *et al.* [119], both present the same fibre angle at the endocardial and epicardial surfaces, however, there is a disagreement on the direction of rotation with respect to the circumferential direction. There are multiple examples of LV models which use this fibre angle distribution, such as Genet *et al.* [109] and Doste *et al.* [88], both of which use a

rule based approach to apply the fibre directions through the transmural direction [183]. Other examples of LV modelling do not use these experimentally obtained values such as: Göktepe *et al.* [115], which assumes the fibre angles vary between -70° at the endocardial surface to 70° at the epicardial surface; Nikou *et al.* [232], which takes a fibre angle of 83° at the endocardial surface and -37° at the epicardial surface; and Holzapfel and Ogden [145], who mention that the fibre angles at the endocardial surface is between 50° and 70° while the fibre angles at epicardial surface is between -50° and -70°.

θ_f^{endo}	θ_f^{epi}	Source
-90°	30° to 60°	[184, 185]
-90°	90°	[285]
$\pm 60°$	$\mp 60°$	[119, 286]
$80° \pm 7°$	$-40° \pm 10°$	[182]
50° to 70°	-50° to -70°	[145, 319]
70°	-70°	[115]
83°	-37°	[220, 232, 291, 328]

Table 6.2: Selection of proposed endocardial and epicardial LV free wall fibre angles in published literature.

There are a plethora of proposed fibre angle distributions in the published literature, however, the distribution of the muscle sheet angles is a topic which is less covered. To the author's knowledge, the sheet angles are either oriented such that they are normal to the endocardial and epicardial surfaces, as seen in [115], or are based on the value of sheet angles presented by Hunter *et al.* [156] stating that the sheet angle is 45° at the endocardial surface and -45° at the epicardial surface. An example of the use of these sheet angles can be found in work by Wang *et al.* [319] and Nikou and co-workers [232].

This work does not consider the helical structure of the myocardium, instead taking values for the fibre and sheet angles at the endocardial and epicardial surfaces to be constant over each surface. A linear variation of the fibre and sheet angles is assumed between the two surfaces, in a similar fashion to [115, 232, 319] for example.

6.3 Background mesh generation

With the physical domain now discretised by MPs and with boundaries represented by B-spline surfaces, the background mesh made up of finite elements is required. This is a relatively simple process as the only requirement of this model is for the background mesh to have a top and bottom edge (in the z direction) to coincide with the upper and lower ring of the physical domain. The mesh is extended in the x and y directions to allow space for the physical domain to deform. The mesh is composed of linear finite elements (which are cubic in shape) with a mesh size calculated based on the minimum distance between the B-spline representations of the endocardial and epicardial surfaces, h_s^{max}. This is done to ensure that there will be at least one element between the surfaces at the start of the simulation. The mesh can be refined to increase the initial number of elements which contain the physical domain during the simulation. It is worth noting that this method of generating the background mesh means that there is a disconnect between the size of the background mesh and the number of MPs used in the analysis as separate meshes are used in each case. This means that the analyst must adjust the value of n_{mp}^{tar} accordingly when refining the mesh to ensure that there is a reasonable number of MPs in the analysis compared to the number of elements in the background mesh in order to obtain suitable numerical integration over the physical domain.

The overall length of the background mesh is simply the distance between the upper edge and lower edge of the B-spline surfaces (where $\eta = 0$ and $\eta = 1$ respectively). As the segmented slices used for the endocardial and epicardial surfaces have the same z coordinate throughout, both surfaces will have the same z coordinate at the upper and lower edge. Therefore, using either surface is suitable, this work uses the epicardial surface as this is also used to determine the lengths of the background mesh in the x and y directions. The length of the mesh in the z direction, L_0^z, is calculated as

$$L_0^z = \max\left(|\{S_z^{epi}\}|\right) - \min\left(|\{S_z^{epi}\}|\right) \tag{6.12}$$

where $\{S_z^{epi}\}$ is a vector containing the global z coordinates of the points on the epicardial B-spline surface. The length of the mesh in the x direction, L_0^x, is found by taking the maximum absolute value of the global x coordinate of points on the epicardial surface such that

$$L_0^x = \max\left(|\{S_x^{epi}\}|\right) \tag{6.13}$$

where $\{S_x^{epi}\}$ is a vector containing the global x coordinates of the points on the epicardial B-spline surface. This is the length of the mesh from the origin, which will fully contain the physical domain in both the positive and negative x directions. The same procedure is carried out to determine the length of the mesh in the y direction. The number of elements used in each direction is calculated based on the minimum distance between the endocardial and epicardial surfaces such that

$$n_{el}^i = a_{mesh}\frac{L_0^i}{h_s^{max}} \qquad \text{for } i = x, y, z \tag{6.14}$$

where a_{mesh} is a mesh refinement factor. As the physical domain is positioned such that the centre of the top ring of the endocardial surface is at the origin, the mesh also has to be extended in the negative x and y directions with the same length as in the positive directions to fully encapsulate the physical domain in the background mesh. In order to allow space for the physical domain to deform, the mesh is extended in the x and y directions (in both the positive and negative directions). This is done by adding extra elements in these directions. This work increases the length of the mesh by 40% to ensure that the physical domain will never coincide with the outer most elements of the background mesh. There is no limit to the number of elements that can be used to extend the mesh as they will often never be involved in the analysis, only the elements which contain the physical domain are used.

To illustrate how the background mesh is generated based on the geometry of the endocardial and epicardial B-spline surface representations, a full 3D model was generated. Figure 6.12 shows a 2D cross section of the physical domain and background mesh through the $x - z$ plane. The endocardial (red lines) and

epicardial (blue lines) surfaces are shown with the MP discretisation mesh created using 2 elements through the thickness of the myocardium and 20 elements in the longitudinal direction, each element in the MP mesh is populated with 2×2 evenly distributed MPs which are shown as black circles. The minimum distance between the endocardial and epicardial surfaces was found to be $h_s^{max} = 4.4\,\text{mm}$. No mesh refinement is used ($a_{mesh} = 1$), therefore, 4.4 mm is the size of the elements in the background mesh. The length of the model in the longitudinal (z) direction is $L_0^z = 80\,\text{mm}$ which, using (6.14), means that 18 elements are used in z direction. The maximum absolute distance in the x direction of the points of the epicardial B-spline surface is $L_0^x = 44.4\,\text{mm}$, which corresponds to 10 elements in the x direction. It is worth noting that these values are the length of the mesh and number of elements from the origin in the positive x direction. The mesh also extends in the negative x direction, as seen in Figure 6.12, to fully contain the physical domain. For this illustrative example, the length of the mesh in the x direction is increased by 20%, this is done by adding 2 extra elements in the x direction. Therefore, 12 elements are now used in the x direction and the length of the mesh in the x direction is $L^x = 53.3\,\text{mm}$.

The boundary conditions which are applied to the background mesh are also shown in Figure 6.12 and will be discussed in the following section along with the boundary conditions applied to the physical domain.

6.4 Boundary conditions

It is important to apply sufficient boundary conditions to the LV model in order to eliminate any rigid body motion during the analysis. The heart within the chest is enclosed in the pericardial sac which will restrict any large deformation. The basal section of the heart is constrained by the aorta and there will also be some interaction between the LV and the RV. It is not feasible to consider all of these factors and some approximations must be made for this model. As with the other

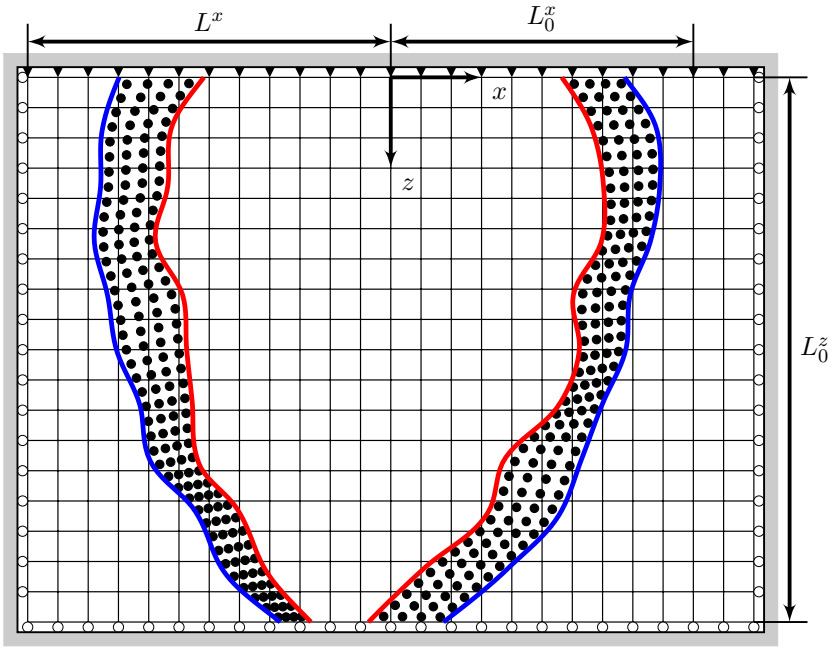

Figure 6.12: 2D illustration of LV model problem setup showing the endocardial surface (red lines), epicardial surface (blue lines), MP discretisation (black circles), background mesh (black lines) and Dirichlet boundary conditions directly applied to the the boundaries of the background mesh.

aspects of the LV model, published literature of LV modelling does not present any definitive method of applying boundary conditions. In order to compare the application of boundary conditions to the LV domain, it is simpler to look at the four key geometric features of the LV model: the basal plane (the top of the model), the apex (the bottom of the model - which is not included in this work), the endocardial surface and the epicardial surface.

The endocardial surface is the easiest to be considered as the majority of researchers have prescribed a pressure boundary condition over this surface [20, 86, 105, 115, 122, 123, 181, 220, 232, 240, 242, 272, 318, 319, 327]. Figure 6.13 shows the physiological LV pressure measured through the cardiac cycle. Two well defined points in the cycle have been highlighted on the plot, ED is shown with the red circle and End-Systole (ES) is shown with the blue circle. This work only considers ED but both stages have been marked to demonstrate the large difference in pressures experienced by the LV throughout the cardiac cycle. The data shown in Figure

6.13 was reported by Göktepe *et al.* [115], stating that the End-Diastolic Pressure (EDP) is approximately 4 mmHg. A review of previous medical studies shows that there is a range of reported LV EDP. Waldman and co-workers have stated the LV pressure is within the range 5 ± 2 mmHg [312] or 4.7 ± 1.5 mmHg [313], while Villareal *et al.* gives the range of LV pressure to be 2.3 ± 1.5 mmHg [310]. For simplicity, this work assumes that the LV EDP is 5 mmHg, which corresponds to a pressure of approximately 0.67 kPa (which is close to the ED pressure of 0.63 kPa used by Guccione *et al.* [123]). For completeness, applying a pressure over the endocardial surface is not used in every LV model in published literature, Genet *et al.* [109] did not only apply pressure but also a change in the LV chamber volume to cause deformation of the model.

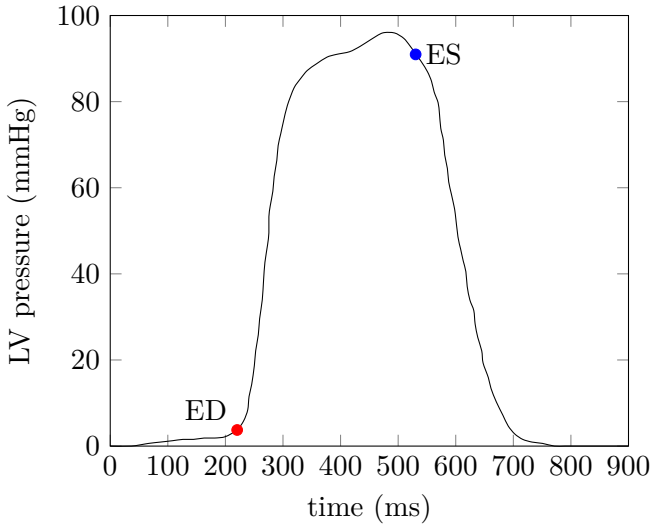

Figure 6.13: Physiological LV pressure through cardiac cycle. For reference, the ED stage is shown as a red circle and the ES stage is shown as a blue circle. Pressure data taken from Göktepe *et al.* [115].

The basal plane is subjected to some form of boundary conditions in the majority of models. In some cases, the entire basal plane is fully fixed in all directions [86, 109, 115, 294], whereas other models will simply fix the basal plane in the longitudinal direction, allowing deformation in other directions [20, 21, 135, 240, 318]. An extra constraint is sometimes imposed to suppress the circumferential displacement of the epicardial surface at the base of the LV [105, 242, 318, 319]. Other models

fully constrain the nodes of the epicardial edge of the base of the LV, allowing the remaining nodes of the basal plane to move in the circumferential and radial directions freely [181, 220, 309, 327]. Shen *et al.* [272] does not apply boundary conditions across the entire basal plane, instead, the nodes at the base of the LV between the midwall and epicardial surface are fully fixed and the remaining nodes are free to move.

While the apex of the LV will not be considered in this work, the author did investigate the boundary conditions applied to the apex in the published literature. There seems to be two main approaches, either the apex is left free to displace in any direction [86, 105, 241, 318, 319], or it is fixed in the longitudinal direction [20, 21, 242, 309].

Finally, there are multiple ways of applying boundary conditions to the epicardial surface of the LV proposed in the published literature. For example, the epicardial surface can be left free to deform in any direction [86, 272, 319]. It is often the case that the epicardial surface is not mentioned in terms of the application of boundary conditions [92, 220, 232], therefore, the author assumes that this means that the epicardial surface is free to deform (the natural finite element boundary condition). Guccione *et al.* [123] constrained the epicardial surface radially, which does not seem to be a popular approach in the literature. Instead, a common approach is to restrain the entire epicardial surface in the circumferential direction [240, 242, 318]. A more physiological approach is to apply a system of linear springs (ie. an impedence-type boundary condition) acting normally to the faces of the elements on the outer wall of the LV [20, 21, 115]. Such a spring constant is not able to be physically measured, therefore, Bettendorff-Bakman and co-workers [20] performed a parametric study to determine a suitable value for the spring constant. If the value is too high, the myocardium will not deform. However, if the spring constant is too low, unrealistic deformation of the myocardium will be seen. Hassabalah *et al.* [135] constrained the LV model using a uniform elastic foundation in a similar manner to Bettendorff-Bakman and co-workers.

Another notable LV model was presented by Veress *et al.* [308], which generated the LV geometry from the segmentation of medical imaging data, however, the full image domain was used to produce a cuboidal 3D FE mesh which contained the LV geometry as well as surrounding tissue (the part of the stack of the medical images which was not segmented, ie. the black section in Figure 6.3a). The LV domain was modelled with a transversely isotropic hyperelastic material while the surrounding tissue was modelled as a soft, isotropic hyperelastic material. To suppress any rigid body motion, every edge of the FE mesh was fully fixed.

This work fully fixes all nodes at the basal plane. This is done by simply fixing all nodes at the top of the background mesh, as this surface of the mesh is coincident with the basal plane. Given that this work's LV model does not consider the apex, it is not suitable to leave the bottom of the model free to deform, therefore, roller boundary conditions are applied to the nodes at the bottom of the mesh. This is akin to fixing the bottom of the model (and apex) longitudinally. These boundary conditions are shown in Figure 6.12 for the 2D representation of the LV model. Roller boundary conditions are also applied to the sides of mesh at $x = -L^x$, $x = L^x$, $y = -L^y$ and $y = L^y$, where L^x and L^y are the lengths of the extended mesh in the x and y directions with the extra elements added (see Figure 6.12). These roller boundary conditions on the sides of the mesh are to prevent any MPs from deforming outside of the background mesh, although if the mesh is extended enough, this should not happen. A uniform pressure is applied over the endocardial surface through integration over the B-spline surface representation, as discussed in Section 3.5. The epicardial surface is free to deform throughout the analysis. It is worth noting that this work uses the ghost stabilisation to mitigate issues surround the small cut problem around the boundary of the physical domain, this essentially acts as a form of spring boundary condition on the gradient of the solution which will pose some resistance to the deformation of the epicardial surface (as well as the endocardial surface due to it being applied over all boundaries of the domain).

Summary

This chapter has presented the steps taken to create a patient-specific LV model using the MPM. Starting with segmented MRI data, B-spline surface representations for the endocardial and epicardial surfaces are generated. These surfaces are not only used for creating the model geometry, but are also used to impose non-conforming boundary conditions. A mesh is created between the two B-spline surfaces, which is populated with the MPs to discretise the physical domain of the LV. The means of determining the local fibre and sheet directions for each MP is defined based on the position on the MP relative to the endocardial and epicardial surfaces. The background computational mesh is generated based on the geometry of the endocardial and epicardial surfaces, with the mesh size given by the minimum distance between these surfaces and the overall length of the mesh calculated such that it fully contains the physical domain. This mesh is also extended further to allow space for deformation. Finally, the boundary conditions applied to the background mesh and the physical domain have been discussed.

The next chapter presents a series of simulations of patient-specific LV models with varying model parameters to analyse the effect of changing the material properties and geometry.

Chapter 7

Left Ventricular Modelling - Model Analysis

The previous chapter explained the generation of a patient-specific model of the Left Ventricle (LV) for a MPM analysis: starting with a stack of segmented image slices; generating the geometry of the endocardial and epicardial surfaces using B-spline representations; populating the physical domain (the space between the two surfaces) with MPs; assigning fibre, sheet and normal directions to each MP for the anisotropic material behaviour; generating the background computational mesh; and a discussion on the choice of boundary conditions which can be applied to the problem. This chapter presents a series of analyses examining the sensitivity the LV mechanical response estimate due to multiple factors, namely: the parameters used in the material model, the orientation of the myocardium fibres, the specified bulk modulus of the material (which controls the level of incompressibility of the material), the applied boundary conditions and geometry of the model based on patient data. It is acknowledged that, due to the relative simplicity of this initial model, the results presented in this chapter may not be physiologically accurate, but solely used for comparison between various model setup parameters and to demonstrate that the MPM is a viable option for LV analysis. Firstly, a baseline model is shown which will be the basis for the parametric study. Each subsequent

analysis for comparison will vary a single parameter in the LV model setup.

Every analysis is performed using the Material Point-Based Arc-Length Method (MP-BALM) presented in Chapter 4 as this provides a more stable analysis compared to using the standard load controlled scheme. It was found during the development phase that with the standard load controlled scheme, large nodal deformations can cause "MP inversion" which resulted in negative MP volumes being calculated. This is mitigated by reducing the load increment over each load step. However, a high number of load steps (>1000 load steps) are then required, increasing the computational cost of each analysis. Given that the MP-BALM restricts the total displacement of the MPs over each load step and automatically controls the allowed displacement based on the convergence performance of the previous load step, the MP inversion issue is less frequent and a larger initial load increment is allowed. An initial pressure increment of $P = 0.067\,\text{mmHg} = 8.9\,\text{Pa}$ is applied over the endocardial surface of the LV, a factor of 75 times less than the typical End-Diastole (ED) pressure of 5 mmHg. The performance of the analyses in terms of number of load steps is not considered in this chapter, however, it is worth noting that the MP-BALM analyses took a maximum of 522 load steps to achieve the target applied pressure, demonstrating the improved computational cost of the MP-BALM over the standard load controlled scheme, which would typically require over 1000 load steps to complete. To improve the stability of all analyses, the ghost stabilisation technique is applied with a ghost stabilisation parameter one order of magnitude lower than the bulk modulus value. This is a relatively high value, but it was found during the development of this work to be necessary for a stable analysis. The F-bar technique is not implemented for any analysis shown in this chapter.

For each comparison (in addition to the fibre stress and radial displacement fields in the LV), two volume measures are examined. The first is the volume of the LV chamber which is calculated as the volume enclosed by the B-spline surface representation of the endocardial surface. The second volume measure is the volume

of the physical domain which is calculated as the sum of each volume associated with the MPs. If required, the normalised relative difference in volumes between an analysis and the baseline model is calculated as

$$\epsilon_V = \frac{|V_i^{model} - V_i^{base}|}{|V_i^{base}|} \tag{7.1}$$

where V_i^{model} is the volume for the modified model and V_i^{base} is the volume of the baseline model at a given pressure.

To aid in the comparison between simulations, the plots of the deformed LV models showing the MP fibre stress and radial displacement fields are given at the end of this chapter. Each set of results show cross sections of the model in the long axis and short axis views. In the long axis view, the cross section through the $y - z$ plane is taken in order to show the septal wall and the free wall. For the short axis view, a cross section in the $x - y$ plane is taken halfway through the longitudinal length of the model.

7.1 Baseline model

The geometry of the reference LV model is generated from the MRI stack of a patient aged 50–59 taken from the healthy ageing study at the Newcastle Magnetic Resonance Centre (NMRC). This patient will also be referred to as "Patient A" in Section 7.6 when comparing patient geometry. The B-spline surface representations of the endocardial and epicardial walls was created using the least squares fitting procedure with a fitting strength parameter of $\zeta = 0$ and 100 sampling points positioned around each fitted B-spline curve for each slice of the image stack. A target number of MPs was set at $n_{mp}^{tar} = 250\,000$, with 16 MPs positioned through the thickness of the LV wall. The MP mesh was generated using $n_{el}^{r} = 4$ and $n_{mp}^{e} = 4$, which gives $n_{el}^{c} = 47$ and $n_{el}^{l} = 21$ as the the number of elements in the MP mesh in the circumferential and longitudinal directions respectively based on (6.2). The physical domain was discretised using this MP mesh with a total of 252 672 generalised interpolation MPs.

The B-spline representations of the endocardial and epicardial surfaces was used when discretising the physical domain with MPs, however, a large number of boundary points were used for these surfaces. For the sake of computational cost, the number of boundary points used for the analysis is based on the number of elements used for the MP mesh such that

$$n_{bp}^{\xi} = n_{el}^{c} + 1 \quad \text{and} \quad n_{bp}^{\eta} = n_{el}^{l} + 1 \tag{7.2}$$

where n_{bp}^{ξ} and n_{bp}^{η} are the number of boundary points used in the local ξ and η directions of the B-spline surface respectively. For the baseline model, $n_{bp}^{\xi} = 48$ and $n_{bp}^{\xi} = 22$ are the number of boundary points for the endocardial and epicardial B-spline surface. Even though the epicardial surface is larger in terms of surface area compared to the endocardial surface, the same number of boundary points are used, as no computation is performed over the epicardial surface and the boundary is used as a means of tracking this surface. The integration of the applied pressure over the endocardial B-spline surface is performed using 3×3 Gauss points over each patch of the surface. This number was selected during the development stage of the model, as it was deemed large enough (given the number of boundary points used) that every element which is cut by the B-spline boundary will be accounted for in the integration.

The minimum distance between the endocardial and epicardial B-spline surface representations, and therefore the maximum size of the background mesh elements, is calculated as $h_s^{max} = 4.86$. The minimum length of the background mesh to contain the physical domain is found, using (6.12) and (6.12), to be $L_0^x = 42.35\,\text{mm}$, $L_0^y = 42.35\,\text{mm}$ and $L_0^z = 80\,\text{mm}$. These lengths correspond to 9 elements in the x and y directions and 17 elements in the z direction. To account for the deformation of the model, the length of the mesh in the x and y directions is increased by 40%, adding an extra 8 elements in the x and y directions. It is worth noting that, the mesh lengths and number of elements for the x and y directions are doubled to account for the fact that the origin of the mesh is located at the centre of the basal plane. Cross sections of the geometry of the physical domain and the background

mesh is shown in Figure 7.1 in the long axis and short axis views where the MPs are shown in red.

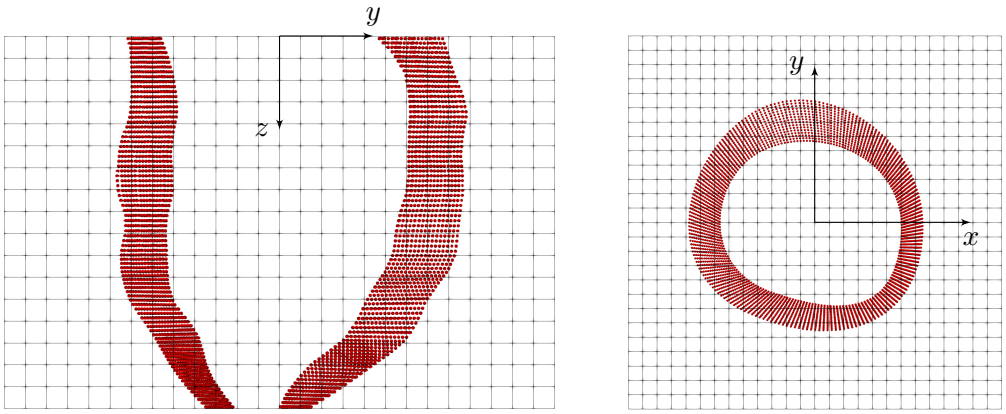

(a) (b)

Figure 7.1: Baseline model geometry and background mesh in (a) long axis and (b) short axis views.

The baseline material parameters used for the Holzapfel-Ogden (H-O) material model are taken to be those proposed by Wang *et al.* [319] (or W-W parameters), which are given as

$$a = 0.2362\,\text{kPa} \quad a_f = 20.037\,\text{kPa} \quad a_s = 3.7245\,\text{kPa} \quad a_{fs} = 0.4108\,\text{kPa}$$
$$b = 10.810 \quad b_f = 14.154 \quad b_s = 5.1645 \quad b_{fs} = 11.300.$$

As discussed in Section 5.2.3, there is little difference in the shear behaviour of a myocardium block using the W-W parameters and those presented by Göktepe *et al.* [115]. The W-W parameters have been chosen due to the closer fit for higher shear values to the experimental data presented by Dokos *et al.* [85]. The bulk modulus of the material is calculated using (5.17) based on a Young's modulus of $E = 10\,\text{kPa}$ [7, 90, 158] and a Poisson's ratio of $\nu = 0.33^*$, giving a baseline bulk modulus of $K = 9.8\,\text{kPa}$. It is worth noting that in Section 7.4, this value of bulk modulus will be used as the reference bulk modulus, K_{ref}, when comparing analyses with different levels of incompressibility. Based on this value of bulk modulus, the ghost stabilisation parameter is $\gamma_G = 0.98\,\text{kPa}$.

*This value is taken such that the material is compressible to study the effect of increasing the bulk modulus in Section 7.4.

The baseline case of fibre orientation is taken as a fibre angle of $\theta_f^{endo} = 70°$ at the endocardial surface and $\theta_f^{epi} = -70°$ at the epicardial surface, which changes linearly in the transmural direction. No rotation of the sheet direction is considered for this case ($\theta_s^{endo} = \theta_s^{epi} = 0°$).

Figure 7.15 shows the fibre stress and radial displacement fields through cross sections of the LV model at the end of the analysis at an applied pressure of 5 mmHg. Figures 7.15a and 7.15b show the fibre stress and radial displacement for each MP in a cross section of the LV wall in the long axis view, where the left section of the wall is the septal wall and the right section is the free wall. The undeformed configuration of these wall segments are shown as black wireframe meshes of the endocardial and epicardial surfaces (using the boundary points from the B-spline surface representations). The variation in fibre stress through the thickness of the LV wall can be clearly seen in Figure 7.15a, with a greater fibre stress at the midwall region and a decrease in stress when moving towards the endocardial or epicardial surfaces. As the pressure is applied, the domain displaces radially outwards and a circumferential strain will be seen in the material. This circumferential strain manifests stresses in the circumferential direction. Due to the nature of the fibre orientation in this model, the maximum fibre stress will be seen when the orientation of the muscle fibres are aligned with the circumferential direction. For the fibre orientation used in this model, the maximum fibre stress occurs at the midwall region. As the muscle fibres transition to the longitudinal direction towards the endocardial and epicardial surfaces, lower fibre stresses will be seen. Larger stresses are in the septal wall compared to the free wall, due to it being thinner and having more deformation, as can be seen in Figure 7.15b. Similar observations can be made from the short axis views in Figures 7.15c and 7.15d, which are at a position halfway through the longitudinal length of the model ($z = 40$ mm). Similar to the long axis views, the underformed endocardial and epicardial walls are shown with black wireframe meshes. In Figure 7.15c, the larger fibre stresses at the midwall region can be seen as well as decrease in fibre

stress closer to the LV surfaces. Figure 7.15d shows the larger radial displacements in the septal wall at the bottom left of the cross section compared to the free wall at the upper right of the plot.

7.2 Effect of material parameters

Firstly, the effect of the material parameters on the results of the LV analysis will be investigated. In Section 5.2.3, a comparison was made between the W-W parameters used in the baseline model and the material parameters proposed by Göktepe *et al.* [115] (or G-K parameters). It was found that the two sets of parameters produce similar stress-strain results for a myocardium block under pure shear. The validation test for the H-O model is not representative of the deformation of a model of the LV. Therefore, the comparison of two models with different material parameters will provide a greater understanding of the effect of the material parameters on the stresses and displacements seen in the LV model.

The analysis of this LV model is generated in the same manner as for the baseline case, however, the material parameters for the anisotropic H-O model are prescribed as

$$a = 0.496\,\text{kPa} \quad a_f = 15.193\,\text{kPa} \quad a_s = 3.283\,\text{kPa} \quad a_{fs} = 0.662\,\text{kPa}$$
$$b = 7.209 \qquad b_f = 20.417 \qquad b_s = 11.176 \qquad b_{fs} = 9.466.$$

Figure 7.16 shows the cross section of the LV model in the long and short axis views for the MP fibre stresses and radial displacements. Comparing these plots to the baseline model in Figure 7.15, it is clear that the two analyses display similar stress distributions and displacement distributions through the LV wall. The overall deformation of the LV wall also appears alike for both sets of parameters. However, the analysis with the G-K parameters displays a larger range of fibre stress values in the long axis, with a larger maximum tensile stress seen. In Figure 7.16a, the fibre stress through the LV wall can be seen, the distribution of the fibre stresses are

reasonably similar compared to the baseline model. The large tensile stress seen in this LV model occurs at the endocardial surface of the basal plane at the septal wall. This may be a numerical error from the MPM at non-conforming boundaries. The short axis view of fibre stress, seen in Figure 7.16c, shows similar MP displacements to the baseline model. The radial displacement fields shown in Figures 7.16b and 7.16d are almost identical, with a slight variation in the calculated maximum and minimum radial displacements, which means that the material parameters have no effect on the displacement field of the LV model.

The LV chamber volume (the volume contained within the B-spline surface representation of the endocardial surface) is calculated throughout the analysis, at intervals of 25 load steps, as the applied pressure is increased. Figure 7.2a shows the calculated chamber volume for the two models: the W-W parameters (baseline model) and the G-K parameters. It can be seen that the chamber volume for both models is very similar throughout the analysis, with the G-K parameters seeing a slightly larger chamber volume at higher pressures. The relative difference between the volumes for the two models are quantified using (7.1) where, for a given applied pressure, V_i^{model} is the volume of the G-K parameter model and a linear interpolation between data points is assumed. The calculated differences in volume are shown in Figure 7.2b where there is less than a 1% difference between the chamber volumes throughout the analysis.

Similarly, the volume of the physical domain is calculated as the sum of the volumes associated with each MP and is shown in Figure 7.3a as the applied pressure is increased through the analysis. As with the chamber volume, the two models display similar domain volumes. This is supported by the relative difference in domain volume shown in Figure 7.3b, where the volume of the G-K model is within 0.1% of the baseline model throughout.

Overall, it is expected that these two sets of material parameters produce results which are alike as they have both demonstrated a close fit to Dokos *et al.* experimental data [85] from myocardium testing. This has been confirmed

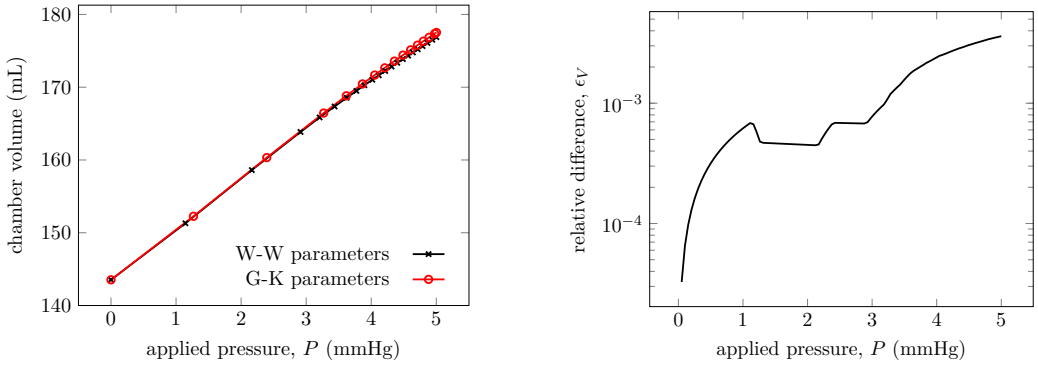

(a) (b)

Figure 7.2: Effect of material parameters: (a) LV chamber volume as pressure is applied and (b) relative difference of volume for G-K model compared to baseline model.

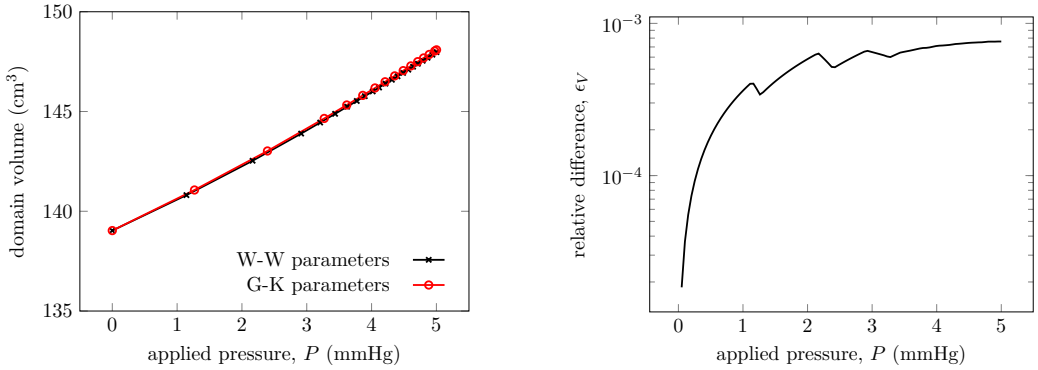

(a) (b)

Figure 7.3: Effect of material parameters: (a) LV MP domain volume as pressure is applied and (b) relative difference of volume for G-K model compared to baseline model.

through the validation case given in Section 5.2.3.

7.3 Effect of fibre orientation

Three fibre orientations are considered in this chapter and are given in Table 7.1. Fibre Orientation A is the baseline case with a fibre angle distribution based on the model presented by Göktepe *et al.* [115], Fibre Orientation B uses the fibre angle distribution proposed by Streeter Jr. *et al.* [286] with the sheet angles proposed by Hunter and co-workers [156] and Fibre Orientation C is the distribution of the fibre

and sheet directions used in the LV model presented by Nikou *et al.* [232]. Other than the variation in fibre and sheet orientations, the LV models are generated in the same manner as the baseline case.

Fibre Orientation	θ_f^{endo}	θ_f^{epi}	θ_s^{endo}	θ_s^{epi}
A	70°	-70°	0°	0°
B	60°	-60°	45°	-45°
C	83°	-37°	45°	-45°

Table 7.1: MP fibre and sheet orientation distributions between the endocardial and epicardial surfaces.

The MP fibre directions for each fibre orientation is shown in Figure 7.4 for a section through the LV wall. The arrows are coloured based on their transmural position (the position through the thickness of the LV wall), with red being at the endocardial surface and blue at the epicardial surface. There are clear differences between the three fibre orientations. Due to Fibre Orientation A not having any sheet rotation, the fibre directions are all parallel to the circumferential direction, whereas, when sheet rotation is introduced in Fibre Orientations B and C, this is no longer the case. Orientations A and B are still aligned with the circumferential directions in the midwall region, due to there being no fibre rotation in this part of the LV wall as the fibre angles at the endocardial and epicardial wall are equal and opposite. However, for Fibre Orientation C, the fibre rotation angles at the two surfaces are not equal and opposite meaning that the midwall region no longer sees the purely circumferential fibre directions.

Figure 7.17 shows the MP fibre stress and radial displacement of the LV model using Fibre Orientation B. This model displays a similar fibre stress distribution to the baseline model with the band of higher fibre stress in the midwall region which reduces nearer the surfaces of the LV wall. The magnitudes of the MP stresses are similar to the baseline case. Looking at the short axis view in Figure 7.17c, the band of higher fibre stress in the midwall region is more prominent for this model, with larger stresses seen in the septum wall portion of the cross section and a higher maximum stress on the bottom right of the plot. The more substantial differences

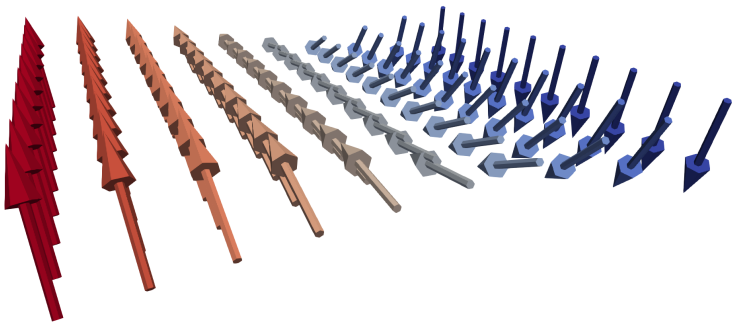

Fibre Orientation A

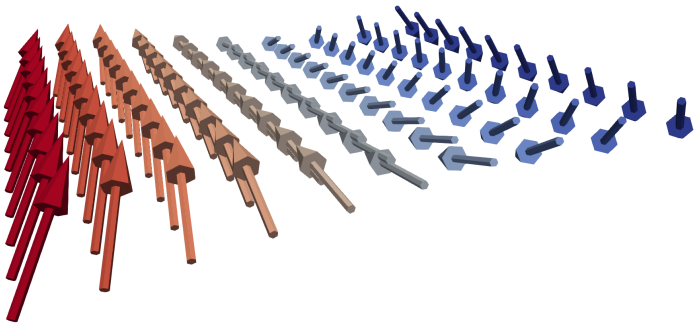

Fibre Orientation B

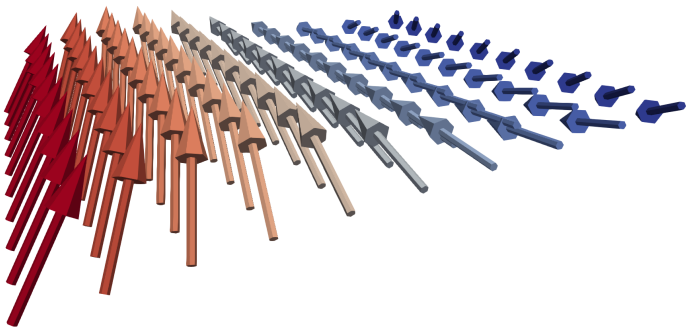

Fibre Orientation C

Figure 7.4: MP fibre direction through the LV wall for the three considered fibre orientation cases (refer to Table 7.1 for rotation angles). The arrows are coloured according to their transmural position, red arrows at the endocardial surface and blue arrows at the epicardial surface.

between the two models can be seen in the radial displacements, where a greater maximum displacement is in the septum wall for both the long axis (Figure 7.17b) and short axis (Figure 7.17d) views. The section of the free wall near the apex region also sees much higher displacement compared to the baseline, as can be seen in Figure 7.17b. This increase in radial displacement may be due to the rotation of the sheet direction which is no longer oriented normal to the LV surfaces, meaning that there is less resistance to the displacement of the wall due to the applied pressure normal to the endocardial surface.

Figure 7.18 shows the results of the LV model using Fibre Orientation C. Initially, it is clear to see that the fibre stress distribution is considerably different to the baseline model. The larger fibre stresses are now seen closer to the epicardial surface, as this is where the fibre directions will be aligned with the circumferential direction, rather than halfway through the thickness of the wall. In Figure 7.18a, the range (difference between the maximum and minimum) of fibre stresses are reasonably similar to the baseline case. However, Figure 7.18c shows a lower maximum tensile stress and a much larger maximum compressive stress (almost an order of magnitude greater) at the endocardial surface. This may be due to the large fibre rotation angle at the endocardial surface, where the fibres are more aligned with the longitudinal direction. This compressive fibre stress is seen across the endocardial section of the LV wall, something that is not seen in the baseline model. As the fibre rotation angle at the epicardial surface is considerably smaller than that at the endocardial surface, larger tensile stresses are seen from the midwall region to the epicardial surface with significantly larger tensile stresses seen at the septum and free wall regions of the LV. A similar radial displacement field as for Fibre Orientation B is seen. However, the LV free wall sees an increased radial displacement, possibly due to the fact that the fibres are more closely oriented to the circumferential direction. Compared to the baseline model, Figure 7.18b shows that the radial displacement of the free wall is more concentrated towards the bottom of the model where the wall is thinner. The larger radial displacement

of the free wall is noticeable in Figure 7.18d when compared with Figure 7.15d.

Figure 7.5a shows the LV chamber volume as the applied pressure is increased for the three LV models with varying fibre orientations. This confirms what was seen in the radial displacement fields where Fibre Orientation B caused a larger displacement of the LV wall compared to the baseline model and Fibre Orientation C saw much greater displacement. The initial evolution of the chamber volume appears to be similar for the three models, until around an applied pressure of 1.5 mmHg. The rate of increase in volume at higher applied pressure varies based on the sheet orientation, Fibre Orientation A has a lower rate of volume increase compared to Fibre Orientations B and C, which are more similar after an applied pressure of 3.5 mmHg. This may be due to the fact that the sheet direction is not aligned with the normal to the endocardial surface for Fibre Orientations B and C.

From Figure 7.5a, it is clear to see the differences in the LV chamber volume for each model compared to the baseline as the applied pressure is increased. For completeness, Figure 7.5b the relative differences in chamber volume for the Fibre Orientation B model (solid red line) and the Fibre Orientation C model (dashed blue line) compared to the baseline model. During the first half of the analysis of Fibre Orientation B, the LV model had a chamber volume lower than the baseline model. However, after an applied pressure of approximately 2.75 mmHg, the chamber pressure for the Fibre Orientation B model showed a higher rate of increase in chamber volume than the baseline model. Overall, the maximum difference between the Fibre Orientation B model and the baseline model was around 0.1%, occurring at the end of the analysis. The Fibre Orientation C model had a LV chamber volume consistently larger than the baseline model throughout the analysis. A maximum difference of 0.35% was seen between the two models and occurred at the end of the analysis also.

The volume of the physical domain is shown in Figure 7.6a, but there are no significant variations in the domain volume with respect to the fibre orientation changes. The relative differences are shown in Figure 7.6b, where the difference

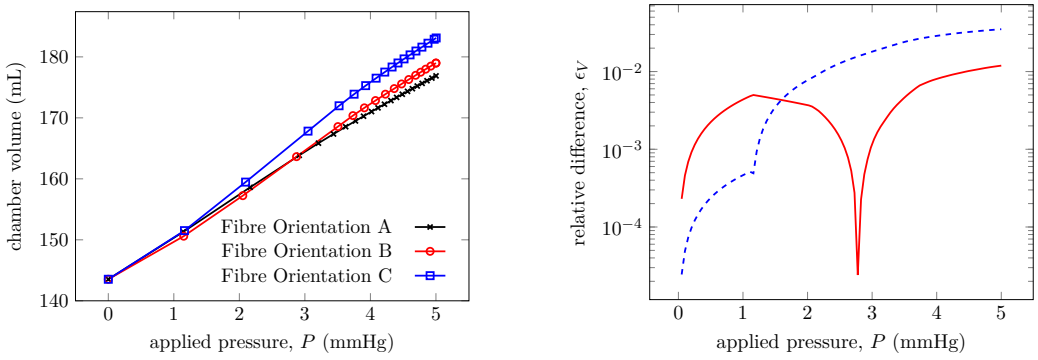

(a) (b)

Figure 7.5: Effect of fibre orientation: (a) LV chamber volume as pressure is applied and (b) relative difference of volume for Fibre Orientation B (solid red line) and Fibre Orientation C (dashed blue line) models compared to baseline model.

between the model using Fibre Orientation B and the baseline is shown as the red line and between the model using Fibre Orientation C and the baseline is shown as the blue line. Both cases have domain volumes within 1% of the baseline across the analyses. This is unsurprising as this is controlled by the material behaviour rather than the directions of the muscle fibre.

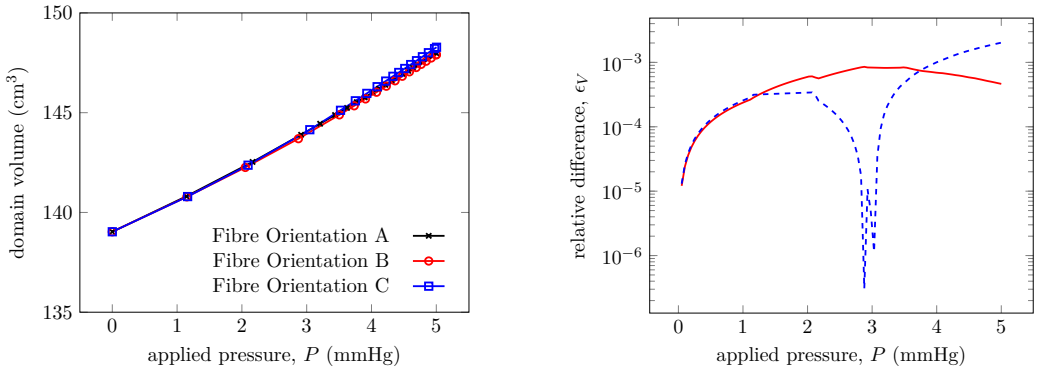

(a) (b)

Figure 7.6: Effect of fibre orientation: (a) LV MP domain volume as pressure is applied and (b) relative difference of volume for Fibre Orientation B (solid red line) and Fibre Orientation C (dashed blue line) models compared to baseline model.

7.4 Effect of incompressibility

It was mentioned in Chapter 5 that myocardium is often modelled as a nearly incompressible material. Therefore, in a similar manner to the validation of the isotropic Ogden model in Section 5.1.1, the bulk modulus used in the LV model is increased to simulate the near incompressibility of the myocardium. Recall, the baseline model had a bulk modulus for a compressible material. Therefore, to enforce near incompressibility for the LV model, the bulk modulus was increased by a factor of 10 and 100. Table 7.2 shows the bulk modulii for the three LV models compared in this section and the equivalent Poisson's ratio for each bulk modulus as a signifier for the level of near incompressibility of each model. It is worth noting that, as the ghost stabilisation parameter, γ_G, for each LV model is calculated based on the bulk modulus value. This means that the ghost stabilisation parameter increases by a factor of 10 and 100 accordingly with the bulk modulus. The values of the ghost stabilisation parameter for each model is given in Table 7.2.

K/K_{ref}	Bulk modulus, K (kPa)	Poisson's ratio, ν	Ghost stabilisation parameter, γ_G (Pa)
1	9.8	0.330	980
10	98	0.483	98
100	980	0.498	9.8

Table 7.2: Bulk modulii values, equivalent Poisson's ratios and ghost stabilisation parameters for the LV models.

Figure 7.19 shows the results of the LV model with a bulk modulus ten times greater than K_{ref} used in the baseline model. The MP fibre stress fields seen in Figures 7.19a and 7.19c have a similar distribution to the baseline model, with a band of higher tensile stresses seen in the midwall region and through the length of the model. The tensile stresses in the myocardium are similar in magnitude compared to the baseline, however, there are larger compressive stresses seen at the epicardial surface, near the apex region of the free wall (bottom right of Figure 7.19a). As this is on the boundary of the physical domain, this may be the typical

boundary errors seen the MPM. The same can be seen in Figure 7.19c, the stress field in the short axis view closely matches the baseline model. However, there is a region in the bottom right which sees a maximum compressive stress around eight times greater than the maximum compressive stress of the baseline model. Again, as this is at the boundary, this can be caused by the small cut problem. The effect of the incompressibility is clearer comparing the undeformed and deformed configurations in Figure 7.19b. It is obvious that the deformation of the physical domain has greatly reduced in both the septal wall and free wall. The maximum radial displacement for this model (seen in the septum wall) has reduced by 34% in both the long axis and short axis views.

Figure 7.20 shows the MP fibre stresses and radial displacements for the LV analysis using a bulk modulus which is 100 times greater than the baseline model. Firstly, there is clear checkerboarding of the MP stresses throughout the physical domain, meaning that volumetric locking is influencing the results. Due to the nature of this parametric study, the F-bar technique [57, 74, 75] was not implemented for any model. As discussed in Section 2.1.5, applying the F-bar technique would overcome the issue of volumetric locking, but is not considered for this study. Thus, an accurate response cannot be estimated for this level of incompressibility. Comparing the radial displacement of the LV model to the baseline, the maximum radial displacement is reduced by 46% in the long axis and 47% in the short axis, with the physical domain not seeing and significant change in shape.

For both models which have an increased bulk modulus, the epicardial surface experiences smaller radial deformation at the free wall of the LV compared to the septum wall, this is seen by all of the LV models. However, looking at the free wall epicardial surface, there is little difference between the undeformed and deformed states. This is because of the increased stiffness of the material which is made clearer when comparing the changes in LV chamber volume as the applied pressure is increased. Figure 7.7 shows the LV chamber volume for the three LV models through each of the analyses, where the baseline model is shown in black,

the model with ten times the bulk modulus is shown in red and the LV model which has a bulk modulus 100 times greater than the baseline is shown in blue. When compared to the baseline model, the model which has a bulk modulus of $K = 10K_{ref}$ shows a 6% decrease in chamber volume at the end of the analysis, whereas using $K = 100K_{ref}$ gives a 8% reduction in the LV chamber volume. As the level of incompressibility increases, the change in chamber volume decreases, which confirms the observation that the radial displacement of the MPs in the domain decrease as the bulk modulus increases.

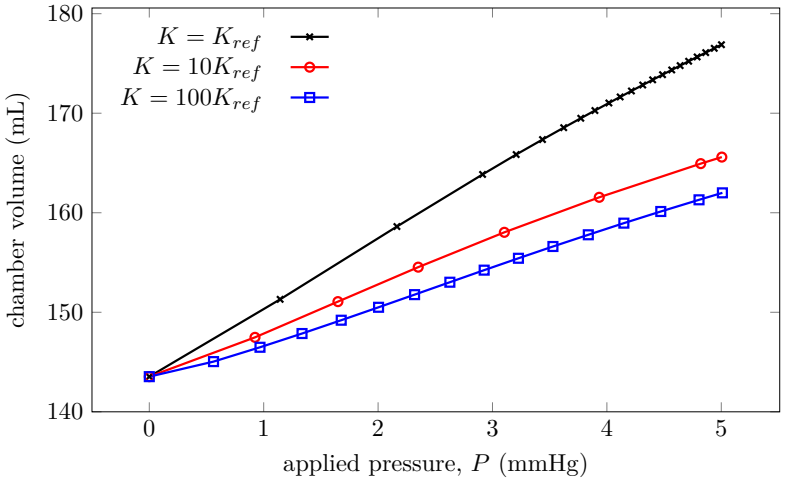

Figure 7.7: Effect of near incompressibility: LV chamber volume as pressure is applied.

The effect of the incompressibility is more obvious when looking at the total volume of the physical domain, as seen in Figure 7.8. It make logical sense that as the level of incompressibility is increased, the change in the physical domain volume decreases. This is evident when there is a significant change in volume for the compressible baseline model, with the volume increasing by 6.4%. When the bulk modulus is increased by a factor of 10, the volume only increases by 0.6%. When the bulk modulus is increased by a factor of 100, the change in domain volume is very small, seeing only a 0.05% increase, which implies that the material can be considered as nearly incompressible. Based on the small deformations seen at the epicardial surfaces of the models, it appears that the majority of the deformation is seen at the endocardial surface and the incompressibility of the material provides

significant resistance to the deformation due to the applied pressure over the endocardial surface which reduces the change in LV chamber volume over the analyses.

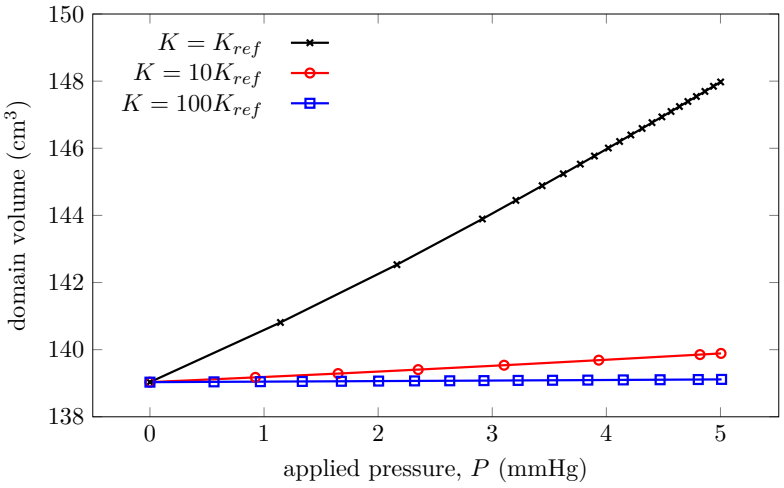

Figure 7.8: Effect of near incompressibility: LV MP domain volume as pressure is applied.

7.5 Effect of external stiffness

In Section 6.4, it was mentioned that Veress *et al.* [308] presented a LV model from segmented medical imaging data where a transversely isotropic hyperelastic material surrounded the domain of the LV wall. Similar to [308], an external stiffness was applied over the outer boundary of the LV domain. This stiffness was applied directly to the elements of the background mesh, assuming a linear elastic material with a Young's modulus of $E_{ext} = 0.3\,\text{kPa}$ and a Poisson's ratio of $\nu_{ext} = 0.3$, as per the material properties given in [308]. At the start of each load step, the elements which contain the B-spline boundary representation of the epicardial surface are determined using the same method as how the elements containing the MPs are determined, and these are referred to as the external elements. Gaussian quadrature is used with $2 \times 2 \times 2$ Gauss points to integrate the external stiffness over the external elements which is added to the global stiffness matrix used in the arc-length solver. It is worth noting that ghost stabilisation is still applied to

this model and will have restrict the gradient of the solution around the boundary of the physical domain and is typically applied to the same nodes associated with these external elements.

Figure 7.21 shows the results of the analysis of the LV model with an applied external stiffness. Between this LV model and the baseline model, almost identical MP fibre stress and radial displacement fields can be seen. The only exception is the maximum compressive fibre stress in Figure 7.21c being slightly lower than the baseline model. This may be due to the slightly higher stiffness around the epicardial boundary suppressing errors due to the small cut problem. Figure 7.9a shows the change in the LV chamber volume as the applied pressure is increased through the analysis, and the two curves appear indistinguishable. The relative difference between the the baseline model and the model with applied external stiffness is shown in Figure 7.9b, where the chamber volume when external stiffness is applied is within 0.1% of the baseline model throughout the analysis. Similarly, the change in the volume of the physical domain and relative differences between the models are shown in Figure 7.10. The physical domain volumes of the two are even more similar than the chamber volumes, with the external stiffness model within 0.01% of the baseline model. The fact that the two models produce such similar results is not unexpected. The added external stiffness is small compared to the stiffness of the material. The equivalent Young's modulus of the myocardium is 10 kPa which is 33 times larger than the applied external stiffness of 0.3 kPa. This means that no considerable change in the global stiffness matrix will be seen due to including the external stiffness.

7.6 Effect of patient geometry

The final part of this numerical study compares the results of LV models generated from two different patients. The baseline model is generated from the medical imaging data from Patient A, aged 50–59, and is compared to a second patient

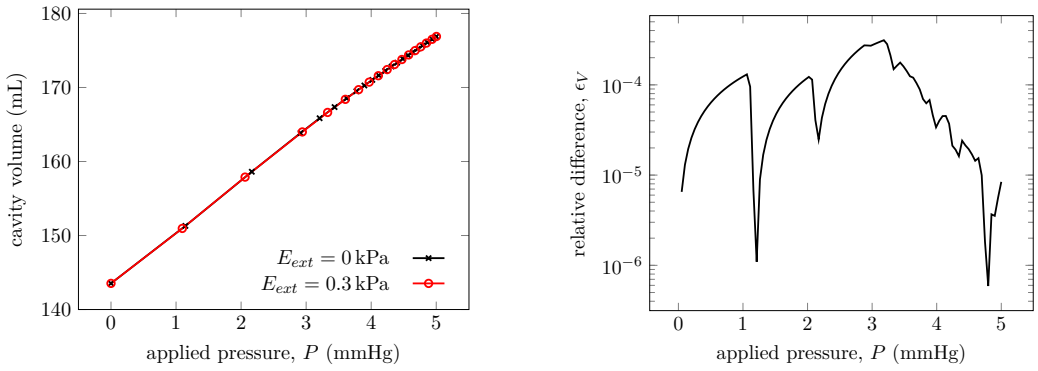

(a) (b)

Figure 7.9: Effect of external stiffness: (a) LV chamber volume as pressure is applied and (b) relative difference of volume when external stiffness is applied compared to baseline model.

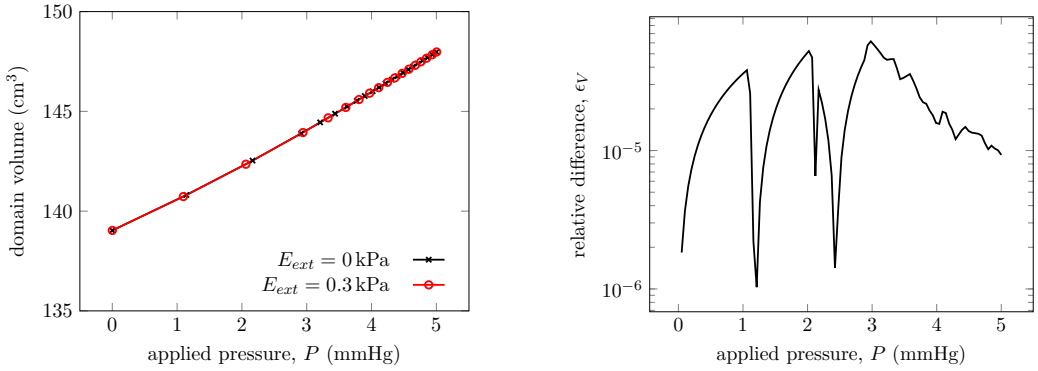

(a) (b)

Figure 7.10: Effect of external stiffness: (a) LV MP domain volume as pressure is applied and (b) relative difference of volume when external stiffness is applied compared to baseline model.

from the NMRC healthy ageing study aged 70–79, this is "Patient B".

For Patient B, the LV model is generated in the same manner as the baseline model, however, due to the different geometry of the LV, the MP and background mesh parameters are different. The B-spline surface representations of the endocardial and epicardial surfaces generated from the stack of segmented medical images of Patient B are shown in Figure 7.11. Using the target of 250 000 MPs in total with 16 MPs through the thickness of the wall, the MP mesh is generated using $n^r_{el} = 4$, $n^c_{el} = 52$ and $n^l_{el} = 19$ with $4 \times 4 \times 4$ evenly distributed generalised interpolation MPs per element of the MP mesh. This generates a physical domain

of the LV which is discretised by a total of 252 928 MPs. For the endocardial and epicardial walls, 53 points are used around the circumferential direction and 20 points are used in the longitudinal direction to generate the grid of boundary points for the B-spline surface representations. For the integration of the pressure over the endocardial surface, 3×3 Gauss points are used for each patch of the B-spline surface representation. The minimum distance between the endocardial and epicardial B-spline surfaces is calculated as $h_s^{max} = 6.02\,\text{mm}$, which is the maximum allowed size of the elements of the background mesh for this model. The minimum length of the background mesh to contain the physical domain is 48 mm, 54 mm and 84 mm in the positive x, y and z directions respectively. It is clear that the size of the LV of Patient B is larger than that of Patient A in length and thickness. To generate a quarter of the background mesh (remembering that the mesh is mirrored in the x and y directions to fully contain the physical domain), 8 elements are used in the x direction, 9 elements in the y direction and 14 elements in the z direction. As with the baseline model, the length of the mesh in the x and y directions is increased by 40%, so that 7 elements are added in the x direction and 8 elements are added in the y direction.

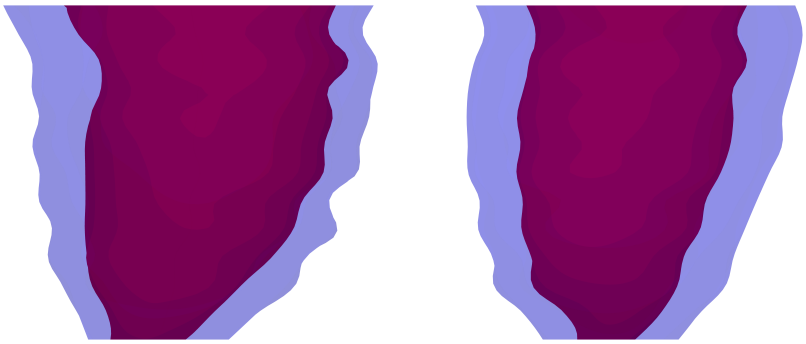

(a) side view (b) front view (into septum wall)

Figure 7.11: Fitted B-spline surface representations of the endocardial surface (red) and epicardial surfaces (blue) generated from the segmented stack of medical images from Patient B.

Figure 7.12 shows cross sections of the geometry of the LV model generated from the medical images of Patient B as well as the background mesh used in the

analysis. Comparing this geometry with the geometry of Patient A in Figure 7.1, the differences in the geometry between the two patients are very clear. There appears to be much more variation in the radial positions of the endocardial and epicardial surfaces along the longitudinal direction of the model. In addition to subject variation, there is also differences due to the segmentation of the medical images. The patient may have moved slightly when the images were taken which will cause a shift in the position of the heart for a single slice of the image stack. As no corrections are made to align the segmented data, sudden shifts in the global coordinates of the data points will affect the B-spline surface generation. This can be seen near the basal region of the septal wall, where a large bulge in the wall is present, and halfway down the free wall, where there is a notch in the epicardial wall. Looking at the long axis view, the septum wall appears to have a more vertical region near the apex compared to Patient A. Patient A displays a smoother curvature of the free wall in the longitudinal direction, Patient B appears to have a vertical section of the wall in the upper portion and transitions to a more diagonal portion towards the apex.

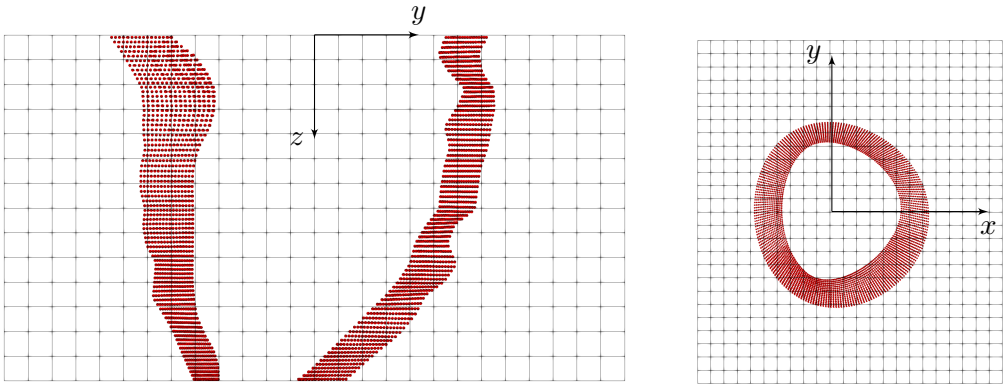

(a) (b)

Figure 7.12: Patient B model geometry and background mesh in (a) long axis and (b) short axis views.

Figure 7.22 shows the results of the analysis of Patient B. The MP fibre stresses in Figure 7.22a display a similar distribution to the baseline model, with the larger stresses in the midwall region due to the fibres being aligned with the

circumferential direction. However, it appears that the free wall of Patient B sees the higher maximum tensile fibre stresses than the septum wall, which is the opposite of what is seen with Patient A. This may be due to the fact that the free wall has a similar thickness to the septum wall, which means that the free wall will deform more than for the baseline model, hence the larger tensile stresses. In terms of the compressive fibres stresses, the free wall sees similar stresses through the longitudinal direction. The septum wall of Patient B sees larger compressive stresses around the basal region compared to the baseline model due to the thickness of this region. The short axis view in Figure 7.22c shows a 25% reduction of maximum tensile fibre stress in the midwall region of the model compared to the baseline, but a 70% increase in the maximum compressive stress. This is due to the difference in the geometry between patients. The thinner wall of Patient B means that there is a higher rate of change of fibre angles through the thickness of the wall so that less MPs will have fibres approximately aligned with the circumferential direction.

The radial displacement of the MPs in Figure 7.22b is considerably different to the baseline model. The maximum and minimum values of the displacement are similar but the MPs displace in a much different manner. Considering the septal wall, where Patient A sees a consistent radial displacement of the MPs through the longitudinal direction, Patient B displays little displacement in the basal region with a gradual increase in displacement towards the apex region. A similar observation can be made for the free wall, where there is a similar displacement at the basal region for both patients but a higher displacement at the apex region for Patient B. It appears that the notch in the free wall has a considerable effect on the deformation of the LV model. Figure 7.22d shows the radial displacement in the short axis halfway through the longitudinal length of the model. A similar displacement field is seen in the septum wall for both patients, however, the free wall of Patient B appears to displace by a similar magnitude to the septum wall, which is not seen the baseline model. This may be due to the the thinner free wall

of the model for Patient B.

Figure 7.13a shows the LV chamber volume through the analyses of each patient. The model generated for Patient B is larger in the longitudinal direction due to having an extra segmented slice of the image stack, which is responsible for the larger volume seen by Patient B. Due to the different geometries of the patient LVs, it is not suitable to simply compare the volumes of the two models. Therefore, it is more beneficial to compare the rate of change of the chamber volume through the analyses, as shown in Figure 7.13b. Both patient models show similar trends in the rate of volume change, with an initial increase in the rate of change followed by a gradual decline in the rate. Patient A sees a continually higher rate of volume change through the analysis than Patient B which is consistent with the observations of the two models, where Patient A displays greater radial displacement of the LV walls compared to Patient B.

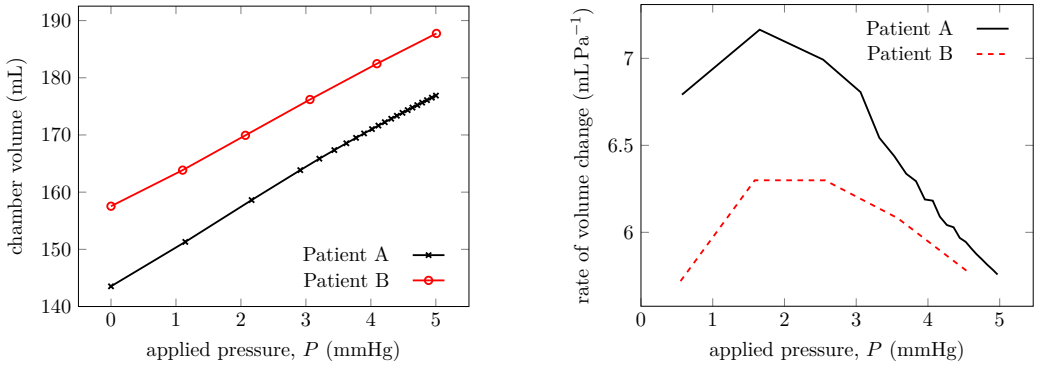

Figure 7.13: Effect of patient geometry: (a) LV chamber volume and (b) rate of change of chamber volume as pressure is applied.

Figure 7.14a shows the volume of the physical domain throughout the analysis of both patient models. As with the chamber volume, it is more useful to compare the rate of change of the domain volumes through the analyses rather than the actual volumes. The rate of volume change against applied pressure for both patient models is shown in Figure 7.14b. Both models demonstrate similar rates of change in volume throughout the analysis. Patient A sees a slightly higher rate compared to

Patient B, but this may be due to the fact that Patient A shows larger deformation of the LV wall.

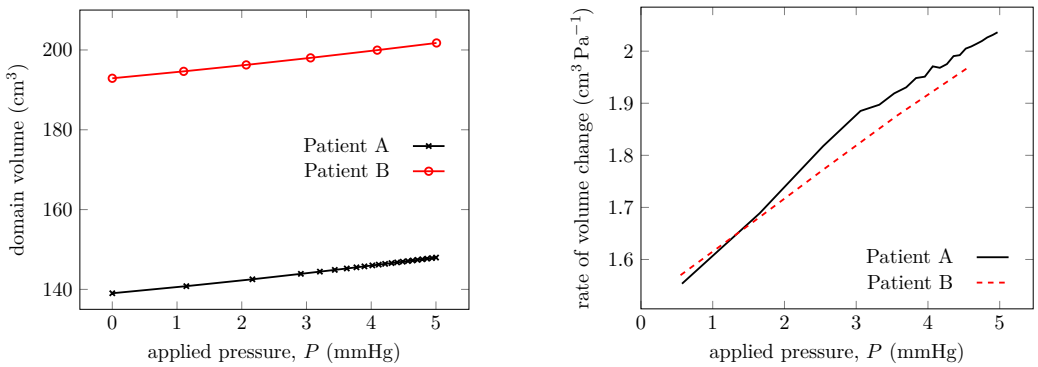

Figure 7.14: Effect of patient geometry: (a) LV MP domain volume and (b) rate of change of domain volume as pressure is applied.

Summary

This chapter presented a numerical study of the first patient-specific model of the human LV using the MPM. The sensitivity of the LV model to a series of parametric changes has been examined, comparing a baseline model to models with varying material properties, fibre orientations, boundary conditions and patient geometries. An overview of the eight models shown in this chapter is given in Table 7.3. Model 1 was taken as the baseline model and the altered parameter for each subsequent model is highlighted in red for reference.

When comparing the material parameters used for the anisotropic H-O material model, it was found that there is very difference in the results of two analyses. This is due to the fact that both sets of material parameters were determined such that the material behaviour matches experimental data. More considerable differences were observed between models with varying fibre orientations. The distribution of the muscle fibres through the thickness of the LV wall determines the position of the maximum fibre stress in the transmural direction, which are typically seen

Material parameters	Fibre orientation	Bulk modulus (kPa)	External stiffness (kPa)	Patient	Section	Figure
W-W	A	9.8	0.0	A	7.1	7.15
G-K	A	9.8	0.0	A	7.2	7.16
W-W	B	9.8	0.0	A	7.3	7.17
W-W	C	9.8	0.0	A	7.3	7.18
W-W	A	98	0.0	A	7.4	7.19
W-W	A	980	0.0	A	7.4	7.20
W-W	A	9.8	0.3	A	7.5	7.21
W-W	A	9.8	0.0	B	7.6	7.22

Table 7.3: Parameters of the LV models used in this numerical study. Altered parameters are highlighted in red for each model.

when the muscle fibres are aligned with the circumferential direction. The volume of the LV chamber was examined, the distribution of fibre orientation in the LV wall appears to have an effect on this, whether it is due to the rotation of the muscle sheet reducing the resistance to the deformation normal to the endocardial surface or having a bias of the muscle fibres angle towards the endocardial surface. This finding is significant due to the fact that it is often not highlighted in the published literature. Many cardiac mechanical models use standard sets of fibre and sheet angle distributions. However, as seen in this analysis, the orientation of the fibres has a significant effect and should be taken into account when considering a patient-specific model. The effect of modelling the myocardium as a nearly incompressible material was also studied by increasing the bulk modulus of the material. As the bulk modulus increased, the level of incompressibility of the myocardium was measured based on the change of volume of the physical domain at the end of each analysis. Increasing the bulk modulus saw a decrease in the change in volume. Increasing the bulk modulus by a factor of 10 showed a considerable reduction in maximum radial displacement of the LV wall. As no mitigation of volumetric locking (an issue seen when modelling near incompressible materials) was implemented, the results when the bulk modulus is increased by a factor of 100 display inaccuracy from volumetric locking. It was found that the inclusion of an external stiffness boundary condition had little effect on the results of the model

due to the fact the external stiffness is relatively small compared to the stiffness of the physical domain. Finally, the patient-specific nature of the LV model was tested using a second patient. The two patients had significantly different LV geometries and this had a great effect on the fibre stress and radial displacement distributions in the myocardium. It was also seen that the LV model is sensitive to the quality of the segmentation of the medical image stack. If there is a sudden change in the cross section of the LV which is not accounted for in the surface generation procedure, sharp features are incorporated into the LV model which may cause stress concentrations in the myocardium.

The models presented in this chapter are the first models of the heart which have been analysed using the MPM. In the next and final chapter of this thesis, a summary of this work will be given where the advantages and limitations of this model will be discussed.

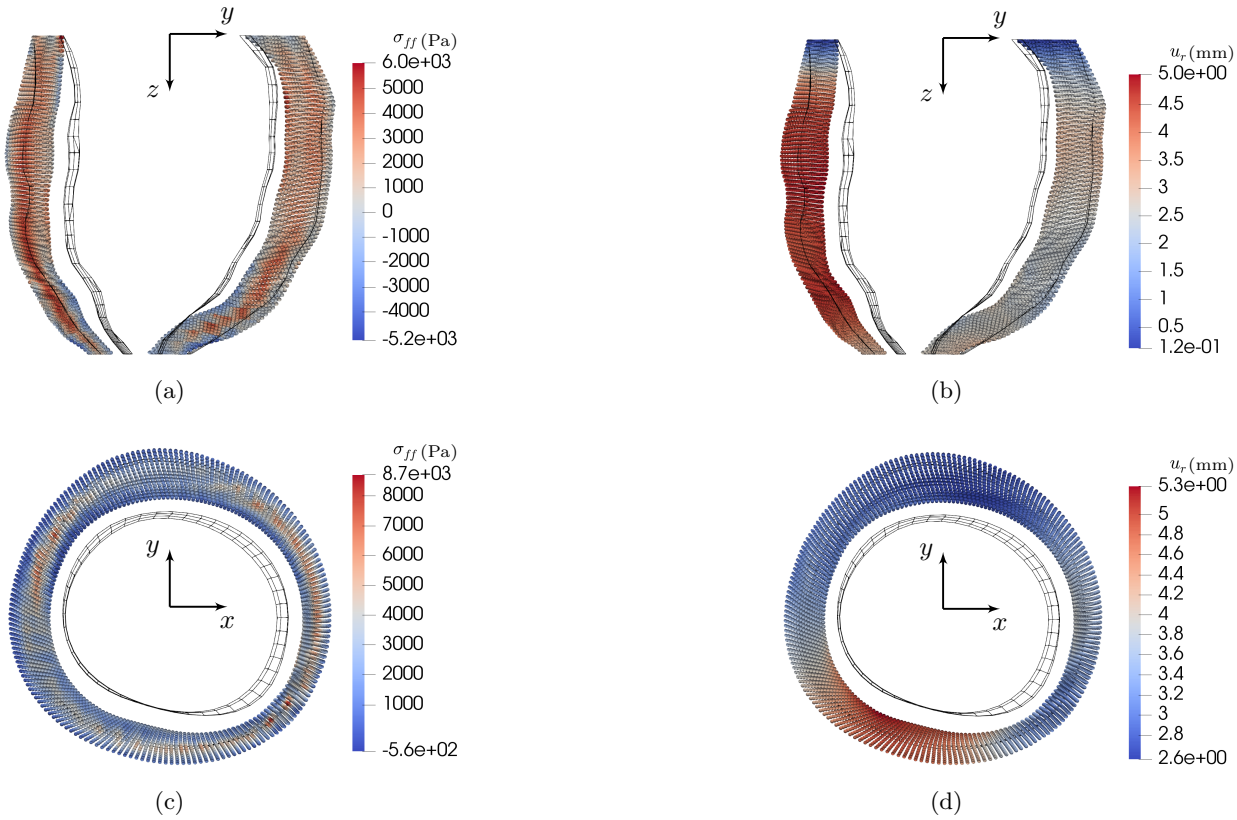

Figure 7.15: MP fibre stress (left) and radial displacement (right) throughout the LV wall for the baseline model in the long axis (top row) and short axis (bottom row) views. The undeformed endocardial and epicardial surfaces are shown as black wireframe meshes for reference.

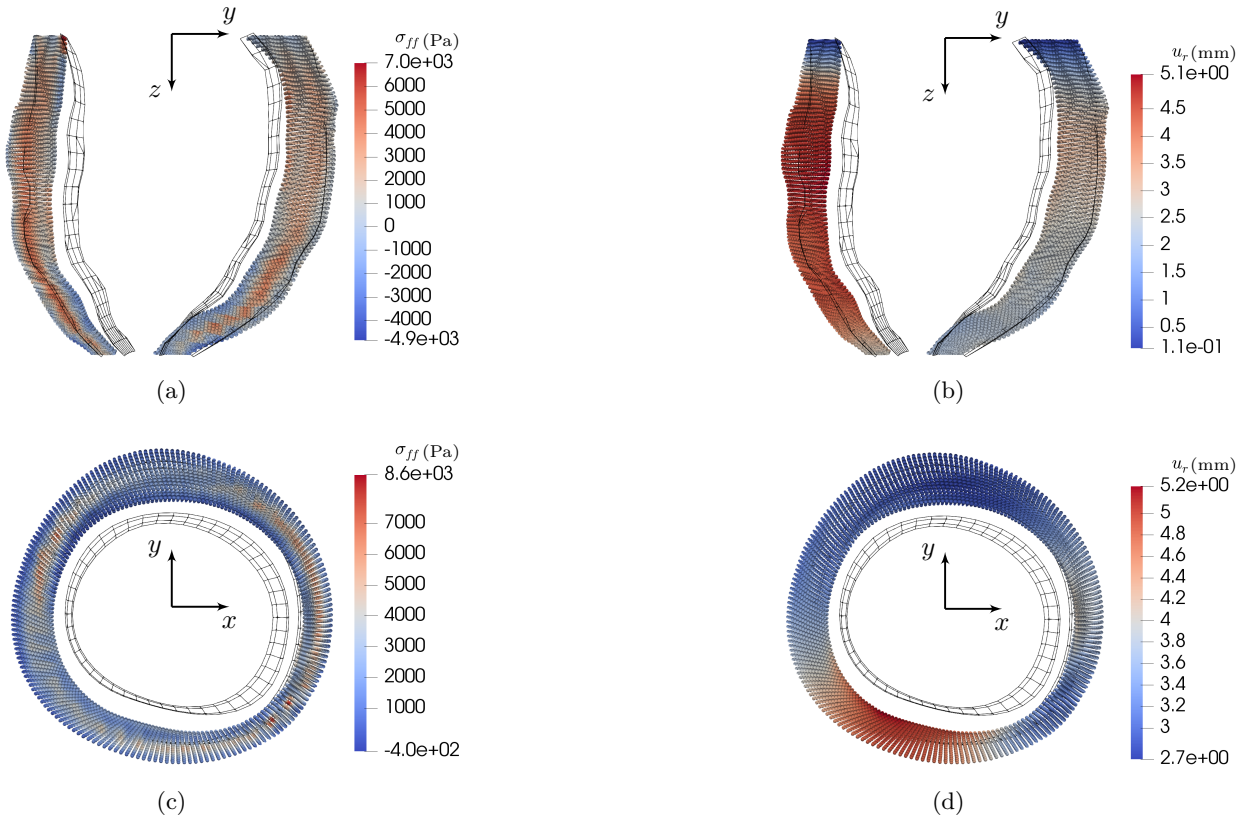

Figure 7.16: MP fibre stress (left) and radial displacement (right) throughout the LV wall for a model with the G-K material parameters in the long axis (top row) and short axis (bottom row) views. The undeformed endocardial and epicardial surfaces are shown as black wireframe meshes for reference.

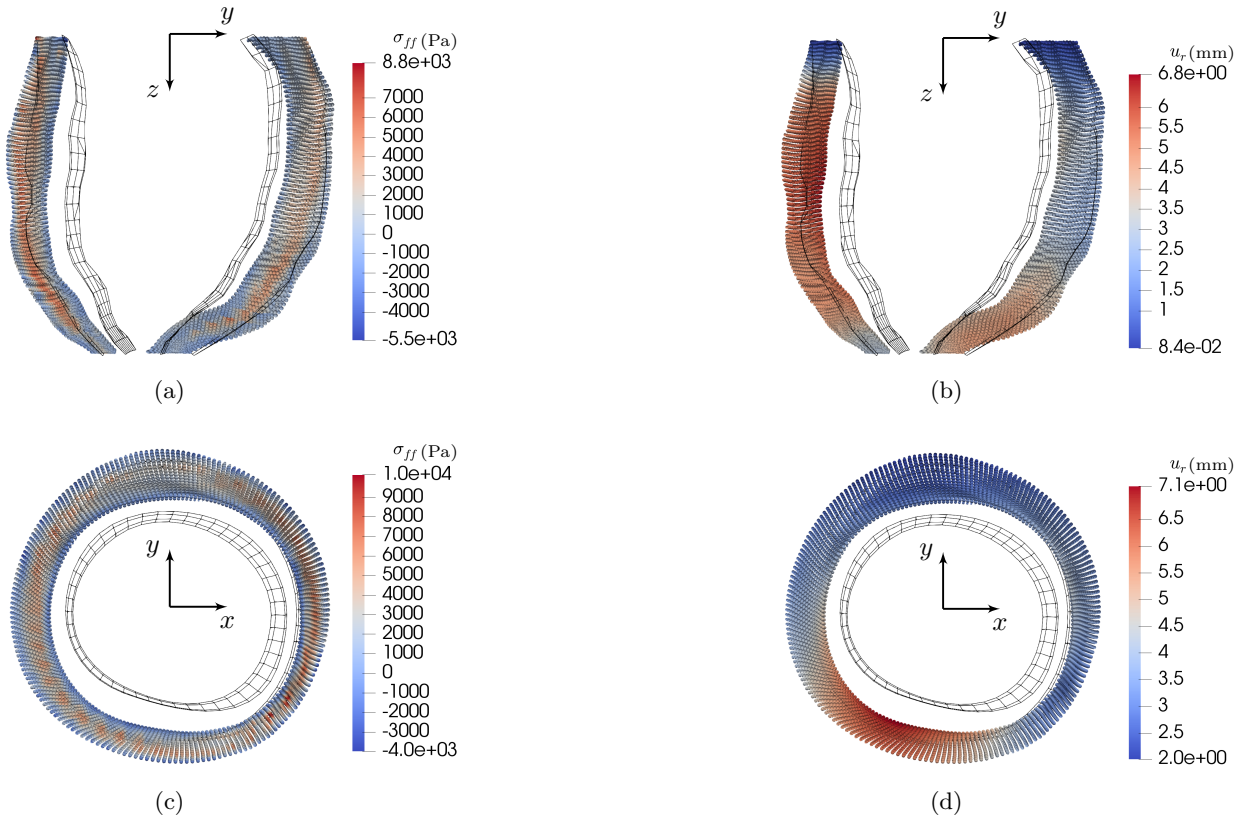

Figure 7.17: MP fibre stress (left) and radial displacement (right) throughout the LV wall for a model with Fibre Orientation B (see Table 7.1) in the long axis (top row) and short axis (bottom row) views. The undeformed endocardial and epicardial surfaces are shown as black wireframe meshes for reference.

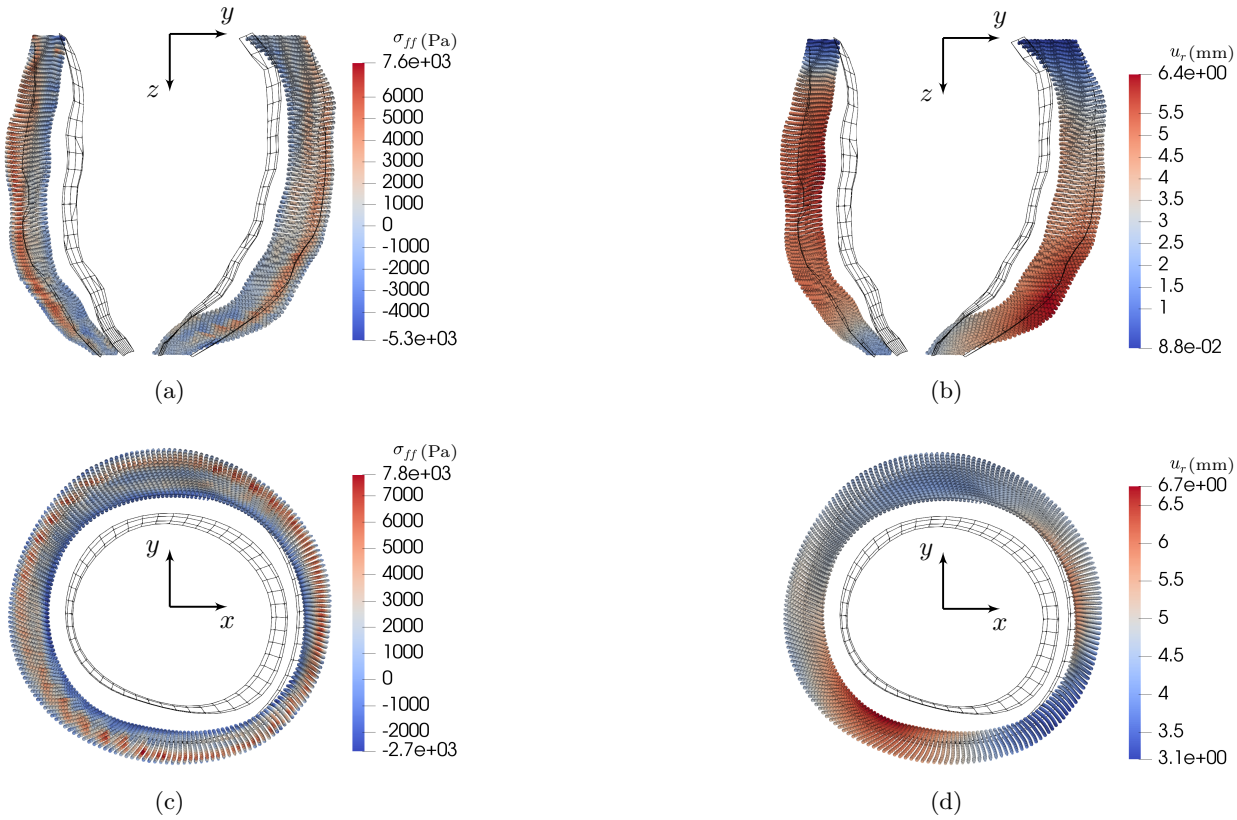

Figure 7.18: MP fibre stress (left) and radial displacement (right) throughout the LV wall for a model with Fibre Orientation C (see Table 7.1) in the long axis (top row) and short axis (bottom row) views. The undeformed endocardial and epicardial surfaces are shown as black wireframe meshes for reference.

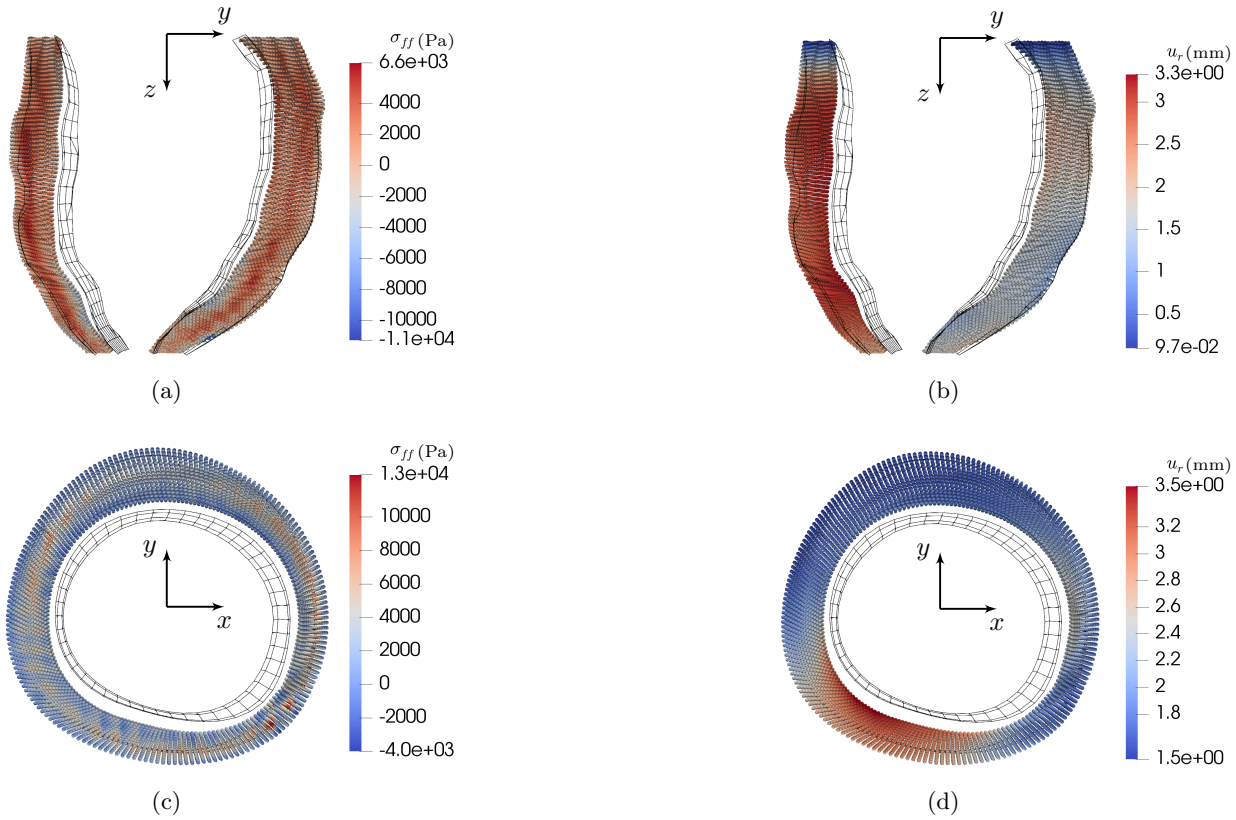

Figure 7.19: MP fibre stress (left) and radial displacement (right) throughout the LV wall for a model with a bulk modulus $K = 10K_{ref}$ in the long axis (top row) and short axis (bottom row) views. The undeformed endocardial and epicardial surfaces are shown as black wireframe meshes for reference.

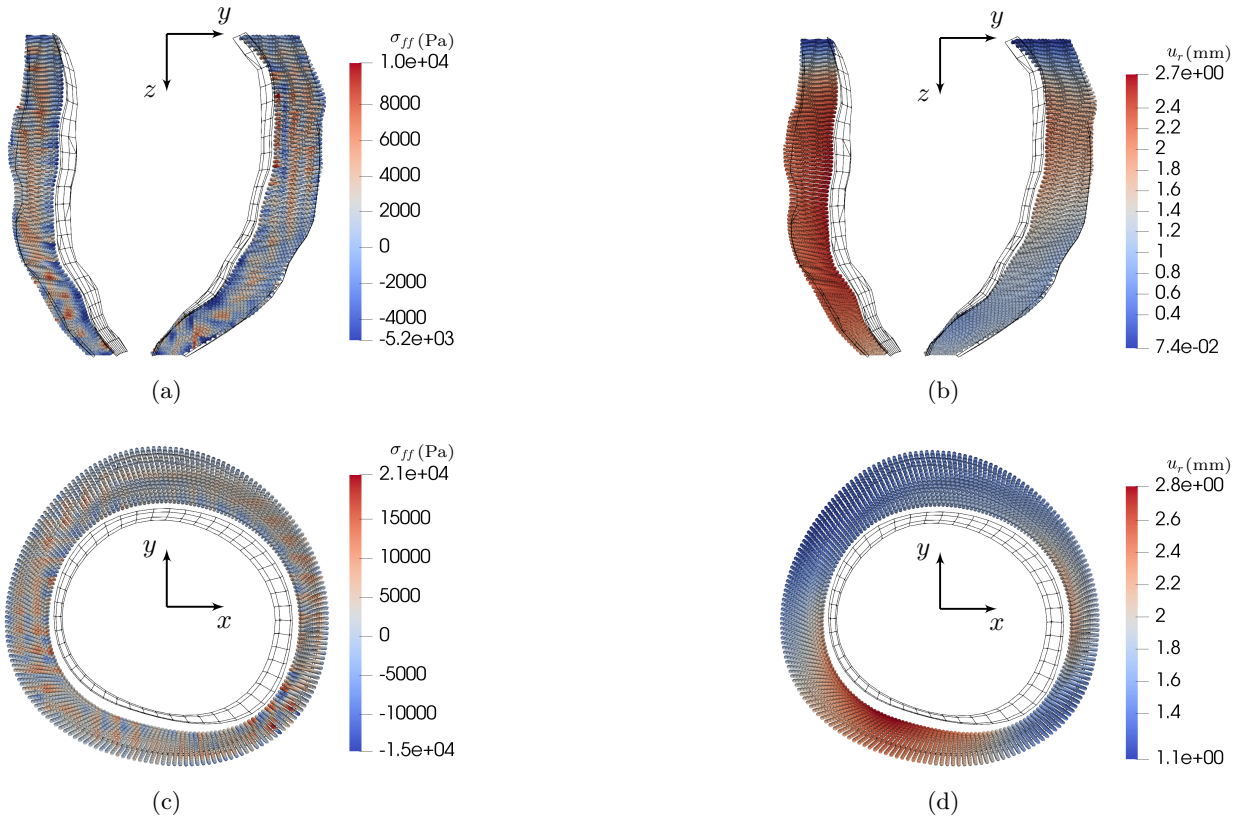

Figure 7.20: MP fibre stress (left) and radial displacement (right) throughout the LV wall for a model with a bulk modulus $K = 100K_{ref}$ in the long axis (top row) and short axis (bottom row) views. The undeformed endocardial and epicardial surfaces are shown as black wireframe meshes for reference.

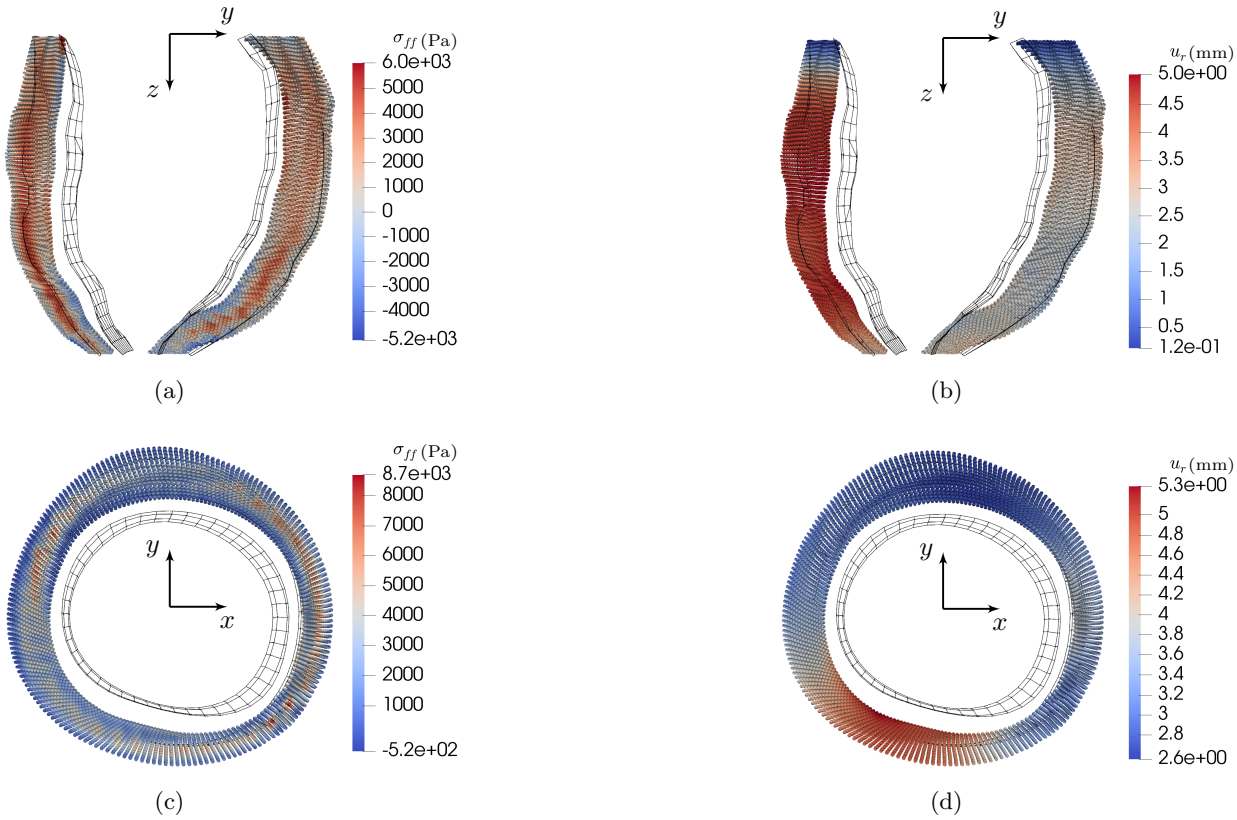

Figure 7.21: MP fibre stress (left) and radial displacement (right) throughout the LV wall for a model with an applied external stiffness in the long axis (top row) and short axis (bottom row) views. The undeformed endocardial and epicardial surfaces are shown as black wireframe meshes for reference.

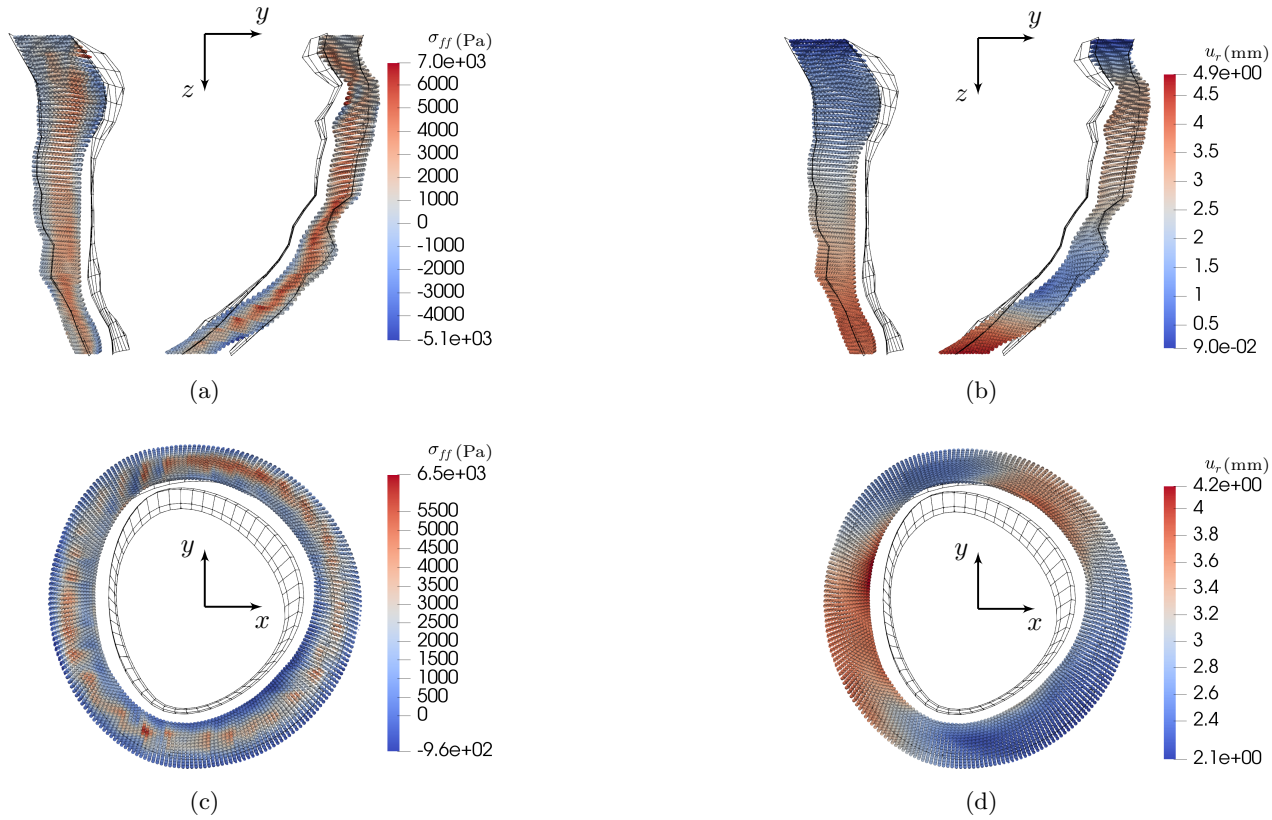

Figure 7.22: MP fibre stress (left) and radial displacement (right) throughout the LV wall for a model generated using Patient B geometry in the long axis (top row) and short axis (bottom row) views. The undeformed endocardial and epicardial surfaces are shown as black wireframe meshes for reference.

Chapter 8

Conclusions

8.1 Thesis summary

This thesis has presented the first mechanical model of the LV using the MPM, an interesting use of this relatively new method in the well established field of cardiac modelling. FEA has typically been the method of choice when modelling the heart, however, some disadvantages of the FEM have been identified in the cardiac modelling literature. While the MPM does not promise to mitigate all of the issues related with the FEM, it does bring some advantages that can be exploited to improve the modelling process. Given that physical domain of a problem does not need to be accurately meshed for the MPM, as it is discretised using MPs, the expensive pre-processing steps can be automated such that the analyst effort is significantly reduced. After the segmentation of the medical images, this work has developed a process of geometry and mesh generation, application of boundary conditions and model analysis to be executed in a single step for the user, rather than the manual approach that is commonplace with FEA models.

As this work is a new application of the MPM, many challenges were encountered where the tools may exist for the MPM but not necessarily in a suitable state for this task. Suitable modifications of these tools and the development of new tools have been required, as shown in the previous chapters, and discussed below.

Chapter 2 presented the background of the MPM with a summary of the published literature on its current applications, showing the relatively little work performed in the biomechanics field. The overview of the method was given for both small strain linear elasticity and finite deformation elasticity, both of which have be utilised in this work. A discussion on the various formulations of the MPM has been given, starting with the standard interpolation MPM and the different basis functions that may be used within the MPM, each coming with their own advantages and disadvantages. This work predominantly used the Generalised Interpolation Material Point Method (GIMPM) as it has been shown to mitigate the cell crossing instability. Given the MP domain has some finite length, the process of updating each MP domain at the end of a load step was also explained. When modelling problems involving nearly incompressible materials, it is well documented that volumetric locking will occur. Therefore, the F-bar approach for the MPM [57] was given to mitigate this issue. Another known issue with the MPM is the small cut problem due to the non-conforming boundaries of the physical domain with respect to the elements of the background computational mesh, which results in an ill-conditioned global system matrix. One method of reducing these errors and improving the stability of the analysis is the ghost stabilisation technique [36, 55] which was detailed and used throughout this work.

Chapter 3 describes the means of handling the non-conforming boundaries of the physical domains in the MPM using B-spline boundary representations. Using the work of Bing *et al.* [24], where B-spline curves were used to represent, track and apply Dirichlet and Neumann boundary conditions to the physical domain for 2D analyses, this work extends into 3D using B-spline surfaces and focusing only on Neumann boundary conditions. Starting with the definition of B-spline basis functions, the generation of B-spline curves and surfaces using a local interpolation scheme was presented. A set of data points is obtained from each segmented slice of the medical image stack, however, there is a pixelated nature of these data points based on the resolution of the medical images. A least squares fitting procedure

was presented in order to create a smoothed representation of the slice data points using B-spline curves. A fitting strength parameter was introduced to control how close the generated B-spline curve is fitted to the set of data points. Bing *et al.* [24] presented the process of imposing inhomogeneous Neumann boundary conditions over a B-spline curve for 2D analyses. This work extended this into the application of traction boundary conditions over B-spline surfaces to model 3D problems. The integration over the B-spline boundary differs in this work from that presented by Bing *et al.* in order to unify the approaches between 2D and 3D analyses. Bing *et al.* determines the sections of the B-spline curve contained within each element of the background mesh using a searching algorithm along the length of the B-spline curve. While this is a relatively simple technique in 2D, it becomes much more difficult for B-spline surfaces in 3D. Therefore, the B-spline boundaries are handled in patches between boundary points where the integration will take place. The imposition of tractions over B-spline boundary representations in 2D and 3D has been validated for problems of a thick walled cylinder under pressure (in 2D and 3D) and a 2D infinite plate under far field stress, with all three analyses showing convergence with mesh refinement.

Previous to this work, there has been no published literature on the handling of highly non-linear problems such as those which present snap-through or snap-back responses in the MPM. Chapter 4 presents the first implementation of the arc-length method within the MPM framework based on the work presented in [106], which expanded the physical problems and the loading scenarios that the MPM can solve. It was shown that it is not suitable to simply incorporate the arc-length solver as used with the FEM due to the presence of large nodal displacements of elements around the boundary of the physical domain, which take up the allowed nodal displacement over a given load step. Using the same principles as the standard arc-length method, a scaled approach was implemented based on the influence a node of the background mesh has on the physical domain, determined by the total of the MP shape functions associated with the node. This

gave rise to the Material Point-Based Arc-Length Method (MP-BALM) which overcomes the issue of the extremely large nodal displacements and allows more efficient analyses. In the first iteration of a load step, a predictor solution is required, this work uses the secant path predictor which bases the solution on the nodal displacements of the previous load step. However, a key feature of the MPM is that the MPs are advected and the background mesh is reset at the end of each load step, therefore, the nodal information from the previous load step is lost. This work reconstructs the nodal displacement field of the previous load step based on the displacements of the MPs in their updated positions using the least squares weighted residual technique. The ability of the MP-BALM to model problems with snap-through responses was demonstrated using a series of numerical examples. The effect of scaling the nodal displacements was examined by observing the progression through an analysis compared with the traditional arc-length approach. It was found that without the scaling, the analysis will "stall" due to the large nodal displacements around the boundary of the physical domain which restricts the total deformation of the model in a single load step. This means that the MP-BALM displays more consistent deformation in each load step and results in a more robust and less computationally expensive analysis. The MP-BALM was also used to model a slope collapse under gravity. While not relevant in the biomechanics field, this problem was included as a demonstration case for the use of the arc-length method in the MPM. Due to the unbounded deformation of the slope, it is not possible to model any deformation after initial failure using the standard load controlled scheme. By restricting the displacement seen in a single load step, it was possible to progress the simulation further and more extreme failure in the slope was observed. This problem provides the reasoning for using the MP-BALM for the LV models in Chapter 7 as it restricts the total deformation in a load step and improves the stability of the analysis.

Chapter 5 presents two hyperelastic material models, the isotropic Ogden model and the anisotropic, structurally based Holzapfel-Ogden (H-O) model. The

implementation of the isotropic Ogden model was used as an exercise in the application of a hyperelastic model into the MPM. Based on a strain-energy function, the Kirchhoff stresses and the consistent tangent matrix were calculated from the principal stresses. The isotropic model was validated for the stretching of a perforated rubber sheet using the FEM. It was through this validation exercise that the importance of the bulk modulus in controlling the level of near incompressibility of the material was noted, where as the bulk modulus is increases, so too does the level of incompressibility. The MP-BALM was then used to validate the Ogden model with the MPM to model a 2D thick walled cylinder under internal pressure which displays a snap-through response. The model was found to match the analytical solution closely for very large deformation of the physical domain. For the LV model, the formulation of the anisotropic H-O material model was detailed using the invariants of the right Cauchy-Green strain and defined muscle fibre and sheet directions. The H-O model was validated using experimental data of a cube of myocardium under pure shear in various directions relative to the fibre, sheet and normal directions. Using sets of material parameters taken from published literature, the implemented model was compared to the experimental data where a good fit to the data was shown for two sets of material parameters, which was later used for the LV modelling.

The steps of generating the LV model are given in Chapter 6. Starting with a stack of segmented medical images, B-spline curves are generated for each slice using the least squares fitting procedure to the data points taken from the segmentation. These B-spline curves are then used to create the geometry of the LV between the basal region (at the uppermost slice) to above the apex of the LV (the lowermost slice). This is essentially modelling the LV as a thick walled cylinder in a similar manner to the early mechanical models of the LV in the 1970's. The B-spline surfaces used to represent the endocardial and epicardial surfaces serve multiple purposes in this work. These B-spline representations are not only used to apply boundary conditions and track the deformation of the two surfaces through the

analysis, but are also used to discretise the physical domain with MPs. A temporary volumetric mesh is generated between the two surfaces which is populated with MPs, this mesh is then discarded. For each MP, fibre and sheet directions are assigned based on the position of the MP relative to the endocardial and epicardial surfaces following a rule based approach given prescribed rotation angles at the two surfaces [88, 109, 121, 183, 319]. The background computational mesh is generated to encapsulate the physical domain and allow space for the deformation of the LV under internal pressure. The size of the elements of the mesh are determined by the geometry of the LV model, with a maximum element size taken to be the minimum distance between the B-spline surface representations of the endocardial and epicardial surfaces. A discussion on the application of boundary conditions to the LV model was also given. Based on the methods presented in published literature, it was determined that the basal plane should be fixed and roller boundary conditions should be applied at the near apex region, the natural boundary condition applied to the epicardial surface and a physiological end-diastolic pressure applied over the endocardial surface.

Chapter 7 presented a numerical study of the patient-specific LV model using the MPM. Analyses were run with a series of changes made in the model generation stage to investigate the sensitivity of the model to various factors. For each analysis, the MP fibre stress and radial displacement was considered as well as the change in LV chamber volume and the volume of the physical domain. It was found that changing the set of material parameters for the H-O model made little difference to all four measures. The calculated fibre stresses and radial displacements were very similar and with a maximum of 1% difference in the volumes between the two models. This was due to the fact that the material parameters had been chosen such that the stress-strain response from the material model matched experimental data from myocardium testing. This means that it was likely that these two sets of material parameters would produce such similar results. More substantial differences were seen when comparing models with different fibre orientations. It

was seen that the distribution of the fibre direction through the thickness of the LV wall determined the position of the maximum fibre stresses where the fibres were aligned with the circumferential direction. It appears that the rotation of the muscle sheets has an effect on the radial displacement of the myocardium due to the reduction in stiffness compared to when the muscle sheet is aligned normal to the LV walls. This effect was also seen when comparing the LV chamber volumes. The bulk modulus of the material was varied to study the effect of incompressibility on the results of the model based on discussions in published literature on the incompressible nature of the myocardium. It was found that increasing the bulk modulus (thus, the level of incompressibility) has little effect on the distribution of the MP fibre stresses. However, the radial displacement of the model is significantly reduced. Without using the F-bar technique, meaning there was no mitigation of volumetric locking (a decision made such that all models are comparable), increasing the bulk modulus by a considerable amount resulted in unreasonable stress fields which presented no useful information. An external stiffness boundary condition was applied but had little effect on the results due to the small stiffness that this provided compared to the stiffness of the physical domain. Finally, as a measure of the patient-specific nature of this work, a comparison between models taken from two different patients was made. It was clear that the stress and displacement fields are highly dependent on the patient geometry and the quality of the segmentation of the medical images. When comparing the change in volumes of the two models, it appeared that both deformed in similar manners.

8.2 Recommendations for future work

Based on the results of this work, a number of key areas for improvement and development have presented themselves which could be addressed in future work.

As made clear when comparing the second patient model in Section 7.6, the results of the LV model are sensitive to the geometry generated from the stack of segmented

medical images. Many adjustments in the creation of the LV can be made to improve the quality of the models. For example, the development of a method to align the data points taken from each segmented slice to account for any patient movement during the imaging procedure. This would require some statistical modelling of the shape of the LV to determine how much realignment would be required for each slice. Another suggestion would be to incorporate machine learning algorithms to segment the medical images to fully automate the modelling process. This was deemed a full project in own right, so was not considered for this work, efforts to automate the subsequent processes were developed instead.

This initial model does not consider the apex of the LV, in a similar manner to the first published FEA models of the LV. It makes sense that the development of this MPM model of the LV should follow the same pathway. Firstly, through the inclusion of the apex to determine the effect that this may have on the rest of the structure. The author's recommendation after this would be to introduce more complexity into the model by including residual stresses. It is well documented that, in a load-free state, there exists compressive circumferential stresses at the endocardial surface and tensile circumferential stresses at the epicardial surface [239]. For the example of an artery, it was determined that if residual stresses were ignored, the tensile circumferential stress at the endocardial surface would be ten times larger than the circumferential stress at the epicardial surface under normal physiological conditions [49]. Hence, it is important to consider these residual stresses in order to obtain physiological results. However, many mechanical models of the LV do not consider the residual stresses due to the complexity in quantifying and modelling these stresses in three dimensions [145]. Therefore, a suitable method of applying the residual stresses is not clear from the published literature.

As well as increasing the complexity of the mechanical model of the LV, further additions could be made to the model such as:

- including the right ventricle, which would require a third B-spline boundary

representation and more consideration for the material properties around the physical domain;

- including electromechanical effects such as the excitation of the muscle fibres causing active contraction of the myocardium; and/or
- including the fluid-solid interaction between the blood within the chambers of the heart and the variation in pressures.

Finally, during the conception of this project, the overall aim was to use this model alongside the medical data of patients to perform an inverse analysis. This would allow for estimation of the material properties of the heart based on the geometry from medical images and pressure values from catheterisation of the patient during the cardiac cycle. This would not be feasible with the model in its current state. However, generating a fully automated model of the heart with the MPM would mean that a clinician/analyst may simply input the medical data into this developed framework and an estimate of the material properties of a patient's myocardium would be produced with little user input. This would act as a useful tool in the medical community by freeing up a considerable amount of time that clinicians would typically spend working on cardiac models.

8.3 Final thoughts

Overall, this work has built a foundation for cardiac mechanical modelling of the human heart using the MPM framework. This initial model of the LV based on a patient's medical images has shown that the MPM can be used to improve the efficiency of model generation when compared to the typical FEM models presented in the current literature. And it is the hope of the author that the MPM can be more widely used in the Biomechanical Engineering field in the future as it can be a powerful tool for large deformation modelling.

References

[1] P. I. Aaronson, J. P. T. Ward and M. J. Connolly, *The Cardiovascular System at a Glance*, Fourth Edition. John Wiley & Sons, 2012.

[2] T. Adams, S. Giani and W. M. Coombs, 'A high-order elliptic PDE based level set reinitialisation method using a discontinuous Galerkin discretisation,' *Journal of Computational Physics*, vol. 379, 373–391, 2019.

[3] H. Akima, 'A New Method of Interpolation and Smooth Curve Fitting Based on Local Procedures,' *Journal of the Association for Computing Machinery*, vol. 17, no. 4, 589–602, 1970.

[4] G. Alfano and M. A. Crisfield, 'Solution strategies for the delamination analysis based on a combination of local-control arc-length and line searches,' *International Journal for Numerical Methods in Engineering*, vol. 58, no. 7, 999–1048, 2003.

[5] S. Andersen and L. Andersen, 'Analysis of spatial interpolation in the material-point method,' *Computers and Structures*, vol. 88, no. 7-8, 506–518, 2010.

[6] P. M. Anselone and R. H. Moore, 'An extension of the Newton-Kantorovič method for solving nonlinear equations with an application to elasticity,' *Journal of Mathematical Analysis and Applications*, vol. 13, no. 3, 476–501, 1966.

[7] A. Arani *et al.*, 'Cardiac MRI Elastography for Quantitative Assessment of Elevated Myocardial Stiffness in Cardiac Amyloidosis,' *Journal of Magnetic Resonance Imaging*, vol. 46, no. 5, 1361–1367, 2017.

[8] T. Arts, R. S. Reneman and P. C. Veenstra, 'A model of the mechanics of the left ventricle,' *Annals of Biomedical Engineering*, vol. 7, no. 3–4, 299–318, 1979.

[9] L. Asner *et al.*, 'Patient-specific modeling for left ventricular mechanics using data-driven boundary energies,' *Computer Methods in Applied Mechanics and Engineering*, vol. 314, 269–295, 2017.

[10] L. Asner, M. Hadjicharalambous, J. Lee and D. Nordsletten, 'STATCOM Challenge: Simulating Left Ventricular Mechanics in the Canine Heart,' in *Statistical Atlases and Computational Models of the Heart - Imaging and Modelling Challenges*, O. Camara, T. Mansi, M. Pop, K. Rhode, M. Sermesant and A. Young, Eds., Springer International Publishing, 2015, 123–134.

[11] R. Avazmohammadi, J. S. Soares, D. S. Li, S. S. Raut, R. C. Gorman and M. S. Sacks, 'A Contemporary Look at Biomechanical Models of Myocardium,' *Annual Review of Biomedical Engineering*, vol. 21, 417–442, 2019.

[12] AZO materials, *Silicone Rubber*, Webpage (`https://www.azom.com/properties.aspx?ArticleID=920`), Accessed 18/02/24.

[13] S. Bandara and K. Soga, 'Coupling of soil deformation and pore fluid flow using material point method,' *Computers and Geotechnics*, vol. 63, 199–214, 2015.

[14] S. G. Bardenhagen, 'Energy Conservation Error in the Material Point Method for Solid Mechanics,' *Journal of Computational Physics*, vol. 180, no. 1, 383–403, 2002.

[15] S. G. Bardenhagen, J. E. Guilkey, K. M. Roessig, J. U. Brackbill, W. M. Witzel and J. C. Foster, 'An Improved Contact Algorithm for the Material Point Method and Application to Stress Propagation in Granular Material,' *Computer Modeling in Engineering and Sciences*, vol. 2, no. 4, 509–522, 2001.

[16] S. G. Bardenhagen and E. M. Kober, 'The Generalized Interpolation Material Point Method,' *Computer Modeling in Engineering and Sciences*, vol. 5, no. 6, 477–496, 2004.

[17] T. Belytschko, W. K. Liu, B. Moran and K. I. Elkhordary, *Nonlinear Finite Elements for Continua and Structures*, Second Edition. Wiley, 2014.

[18] P. G. Bergan, G. Horrigmoe, B. Kråkeland and T. H. Søreide, 'Solution techniques for non-linear finite element problems,' *International Journal for Numerical Methods in Engineering*, vol. 12, no. 11, 1677–1696, 1978.

[19] P. G. Bergan and T. H. Søreide, 'Solution of large displacement and instability problems using the current stiffness parameter,' in *Finite Elements in Nonlinear Mechanics*, vol. 2, Tapir Trondheim, 1978, 647–669.

[20] D.-E. Bettendorff-Bakman, P. Schmid, P. P. Lunkenheimer and P. Niederer, 'A finite element study relating to the rapid filling phase of the human ventricles,' *Journal of Theoretical Biology*, vol. 238, 303–316, 2006.

[21] D.-E. Bettendorff-Bakman, P. Schmid, P. P. Lunkenheimer and P. Niederer, 'Diastolic ventricular aspiration: A mechanism supporting the rapid filling phase of the human ventricles,' *Journal of Theoretical Biology*, vol. 250, 581–592, 2008.

[22] L. Beuth, T. Benz, P. Vermeer and Z. Więckowski, 'Large deformation analysis using a quasi-static material point method,' *Journal of Theoretical and Applied Mechanics*, vol. 38, no. 1-2, 45–60, 2008.

[23] J. Bezanson, A. Edelman, S. Karpinski and V. B. Shah, 'Julia: A Fresh Approach to Numerical Computing,' *SIAM Review*, vol. 59, no. 1, 65–98, 2017.

[24] Y. Bing, M. Cortis, T. J. Charlton, W. M. Coombs and C. E. Augarde, 'B-spline based boundary conditions in the material point method,' *Computers and Structures*, vol. 212, 257–274, 2019.

[25] Y. Bing, 'B-spline based Boundary Method for the Material Point Method,' Masters Thesis, Durham University, 2017.

[26] P. Bo, R. Ling and W. Wang, 'A revisit to fitting parametric surfaces to point clouds,' *Computers and Graphics*, vol. 36, 534–540, 2012.

[27] W. Böhm, G. Farin and J. Kahmann, 'A survey of curve and surface methods in CAGD,' *Computer Aided Geometric Design*, vol. 1, 1–60, 1984.

[28] J. U. Brackbill, D. B. Koth and H. M. Ruppel, 'FLIP: A Low-Dissipation, Particle-in-Cell Method for Fluid Flow,' *Computer Physics Communications*, vol. 48, no. 1, 25–38, 1988.

[29] J. U. Brackbill and H. M. Ruppel, 'FLIP: A Method for Adaptively Zoned, Particle-in-Cell Calculations of Fluid Flows in Two Dimensions,' *Journal of Computational Physics*, vol. 65, no. 2, 314–343, 1986.

[30] R. Brannon, *Holey Particle Basis functions for 2D CPDI*, Blog post (`https://csmbrannon.net/2014/03/09/holey-particle-basis-functions-for-2d-cpdi/`), Accessed 13/11/23, Mar. 2014.

[31] E. Braunwald, 'Heart Failure,' *Journal of the American College of Cardiology: Heart Failure*, vol. 1, no. 1, 1–20, 2013.

[32] British Heart Foundation, *BHF Statistics Factsheet - UK*, Online (`https://www.bhf.org.uk/what-we-do/our-research/heart-statistics`), Accessed 05/03/24, Jan. 2024.

[33] M. Bürg, L. J. Lim and R. Brinkgreve, 'Application of a Second-order Implicit Material Point Method,' *Procedia Engineering*, vol. 175, 279–286, 2017.

[34] J. Burghardt, R. Brannon and J. Guilkey, 'A nonlocal plasticity formulation for the material point method,' *Computer Methods in Applied Mechanics and Engineering*, vol. 225-228, 55–64, 2012.

[35] R. K. Burla and A. V. Kumar, 'Implicit boundary method for analysis using uniform B-spline basis and structured grid,' *International Journal for Numerical Methods in Engineering*, vol. 76, no. 13, 1993–2028, 2008.

[36] E. Burman, 'Ghost penalty (La pénalisation fantôme),' *Comptes Rendus Mathematique*, vol. 348, no. 21–22, 1217–1220, 2010.

[37] E. Burman, S. Claus, P. Hansbo, M. G. Larson and A. Massing, 'CutFEM: Discretizing geometry and partial differential equations,' *International Journal for Numerical Methods in Engineering*, vol. 104, 472–501, 2015.

[38] E. Burman, D. Elfverson, P. Hansbo, M. G. Larson and K. Larsson, 'Shape optimization using the cut finite element method,' *Computer Methods in Applied Mechanics and Engineering*, vol. 328, 242–261, 2018.

[39] I. Carol, C. M. López and O. Roa, 'Micromechanical analysis of quasi-brittle materials using fracture-based interface elements,' *International Journal for Numerical Methods in Engineering*, vol. 52, no. 1–2, 193–215, 2001.

[40] E. Carrera, 'A study on arc-length-type methods and their operation failures illustrated by a simple model,' *Computers and Structures*, vol. 50, no. 2, 217–229, 1994.

[41] S. Cassidy *et al.*, 'Cardiac structure and function are altered in type 2 diabetes and Non-alcoholic fatty liver disease and associate with glycemic control,' *Cardiovascular Diabetology*, vol. 14, no. 23, 1–11, 2015.

[42] P. Chadwick and R. W. Ogden, 'A Theorem of Tensor Calculus and its Application to Isotropic Elasticity,' *Archive for Rational Mechanics and Analysis*, vol. 44, 54–68, 1971.

[43] T. J. Charlton, W. M. Coombs and C. E. Augarde, 'iGIMP: An implicit generalised interpolation material point method for large deformations,' *Computers and Structures*, vol. 190, 108–125, 2017.

[44] K. Chatterjee and B. Massie, 'Systolic and Diastolic Heart Failure: Differences and Similarities,' *Journal of Cardiac Failure*, vol. 13, no. 7, 569–576, 2007.

[45] Z. Chen, W. Hu, L. Shen, X. Xin and R. Brannon, 'An evaluation of the MPM for simulating dyamic failure with damage diffusion,' *Engineering Fracture Mechanics*, vol. 69, no. 17, 1873–1890, 2002.

[46] Z. Chen and R. Brannon, 'An Evaluation of the Material Point Method,' Sandia National Laboratories, Tech. Rep., 2002.

[47] Z. Chen, S. Jiang, Y. Gan, H. Liu and T. D. Sewell, 'A particle-based multiscale simulation procedure within the material point framework,' *Computational Particle Mechanics*, vol. 1, 147–158, 2014.

[48] K. Chong *et al.*, 'Visualization of vascular injuries in extremity trauma,' *Medical and Biological Engineering and Computing*, vol. 55, 1709–1718, 2017.

[49] C. J. Chuong and Y. C. Fung, 'Three-Dimensional Stress Distribution in Arteries,' *Journal of Biomechanical Engineering*, vol. 105, no. 3, 268–274, 1983.

[50] B. Cochelin, 'A path-following technique via an asymptotic-numerical method,' *Computers and Structures*, vol. 53, no. 5, 1181–1192, 1993.

[51] C. J. Coetzee, 'Discrete and continuum modelling of soil cutting,' *Computational Particle Mechanics*, vol. 1, 409–423, 2014.

[52] C. J. Coetzee, A. H. Basson and P. A. Vermeer, 'Discrete and continuum modelling of excavator bucket filling,' *Journal of Terramechanics*, vol. 44, no. 2, 177–186, 2007.

[53] C. J. Coetzee, P. A. Vermeer and A. H. Basson, 'The modelling of anchors using the material point method,' *International Journal for Numerical and Analytical Methods in Geomechanics*, vol. 29, no. 9, 879–895, 2005.

[54] C. A. Conti *et al.*, 'Left ventricular modelling: a quantitative functional assessment tool based on cardiac magnetic resonance imaging,' *Interface Focus*, vol. 1, no. 3, 384–395, 2011.

[55] W. M. Coombs, 'Ghost stabilisation of the material point method for stable quasi-static and dynamic analysis of large deformation problems,' *International Journal for Numerical Methods in Engineering*, vol. 124, no. 21, 4841–4875, 2023.

[56] W. M. Coombs and C. E. Augarde, 'AMPLE: A Material Point Learning Environment,' *Advances in Engineering Software*, vol. 139, 102748, 2020.

[57] W. M. Coombs, T. J. Charlton, M. Cortis and C. E. Augarde, 'Overcoming volumetric locking in material point methods,' *Computer Methods in Applied Mechanics and Engineering*, vol. 333, 1–21, 2018.

[58] W. M. Coombs, O. A. Petit and Y. G. Motlagh, 'NURBS plasticity: Yield surface representation and implicit stress integration for isotropic inelasticity,' *Computer Methods in Applied Mechanics and Engineering*, vol. 304, 342–358, 2016.

[59] W. M. Coombs *et al.*, 'On Lagrangian mechanics and the implicit material point method for large deformation elasto-plasticity,' *Computer Methods in Applied Mechanics and Engineering*, vol. 358, 112622, 2020.

[60] W. M. Coombs, 'Finite deformation of particlulate geomaterials: frictional and anisotropic Critical State elasto-plasticity,' PhD Thesis, Durham University, Jun. 2011.

[61] M. Cortis, W. M. Coombs, C. E. Augarde, M. Brown, A. Brennan and S. Robinson, 'Imposition of essential boundary conditions in the material point method,' *International Journal for Numerical Methods in Engineering*, vol. 113, no. 1, 130–152, 2018.

[62] K. D. Costa, P. J. Hunter, J. S. Wayne, L. K. Waldman, J. M. Guccione and A. D. McCulloch, 'A Three-Dimensional Finite Element Method for Large Elastic Deformations of Ventricular Myocardium: II - Prolate Spheroidal Coordinates,' *Journal of Biomechanical Engineering*, vol. 118, no. 4, 464–472, 1996.

[63] K. D. Costa, J. W. Holmes and A. D. McCulloch, 'Modelling Cardiac Mechanical Properties in Three Dimensions,' *Philosophical Transactions: Mathematical, Physical and Engineering Sciences*, vol. 359, no. 1783, 1233–1250, 2001.

[64] M. G. Cox, 'The Numerical Evaluation of B-Splines,' *IMA Journal of Applied Mathematics*, vol. 10, no. 2, 134–149, 1972.

[65] M. A. Crisfield, 'A fast incremental/iterative solution procedure that handles "snap-through",' *Computers and Structures*, vol. 13, 55–62, 1981.

[66] M. A. Crisfield, *Non-linear Finite Element Analysis of Solids and Structures*, First Edition, John Wiley & Sons, Ed. John Wiley & Sons, 1991.

[67] P. Dahal, *Layers of the Heart: Epicardium, Myocardium, Endocardium*, Online (`https://microbenotes.com/layers-of-the-heart/`), Accessed 06/03/24, Aug. 2023.

[68] S. Dattani, V. Samborska, H. Ritchie and M. Roser, 'Cardiovascular Diseases,' *Our World in Data*, 2023, Online (`https://ourworldindata.org/cardiovascular-diseases`), Accessed 05/03/24.

[69] C. de Boor, *A Practical Guide to Splines*, First Edition, ser. Applied Mathematical Sciences. Springer New York, NY, 1978.

[70] C. de Boor, 'On calculating with B-splines,' *Journal of Approximation Theory*, vol. 6, no. 1, 50–62, 1972.

[71] R. de Borst, M. A. Crisfield, J. J. C. Remmers and C. V. Verhoosel, *Non-Linear Finite Element Analysis of Solids and Structures*, Second Edition. John Wiley & Sons, 2012.

[72] P. d. de Casteljau, *Shape mathematics and CAD*, First Edition. Kogan Page, 1986.

[73] P. de Koster, R. Tielen, E. Wobbes and M. Möller, 'Extension of B-spline Material Point Method for unstructured triangular grids using Powell-Sabin splines,' *Computational Particle Mechanics*, vol. 8, 273–288, 2021.

[74] E. A. de Souza Neto, F. M. Andrade Pires and D. R. J. Owen, 'F-bar based linear triangles and tetrahedra for finite strain analysis of nearly incompressible solids. Part I: formulation and benchmarking,' *International Journal for Numerical Methods in Engineering*, vol. 62, no. 3, 353–383, 2005.

[75] E. A. de Souza Neto, D. Perić, M. Dutko and D. R. J. Owen, 'Design of Simple Low Order Finite Elements for Large Strain Analysis of Nearly Incompressible Solids,' *International Journal of Solids and Structures*, vol. 33, no. 22-22, 3277–3296, 1996.

[76] E. A. de Souza Neto, D. Perić and D. R. J. Owen, *Computational Methods for Plasticity: Theory and Applications*, John Wiley & Sons Ltd, Ed. Wiley, 2008.

[77] A. de Vaucorbeil, V. P. Nguyen, S. Sinaie and J. Y. Wu, 'Material point method after 25 years: theory, implementation and applications,' *Advances in Applied Mechanics*, vol. 53, 185–398, 2020.

[78] G. Del Corso, R. Verzicco and F. Viola, 'A fast computational model for the electrophysiology of the whole human heart,' *Journal of Computational Physics*, vol. 457, 111084, 2022.

[79] L. L. Demer and F. C. Yin, 'Passive biaxial mechanical properties of isolated canine myocardium,' *Journal of Physiology*, vol. 339, 615–630, 1983.

[80] J. W. Demmel, 'On condition numbers and the distance to the nearest ill-posed problem,' *Numerische Mathematik*, vol. 51, 251–289, 1987.

[81] O. Devillers, S. Pion and M. Teillaud, 'Walking in a triangulation,' *International Journal of Foundations of Computer Science*, vol. 13, no. 2, 181–199, 2002.

[82] T. R. Dhakal and D. Z. Zhang, 'Material point methods applied to one-dimensional shoch waves and dual domain material point method with sub-points,' *Journal of Computational Physics*, vol. 325, 301–313, 2016.

[83] M. Ding, X. Han, S. Wang, T. F. Gast and J. M. Teran, 'A thermomechanical material point method for baking and cooking,' *ACM Transactions on Graphics*, vol. 38, no. 6, 2019, Article 192.

[84] T. Dokken, T. Lyche and K. F. Pettersen, 'Polynomial splines over locally refined box-partitions,' *Computer Aided Geometric Design*, vol. 30, no. 3, 331–356, 2013.

[85] S. Dokos, B. H. Smaill, A. A. Young and I. J. LeGrice, 'Shear properties of passive ventricular myocardium,' *American Journal of Physiology - Heart and Circulatory Physiology*, vol. 283, no. 6, H2650–H2659, 2002.

[86] F. Dorri, P. F. Neiderer and P. P. Lunkenheimer, 'A finite element model of the human left ventricular systole,' *Computer Methods in Biomechanics and Biomedical Engineering*, vol. 9, no. 5, 319–341, 2006.

[87] F. Dorri, 'A finite element model of the human left ventricular systole, taking into account the fibre orientation pattern,' PhD Thesis, Swiss Federal Institue of Technology Zurich, 2004.

[88] R. Doste *et al.*, 'A rule-based method to model myocardial fiber orientation in cardiac biventricular geometries with outflow tracts,' *International*

Journal for Numerical Methods in Biomedical Engineering, vol. 35, no. 4, e3185, 2019.

[89] T. C. Doyle and J. L. Ericksen, 'Nonlinear Elasticity,' *Advances in Applied Mechanics*, vol. 4, 53–115, 1956.

[90] R. Emig *et al.*, 'Passive myocardial mechanical properties: meaning, measurement, models,' *Biophysical Reviews*, vol. 13, no. 5, 587–610, 2021.

[91] A. Eriksson, 'Structural instability analyses based on generalised path-following,' *Computer Methods in Applied Mechanics and Engineering*, vol. 156, no. 1–4, 45–74, 1998.

[92] T. S. E. Eriksson, A. J. Prassl, G. Plank and G. A. Holzapfel, 'Influence of myocardial fiber/sheet orientation on left ventricular mechanical contraction,' *Mathematics and Mechanics of Solids*, vol. 18, no. 6, 592–606, 2013.

[93] M. W. Evans, F. H. Harlow and E. Bromberg, 'The Particle-in-Cell Method for Hydrodynamic Calculations,' Los Alamos Scientific Laboratory of the University of California, Tech Report, 1957.

[94] M. Fafard and B. Massicotte, 'Geometrical interpretation of the arc-length method,' *Computers and Structures*, vol. 46, no. 4, 603–615, 1993.

[95] Z. Fang, A. N. Ranslow and R. H. Kraft, 'Computational micromechanics of trabecular porcine skull bone using the material point method,' in *ASME International Mechanical Engineering Congress and Exposition*, Article 2602047, vol. 3, 2016.

[96] L. Feng, H. Gao and X. Luo, 'Whole-heart modelling with valves in a fluid-structure interaction framework,' *Computer Methods in Applied Mechanics and Engineering*, vol. 420, 116724, 2024.

[97] Y. T. Feng, D. Perić and D. R. J. Owen, 'A new criterion for derermination of initial loading parameter in arc-length methods,' *Computers and Structures*, vol. 58, no. 3, 479–485, 1996.

[98] Y. T. Feng, D. Perić and D. R. J. Owen, 'Determination of travel directions in path-following methods,' *Mathematical and Computer Modelling*, vol. 21, no. 7, 43–59, 1995.

[99] E. Fern, A. Rohe, K. Soga and E. Alonso, *The Material Point Method for Geotechnical Engineering: A Practical Guide*, E. Fern, A. Rohe, K. Soga and E. Alonso, Eds. Taylor & Francis, 2019.

[100] S. Fernández-Méndez and A. Huerta, 'Imposing essential boundary conditions in mesh-free methods,' *Computer Methods in Applied Mechanics and Engineering*, vol. 193, 1257–1275, 2004.

[101] S. Foster, 'An application of the arc length method involving concrete cracking,' *International Journal for Numerical Methods in Engineering*, vol. 33, no. 2, 269–285, 1992.

[102] I. Fried, 'Finite element analysis of incompressible material by residual energy balancing,' *International Journal of Solids and Structures*, vol. 10, no. 9, 993–1002, 1974.

[103] Y. C. Fung, *Biomechanics: Mechanical Properties of Living Tissues*, Second Edition. Springer-Verlag, 1993.

[104] Y. Gan, Z. Sun, Z. Chen, X. Zhang and Y. Liu, 'Enhancement of the material point method using B-spline basis functions,' *International Journal for Numerical Methods in Engineering*, vol. 113, no. 3, 411–431, 2017.

[105] H. Gao, W. G. Li, L. Cai, C. Berry and X. Y. Luo, 'Parameter estimation in a Holzapfel-Ogden law for healthy myocardium,' *Journal of Engineering Mathematics*, vol. 95, 231–248, 2015.

[106] N. D. Gavin, G. Pretti, W. M. Coombs, J. C. Brigham and C. E. Augarde, 'On the implementation of a material point-based arc-length method,' *International Journal for Numerical Methods in Engineering*, vol. 125, no. 9, e7438, 2024.

[107] D. C. Gaze, Ed., *The Cardiovascular System: Physiology, Diagnostics and Clinical Implications*. IntechOpen, 2012.

[108] M. Genet, L. C. Lee, B. Baillargeon, J. M. Guccione and E. Kuhl, 'Modeling Pathologies of Diastolic and Systolic Heart Failure,' *Annals of Biomedical Engineering*, vol. 44, 112–127, 2016.

[109] M. Genet *et al.*, 'Distribution of normal human left ventricular myofiber stress at end diastole and end systole: a target for in silico design of heart failure treatments,' *Journal of Applied Physiology*, vol. 117, 142–152, 2014.

[110] C. Giannelli, B. Jüttler and H. Speleers, 'THB-splines: The truncates basis for hierarchical splines,' *Computer Aided Geometric Design*, vol. 29, no. 7, 485–498, 2012.

[111] F. A. Gilabert, V. Cantavella, E. Sánchez and G. Mallol, 'Modelling fracture process in ceramic materials using the Material Point Method,' *EPL (Europhysics Letters)*, vol. 96, no. 2, 24002, 2011.

[112] S. H. Gilbert, A. P. Benson, P. Li and A. V. Holden, 'Regional localisation of left ventricular sheet structure: integration with current models of cardiac fibre, sheet and band structure,' *European Journal of Cardio-thoracic Surgery*, vol. 32, 231–249, 2007.

[113] A. Gilmanov and S. Acharya, 'A hybrid immersed boundary and material point method for simulation 3D fluid-structure interaction problems,' *International Journal for Numerical Methods in Fluids*, vol. 56, no. 12, 2151–2177, 2007.

[114] L. Glass, P. Hunter and A. McCulloch, *Theory of heart: biomechanics, biophysics, and nonlinear dynamics of cardiac function*. New York: Springer-Verlag, 1991.

[115] S. Göktepe, S. N. S. Acharya, J. Wong and E. Kuhl, 'Computational modeling of passive myocardium,' *International Journal for Numerical Methods in Biomedical Engineering*, vol. 27, 1–12, 2011.

[116] S. Göktepe, O. J. Abilez and E. Kuhl, 'A generic approach towards finite growth with examples of athlete's heart, cardiac dilation, and cardiac wall thickening,' *Journal of the Mechanics and Physics of Solids*, vol. 58, no. 10, 1661–1680, 2010.

[117] S. Göktepe and E. Kuhl, 'Electromechanics of the heart: A unified approach to the strongly coupled excitation-contraction problem,' *Computational Mechanics*, vol. 45, no. 2–3, 227–243, 2010.

[118] R. P. Grant, 'Notes on the Muscular Architecture of the Left Ventricle,' *Circulation*, vol. 32, 301–308, 1965.

[119] R. A. Greenbaum, S. Y. Ho, D. G. Gibson, A. E. Becker and R. H. Anderson, 'Left ventricular fibre architecture in man,' *British Heart Journal*, vol. 45, no. 3, 248–263, 1981.

[120] W. Grossman, D. Jones and L. P. McLaurin, 'Wall stress and patterns of hypertrophy in the human left ventricle,' *The Journal of Clinical Investigation*, vol. 56, no. 1, 56–64, 1975.

[121] D. Guan, J. Yao, X. Luo and H. Gao, 'Effect of myofibre archituecture on ventricular pump function by using a neonatal porcine heart model: from DT-MRI to rule-based methods,' *Royal Society Open Science*, vol. 7, no. 4, 191655, 2020.

[122] J. M. Guccione, A. D. McCulloch and L. K. Waldman, 'Passive Material Properties of Intact Ventricular Myocardium Determined From a Cylindrical Model,' *Journal of Biomechanical Engineering*, vol. 113, no. 1, 42–55, 1991.

[123] J. M. Guccione, K. D. Costa and A. D. McCulloch, 'Finite Element Stress Analysis of Left Ventricular Mechanics in the Beating Dog Heart,' *Journal of Biomechanics*, vol. 28, no. 10, 1167–1177, 1995.

[124] J. E. Guilkey, J. B. Hoying and J. A. Weiss, 'Computational modelling of multicellular constructs with the material point method,' *Journal of Biomechanics*, vol. 39, 2074–2086, 2006.

[125] J. E. Guilkey and J. A. Weiss, 'Implicit time integration for the material point method: Quantitative and algorithmic comparisons with the finite element method,' *International Journal for Numerical Methods in Engineering*, vol. 57, 1323–1338, Jul. 2003.

[126] Y. Guo and J. A. Nairn, 'Calculation of J-Integral and Stress Intensity Factors using the Material Point Method,' *Computer Modeling in Engineering and Sciences*, vol. 6, no. 3, 295–308, 2004.

[127] Y. J. Guo and J. A. Nairn, 'Three-Dimensional Dynamic Fracture Analysis Using the Material Point Method,' *Computer Modeling in Engineering and Sciences*, vol. 16, no. 3, 141–156, 2006.

[128] A. C. Guyton and J. E. Hall, *Textbook of Medical Physiology*, Eleventh Edition. Elsevier, 2006.

[129] J. E. Hall and A. C. Guyton, *Guyton and Hall: Textbook of Medical Physiology*, Thirteenth Edition. Elsevier, 2016.

[130] K. Hallsworth *et al.*, 'Cardiac structure and function are altered in adults with non-alcoholic fatty liver disease,' *Journal of Hepatology*, vol. 58, no. 4, 757–762, 2013.

[131] F. M. Hamad, 'Formulation of a Dynamic Material Point Method and Applications to Soil-Water-Geotextile Systems,' Ph.D. dissertation, University of Stuttgart, May 2014.

[132] X. Han, T. F. Gast, Q. Guo, S. Wang, C. Jiang and J. Teran, 'A Hybrid Material Point Method for Frictional Contact with Diverse Materials,' *Proceedings of the ACM on Computer Graphics and Interactive Techniques*, vol. 2, no. 2, 1–24, 2019, Article 17.

[133] S. Hartmann and P. Neff, 'Polyconvexity of generalized polynomial-type hyperelastic strain energy functions for near-incompressibility,' *International Journal of Solids and Structures*, vol. 40, no. 11, 2767–2791, 2003.

[134] A. Haselbacher, F. M. Najjar and J. P. Ferry, 'An efficient and robust particle-localization algorithm for unstructured grids,' *Journal of Computational Physics*, vol. 225, no. 2, 2198–2213, 2007.

[135] A. I. Hassaballah, M. A. Hassan, A. N. Mardi and M. Hamdi, 'An Inverse Finite Element Method for Determining the Tissue Compressibility of Human Left Ventricular Wall during the Cardiac Cycle,' *PLoS ONE*, vol. 8, no. 12, e82703, 2013.

[136] D. M. Haughton and R. W. Ogden, 'Bifurcation of inflated circular cylinders of elastic material under axial loading - II. Exact theory for thick-walled tubes,' *Journal of the Mechanics and Physics of Solids*, vol. 27, no. 5–6, 489–512, 1979.

[137] A. Heidari *et al.*, 'Patient-specific finite element analysis of heart failure and the impact of surgical intervention in pulmonary hypertension secondary to mitral valave disease,' *Medical and Biological Engineering and Computing*, vol. 60, 1723–1744, 2022.

[138] H.-B. Hellweg and M. A. Crisfield, 'A new arc-length method for handling sharp snap-backs,' *Computers and Structures*, vol. 66, no. 5, 704–709, 1998.

[139] Y. Higo, F. Oka, S. Kimoto, Y. Marinaka, Y. Goto and Z. Chen, 'A Coupled MPM-FDM Analysis Method for Multi-Phase Elasto-Plastic Soils,' *Soils and Foundations*, vol. 50, no. 4, 515–532, 2010.

[140] K. Höllig, C. Apprich and A. Streit, 'Introduction to the Web-method and its applications,' *Advances in Computational Mathematics*, vol. 23, no. 1–2, 215–237, 2005.

[141] K. Höllig and U. Reif, 'Nonuniform web-splines,' *Computer Aided Geometric Design*, vol. 20, no. 5, 277–294, 2003.

[142] K. Höllig, U. Reif and J. Wipper, 'Weighted Extended B-Spline Approximation of Dirichlet Problems,' *SIAM Journal on Numerical Analysis*, vol. 39, no. 2, 442–462, 2001.

[143] K. G. Hollingsworth, A. M. Blamire, B. D. Keavney and G. A. MacGowan, 'Left ventricular torsion, energetics, and diastolic function in normal human aging,' *American Journal of Physiology - Heart and Circulatory Physiology*, vol. 302, no. 4, H885–92, 2012.

[144] K. G. Hollingsworth *et al.*, 'Subepicardial dysfunction leads to global left ventricular systolic impairment in patients with limb girdle muscular dystrophy 2I,' *Eurpoean Journal of Heart Failure*, vol. 15, no. 9, 986–994, 2014.

[145] G. A. Holzapfel and R. W. Ogden, 'Constitutive modelling of passive myocardium: a structurally based framework for material characterization,' *Philosophical Transactions of the Royal Society A: Mathematical, Physical and Engineering Sciences*, vol. 367, no. 1902, 3445–3475, 2009.

[146] B. D. Hong, M. J. Moulton and T. W. Secomb, 'Modeling left ventricular dynamics with characteristic deformation modes,' *Biomechanics and Modeling in Mechanobiology*, vol. 18, no. 6, 1683–1696, 2019.

[147] C. O. Horgan and G. Saccomandi, 'A new constitutive theory for fibre-reinforces incompressible nonlinearly elastic solids,' *Journal of the Mechanics and Physics of Solids*, vol. 53, no. 9, 1985–2015, 2005.

[148] G. A. Hrinda, 'Geometrically Nonlinear Static Analysis of 3D Trusses Using the Arc-length Method,' in *WIT Transactions on Modelling and Simulation*, WIT Press, Ed., vol. 46, 2007, 243–252.

[149] W. Hu and Z. Chen, 'A multi-mesh MPM for simulating the meshing process of spur gears,' *Computers and Structures*, vol. 81, no. 20, 1991–2002, 2003.

[150] W. Hu and Z. Chen, 'Model-based simulation of the synergistic effects of blast and fragmentation on a concrete wall using the MPM,' *International Journal of Impact Engineering*, vol. 32, no. 12, 2066–2096, 2006.

[151] P. Huang, X. Zhang, S. Ma and X. Huang, 'Contact algorithms for the material point method in impact and penetration simulation,' *International Journal for Numerical Methods in Engineering*, vol. 85, no. 4, 498–517, 2010.

[152] T. J. R. Hughes, J. A. Cottrell and Y. Bazilevs, 'Isogeometric analysis: CAD, finite elements, NURBS, exact geometry and mesh refinement,' *Computer Methods in Applied Mechanics and Engineering*, vol. 194, 4135–4195, 2005.

[153] J. D. Humphrey, R. K. Strumpf and F. C. Yin, 'Determination of a constitutive relation for passive myocardium: I. A new functional form,' *Journal of Biomechanical Engineering*, vol. 112, no. 3, 333–339, 1990.

[154] J. D. Humphrey and F. C. Yin, 'Constitutive relations and finite deformations of passive cardiac tissue II: stress analysis in the left ventricle,' *Circulation Research*, vol. 65, no. 3, 805–817, 1989.

[155] J. D. Humphrey and F. C. Yin, 'On constitutive relations and finite deformations of passive cardiac tissue: I. A pseudostrain-enery function,' *Journal of Biomechanical Engineering*, vol. 109, no. 4, 298–304, 1987.

[156] P. J. Hunter, M. P. Nash and G. B. Sands, 'Computational Biology of the Heart,' in A. V. Panfilov and A. V. Holden, Eds. John Wiley & Sons, 1997, ch. Computational Electromechanics of the Heart, 345–407.

[157] P. J. Hunter, B. H. Smaill, P. M. F. Nielsen and I. J. Le Grice, 'Computational Biology of the Heart,' in A. V. Panfilov and A. V. Holden, Eds. John Wiley & Sons, 1997, ch. A Mathematical Model of Cardiac Anatomy, 171–215.

[158] L. D. Huyer *et al.*, 'Biomaterial based cardiac tissue engineering and its applications,' *Biomedical Materials*, vol. 10, no. 3, 034004, 2015.

[159] I. Ionescu, J. Guilkey, M. Berzins, R. M. Kirby and J. Weiss, 'Computational simulation of penetrating trauma in biological soft tissues using the Material Point Method,' *Studies in Health Technology and Informatics*, vol. 111, 213–218, 2005.

[160] I. Ionescu, J. E. Guilkey, M. Berzins, R. M. Kirby and J. A. Weiss, 'Simulation of Soft Tissue Failure Using the Material Point Method,' *Journal of Biomechanical Engineering*, vol. 128, no. 6, 917–924, 2006.

[161] I. Ionescu, J. A. Weiss, J. Guilkey, M. Cole, R. M. Kirby and M. Berzins, 'Ballistic injury simulation using the Material Point Method,' *Studies in Health Technology and Informatics*, vol. 119, 228–233, 2006.

[162] D. G. Jakovljevic *et al.*, 'Effect of Physical Activity on Age-Related Changes in Cardiac Function and Performance in Women,' *Circulation: Cardiovascular Imaging*, vol. 8, no. 1, e002086, 2015.

[163] I. Jassim, D. Stolle and P. Vermeer, 'Two-phase dynamic analysis by the material point method,' *International Journal for Numerical and Analytical Methods in Geomechanics*, vol. 37, no. 15, 2502–2552, 2012.

[164] M. Jaworska-Wilczynska, P. Trzaskoma, A. A. Szczepankiewicz and T. Hryniewiecki, 'Paricardium: structure and function in health and disease,' *Folia Histochemica et Cytobiologica*, vol. 54, no. 3, 121–125, 2016.

[165] C. Jiang, T. Gast and J. Teran, 'Anisotropic elastoplasticity for cloth, knit and hair frictional contact,' *ACM Transactions on Graphics*, vol. 36, no. 4, 2017, Article 152.

[166] C. Kadapa, 'A simple extrapolated predictor for overcoming the starting and tracking issues in the arc-length method for nonlinear structural mechanics,' *Engineering Structures*, vol. 234, 111755, 2021.

[167] C. Kadapa, 'Novel quadratic Bézier triangular and tetrahedral elements using existing mesh generators: Extension to nearly incompressible implicit and explicit elastodynamics in finite strains,' *International Journal for Numerical Methods in Engineering*, vol. 119, no. 2, 75–104, 2019.

[168] C. Kadapa, 'Novel quadratic Bézier triangular and tetrahedral elements using mesh generators: Applications to linear nearly incompressible elastostatics and implicit and explicit elastodynamics,' *International*

Journal for Numerical Methods in Engineering, vol. 117, no. 5, 543–573, 2018.

[169] I. K. J. al-Kafaji, 'Formulation of a Dynamic Material Point Method (MPM) for Geomechanical Problems,' PhD Thesis, University of Stuttgart, 2013.

[170] K. Kamojjala, R. Brannon, A. Sadeghirad and J. Guilkey, 'Verification tests in solid mechanics,' *Engineering with Computers*, vol. 31, 193–213, 2015.

[171] E. Kayvanpour *et al.*, 'Towards Personalized Cardiology: Multi-Scale Modeling of the Failing Heart,' *PLoS ONE*, vol. 10, no. 7, e0134869, 2015.

[172] R. C. P. Kerckhoffs, M. L. Neal, Q. Gu, J. B. Bassingthwaighte, J. H. Omens and A. D. McCulloch, 'Coupling of a 3D Finite Element Model of Cardiac Ventricular Mechanics to Lumped Systems Models of the Systemic and Pulmonary Circulation,' *Annals of Biomedical Engineering*, vol. 35, 1–18, 2007.

[173] G. Klár *et al.*, 'Druker-prager elastoplasticity for sand animation,' *ACM Transactions on Graphics*, vol. 35, no. 4, 2016, Article a103.

[174] D. Klepach *et al.*, 'Growth and remodeling of the left ventricle: A case study of myocardial infarction and surgical ventricular restoration,' *Mechanics Research Communities*, vol. 42, 134–141, 2012.

[175] W. T. Koiter, 'The stability of elastic equilibrium (translated from Dutch),' Airforce Flight Dynamics Laboratory, Wright-Patterson Air Force Base, Ohio, Tech. Rep. AFFDL-TR-70-25, Feb. 1970.

[176] A. Krishnamurthy *et al.*, 'Patient-specific models of cardiac biomechanics,' *Journal of Computational Physics*, vol. 244, 4–21, 2013.

[177] A. V. Kumar, R. Burla, S. Padmanabhan and L. Gu, 'Finite Element Analysis Using Nonconforming Mesh,' *Journal of Computing and Information Science in Engineering*, vol. 8, no. 3, 031005, 2008.

[178] A. V. Kumar, S. Padmanabhan and R. Burla, 'Implicit boundary method for finite element analysis using non-conforming mesh or grid,' *International Journal for Numerical Methods in Engineering*, vol. 74, 1421–1447, 2008.

[179] J. H. Kweon and C. S. Hong, 'An improved arc-length method for postbuckling analysis of composite cylindrical panels,' *Computers and Structures*, vol. 53, no. 3, 541–549, 1994.

[180] W. F. Lam and C. T. Morley, 'Arc-length Method for Passing Limit Points in Structural Calculation,' *Journal of Structural Engineering*, vol. 118, no. 1, 169–185, 1992.

[181] L. C. Lee *et al.*, 'Patient-specific finite element modeling of the Cardiokinetix Parachute device: effects on left ventricular wall stress and function,' *Medical and Biological Engineering and Computing*, vol. 52, 557–566, 2014.

[182] W.-N. Lee *et al.*, 'Mapping myocardial fibre orientation using echocardiography-based shear wave imaging,' *IEEE Transactions on Medical Imaging*, vol. 31, no. 3, 554–562, 2012.

[183] I. J. LeGrice, P. J. Hunter and B. H. Small, 'Laminar structure of the heart: a mathematical model,' *American Journal of Physiology - Heart and Circulatory Physiology*, vol. 272, no. 5, 2466–2476, 1997.

[184] I. J. LeGrice, B. H. Smaill, L. Z. Chai, S. G. Edgar, J. B. Gavin and P. J. Hunter, 'Laminar structure of the heart: ventricular myocyte arrangement and connective tissue architecture in the dog,' *American Journal of Physiology - Heart and Circulatory Physiology*, vol. 269, no. 2, H571–H582, 1995.

[185] I. LeGrice, P. Hunter, A. Young and B. Smaill, 'The architecture of the heart: a data-based model,' *Philosophical Transactions of the Royal Society of London. Series A: Mathematical, Physical and Engineering Sciences*, vol. 359, no. 1783, 1217–1232, 2001.

[186] S. Leroch, P. G. Grützmacher, H. Heckes and S. J. Eder, 'Towards a multi-abrasie grinding model for the material point method,' *Frontiers in Manufacturing Technology*, vol. 3, 1114414, 2023.

[187] M. Lev and C. S. Simkins, 'Architecture of the human ventricular myocardium; technic for study using a modification of the Mall-MacCallum method,' *Laboratory Investigation*, vol. 5, no. 5, 396–409, 1956.

[188] J. R. Levick, *An Introduction to Cardiovascular Physiology*, Fifth Edition, H. Arnold, Ed. Hodder Arnold, 2010.

[189] F. Li, J. Pan and C. Sinka, 'Modelling adhesive contact between fine particles using the material point method,' *Mechanics of Materials*, vol. 43, no. 3, 157–167, 2011.

[190] F. Li, J. Pan and C. Sinka, 'Modelling brittle impact failure of disc particles using material point method,' *International Journal of Impact Engineering*, vol. 38, no. 7, 653–660, 2011.

[191] J. G. Li, Y. Hamamoto, Y. Liu and X. Zhang, 'Sloshing impact simulation with material point method and its experimental validations,' *Computers and Fluids*, vol. 103, 86–99, 2014.

[192] M. Li, Y. Lei, D. Gao, Y. Hu and X. Zhang, 'A novel material point method (MPM) based needle-tissue interaction model,' *Computer Methods in Biomechanics and Biomedical Engineering*, vol. 24, no. 12, 1393–1407, 2021.

[193] W. Li, 'Biomechanics of infarcted left ventricle: a review of modelling,' *Biomedical Engineering Letters*, vol. 10, no. 3, 387–417, 2020.

[194] Y. P. Lian, X. Zhang and Y. Liu, 'An adaptive finite element material point method and its application in extreme deformation problems,' *Computer Methods in Applied Mechanics and Engineering*, vol. 241-244, 275–285, 2012.

[195] Y. P. Lian, X. Zhang and Y. Liu, 'Coupling of finite element method with material point method by local multi-mesh contact method,' *Computer Methods in Applied Mechanics and Engineering*, vol. 200, no. 47-48, 3482–3494, 2011.

[196] Y. Lian, J. Chen, M.-J. Li and R. Gao, 'A multi-lysics material point method for thermo-fluid-solid coupling problems in metal additive manufacturing processes,' *Computer Methods in Applied Mechanics and Engineering*, vol. 416, 116297, 2023.

[197] W. Liang and J. Zhao, 'Multiscale modeling of large deformation in geomechanics,' *International Journal for Numerical and Analytical Methods in Geomechanics*, vol. 43, no. 5, 1080–1114, 2019.

[198] Y. Liang, J. Given and K. Soga, 'The imposition of nonconforming Neumann boundary condition in the material point method without boundary representation,' *Computer Methods in Applied Mechanics and Engineering*, vol. 404, 115785, 2023.

[199] Y. Liu, X. Qiu, H. Ma, W. Fu and T. X. Yu, 'A study of woodpecker's pecking process and the impact response of its brain,' *International Journal of Impact Engineering*, vol. 108, 263–271, 2017.

[200] Y. Liu, X. Qiu, X. Zhang and T. X. Yu, 'Response of a Woodpeckers's Head during Pecking Process Simulated by Material Point Method,' *PLoS ONE*, vol. 10, no. 4, e0122677, 2005.

[201] Z. Liu *et al.*, 'Material Point Simulation Method for Concrete Medium Fracture and Fragmentation under Blast Loading,' *Applied Sciences*, vol. 13, no. 14, 8533, 2023.

[202] C. C. Long, D. Z. Zhang, C. A. Bronkhorst and G. T. Gray III, 'Rpresenting ductile damage with the dual domain material point method,' *Computer Methods in Applied Mechanics and Engineering*, vol. 300, 611–627, 2016.

[203] E. Love and D. L. Sulsky, 'An energy-consistent material-point method for dynamic finite deformation plasticity,' *International Journal for Numerical Methods in Engineering*, vol. 65, no. 10, 1608–1638, 2006.

[204] E. Love and D. L. Sulsky, 'An unconditionally stable, energy-momentum consistent implementation of the material-point method,' *Computer Methods in Applied Mechanics and Engineering*, vol. 195, no. 33-36, 3903–3925, 2006.

[205] K. Lu, C. E. Augarde, W. M. Coombs and Z. Hu, 'Weak impositions of Dirichlet boundary conditions in solid mechanics : a critique of current approaches and extension to partially prescribed boundaries,' *Computer Methods in Applied Mechanics and Engineering*, vol. 348, 632–659, 2019.

[206] Y.-C. Lu *et al.*, 'A 3D Computational Head Model Under Dynamic Head Rotation and Head Extension Validated Using Live Human Brain Data, Including the Falx and the Tentorium,' *Annals of Biomedical Engineering*, vol. 47, no. 9, 1923–1940, 2019.

[207] A. Lv, Y. Zhu and C. Xian, 'Efficient cloth simulation based on the material point method,' *Computer Animation and Virtual Worlds*, vol. 33, no. 3-4, e2073, 2022.

[208] S. Ma, X. Zhang and X. M. Qiu, 'Comparison study of MPM and SPH in modeling hypervelocity impact problems,' *International Journal of Impact Engineering*, vol. 36, no. 2, 272–282, 2009.

[209] X. Ma, P. T. Giguere, B. Jayaraman and D. Z. Zhang, 'Distribution coefficient algorithm for small mass nodes in material point method,' *Journal of Computational Physics*, vol. 229, no. 20, 7819–7833, 2010.

[210] P. Mackenzie-Helnwein, P. Arduino, W. Shin, J. A. Moore and G. R. Miller, 'Modeling strategies for multiphase drag interactions using the material point method,' *International Journal for Numerical Methods in Engineering*, vol. 83, no. 3, 295–322, 2010.

[211] A. A. Madadi and B. Dortdivanlioglu, 'A subdivision-stabilized B-spline mixed material point method,' *Computer Methods in Applied Mechanics and Engineering*, vol. 418, no. B, 116567, 2024.

[212] M. T. Maeder and D. M. Kaye, 'Heart Failure With Normal Left Ventricular Ejection Fraction,' *Journal of the American College of Cardiology*, vol. 53, no. 11, 905–918, 2009.

[213] S. S. Martin *et al.*, '2024 Heart Disease and Stroke Statistics: A Report of US and Global Data From the American Heart Association,' *Circulation*, vol. 149, no. 8, e347–e913, 2024.

[214] C. M. Mast, *Representing Arbitrary Bounding Surfaces in the Material Point Method*, 6th MPM Workshop, Albuquerque, New Mexico (`https://math.unm.edu/~sulsky/MPMWorkshop/Abstracts.html`), Accessed 15/03/24, Aug. 2010.

[215] C. M. Mast, P. Arduino, G. R. Miller and P. Mackenzie-Helwein, 'Avalanche and landslide simulation using the material point method: Flow dynamics and force interaction with structures,' *Computational Geosciences*, vol. 18, no. 5, 817–830, 2014.

[216] C. M. Mast, P. Mackenzie-Helnwein, P. Arduino and G. R. Miller, 'Landslide and Debris Flow-Induced Static and Dynamic Loads on Protective Structures,' in *Multiscale and Multiphysics Processes in Geomechanics*, R. I. Borja, Ed., Springer Berlin Heidelberg, 2011, 169–172.

[217] J. Matthews, 'Coordinate-free rotation formalism,' *American Journal of Physics*, vol. 44, 1210, 1976.

[218] B. Memon and X. Su, 'Arc-length technique for nonlinear finite element analysis,' *Journal of Zhejiang University Science*, vol. 5, no. 5, 618–628, 2004.

[219] C. Miehe, 'Comparison of Two Algorithms for the Computation of Fourth-Order Isotropic Tensor Functions,' *Computers and Structures*, vol. 66, no. 1, 37–43, 1998.

[220] D. Mojsejenko *et al.*, 'Estimating passive mechanical properties in a myocardial infarction using MRI and finite element simulations,' *Biomechanics and Modeling in Mechanobiology*, vol. 14, 633–647, 2015.

[221] J. Mojumder *et al.*, 'Computational analysis of ventricular mechanics in hypertropic cardiomyopathy patients,' *Scientific Reports*, vol. 13, 958, 2023.

[222] Y. G. Motlagh and W. M. Coombs, 'An Implicit High-order Material Point Method,' *Procedia Engineering*, vol. 175, 8–13, 2017.

[223] J. G. Murphy, 'Transversely isotropic biological, soft tissue must be modelled using both anisotropic invariants,' *European Journal of Mechanics - A/Solids*, vol. 42, 90–96, 2013.

[224] J. C. Nagtegaal, D. M. Parks and J. R. Rice, 'On numerically accurate finite element solutions in the fully plastic range,' *Computer Methods in Applied Mechanics and Engineering*, vol. 4, no. 2, 153–177, 1974.

[225] A. Nair and S. Roy, 'Implicit Time Integration in the Generalized Interpolation Material Point Method for Finite Deformation Hyperelasticity,' *Mechanics of Advanced Materials and Structures*, vol. 19, no. 6, 465–473, 2012.

[226] J. A. Nairn, 'Material Point Method Calculations with Explicit Cracks,' *Computer Modeling in Engineering and Sciences*, vol. 4, no. 6, 649–663, 2003.

[227] S. Nemat-Nasser and H. D. Shatoff, 'Numerical analysis of pre- and post-critical response of elastic continua at finite strains,' *Computers and Structures*, vol. 3, no. 5, 983–999, 1973.

[228] V. P. Nguyen, C. T. Nguyen, T. Rabczuk and S. Natarajan, 'On a family of convected particle domain interpolations in the material point method,' *Finite Elements in Analysis and Design*, vol. 126, 50–64, 2017.

[229] V. P. Nguyen, A. de Vaucorbeil and S. Bordas, *The Material Point Method: Theory, Implementations and Applications*. Springer Cham, 2023.

[230] D. W. Nicholson, 'Stiff arc length constraint in nonlinear FEA,' *Acta Mechanica*, vol. 175, 123–137, 2005.

[231] S. A. Niederer, K. S. Campbell and S. G. Campbell, 'A short history of the development of mathemtical models of cardiac mechanics,' *Journal of Molecular and Cellular Cardiology*, vol. 127, 11–19, 2019.

[232] A. Nikou *et al.*, 'Computational Modeling of Healthy Myocardium in Diastole,' *Annals of Biomedical Engineering*, vol. 44, no. 4, 980–992, 2016.

[233] X. Ning and S. Pellegrino, 'Imperfection-insensitive axially loaded thin cylindrical shells,' *International Journal of Solids and Structures*, vol. 62, 39–51, 2015.

[234] D. J. O'Shea, M. M. Attard and D. C. Kellermann, 'On fibre dispersion in anisotropic soft biological tissues using fourth-order structural tensors,' *International Journal of Solids and Structures*, vol. 236–237, 111052, 2022.

[235] J. T. Oden, *Finite elements of nonlinear continua*. London: McGraw-Hill, 1972.

[236] R. W. Ogden, 'Large deformation isotropic elasticity - on the correlation of theory and experiment for incompressible rubberlike solids,' *Proceedings of the Royal Society of London. A. Mathematical and Physical Sciences*, vol. 326, no. 1567, 565–584, 1972.

[237] R. W. Ogden, *Non-Linear Elastic Deformations*. Dover Publications, 1997.

[238] S. Okhovatian, M. H. Mohammadi, N. Rafatian and M. Radisic, 'Engineering Models of the Heart Left Ventricle,' *ACS Biomaterials Science and Engineering*, vol. 8, no. 6, 2144–2160, 2022.

[239] J. H. Omens and Y. C. Fung, 'Residual Strain in Rat Left Ventricle,' *Circulation Research*, vol. 66, no. 1, 37–45, Jan. 1990.

[240] A. Palit, S. K. Bhudia, T. N. Arvanitis, G. A. Turley and M. A. Williams, 'Computational modelling of left-ventricular diastolic mechanics: Effect of fibre orientation and right ventricle topology,' *Journal of Biomechanics*, vol. 48, 604–612, 2015.

[241] A. Palit, P. Franciosa, S. K. Bhudia, T. N. Arvanitis, G. A. Turley and M. A. Williams, 'Passive diastolic modelling of human ventricles: Effect of base movement and geometrical heterogeneity,' *Journal of Biomechanics*, vol. 52, 95–105, 2017.

[242] A. Palit *et al.*, 'Effect of Fibre Orientation on Diastolic Mechanics of Human Ventricle,' in *2015 37th Annual International Conference of the IEEE Engineering in Medicine and Biology Society (EMBC)*, 2015, 6523–6526.

[243] J. D. Parikh, K. G. Hollingsworth, D. Wallace, A. M. Blamire and G. A. MacGowan, 'Left ventricular functional, structural and energetic effects of normal aging: Comparison with hypertension,' *PLoS ONE*, vol. 12, no. 5, e0177404, 2017.

[244] H. Parisch, 'Efficient non-linear finite element shell formulation involving large strains,' *Engineering Computations*, vol. 3, no. 2, 121–128, 1986.

[245] S. Pezzuto and D. Ambrosi, 'Active contraction of the cardiac ventricle and distortion of the microstructural architecture,' *International Journal for Numerical Methods in Biomedical Engineering*, vol. 30, no. 12, 1578–1596, 2014.

[246] N. T. V. Phuong, A. F. van Tol, A. S. K. Elkadi and A. Rohe, 'Numerical investigation of pile installation effects in sand using material point method,' *Computers and Geotechnics*, vol. 73, 58–71, 2016.

[247] L. A. Piegl, 'Interactive Data Interpolation by Rational Bezier Curves,' *IEEE Computer Graphics and Applications*, vol. 7, 45–58, 1987.

[248] L. A. Piegl and W. Tiller, *The NURBS book*, Second Edition. Springer, 1997.

[249] G. Powell and J. Simons, 'Improved Iteration Strategy for Nonlinear Structures,' *International Journal for Numerical Methods in Engineering*, vol. 17, 1455–1467, 1981.

[250] M. J. D. Powell and M. A. Sabin, 'Piecewise Quadratic Approximations on Triangles,' *ACM Transactions on Mathematical Software*, vol. 3, no. 4, 316–325, 1977.

[251] G. Pretti, W. M. Coombs and C. E. Augarde, 'A displacement-controlled arc-length solution scheme,' *Computers and Structures*, vol. 258, 106674, 2022.

[252] N. S. Pruijn, 'The improvement of the material point method by increasing efficiency and accuracy,' M.S. thesis, Delft Unoversity of Technology, Delft, Netherlands, 2016.

[253] A. Quarteroni, L. Dedè and F. Regazzoni, 'Modeling the cardiac electromechanical function: A mathematical journey,' *Bulletin of the American Mathematical Society*, vol. 59, no. 2, 2022.

[254] E. Ramm, 'Strategies for Tracing the Nonlinear Response Near Limit Points,' in *Nonlinear Finite Element Analysis in Structural Mechanics*, W. Wunderlich, E. Stein and K.-J. Bathe, Eds., Berlin, Heidelberg: Springer Berlin Heidelberg, 1981, 63–89.

[255] A. Rania, N. Benameur, T. Kraiem and S. Labibi, 'Finite Element of Biomechanical Model of the Human Myocardium from a Cardiac MRI Images,' in *Proceedings of Seventh International Congress on Information and Communication Technology*, X. S. Yang, S. Sherratt, N. Dey and A. Joshi, Eds., ser. Lecture Notes in Networks and Systems, vol. 464, Singapore: Springer, 2022, 73–81.

[256] S. N. Al-Rasby, 'Solution techniques in nonlinear structural analysis,' *Computers and Structures*, vol. 40, no. 4, 985–993, 1991.

[257] S. Reese and P. Wriggers, 'A stabilization technique to avoiding hourglassing in finite elasticty,' *International Journal for Numerical Methods in Engineering*, vol. 48, no. 1, 79–109, 2000.

[258] G. Remmerswaal, 'Development and implementation of moving boundary conditions in the Material Point Method,' Masters Thesis, Delft University of Technology, 2017.

[259] G. Renner, 'A Method of Shape Description for Mechanical Engineering Practice,' *Computers in Industry*, vol. 3, 137–142, 1982.

[260] E. Riks, 'An incremental approach to the solution of snapping and buckling problems,' *International Journal of Solids and Structures*, vol. 15, no. 7, 529–551, 1979.

[261] E. Riks, 'Some computational aspects of the stability analysis of nonlinear structures,' *Computer Methods in Applied Mechanics and Engineering*, vol. 47, no. 3, 219–259, 1984.

[262] E. Riks, 'The Application of Newton's Method to the Problem of Elastic Stability,' *Journal of Applied Mechanics*, vol. 39, no. 4, 1060–1065, 1972.

[263] M. Ritto-Corrêa and D. Camotim, 'On the arc-length and other quadratic control methods: Established, less known and new implementation procedures,' *Computers and Structures*, vol. 86, no. 11–12, 1353–1368, 2008.

[264] P. Rossignol, A. F. Hernandez, S. D. Solomon and F. Zannad, 'Heart failure drug treatment,' *The Lancet*, vol. 393, no. 10175, 1034–1044, 2019.

[265] A. Sadeghirad, R. M. Brannon and J. Burghardt, 'A convected particle domain interpolation technique to extend applicability of the material point method for problems involving massive deformations,' *International Journal for Numerical Methods in Engineering*, vol. 86, no. 12, 1435–1456, 2011.

[266] A. Sadeghirad, R. M. Brannon and J. E. Guilkey, 'Second-order convected particle domain interpolation (CPDI2) with enrichment for weak

discontinuities at material interfaces,' *International Journal for Numerical Methods in Engineering*, vol. 95, no. 11, 928–952, 2013.

[267] G. B. Sands, D. A. G. andDarren A. Hooks, C. R. Green, B. H. Smaill and I. J. LeGrice, 'Automated imaging of extended tissue volumes using confocal microscopy,' *Microscopy Research and Technique*, vol. 67, no. 5, 227–239, 2005.

[268] H. Schmid, M. P. Nash, A. A. Young and P. J. Hunter, 'Myocardial Material Parameter Estimation - A Comparative Study for Simple Shear,' *Journal of Biomechanical Engineering*, vol. 128, no. 5, 742–750, 2006.

[269] P. Schmid, P. Niederer, P. P. Lunkenheimer and F. Torrent-Guasp, 'The anisotropic structure of the human left and right ventricles,' *Technology and Health Care*, vol. 5, 29–43, 1997.

[270] C. Schreck and C. Wojtan, 'A Practical Method for Animating Anisotropic Elastoplastic Materials,' in *Eurographics 2020*, D. Panozzo and U. Assarsson, Eds., vol. 39, Wiley and Sons Ltd., 2020, 89–100.

[271] K. H. Schweizerhof and P. Wriggers, 'Consistent linearization for path following methods in FE analysis,' *Computer Methods in Applied Mechanics and Engineering*, vol. 59, no. 3, 261–279, 1986.

[272] J. J. Shen, F. Y. Xu and W. A. Yang, 'Finite element analysis of left ventricle during cardiac cycles in viscoelasticity,' *Computers in Biology and Medicine*, vol. 75, 63–73, 2016.

[273] L. Shen and Z. Chen, 'A Slient Boundary Scheme with the Material Point Method for Dynamic Analyses,' *Computer Modeling in Engineering and Sciences*, vol. 7, no. 3, 305–320, 2005.

[274] W. Shen, G. R. Miller, P. Arduino and P. Mackenzie-Helnwein, 'Dynamic Meshing for Material Point Method Computations,' *World Academy of Science, Engineering and Technology*, vol. 4, no. 8, 379–387, 2010.

[275] J. C. Simo and R. L. Taylor, 'Quasi-incompressible finite elasticity in principal stretches. continuum basis and numerical algorithms,' *Computer Methods in Applied Mechanics and Engineering*, vol. 85, no. 3, 273–310, 1991.

[276] W. T. Sołowski *et al.*, 'Material point method: Overview and challenges ahead,' *Advances in Applied Mechanics*, vol. 54, 113–204, 2021.

[277] A. J. M. Spencer, *Continuum Mechanics*. Dover Publications Inc., 2004.

[278] M. Steffen, P. C. Wallstedt, J. E. Guilkey, R. M. Kirby and M. Berzins, 'Examination and Analysis of Implentation Choices within the Material Point Method (MPM),' *Computer Modeling in Engineering and Sciences*, vol. 31, no. 2, 107–128, 2008.

[279] M. Steffen, R. M. Kirby and M. Berzins, 'Analysis and Reduction of Quadrature Errors in the Material Point Method (MPM),' *International Journal for Numerical Methods in Engineering*, vol. 76, no. 6, 922–948, 2008.

[280] M. Steffen, R. M. Kirby and M. Berzins, 'Decoupling and balancing of space and time errors in the material point method (MPM),' *International Journal for Numerical Methods in Engineering*, vol. 82, no. 10, 1207–1243, 2010.

[281] C. Stevens, E. Remme, I. LeGrice and P. Hunter, 'Ventricular mechanics in diastole: material parameter sensitivity,' *Journal of Biomechanics*, vol. 36, no. 5, 737–748, 2003.

[282] S. Sticko, G. Ludvigsson and G. Kreiss, 'High-order cut finite elements for the elastic wave equation,' *Advances in Computational Mathematics*, vol. 46, no. 45, 2020.

[283] A. Stomakhin, C. Schroeder, L. Chai, J. Teran and A. Selle, 'A material point method for snow simulation,' *ACM Transactions on Graphics*, vol. 32, no. 4, 1–10, Jul. 2013.

[284] A. Stomakhin, C. Schroeder, C. Jiang, L. Chai, J. Teran and A. Selle, 'Augmented MPM for phase-change and varied materials,' *ACM Transactions on Graphics*, vol. 33, no. 4, 2014, Article 138.

[285] D. D. Streeter Jr. and D. L. Bassett, 'An engineering analysis of myocardial fiber orientation in pig's left ventricle in systole,' *The Anatomical Record*, vol. 155, no. 4, 503–511, 1966.

[286] D. D. Streeter Jr., H. M. Spotnitz, D. P. Patel, J. Ross Jr. and E. H. Sonnenblick, 'Fiber Orientation in the Canine Left Ventricle during Diastole and Systole,' *Circulation Research*, vol. 24, 339–347, 1969.

[287] D. Sulsky, Z. Chen and H. L. Schreyer, 'A particle method for history-dependent materials,' *Computer Methods in Applied Mechanics and Engineering*, vol. 118, 179–196, 1994.

[288] D. Sulsky and A. Kaul, 'Implicit dynamics in the material-point method,' *Computer Methods in Applied Mechanics and Engineering*, vol. 193, no. 12, 1137–1170, 2004.

[289] D. Sulsky and H. L. Schreyer, 'Axisymmetric form of the material point method with applications to upsetting and Taylor impact problems,' *Computer Methods in Applied Mechanics and Engineering*, vol. 139, no. 1-4, 409–429, 1996.

[290] D. Sulsky, S.-J. Zhao and H. L. Schreyer, 'Application of a particle-in-cell method to solid mechanics,' *Computer Physics Communications*, vol. 87, 236–252, 1995.

[291] K. Sun *et al.*, 'A Computationally Efficient Formal Optimization of Regional Myocardial Contractility in a Sheep with Left Ventricular Aneurysm,' *Journal of Biomechanical Engineering*, vol. 131, no. 11, 111001, 2009.

[292] T. Sussman and K.-J. Bathe, 'A finite element formulation for nonlinear incompressible elastic and inelastic analysis,' *Computers and Structures*, vol. 26, no. 1–2, 357–409, 1987.

[293] L. A. Taber, *Nonlinear Theory of Elasticity. Applications in Biomechanics*, First Edition. World Scientific Publishing, 2004.

[294] L. A. Taber, M. Yang and W. W. Podszus, 'Mechanics of Ventricular Torsion,' *Journal of Biomechanics*, vol. 29, no. 6, 745–752, 1996.

[295] X. G. Tan, R. N. Saunders and A. Bagchi, 'Coupled Modeling for Investigation of Blast Induced Traumatic Brain Injury,' in *VII International Conference on Computational Methods for Coupled Problems in Science and Engineering, Coupled Problems 2017*, M. Papdrakakis, E. Oñate and B. Schrefler, Eds., vol. 2017, Jun. 2017, 462–473.

[296] J. M. T. Thompson and A. C. Walker, 'A general theory for the branching analysis of discrete structural systems,' *International Journal of Solids and Structures*, vol. 5, no. 4, 281–288, 1969.

[297] R. Tielen, E. Wobbes, M. Möller and L. Beuth, 'A High Order Material Point Method,' *Procedia Engineering*, vol. 175, 265–272, 2017.

[298] S. Timoshenko and J. N. Goodier, *Theory of Elasticity*, Third Edition, McGraw-Hill, Ed. McGraw-Hill, 1970.

[299] M. Torre, S. Morganti, F. S. Pasqualini and A. Preali, 'Current progress toward isogeommetric modeling of the heart biophysics,' *Biophysics Reviews*, vol. 4, 041301, 2023.

[300] F. Torrent-Guasp *et al.*, 'Towards new understanding of the heart structure and function,' *European Journal of Cardio-thoracic Surgery*, vol. 27, no. 2, 191–201, 2005.

[301] F. Torrent-Guasp, W. F. Whimster and K. Redmann, 'A silicone rubber mould of the heart,' *Technology and Health Care*, vol. 5, 13–20, 1997.

[302] N. Tueni, J.-M. Allain and M. Genet, 'On the structural origin of the anisotropy in the myocardium: Multiscale modeling and analysis,' *Journal of the Mechanical Behaviour of Biomedical Materials*, vol. 138, 105600, 2023.

[303] K. Upadhyay *et al.*, 'Data-driven uncertainty quantification in computational human head models,' *Computer Methods in Applied Mechanics and Engineering*, vol. 398, 115108, 2022.

[304] T. P. Usyk, R. Mazhari and A. D. McCulloch, 'Effect of Laminar Orthotropic Myofiber Architecture on Regional Stress and Strain in the Canine Left Ventricle,' *Journal of Elasticity and the Physical Science of Solids*, vol. 61, 143–164, 2000.

[305] T. P. Usyk, I. J. LeGrice and A. D. McCulloch, 'Computational model of three-dimensional cardiac electromechanics,' *Computing and Visualization in Science*, vol. 4, 249–257, 2002.

[306] L. C. van Griethuysen, 'Analysis of a Nuclear Reactor Boiler Closure Unit Through Development of a 3D Parallel Finite Element Code,' Ph.D. dissertation, Durham University, 2012.

[307] S. Venkatesan, *What is the mechanism of pericardial rub?* Blog post (`https://drsvenkatesan.com/2008/09/28/what-is-the-mechanism-of-pericardial-rub/`), Accessed 09/05/21, Sep. 2008.

[308] A. I. Veress, G. T. Gullberg and J. A. Weiss, 'Measurement of Strain in the Left Ventricle during Diastole with cine-MRI and Deformable Image Registration,' *Journal of Biomedical Engineering*, vol. 127, no. 7, 1195–1207, 2005.

[309] F. J. Vetter and A. D. McCulloch, 'Three-Dimensional Stress and Strain in Passive Rabbit Left Ventricle: A Model Study,' *Annals of Biomedical Engineering*, vol. 28, no. 7, 781–792, 2000.

[310] F. J. Villareal, W. Y. Lew, L. K. Waldman and J. W. Covell, 'Transmural Myocardial Deformation in the Ischemic Canine Left Ventricle,' *Circulation Research*, vol. 68, no. 2, 368–381, 1991.

[311] F. Viola, G. Del Corso and R. Verzicco, 'High-fidelity model of the human heart: An immersed boundary implementation,' *Physical Review Fluids*, vol. 8, no. 10, 100502, 2023.

[312] L. K. Waldman, Y. C. Fung and J. W. Covell, 'Transmural Myocardial Deformation in the Canine Left Ventricle: Normal in Vivo Three-Dimensional Finite Strains,' *Circulation Research*, vol. 57, no. 1, 152–163, 1985.

[313] L. K. Waldman, D. Nosan, F. Villareal and J. W. Covell, 'Relation between transmural deformation and local myofiber direction in canine left ventricle,' *Circulation Research*, vol. 63, no. 3, 550–562, 1988.

[314] A. C. Walker, 'A non-linear finite element analysis of shallow circular arches,' *International Journal of Solids and Structures*, vol. 5, no. 2, 97–107, 1969.

[315] P. C. Wallstedt and J. E. Guilkey, 'A weighted least squares particle-in-cell method for solid mechanics,' *International Journal for Numerical Methods in Engineering*, vol. 85, no. 13, 1687–1704, 2011.

[316] P. C. Wallstedt and J. E. Guilkey, 'An evaluation of explicit time integration schemes for use with the generalized interpolation material point method,' *Journal of Computational Physics*, vol. 227, no. 22, 9628–9642, 2008.

[317] B. Wang, P. J. Vardon, M. A. Hicks and Z. Chen, 'Development of an implicit material point method for geotechnical applications,' *Computers and Geotechnics*, vol. 71, 159–167, 2016.

[318] H. M. Wang *et al.*, 'A modified Holzapfel-Ogden law for a residually stressed finite strain model of the human left ventricle in diastole,' *Biomechanics and Modeling in Mechanobiology*, vol. 13, 99–113, 2014.

[319] H. M. Wang *et al.*, 'Structure-based finite strain modelling of the human left ventricle in diastole,' *International Journal for Numerical Methods in Biomedical Engineering*, vol. 29, 83–103, 2013.

[320] L. Wang *et al.*, 'On the use of domain-based material point methods for problems involving large distortion,' *Computer Methods in Applied Mechanics and Engineering*, vol. 355, 1003–1025, 2019.

[321] L. Wang *et al.*, 'An efficient and locking-free material point method for three-dimensional analysis with simplex elements,' *International Journal for Numerical Methods in Engineering*, vol. 122, no. 15, 3876–3899, 2021.

[322] V. Y. Wang, H. I. Lam, D. B. Ennis, B. R. Cowan, A. A. Young and M. P. Nash, 'Modelling passive diastolic mechanics with quantitative MRI of cardiac structure and function,' *Medical Image Analysis*, vol. 13, 773–784, 2009.

[323] Y. Wang and H. Waisman, 'An arc-length method for controlled cohesive crack propagation using high-order XFEM and Inwin's crack closure integral,' *Engineering Fracture Mechanics*, vol. 199, 235–256, 2018.

[324] Y. Wang, H. G. Beom, M. Sun and S. Lin, 'Numerical simulation of explosive welding using the material point method,' *International Journal of Impact Engineering*, vol. 38, no. 1, 51–60, 2011.

[325] Z. J. Wang *et al.*, 'Efficient estimation of load-free left ventricular geoemetry and passive myocardial properties using principal component analysis,' *International Journal for Numerical Methods in Biomedical Engineering*, vol. 36, no. 3, 1–17, 2020.

[326] G. A. Wempner, 'Discrete approximations related to nonlinear theories of solids,' *International Journal of Solids and Structures*, vol. 7, no. 11, 1581–1599, 1971.

[327] J. F. Wenk *et al.*, 'Biventricular Finite Element Modeling of the Acorn CorCap Cardiac Support Device on a Failing Heart,' *The Annals of Thoracic Surgery*, vol. 95, no. 6, 2022–2027, 2013.

[328] J. F. Wenk *et al.*, 'Regional Left Ventricular Myocardial Contractility and Stress in a Finite Element Model of Posterobasal Myocardial Infarction,' *Journal of Biomechanical Engineering*, vol. 133, no. 4, 044501, 2011.

[329] S. C. White and P. M. Weaver, 'Towards imperfection insensitive buckling response of shell structures-shells with plate-like post-buckled responses,' *The Aeronautical Journal*, vol. 120, no. 1224, 233–253, 2016.

[330] Z. Więckowski, 'The material point method in large strain engineering problems,' *Computer Methods in Applied Mechanics and Engineering*, vol. 193, no. 39-41, 4417–4438, 2004.

[331] R. Willems, K. L. P. M. Janssens, P. H. M. Bovendeerd, C. V. Verhoosel and O. van der Sluis, 'An isogeomtric analysis framework for ventricular cardiac mechanics,' *Computational Mechanics*, vol. 73, 465–506, 2023.

[332] A. D. Wisneski *et al.*, 'Left Ventricle Biomechanics of Low-Flow, Low-Gradient Aortic Stenosis: A Patient-Specific Computational Model,' *Frontiers in Physiology*, vol. 13, 848011, 2022.

[333] J. Wolper *et al.*, 'AnisoMPM: Animating Aniostropic Damage Mechanics,' *ACM Transactions on Graphics*, vol. 39, no. 4, 2020, Article 37.

[334] Y. Yamaguchi, S. Moriguchi and K. Terada, 'Extended B-spline-based implicit material point method,' *International Journal For Numerical Methods in Engineering*, vol. 122, no. 7, 1746–1769, 2020.

[335] F. C. P. Yin, R. K. Strumpf, P. H. Chew and S. L. Zeger, 'Quantification of the mechanical properties of noncontracting canine myocardium under simultaneous biaxial loading,' *Journal of Biomechanics*, vol. 20, no. 6, 577–589, 1987.

[336] A. R. York III, D. Sulsky and H. L. Schreyer, 'The material point method for simulation of thin membranes,' *International Journal for Numerical Methods in Engineering*, vol. 44, no. 10, 1429–1456, 1999.

[337] A. A. Young, I. J. LeGrice, M. A. Young and B. H. Smaill, 'Extended confocal microscopy of myocardial laminae and collagen network,' *Journal of Microscopy*, vol. 192, no. 2, 139–150, 1998.

[338] J. Yu, J. Zhao, W. Liang and S. Zhao, 'A semi-implicit material point method for coupled thermo-hydro-mechanical simulation of saturated porous media in large deformation,' *Computer Methods in Applied Mechanics and Engineering*, vol. 418, no. A, 116462, 2024.

[339] W.-H. Yuan, H. Zheng, X. Zheng, B. Wang and W. Zhang, 'An improved semi-implicit material point method for simulating large deformation problems in saturated geomaterials,' *Computers and Geotechnics*, vol. 161, 105614, 2023.

[340] P. A. Yushkevich *et al.*, 'User-guided 3D active contour segmentation of anatomical structures: Significantly improved efficiency and reliability,' *Neuroimage*, vol. 31, no. 3, 1116–1128, 2006, (`www.itksnap.org`).

[341] C. Zhang, H. Zhu and H. Li, 'Modeling pipe-soil interaction under vertical downward relative offset using B-spline material point method,' *Journal of Rock Mechanics and Geotechnical Engineering*, vol. 15, no. 6, 1520–1534, 2023.

[342] D. D. Zhang, X. Ma and P. T. Giguere, 'Material point method enhances by modified gradient of shape function,' *Journal of Computational Physics*, vol. 230, no. 16, 6379–6398, 2011.

[343] H. W. Zhang, K. P. Wang and Z. Chen, 'Material point method for dynamic analysis of saturated porous media under external contact/impact of solid bodies,' *Computer Methods in Applied Mechanics and Engineering*, vol. 198, no. 17-20, 1456–1472, 2009.

[344] L. W. Zhang, A. S. Ademiloye and K. M. Liew, 'Meshfree and Particle Methods in Biomechanics: Prospects and Challenges,' *Archives of Computational Methods in Engineering*, vol. 26, 1547–1576, 2019.

[345] W. Zhang and L. Zhao, 'Exact imposition of inhomogeneous Dirichlet boundary conditions based on weighted finite cell method and level-set function,' *Computer Methods in Applied Mechanics and Engineering*, vol. 307, 316–338, 2016.

[346] W. Zhang, L. Zhao and S. Cai, 'Shape optimization of Dirichlet boundaries based on weighted B-spline finute cell method and level-set function,' *Computer Methods in Applied Mechanics and Engineering*, vol. 294, 359–383, 2015.

[347] W. Zhang, J. Jilberto, G. Sommer, M. S. Sacks, G. A. Holzapfel and D. A. Nordsletten, 'Simulating hyperelasticity and fractional viscoelasticity in the human heart,' *Computer Methods in Applied Mechanics and Engineering*, vol. 411, 116048, 2023.

[348] X. Zhang, K. Y. Sze and S. Ma, 'An explicit material point finite element method for hyper-velocity impact,' *International Journal for Numerical Methods in Engineering*, vol. 66, no. 4, 689–706, 2005.

[349] X. Zhang, Z. Chen and Y. Liu, *The Material Point Method: A Continuum-Based Particle Method for Extreme Loading Cases*. Elsevier, 2017.

[350] Z. Zhang and A. V. Kumar, 'Immersed boundary modal analysis and forced vibration simulation using step boundary method,' *Finite Elements in Analysis and Design*, vol. 126, 1–12, 2017.

[351] X. Zheng *et al.*, 'A material point/finite volume method for coupled shallow water flows and large dynamic deformations in seabeds,' *Computers and Geotechnics*, vol. 162, 105673, 2023.

[352] S. Zhou, J. Stormont and Z. Chen, 'Simulation of geomembrane response to settlement in landfills by using the material point method,' *International Journal for Numerical and Analytical Methods in Geomechanics*, vol. 23, no. 15, 1977–1994, 1999.

[353] X. Zhou, Y. Hua and Z. Sun, 'Application of Cross model for granular flow and impact analysis using three-dimensional B-spline material point method,' *Journal of Non-Newtonian Fluid Mechanics*, vol. 322, 105145, 2023.